Sorption of small polar molecules on micro- and mesoporous zeolitic materials

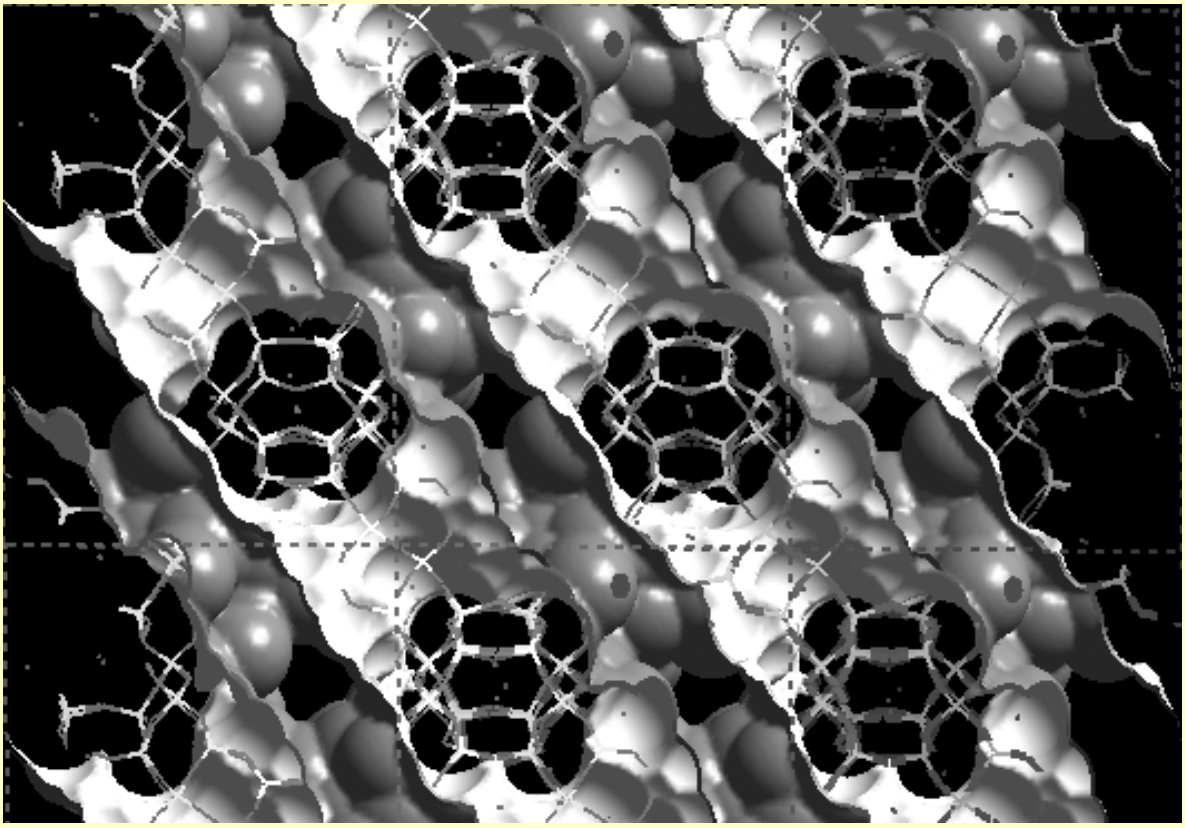

Renate Schenkel

Institut für Technische Chemie, Lehrstuhl II

Sorption of small polar molecules on micro- and mesoporous zeolitic materials

Renate Schenkel

Vollständiger Abdruck der von der Fakultät für Chemie der Technischen Universität München zur Erlangung des akademischen Grades eines

Doktors der Naturwissenschaften (Dr. rer. nat.)

genehmigten Dissertation.

Vorsitzender: Univ.-Prof. Dr. Th. F. Fässler

Prüfer der Dissertation:

1. Univ.-Prof. Dr. J. A. Lercher
2. Univ.-Prof. Dr. K. Köhler

Die Dissertation wurde am 02.02.2004 bei der Technischen Universität München eingereicht und durch die Fakultät für Chemie am 08.03.2004 angenommen.

"Um klar zu sehen, genügt oft ein Wechsel der Blickrichtung."

Antoine de Saint-Exupery

für meine Eltern,
meine Oma und
all meine Schwestern

Danksagung

Enschede, Niederlande, wurde für mich während meiner Diplomarbeit zur weiten Welt und die internationale Gruppe von Prof. Johannes A. Lercher zu einer zweiten Familie. Nach unserem Umzug zurück in meine Geburtsstadt München entschied ich mich aufgrund der wissenschaftlich-thematischen Herausforderung und des harmonischen Arbeitsklimas zu einer Promotion unter der Leitung von Johannes.

Ich danke Dir, Johannes, für die Überlassung dieses hochinteressanten Dissertationsthemas. Angesichts ihrer inhaltlichen Vielfalt hat mich die Arbeit sofort angesprochen und ich habe sie mit Freude durchgeführt. Zudem hast Du mir durch Deine fundierten, fachlichen Kenntnisse und großzügige finanzielle Unterstützung die Möglichkeit gegeben, wissenschaftliche Untersuchungen an diversen Großforschungseinrichtungen durchzuführen, an fachlichen und fachübergreifenden Fortbildungen teilzunehmen und meine anerkannten Ergebnisse auf diversen nationalen, wie internationalen Konferenzen erfolgreich zu präsentieren. Danke Johannes, in Deiner Gruppe arbeiten zu dürfen hat mein Leben sehr bereichert und meine persönliche Entwicklung stark gefördert.

Ein herzliches Dankeschön an all meine ehemaligen und jetzigen Betreuer und Kollegen unterschiedlichster Nationalität für unsere gemeinsame Zeit. Unter Euch habe ich viele Freunde gefunden und Eurer Unterstützung konnte ich mir ausnahmslos jederzeit sicher sein. Am Institut in München sind bzw. waren: Adam, Alex H., Alex G., Andreas F., Andreas J., Anil, Ayumu, Balkrishna, Benjamin, Bertha, Dr. Bratz, Carsten, Chintan, Christian S., Christian W., Elvira, Fax, Felix, Florencia, Frederic, Gabi, Hendrik, Hilton, Hiroaki, Hitrisia, Iker, “Dr. K.“ Jan K., mein “weißer Hai“ Jan-Olaf, Jochen, Josef, Laurent, Linda, Martin S., “Altes Haus“ Märi, Oriol, Peter, Philipp, Dr. Prauser, Rheno, Frau Su, die “Frau von Welt“, Tatjana, Thomas, Toshi, Shourong, Stefan G., Stefan V., Vannhu, Virginia, Volker, Xuebing und am KPM in Twente waren: Bert, Cis, Cristina, Gautam, Gerhard, He, Jan, Jean-Pierre, Katja, Laszlo D., Laszlo L., Manja, Marco, Martha, Martijn, Oliver, Sergio, Seshan, Sheila und Victor, Virginia, Volker, Wolfgang und viele mehr. Über Kooperationen habe ich Eleni, Elli und Maria von der Aristoteles Universität in Thessaloniki, Griechenland, sowie Ralf und Markus von der Universität Erlangen und Stefan von der Ludwig-Maximilians-Universität in München kennengelernt.

Dem technischen Team, unseren unersetzbaren Heinzelmännchen, danke ich besonders. Andreas M., “Arnie“ Neukamm und Xaver. Ihr tragt mit großem Anteil zu den hoch qualitativen, wissenschaftlichen Arbeiten bei. Im besonderen bedanke ich mich auch bei Frau Heike Schüler und Frau Heidi Herrmann für die unermüdliche Hilfe bei der Bewältigung des Institutalltags.

Ihr alle habt mir Einblicke und Aufgeschlossenheit zu unzähligen wissenschaftlichen, kulturellen und ideologischen Bereichen gegeben. So kann ich schöne Bilder unvergessener Momente in Erinnerung behalten. Abgesehen von den vielen fruchtvollen, wissenschaftlichen Diskussionen möchte ich einige der privaten Highlights erwähnen. Da fallen mir spontan die Gruppenexkursionen nach Serfaus und Belgien ein, sowie die Erkundung englischer Pubs, der Genuss exzellenter französischer, belgischer, japanischer und sizilianischer Küche, aber auch der gutbürgerlichen Kost aus Sachsenhausen, Hochzeit im fernen Mexiko, Schnorcheln um die Isola Bella, die Begegnung mit dem weißen Hai am Strand von Montpellier

und Einkaufstouren in Metzingen. Das Folgen in den Fußspuren der Nürnberger Stadtväter wurde ehrenhaft mit einem Stadtführer ausgezeichnet. Einen großen Beitrag zur Völkerverständigung zwischen Deutschland, Mexiko und Spanien hat auch die Wohngemeinschaft in Enschede geleistet.

Dank an all meine Freunde außerhalb der Universität und besonders an Barbara und Dieter Hornung, Helen, Jean-Come, Jan, Kerstin und Ried, Kurti, Mareike, Marion, Markus M., mein Clubmitglied Markus W., meinen “großen Bruder“ Martin, Mel, Nick, Quirin, Rabl, Riehli, Rosi, Severin, Sus(h)i, Sylvia Rothe und – nie vergessen – an meinen lieben Geist Phil. Ihr habt mich unterstützt, ermutigt, unterhalten und mein Leben in großen Maßen bereichert.

Besonderer Dank und Liebe gilt meinen Eltern Christl und Clemens, sowie meiner liebsten Oma Lisl und meinen Schwestern Moni, Floh und Babi und ihren Freunden. Durch Eure Unterstützung, Fröhlichkeit, Nachsicht und Euer Vertrauen habt Ihr mir diesen Bildungsweg und meine persönliche Entwicklung erst ermöglicht.

Schön, dass es Euch alle gibt!

Table of Contents

Chapter 1

General introduction

Abstract:
This chapter presents an overview of solid catalysts for industrial application. A description focuses on the structure of the zeolite families FAU and MWW. The dependence of the acid-base character on the aluminum content will be reviewed in detail.

1.1 Solid catalysts and their industrial applications

Over the last 25 years, the public has been concerned by environmental problems since the quality of life is strongly dependent on the pollution levels. Development of new catalysts and new process technologies should focus on the prevention of waste production, a 100 % selectivity, as well as zero emissions. In addition, low investments, high yields, non-corrosive catalysts, and a high lifetime are also aimed at. Solid acid-base catalysis is one of the economically and ecologically important fields in catalysis and the replacement of homogeneous catalysts with heterogeneous ones opens an important field in chemical and life science industry. Solid catalysts have many claimed advantages over liquid Brønsted- and Lewis-acid and -base catalysts. They are non-corrosive and environmentally friendly, presenting fewer disposal problems, a reduced waste formation, and allowing easier separation from the product as well as possible regeneration and reuse. In addition, solid materials can be designed to give higher activity, selectivity, and longer catalyst life.

In 1999, Tanabe and Hölderich [1] presented a survey of industrial processes using solid acid-base catalysts. Processes such as dehydration and condensation, isomerization, alkylation, etherification, amination, cracking, MTG/MTO-processes, etc. (Figure 1.1), and catalysts such as zeolites, oxides, complex oxides, phosphates, ion-exchange resins, clays, immobilized enzymes, etc. (Figure 1.2), are known.

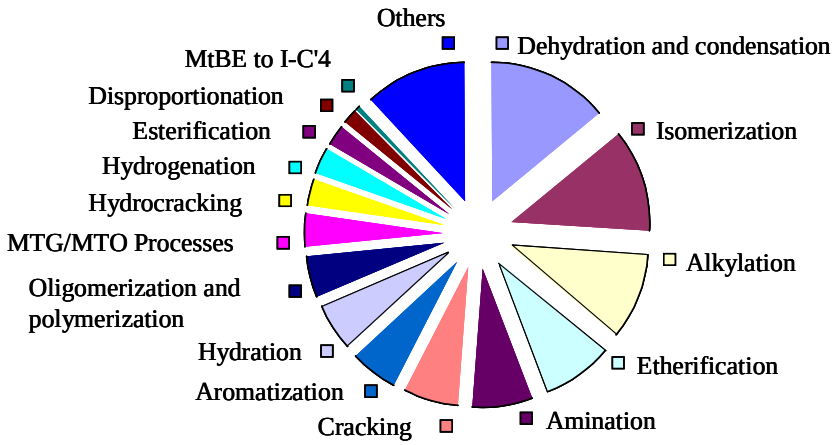

Figure 1.1 Industrial processes using acid-base catalysis (in total 127 processes)**.**

In total, the number of processes of different reaction types and catalysts used are reported to be 127 and 180 [1], respectively. Solid acids have received most of the attention in industrial applications, due to their demand in the great progress of petroleum and petrochemical industry for the last four decades (Figure 1.3). However, as solid basic and bifunctional catalysts are also commercially relevant, the search for novel solids that catalyze transformations with high product selectivity, high reaction rate, and low deactivation rate is an ongoing process.

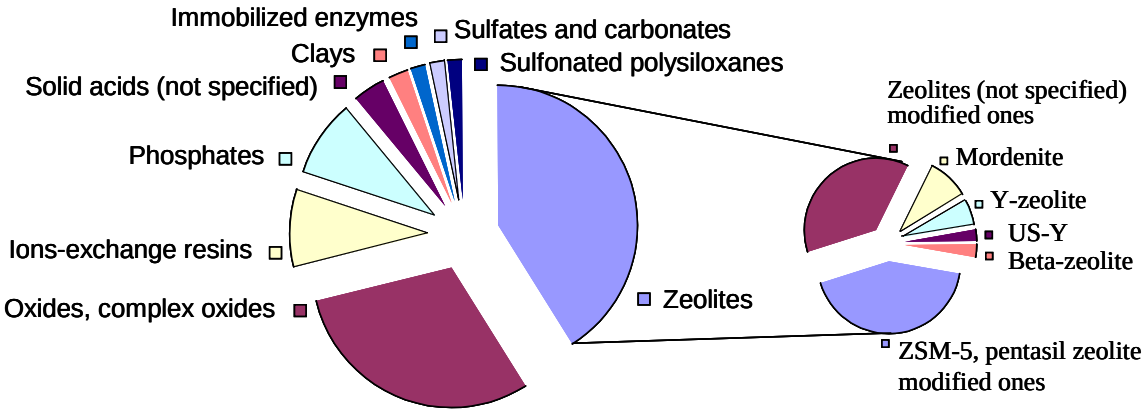

Figure 1.2 Types of catalysts and detailed kinds of zeolitic catalysts used in industrial processes (in total 180 catalysts).

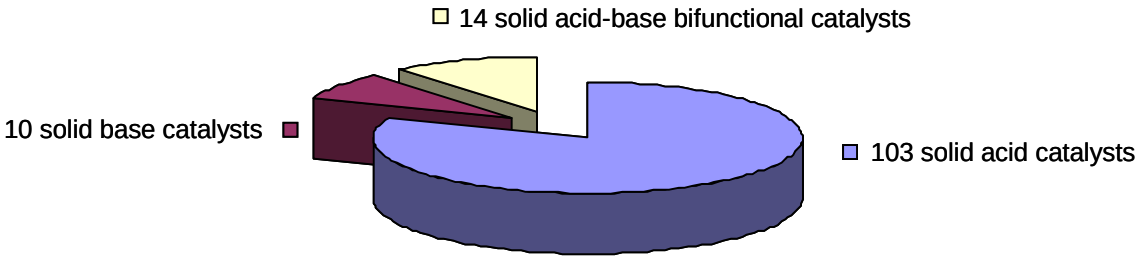

Figure 1.3 Number of solid-acid, solid-base and solid-acid-base bifunctional catalysts in industrial processes (in total 127 catalysts).

1.1.1 Solid acid catalysts

The industrial production of alkylated gasoline, replacing the conventional HF or H_2SO_4 catalysts for the conversion of isobutene with butene or mixed C_3-C_5 olefins [2] by solid acid catalysts (triflic acid supported on various carriers such as silica, titania, and zirconia) is made with Amoco's unit using Haldor Topsoe-Kellog's fixed bed alkylation-process [3]. Numerous industrial processes are catalyzed by zeolites. ZSM-5 and high silica pentasil zeolites are the most widely employed among various zeolites. Reactions worth mentioning among the industrial processes are alkylation reactions, like the acid aromatic alkylation following the Mobil / Badger Process for the production of ethylbenzene from benzene and ethylene over acidic ZSM-5 zeolite [4], and for the production of cumene, from propylene and benzene using a novel zeolite catalyst to replace solid phosphoric acid or aluminum trichloride [5]. The production of methylamine from methanol and ammonia by a gas phase reaction via the Nitto-process [6] is possible in the presence of modified ion-exchanged mordenite, while BASF created the pentasil zeolite for the production of t-butylamine [7]. The industrial production of cyclohexanol by the hydration of cyclohexene over special H-ZSM-5 is reported as the Asahi Process [8]. For all these processes, the replacement of the classic acid catalysts by (modified) zeolites results in a much better composition of the product mixture, satisfying commercial requirements. The enhancement, obtained by using zeolites, arises from the product shape selectivity and the possibility of adjusting their acidity and their pore opening as well as the poisoning of the outer surface.

1.1.2 Solid base catalysts

The dehydration of alcohols, the isomerization of olefins (isomerization of 1-butene), cyclizations (cyclo-addition of carbon dioxide to ethylene oxide), and side-chain alkylation of aromatics (alkylation of toluene with methanol or ethylene) are important reactions catalyzed under basic conditions. Many of these processes are carried out industrially using liquid bases as catalysts. These applications may require nearly stoichiometric amounts of the liquid base for conversion to the desired product. Therefore, they strongly pollute the environment and open a wide and important research field developing energetically and economically favorable as well as environmentally friendly alternative routes by solid base catalysis. Typical solid basic

catalysts are metal oxides and mixed oxides (like MgO and MgO/TiO_2), supported alkali metals ($Na/NaOH/\gamma\text{-}Al_2O_3$) and X zeolites (faujasite) modified by cation exchange, impregnation, or isomorphous substitution.

The alkylation of phenol with methanol over MgO to 2,6-xylenol, a monomer of PPO resin, is an old industrial process developed by General Electrics using solid base catalysts [9]. In the presence of the solid superbase $Na/NaOH/\gamma\text{-}Al_2O_3$ the production of vinylbicycloheptene, important for vulcanization, via double-bond isomerization is commercialized since 1986 (Sumitomo-Process) while the isomerization of 2,3-dimethylbut-1-ene to 2,3-dimethylbut-2-ene is still under design. The latter is a valuable intermediate for the production of synthetic pyrethroids. Another commercialized Sumitomo-process is the synthesis of t-amylbenzene due to side-chain alkylation of cumene with ethylene over $K/KOH/\gamma\text{-}Al_2O_3$. Also base catalyzed is the side-chain alkylation of o-xylene with butadiene to form 5-(o-tolyl)-2-penene over K/CaO or Na/K_2CO_3 being the first step in the production of dimethyl-2,6-naphthalenedicarboxylate (NDC) following the Amoco Process [10], which is a valuable intermediate for the production of high performance engineering plastics such as polyethylenenaphthalate (PEN) [11], applied in manufacturing magnetic recording tapes, in electronic and speciality films, in the field of packing resins for flexible and rigid containers and bottles and of industrial fibers. Unfortunately, the production costs of NDC monomer are very high. An industrial process utilizing a basic zeolite catalyst has not been commercialized but a couple of processes have

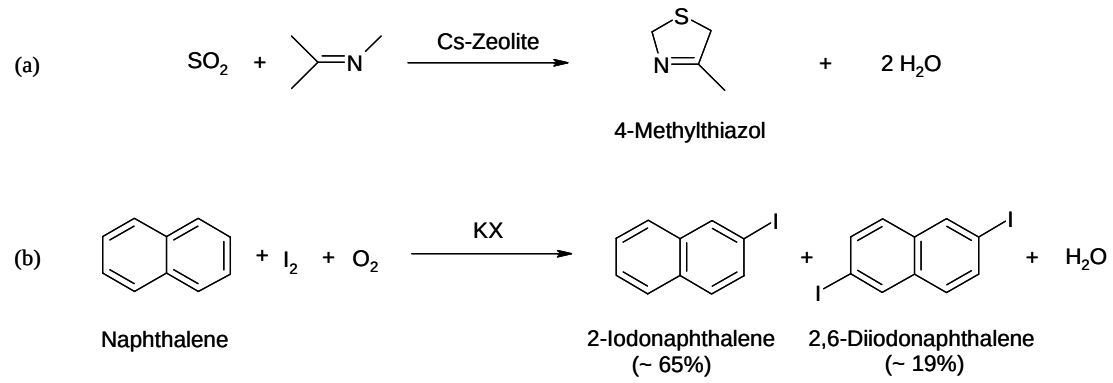

Figure 1.4 (a) Synthesis of methylthiazol catalyzed by Cs-loaded ZSM-5; (b) oxyiodination of naphthalene catalyzed by K-exchanged X-zeolite.

reached pilot plant scale. Merck and Co. used cesium sulfate impregnated into ZSM-5 as catalyst for the synthesis of 4-methyl thiazol [12] (Figure 1.4a). Another process catalyzed by basic zeolites is the oxyiodination of naphthalene over potassium-exchanged zeolite X [13] (Figure 1.4b).

1.1.3 Solid acid-base bifunctional catalysts

Bifunctional catalysts, offering both, weak acid and weak basic sites in a suitable orientation to the reactant molecule, are found to exhibit high catalytic activity and selectivity and a long life. For the industrial applications, 14 kinds of processes have been developed [1] including the production of vinylcyclohexane (Sumitomo Process [14]; ZrO_2/NaOH), of ethyleneimine (Nippon Shokubai Process; Si-Ba-Cs-P-O) and of aromatic aldehydes (Mitsubishi Process, ZrO_2/Cr_2O_3). The products are important commercial chemicals used for the production of polypropylene, pharmaceuticals and functional polymers for coatings of paper and textile, and fine chemicals like agrochemicals and perfumes, respectively.

1.2 Microporous molecular sieves: Zeolites

Zeolites are microporous, crystalline solids with a very well defined three-dimensional silica-alumina structure. Zeolites are widely used in different fields like heterogeneous catalysis, selective separation and adsorption, purification and drying, as well as ion exchange processes and as supports for active metals, reagents or enzymes**.** Most of the zeolites used commercially are produced synthetically. Their synthesis is well established and they are prepared in different cationic forms [15]. Their composition can be altered in many ways, including the incorporation of new elements into the zeolite structure [16].

Generally, zeolite can be described as $M_{x/n}(AlO_2)_x(SiO_2)_y(H_2O)_w$. M is the amount of exchangeable alkaline or earth alkaline metals, or protons with the charge n. The sum of x and y gives the total number of tetrahedrally coordinated cations per unit cell. The amount of water molecules in the voids of the structure is indicated by w. Three-letter codes are assigned to the zeolite structures by the International Zeolite Association (IZA) structure commission. Structures and codes are published in the IZA Atlas of Zeolite Structure Types [17].

An aluminosilicate-type zeolite is a microporous material with framework anions and exchangeable cations in its structure. The anion-cation pairs form electrostatic fields [18], which strongly interact with polar adsorbates. They are highly stable; exhibit a high surface area and an excellent activity in acid mediated reactions. Thus, zeolites have great potential as acid-base catalysts and constitute an important class of heterogeneous catalysts in fine-chemical and pharmaceutical manufacture and in petroleum refining, some of them already mentioned above. In addition, they are widely used as adsorbents and catalyst supports as well as in waste-gas adsorption and waste-water treatment [19]. Basic zeolites are excellent supports for nanometer-sized Ru-metal clusters used to catalyze the ammonia synthesis reaction [20]. Faujasites are used in industry to separate C_8 aromatics (para-, ortho-, metha-xylenes, and ethylbenzene) [21]. The most valuable product para-xylene, is preferentially adsorbed in X or Y zeolites exchanged with adequate cations (BaX). This selectivity has been attributed to thermodynamic effects.

1.2.1 Structural properties of zeolites

The adsorption behavior of molecules on porous adsorbents depends strongly on the characteristics of pores, i.e., shape, size, and chemical composition. In the zeolite framework, silicon and aluminum atoms are coordinated by oxygen atoms forming the primary building units TO_4 tetrahedra (T = Si, Al) (Figure 1.5) [22]. In general, zeolites have identical repeating structural sub-units, so called secondary building units (SBUs) [17, 23] (Figure 1.6). The corners correspond to the TO_4 tetrahedra connected through oxygen atoms. When the secondary building units are joined to create the infinite lattice they can build larger rings, the oxygen windows, containing 8, 10 or 12 linked tetrahedra. The connection of four and six rings leads to the tertiary building unit so called β- or sodalite cage (Figure 1.7a), while a further connection of the sodalite cage via the six ring plains in the shape of a hexagonal prism leads finally to the tertiary building unit of the faujasite (Figure 1.7b) [17]. All corners of the tetrahedra are linked to each other by sharing their oxygen atoms. Depending on the way these tetrahedra

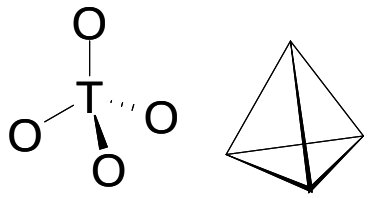

Figure 1.5 Representation of $[SiO_4]^{4-}$ or $[AlO_4]^{5-}$ tetrahedra (T = Si, Al).

are linked, a remarkable variety of structures containing channels and/or cavities of different dimensions are formed [17] (Table 1.1). About 140 different zeolite structures are known varying in cage sizes, pore diameters and channel dimension. The channel systems can be uniform or consist of interconnected cage-like voids. Within the pore structure the major amount of active sites is confined.

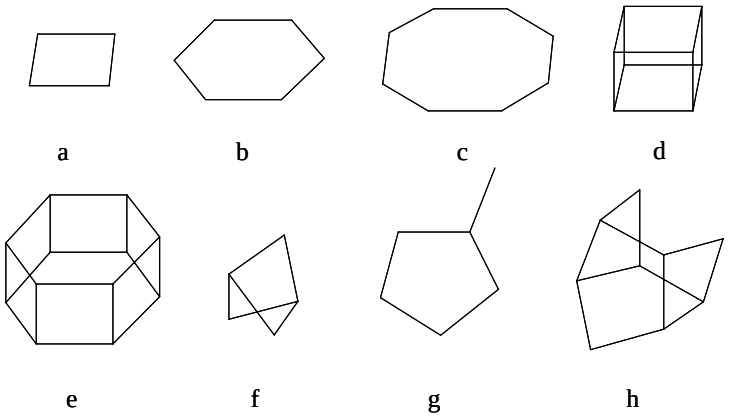

Figure 1.6 Some secondary building units (SBUs) recognized in zeolite frameworks; (a) single four ring (S4R), (b) single six ring (S6R), (c) single eight ring (S8R), (d) double four ring (D4R), (e) double six ring (D6R), (f) double eight ring (D8R), (g) complex 4-1, and (h) complex 5-1 (i) [17].

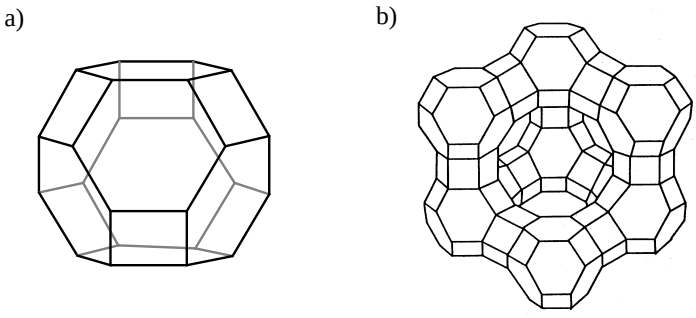

Figure 1.7 (a) Sodalite cage; (b) faujasite structure [15].

Table 1.1 The structural properties of some typical porous materials [17].

Biggest ring		Second biggest ring						
		none	7-ring	**8-ring**		**10-ring**		12-ring
	Channel dimension	-	1-dim	**1-dim**	3-dim	1-dim	**2-dim**	1-dim
6-ring	-							
8-ring	1-dim							
	3-dim							
9-ring	1-dim							
10-ring	**1-dim**						**MFI(i)**	
	2-dim						**MWW(c)**	
	3-dim							
12-ring	**1-dim**			**MOR(i)**				
	3-dim	**FAU**						
14-ring	1-dim							
18-ring	1-dim							
20-ring	3-dim							

(i) = channels intersect, (c) = channels cross without intersecting

Access to the cavities of zeolites is possible through voids of various sizes; their size is comparable to that of small molecules. In the void space, cations, water or other molecules can be hosted. Two or three-dimensional pore structures are preferred in order to obtain rapid intracrystalline diffusion. The pore diameter depends on the number of tetrahedra in a ring, while the actual pore size also depends on the type of cation that is present in the zeolite structure.

1.2.2 Acid and basic properties in zeolites

1.2.2.1 Acidity in protonated and dealuminated zeolites

Zeolites are mesoporous aluminosilicates with multiple applications as molecular sieves and as acid-based catalysts [90]. Ideal, pure siliceous zeolites consist of a loosely connected network of SiO_4 -tetrahedra. In natural zeolites, Al replaces a fraction of the tetrahedrally coordinated Si atoms. The substitution of Al for Si in a silica framework leads to a charge imbalance that is restored by introducing ‘counter-ions’ like protons or exchangeable cations into the cages, yielding electronical neutrality. Increasing the content of aluminum in the framework structure can increase the number of active sites. The minimum Si/Al ratio is one. According to the Löwenstein’s rule [24], the existence of ≡Al-O-Al≡ fragments in zeolite lattices is

virtually excluded. The Al atoms are isolated from each other, because adjacent aluminum tetrahedra would cause a local electrostatic repulsion and destabilize the zeolite framework.

Aluminum within zeolites plays a key role in catalytic reactions. Acid properties depend on the site, the geometry, and the coordination number of Al in the zeolites. The location of Al within the zeolite structure determines its function, for example, as Brønsted or Lewis acid sites. Brønsted acid-sites are produced due to the presence of H^+-ions covalently bound to an oxygen-atom next to aluminum. Protonic zeolites display very strong Brønsted acidity that allows these materials to be used in acid-catalyzed petrochemical processes such as fluid catalytic cracking [25].

Aluminum fragments removed from the framework and remaining in the cavities are called extra-framework aluminum. This refers to species, such as nanoparticles possessing Lewis acidity [26] on the surface, tri-coordinated Al atoms or/and aluminum cations [27]. Although, protonic forms of zeolites should exhibit only Brønsted acidity, it has been shown that also Lewis acidity can be found due to extra-framework material [64].

The total acidity of a zeolite catalyst [28] may be considered to be a contribution of both, an extensive factor, corresponding to the number of acid sites, and an intensive factor, corresponding to the strength of acid sites [29, 30]. The protonic form of zeolites containing extra-framework alumina generated by steam dealumination exhibits three families of acid sites depending on their strength: weak, moderately strong and strong sites.

Weak sites are mostly of Lewis type and similar to amorphous silica-alumina. They predominate in dealuminated zeolites originated from the degradation of the crystalline structure of the zeolites during steaming. Part of the weak sites are of Brønsted type that exist in the protonic form of Y zeolites and are probably those sites corresponding to the protons surrounded by three aluminum atoms as second-nearest neighbors [31]. With increasing steam treatment of the zeolite structure the amount of weak Brønsted sites decreases because dealumination occurs preferably in areas of high aluminum content.

Sites of *moderate strength* are mostly Brønsted acid sites. They are related to framework bridged hydroxyl groups having less than three second-nearest neighbor aluminum atoms surrounded. Their strength also decreases with increasing dealumination. A possible reason might be the perturbation of acidic high frequency

OH groups located in the supercages by molecules adsorbed on low frequency OH groups located in the hexagonal prisms and the sodalite cages [32] or on extra framework aluminum fragments.

Strong structural Brønsted sites can be found in protonated and dealuminated zeolites [28]. They may arise from interaction of bridged hydroxyl groups with Lewis sites [33, 34] or by formation of amorphous silica-alumina inside the pores [35], or by an inductive effect of aluminum cations located in the sodalite cages [36].

Dealuminated zeolites exhibit even *stronger* sites of Lewis and Brønsted type. The Lewis sites might be referred to as extra-framework tetrahedral aluminum [37]. The sites of Brønsted type are located in extra-framework aluminum-containing debris [38]. Interactions between Lewis and Brønsted sites and/or neighborhood of cationic aluminum species might be the reason of the high strength. These aluminum species are either of extra-framework character (cationic, tetra-coordinated) or related to framework defects (tri-coordinated).

1.2.2.2 Basicity in cation exchanged zeolites

In contrast to the situation found with acid catalyzed reactions, the role of zeolites for base catalyzed reactions is less well defined. This is related to the fact that zeolites with basic properties typically contain alkali cations, which also act as (weak) Lewis acid sites [39]. It should be stressed that for acid/base-catalyzed reactions both sites are involved in the reaction pathway. For many of the acid catalyzed reactions, however, the importance of the acid sites strongly dominates and, therefore, the main attention is paid only to the acidic function. In a base catalyzed reaction the strength of the base sites is high enough to stabilize anionic or polarized species (being part of the catalytic cycle) with a marked negative charge [40]. Another problem in characterization of the catalytically active site for base catalyzed reactions is related to the high number of basic sites (zeolite-O atoms next to Al atoms) [41].

In zeolites, base sites can be formed by alkali metal cation exchange, incorporation of alkali metal oxides and alkali metals, or by using the zeolite as support for transition metals as the active component. Alkali metal cation exchanged aluminosilicate zeolites, mainly prepared by liquid cation exchange, contain both acidic and basic sites [42]. The exchanged cations (counter cations) act as Lewis acid sites and the framework oxygen atoms bearing partial negative charge behave as basic

sites [43]. These basic sites are called structural basic sites or framework basic sites. Brønsted basic sites, i.e., framework basic OH groups are not present. Hydroxyls with basic properties may act as ligand to extra framework charge-compensating multivalent cations, as a result of hydrolysis [44].

Incorporation of alkali metal oxide clusters in zeolite cages by thermal decomposition of impregnated alkali metal salts results in a further increase in the basicity of ion-exchanged materials [45]. However, the resulting materials do not appear to be as strong as bulk phase alkali metal oxides. The supported species can be inserted through wet or incipient impregnation of a solution containing the solvated precursor into the zeolite pores. After calcination, supported alkali metal oxides are present as a result of the decomposition of the embedded compounds.

Zeolites with alkali metals introduced in the cages have been determined as high-strength solid base catalysts. Alkali metal clusters are prepared via the thermal decomposition of alkali metal azides in the presence of a zeolite [46, 47]. Decomposition of the supported azide is dependent on the heating rate and results in ionic clusters or neutral metal clusters [46].

Lewis base strength of the zeolite-O atom can be modified by changing the Si/Al ratio or the type of cation increasing the number of framework oxygen atoms located next to an aluminum atom and its average negative charge $-\delta_O$. The relatively high aluminum content of zeolite X results in a substantial framework negative charge, which makes X one of the most basic zeolites when it exists in the alkali-exchange form. An excellent discussion of basic zeolites is given by Barthomeuf [48]. As shown by computational studies, the strength of Lewis acidic centers (metal cations) and basic framework oxygen centers depends on the number of aluminum atoms in the zeolite model cluster [49]. The negative charge of the framework oxygen atom can be calculated by a rather simple technique [50], based on the averaged electronegativity of the zeolite according to Sanderson [51] following the equation 1.1

$$-\delta_O = (S_{int} - S_O)/[2.08(S_O^{½})] \qquad \text{(Equation 1.1)}$$

and is a measure of the average framework basicity. The joint electronegativity of all atoms in a compound $P_pQ_qR_rT_t$ can be described by the geometric mean of the contribution of each of the atoms. From the theoretical unit cell composition of the

zeolites -δ_O can be calculated. The negative charge, i.e., the basic strength varies in the opposite way with the intermediate electronegativity [52]. The Intermediate Sanderson Electronegativity for a compound follows the equation 1.2 [50]:

$$S_{int} = (S_P^{p} \cdot S_Q^{q} \cdot S_R^{r} \cdot S_T^{t})^{1/(p+q+r+t)} . \qquad \text{(Equation 1.2)}$$

Besides the pore diameter, chemical properties can be modified through the incorporation of active species in the pores by various methods, for instance ion exchange of alkali metal cations, deposition of clusters of alkali metals in the pores of faujasite-type zeolites, and deposition in occluded oxides [53].

Vibrational spectroscopy is the most widely used technique to characterize the chemical activity of the acid-sites. Several probe molecules have been used to determine the acid-base properties of zeolites commonly followed by infrared and UV-vis spectroscopy and temperature-programmed desorption. Appropriate probe molecules used for acid site determination are ammonia and pyridine. By adsorption of pyridine, differentiation between Brønsted and Lewis acid sites is possible [54]. Often used probe molecules for basic sites are carbon dioxide [55, 56], pyrrole [57, 58], chloroform [59, 60] and iodine [61, 62]. Carbon monoxide has been widely employed to probe Lewis acid sites in zeolites [63].

Characterization of ion-exchanged zeolites indicates that they expose solid base sites, especially after exchange with heavy alkali metal cations. Experimentally, the basicity has been characterized by using either direct methods or indirect ones with the help of probe molecules [48]. By using O1s binding energy, evaluated by X-ray photoelectron spectroscopic studies, which reflects the electron density of the framework oxygen atoms, it was shown that the framework basicity of faujasite-type zeolites increases in the order $Li^+ < Na^+ < K^+ < Rb^+ < Cs^+$ [48]. The Lewis acidity of an ion corresponds to its ionic potential, which is conversely proportional to the ionic radius, thus decreases from small to large cations, that is, from Li^+ to Cs^+.

1.2.3 Zeolites of the FAU type

1.2.3.1 Structure of FAU and extra framework cation position

Zeolite X, the synthetic form of the naturally occurring aluminosilicate mineral faujasite, is a very important catalytic material. It has the most open framework of all the natural zeolites, with a 51% void volume. The faujasite unit cell consists of eight supercages, eight sodalite cages and 16 hexagonal prisms (Figure 1.8) [64]. The spherical cavities, or supercages, have a diameter of 1.3 nm. They are accessible through 12-member ring windows of 0.74 nm diameter tetrahedrally arranged around the supercage. The large dimensions of these structural units allow sorbates of a wide range of kinetic diameters to access the pore structure. The unit cell of faujasite is cubic with a large cell dimension of nearly 2.5 nm and a content of about 192 TO_4 tetrahedra cubic (space group *Fd3* or *Fd3m*). The empirical formula of zeolite X is depicted as $Na_{88}[(AlO_2)_{88}(SiO_2)_{104}]\cdot 220H_2O$ [17]. The water in the zeolite pore system can generally be removed reversibly leaving intact a crystalline host structure [65]. Usually, the amount of aluminum ions in the unit cell of zeolite X varies from 76 to 96 and the Si/Al ratio from 1.0 to 1.5.

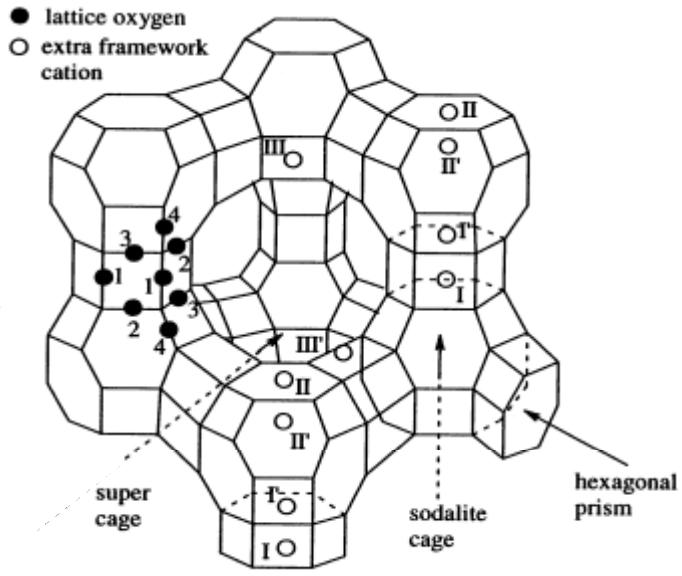

Figure 1.8 Faujasite structure (zeolite X and Y). Roman numbers indicate the different cation sites. The numbers 1-4 indicate the different oxygen atoms [66].

The faujasite structure incorporates a high number of charge-compensating cations, which occupy a number of well-defined positions, limited by symmetry and charge conditions, in the zeolite structure shown in Figure 1.8. The charge balancing counter cations are mainly located in five extra framework crystallographic sites, SI, SI', SII', SII and SIII' [67]. The SI position is located in the hexagonal prism, coordinated to the six nearest oxygen atoms at distances of ca. 0.25 nm, while both SI' and SII' are located on a threefold axis in the sodalite cage, with SI' in front of the hexagonal prism and SII' in front of the six-ring leading to the supercage. The SI', SII' and SII positions are coordinated to three nearby oxygen atoms and three more distant ones. SIII is centered over the four-rings in the supercage and lies on the intersection of two mirror planes. Two oxygen atoms, O1 and O4, each positioned in a corner of the four-ring window where the aluminum is located and four more distant oxygen atoms, coordinate these cations and make the SIII position energetically less favorable compared to SII. In addition to SII, Olson *et al.* [68] found for a Na-X material ($Na_{88}Al_{88}Si_{104}O_{384}$), three sites in the supercages, so called SIII'. They are all within 0,28 nm of the hypothetical site III, symmetrically centered on the sodalite four-ring window in the 12-ring window. The cations are found at the side of the ring where the aluminum atom is located, which seems reasonable in relation to charge compensation. Preferentially, Na^+ cations were located in sites SI' (sodalite cage) and SII (supercage), both being fully occupied. SI position is unoccupied in Na-X, but occupied in Na-Y. Note, that SI' will only be occupied if the adjacent SI position is vacant [69]. The amount of SI' (32 possible sites) represents the double of SI (16 possible sites) and furthermore, only one of them can be occupied at the same time. An occupation in SI would lead to an occupation of energetically less favorable SIII in Y. Although there are several possible cation configurations for a given Si/Al ration, Na-Y zeolite with Si/Al = 2 has the structure with the majority of the SII cation sites occupied by Na^+ cations (ca 30 per supercage with the occupation factor of ca. 95 %), while the SIII positions (96 possible sites) remain free [70, 71]. The fraction of sodium ions inside the supercages of Y-type zeolite is about 60 % [64], while according to a X-ray study of a single crystal of Na-X zeolite with Si/Al = 1.2, the total fraction of sodium ions populating both SII and SIII is equal to 65 % [68]. Due to the lower Al content of zeolite Y compared to X, there are no aluminum atoms located in the 4-ring (SIII positions).

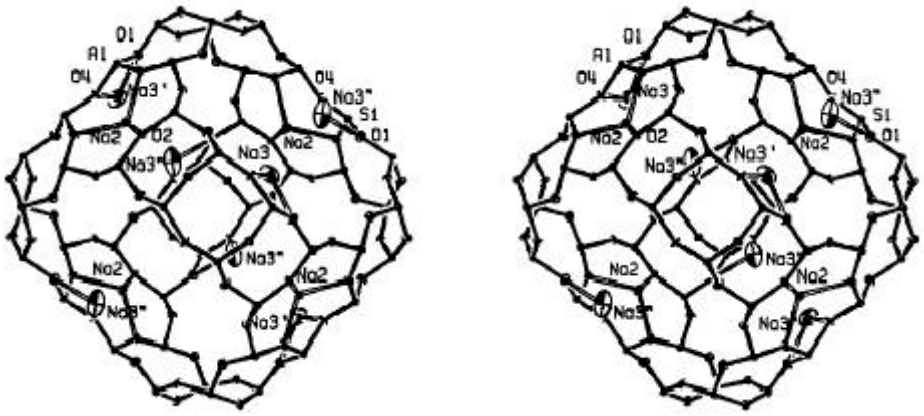

Figure 1.9 Stereo view of the supercage in dehydrated Na_{92}-X [72].

1.2.3.2 Change of cation position in alkali metal cation exchanged zeolites

Cations are mobile and may undergo ion exchange [73]. In Table 1.2, the locations of alkali metal cations are given for exchanged X zeolites as determined by X-ray diffraction techniques. In general, cations always have been observed occupying sites where a maximal coordination by framework oxygen and or guest molecules is granted [74, 75]. The cation positions for smaller ions (Li^+, Na^+) are located near the centers of the six-membered rings, while the larger ions (K^+, Rb^+, Cs^+) are displaced for steric reasons to one side of the rings [76]. In SIII/III' positions, all alkali cations showed displacement further into the supercage above the smaller 4-membered ring.

Table 1.2 Cations per site per unit cell of the alkali metal cation exchanged X zeolites obtained by X-ray crystallographic data. See Figure 1.8 for site numbering.

Location	**Na_{88}-X** [69]	**$K_{86.5}$-X** [105]	**$Rb_{71}Na_{21}$-X** [140]	**$Cs_{46.1}Na_{49.5}$-X** [71]	**Na_{57}-Y** [141]
Si/Al	1.18	1.22	1.09	1.11	2.37
Site I	2.9	9.2	4.5 (Rb^+) 7.0 (Na^+)	1.0 (Cs^+) 2.0 12.5 (Na^+)	7.0
Site I'	29.1	13.6	8.9 (Rb^+)	5.6 (Cs^+)	13.8
Site II	31	25.6	17.7 (Na^+) 12.7 (Rb^+)	32 (Na^+)	29.4
Site II'	0	0	2.6 (Rb^+)	1.6 (Cs^+)	0
Site III	0	0	32.9 (Rb^+)	0	0
Site III'	29.8	38.2	5.2 (Rb^+)	37.9 (Cs^+)	0

All alkali metal cations, except Li^+, located at either SII or SIII were accessible to small probe molecules, like O_2 and N_2 [67]. The small Li^+ ion is nearly submerged in the wall of the zeolite, while Cs^+ is completely exposed providing more easy O_2 interactions with the Cs^+ cations. For Li^+, it is difficult for more (second) molecules to approach the site [77]. By ^6Li and ^7Li MAS NMR, a paramagnetic shift was observed upon O_2 adsorption for Li^+ at the SIII position only, indicating that just this site is accessible to O_2 [78, 79]. Cages are accessible for alkali metal cations depending on the cation size. Na^+ and K^+ ions are found to penetrate into all cages, including the hexagonal prisms [69]. The structure of dehydrated K_{90}-X was found to be more complex than that of dehydrated Na-X. Up to nine crystallographic sites, a large number due to cation crowding, have been reported [80]. Cations were placed at SIa (6 cations), SIb (8 cations), SI'[a, b, c] (4 cations), SII (28 cations) SIII (12.2), SIII'a (10.7), and SIII'b (12.8). The exclusion of larger cations from smaller cages leads to partially exchanged zeolites. Large Cs^+ ions hardly occupy SI, while all the other sites may be occupied [81]. The double six-rings are not very flexible, making it difficult to accommodate these large cations. Additional differences in cation stabilization between the sites cause preferred cation distributions depending on the cation size. In CsNa-X, the larger Cs^+ ions were mainly located in SIII' and SI' position, while SII were completely occupied by sodium cations [69].

The decreasing binding energy differences between SII and SIII, with increasing cation size (K to Cs), induce a higher negative charge on the zeolite framework [76]. Because of its function as an effective electron donor, especially when a heavy alkali metal cation is present for charge compensation, X is one of the most basic zeolites in the alkali-exchanged form [48]. Methanol on K-X decomposes at temperatures 40 K lower than for Na-X, indicating a higher activity for the K-X catalyst [82]. This increase in activity is probably a result of the increase in basicity of the K-X over Na-X. For a zeolite with a given aluminum content, exchange of Na^+ with K^+ cations results in a large increase of the framework oxygen charge [83]. Introduction of Cs^+ cations rather than K^+ cations, on the other hand, results in only a slightly higher framework oxygen charge than for K-X. A very interesting base catalyzed reaction, exceeding the highest activities and selectivities over alkali metal cation-exchanged X zeolites, is the side-chain alkylation of toluene with methanol to form styrene and/or ethylbenzene [84, 85].

1.2.4 Catalytic properties

Properties of zeolites can be varied by a large number of modification procedures to tailor them for the particular application that is envisioned. Therefore, zeolites can be used in numerous fields. Zeolite activity is related to both the composition and the geometry of the zeolite. Differences in the Si/Al ratio, alkali metal cations, and zeolite topology influence the basicity of the zeolites. It increases with the framework aluminum content and decreases with the electrostatic potential of the counter ion. The strength of molecule-zeolite bonding also changes with the zeolite composition (Si/Al ratio and cation type).

Cations in zeolites are ion exchangeable and allow the introduction of other cations with various catalytic properties [86, 87]. Location and nature of the cations are important for the catalytic activity. Type II and III' sites, in the large faujasite cages, are easily accessible for reactants and therefore, of higher importance for the catalytic activity than type I, I', and II' sites in the dense cages. The limited dimensions of the apertures that control the access to these small cavities are frequently considered as a factor that limits the ion exchange [88]. Thus, controlling the ion exchange conditions can result in some control of the occupation of specific sites by cations.

The modification of cation site occupancy causes relatively large changes in the framework structure. Pore size modification is a very promising engineering process to increase the range of available catalysts [89]. A transient modification can be carried out by pre-adsorption of polar molecules (water, amines) and coke deposition, while a permanent modification includes introduction of bulky compounds inside the porous structure [90, 91]. Both modifications influence the accessibility and the geometrical neighborhood of the active sites as well as the acid properties of these sites.

Chemical or hydrothermal treatments (steaming), which remove partially aluminum from the crystal framework, increase the stability and alter structural properties of the zeolites. Dealumination dramatically affects the crystallinity of the zeolites. Both treatments cause a decrease of the number of acid sites and an increase of their average strength. Therefore, the catalytic activity and selectivity of the zeolite are modified.

1.3 Sorption studies and sorption structures

A high number of studies have been performed to investigate the relationships between the crystal structure, the chemical composition, and the acid-base properties of the zeolites [92 93]. In the following, some examples of adsorption-complexes on zeolites will be given.

By changing the acid-base properties of the catalyst, the reaction pathway can be altered and the selectivity of the reaction can change, like the ring alkylation of toluene by methanol over acidic zeolites and the side-chain alkylation using zeolites exhibiting basic properites. Methanol adsorption on zeolites has been shown to have a large dependence on the acid-base properties of the zeolite material [85]. Adsorbed methanol molecules form strong hydrogen bonds to the Brønsted acid-OH groups on the protonated zeolite, while the active site on alkali metal cation exchanged zeolites, which should be envisioned as a combination of a Lewis acid and a Lewis base site, leads to methanol-cation and methanol-zeolite interactions. Pyrrole and pyridine pre-adsorption experiments have shown that methanol is chemisorbed on basic and/or cationic sites on the zeolites [94]. The interaction strength between sorbent and sorbate changed with the Si/Al ratio as well as with the framework cation [95]. Enhanced hydrogen bond formation to the zeolite framework with increasing framework polarity has been determined [95].

In general, if molecules with polar functional groups or π–bonds are adsorbed on cation exchanged zeolites, they interact strongly with the counter cations [96]. Note that also for non-polar molecules, like H_2 adsorbed on alkali cation exchanged X zeolites, the counter cations located in the zeolite structure were reported to play the role of adsorption sites [97]. Besides the direct sorbate-cation coordination, bridged adsorption structures have also been reported. At low loadings (11 water-cation complexes per unit cell containing 88 Na^+ ions; Si/Al = 1.18) water molecules were found to be exclusively situated between sodium ions on SIII and SII positions of Na-X as determined by X-ray powder diffraction studies [98]. In most cases this results in a coordination of the sodium ions on SII in a distorted octahedron [99]. In partially exchanged X zeolites, water binds only to Lewis acid Na^+ ions at low coverage. When large amounts of potassium ions are present ($K_{66.1}Na_{22}Al_{88.1}Si_{103.9}O_{384}$), sodium ions are located only on the SII positions. In such a sample almost no water molecules are found between SII (Na^+) and SIII (K^+). At a very low Cs^+ exchange degree

($Cs_{4.4}Na_{83.7}Al_{88.1}Si_{103.9}O_{384}$), the same cation-water formation as in Na-X is encountered (Figure 1.10) [98]. Bridging alcohol molecules between adjacent cations in the supercage may also be considered at low sorbate coverage on zeolite X. The cation-cation distance between SII and SIII sites, which is about 0.47-0.48 nm, has a similar value to that of zeolite A. For zeolite A, bridging methanol structures have been shown [100]. But note, this is only expected if there is no large difference in binding energy of the different cations to the framework oxygens and the repulsion between the cation and the alkyl group is not of hindrance.

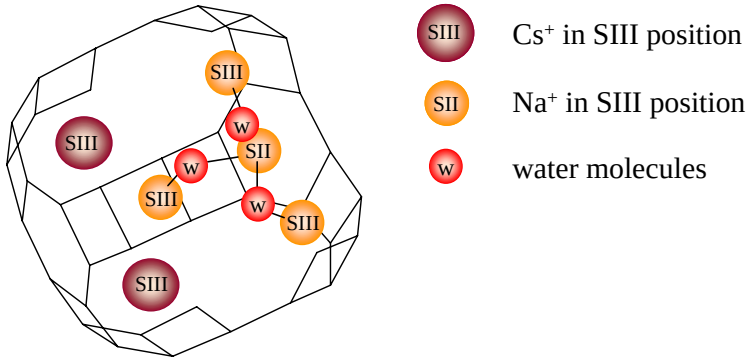

Figure 1.10 Location of water molecules on CsNa-X at low loading [98].

At low loadings, the stronger cation sites will be occupied first and only second sorbate-sorbate interactions are favored. Note that sorbate-sorbate interactions of molecules adsorbed on neighboring counter cations are dependent on the site density. Liquid like sorption structures of methanol (water) have been found on X but not on Y [95]. On the aluminum richer zeolite X, a higher number of sites is present than on Y. Thus, cation-sorbent complexes are further apart on Y and intermolecular interactions are less conceivable.

At high sorbate loading, cation movements have been reported. At a loading of 89 H_2S molecules per Mn_{46}-X unit cell [101], 25 molecules of H_2S have been observed on Mn^{2+} cations in SII positions, while 56 molecules were located on two different SIII' positions held only by weak hydrogen bonds to the framework. In addition, five Mn^{2+} ions were found in the sodalite cavities coordinating to bridging atoms (likely HS^-). These Mn^{2+} ions have moved from the supercage in dehydrated Mn_{46}-X [102] to the sodalite cavities upon this coordination. Water has been found to diffuse through the 6-membered ring into the sodalite cage of Na-X as well as into the hexagonal

prism and induce migration of Na^+ cations form sites I and I' to positions in the supercage [103, 104]. In hydrated Na-X, measurements of self-diffusion kinetics of Na^+ have demonstrated high cation mobility, so that energy barriers for ion movements from one part of the hydrated crystal to another are small.

The diffusion of methanol and higher alcohols and amines into the sodalite cage and/or hexagonal prism of cation exchanged faujasites is not possible. This has been concluded from the value of the kinetic diameter of the sorbates (methanol ~ 0.44 nm), which is nearly double that of the opening of the 6-membered ring to both sodalite and hexagonal prism (~ 0.24 nm) [105]. For H-Y zeolites, penetration of only the methanol-hydroxyl group into the sodalite cage and interaction with the LF hydroxyl band was detected. For cation exchanged faujasite zeolites X and Y, this is excluded due to the hindrance of the counter cations in SII position. From ^{133}Cs MAS NMR it has been found upon O_2 adsorption on CsY that the sodalite sites are inaccessible to O_2 [67]. The SII' and SI' resonances were hardly shifted by O_2 at low temperature, which is consistent with the inaccessibility of these sites. On the other hand, the ammonia molecule is small enough to access the sodalite cavities of the zeolite [106]: sorption by sodalite, although slow, occurs [107]. But in the case of a large-pore zeolite such as zeolite X, the effective pore size may be controlled by the formation of a stable inorganic complex. The strong interaction between the zeolite cation and the dipole moment of ammonia produces a diffusion block by clustering ammonia molecules close to the cation in the channels [108]. When small amounts of ammonia are presorbed on a dehydrated zeolite, the sorption of a second less polar sorbate such as oxygen is drastically reduced [109, 110].

The adsorption of benzene on large pore zeolites Na-X (Si/Al = 1.2), Na-Y (Si/Al = 3.6, 3.4, and 2.3), and Na-EMT (Si/Al = 3.6), is influenced by the zeolite structure and Si/Al ratio. Two sorption sites, Na^+ ions and 12-membered ring windows, as well as similar adsorption capacity have been reported for the three Y zeolites independent of their Si/Al ratios and Al distribution. On the structurally different Na-EMT, which is a hexagonal analogue to faujasites [17], only the stronger interaction to the Na^+ sites was observed [111]. The mobility of benzene in a series of Na-Y zeolites has been reported to increase with increasing Si/Al ration, and a high benzene loading in these zeolites reduces the mobility of benzene [112]. The high amount of benzene molecules found interacting to Na^+ on EMT zeolite in the large cages indicated that a migration of the sodium cations from small cages towards large

cages occurs and all the Na^+ ions are present in the large cages in the presence of benzene [113].

The high flexibility of the zeolite structure and of sorbate molecules has been shown by adsorption of bulky aromatic molecules into the zeolite. One molecule of 1,3,4-tri-*t*-butylbenzene and 2,4,6-tribromo-1,3,5-triethylbenyzene, with diameters of approximately 0.90 and 0.95 nm exceeding the nominal 0.74 nm pore openings of Na-X, have been found adsorbed per faujasite cage [114]. The mobility of these molecules was restricted in the zeolite pore system. Adsorption of naphthalene [115] and p-xylene [116] on MFI led to pore deformation and symmetry changes of the zeolite structure.

Many sorption complexes have been studied by Seff *et al.* using single crystal X-ray diffraction techniques. The adsorption of ethylene on dehydrated, fully oxidized $(Ag^+)_{92}Al_{92}Si_{100}O_{384}$ induces a strong lateral ethylene-Ag^+ π-complex (27 complexes observed) with only Ag^+ cations located in SII position [117]. Each ethylene molecule can hydrogen bond by two *cis* hydrogen atoms to the zeolite framework. Mesitylene sorption on dehydrated fully Ca^{2+} cation exchanged zeolite X ($Ca_{46}Al_{92}Si_{100}O_{384}$) crystal led to the adsorption of eight distorted C_9H_{12} molecules [101]. This indicates the presence of one molecule per supercage. Each mesitylene molecule has been determined to lie on a 3-fold axis where it interacts facially with a Ca^{2+} cation in SII position. The three hydrogen atoms of the sorbate and one hydrogen atom of each methyl group interact via hydrogen bonds to the zeolite oxygen atoms.

The formation of the metal-sorbate complex can change the location of the bare cations, by moving them further away from the zeolite framework in order to minimize sorption energy of the complex. Ag^+ ions in SII position on Ag_{27}-X were extended 0.08 nm along their 3-fold axis from the plane of the three oxygen atoms to which it is bound more deeply into the supercage [117], while SII-Ca^{2+} cations of Ca_{46}-X showed a displacement of 0.058 nm upon mesitylene adsorption [101], and SII-Mg^{2+} cations on Mg_{46}-X were extended 0.049 nm after hydrogen sulfide adsorption [118].

1.4 Zeolite MCM-22 and its mesoporous and delaminated homologues

Although zeolites show excellent catalytic properties, the relatively small dimensions of their pore openings limit their applications. On the other hand, catalysts based on oxide materials contain easily accessible active sites on the external surface, but show a wide distribution of the number of sites and of their site strength. Thus, the goal is designing catalysts with isolated active sites of the same type and strength, accessible also for large sorbate molecules. The discovery of new synthetic methods has enabled the synthesis of novel mesoporous materials [119] and mono-layered materials [120].

Zeolite MCM-22, which is a relatively new, layered zeolitic material [121], has shown good catalytic properties for various reactions, such as olefin isomerization [122], isoalkane/olefin alkylation [123], and catalytic cracking [124]. The zeolite is remarkably useful for the production of high density, cycloparaffin-rich jet fuel [123].

The synthesis product referred to as an MCM-22 precursor undergoes a structural transformation during calcination and the resulting MCM-22 zeolite consists of thin sheets of platelets exhibiting hexagonal morphology with the unit cell c-axis perpendicular to the plate surface. MCM-22 has a unique and unusual crystal structure. Based on high-resolution electron micrographs and synchrotron X-ray diffraction experiments for pure silica MCM-22, a three dimensional dodecasil-1-H like lattice has been proposed. The lattice is composed of interconnected $\{4^3 5^6 6^3 [4^3]\}$ building units and belongs to the space group P6/mmm or C/mmm [125].

Zeolite MCM-22 possesses two non-interconnected pore systems both accessible through 10-membered rings (Figure 1.11). The first one consists of two-dimensional sinusoidal channels with elliptical, folded apertures. The other two-dimensional pore system consists of supercages with an inner diameter of approximately 0.71 nm and an inner height of 1.82 nm. The later pore system is formed due to thin monolayers, terminated from both sides by a wall of 12-ring pockets (cups), which are bonded together through double six-rings, that cap the 12-ring pockets and create a 10-membered ring channel. The evidence of the 12-ring pockets (each of which is half the supercage) on the surface of the MCM-22 crystal was found by high-resolution electron microscopy (Figure 1.12).

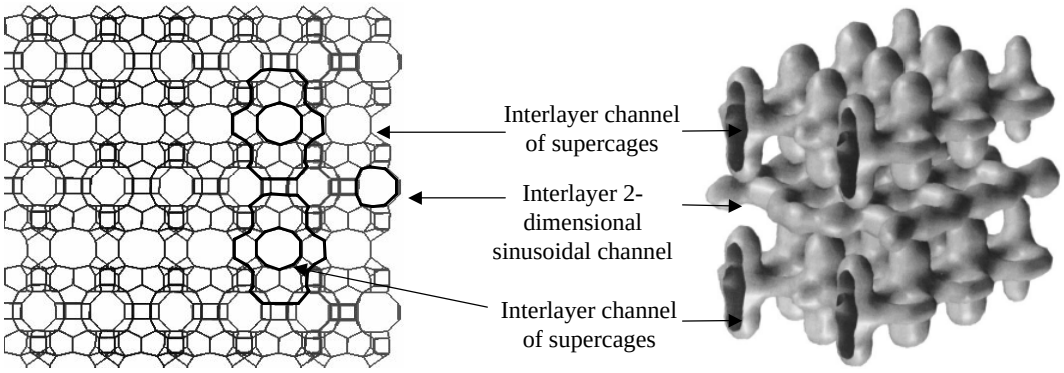

Figure 1.11 Schematic representation of the MCM-22 crystall and its pore structure [126].

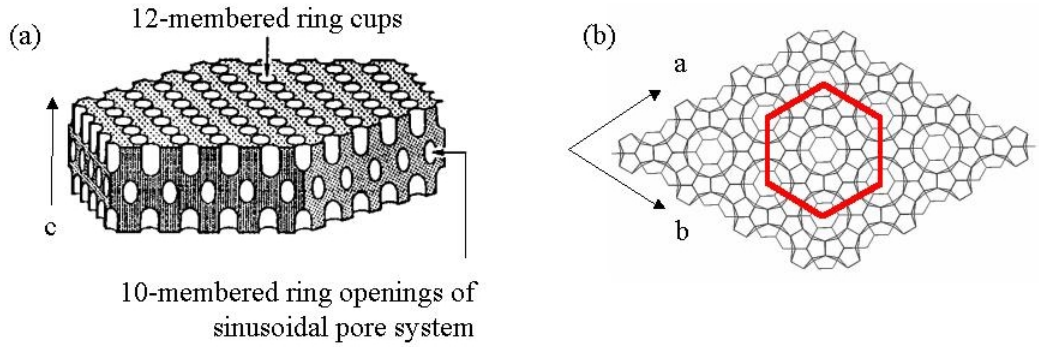

Figure 1.12 Schematic representation of 12-ring pockets on the surface of the MCM-22 crystal; (a) side view and (b) top view.

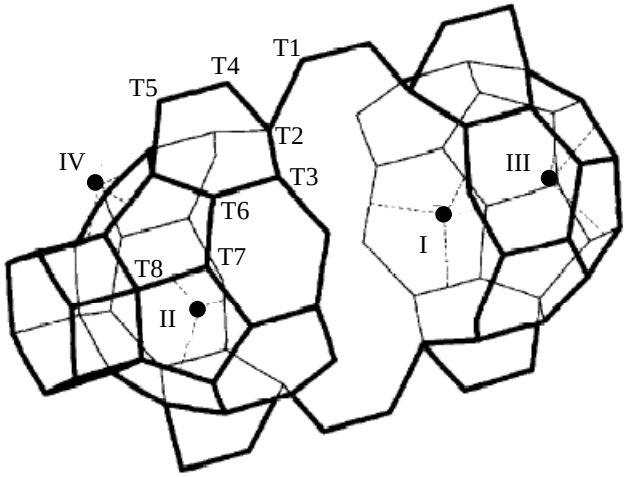

Figure 1.13 Structure of MCM-22 showing all T-sites, which constitute a unit cell. Roman numbers indicate the different cation sites.

The MCM-22 structure, shown in Figure 1.13, exhibits all eight different T positions of a unit cell [127]. The unit cell of MCM-22 shows four potential sites where the charge balancing cations are mainly located [128]. The SI position is located in front of a bent six-ring in the supercages (12 possible sites), while SII is in front of a five-ring in the supercage (12 possible sites). The SIII position is in front of a six-ring of the hexagonal prism at the bottom of the supercage (2 possible sites). Finally. SIV is located in front of a five-ring in the two-dimensional sinusoidal channel (12 possible sites). Site II and site IV are not occupied simultaneously, thus the total number of those sites is 12.

1.5 MCM-36

Starting from as-synthesized MCM-22 precursor, a new material could be synthesized by swelling and applying a pillaring agent (Figure 1.14) [129]. The material pillared with tetraethylorthosilicate (TEOS) contained micro- and mesopores and was denoted as MCM-36. By incorporation of the pillars, the accessibility of the pore system of MCM-22 consisting of supercages is increased, leading to mesopores between 3 and 3.5 nm in size. The pore system consisting of sinusoidal 10-membered-ring channels remains unaffected (Figure 1.15) [130] as shown from sorption of alkanes taking place in the same local environment [131]. Swelling and pillaring lead to changes in morphology, in pore size distribution, and in the concentration of the acid sites of MCM-22. The insertion of all silica pillars increases the concentration of terminal Si-OH groups in the sample. The concentration of the Brønsted acidic Si-OH-Al groups, however, was found to be markedly lower for MCM-36 than for MCM-22 as seen from lower alkane loadings on MCM-36 than on MCM-22 [132]. This decrease is attributed to dealumination procedures caused during swelling and pillaring processes. The major fraction of the Brønsted acid OH-sites and, thus, the favored sorption sites was found to be located in the 10-membered-ring channels of MCM-22 [133]. The relatively open structure of MCM-36 indicates high potential for interesting catalyzed reactions involving sterically demanding molecules, like the isoparaffin-olefin alkylation [134]. By changing the composition of the oxide pillars using combinations of SiO_2, Al_2O_3, MgO, and BaO [135], strong acid and base sites have been introduced, the chemical properties varied and thus, the possible field of application of MCM-36 type materials.

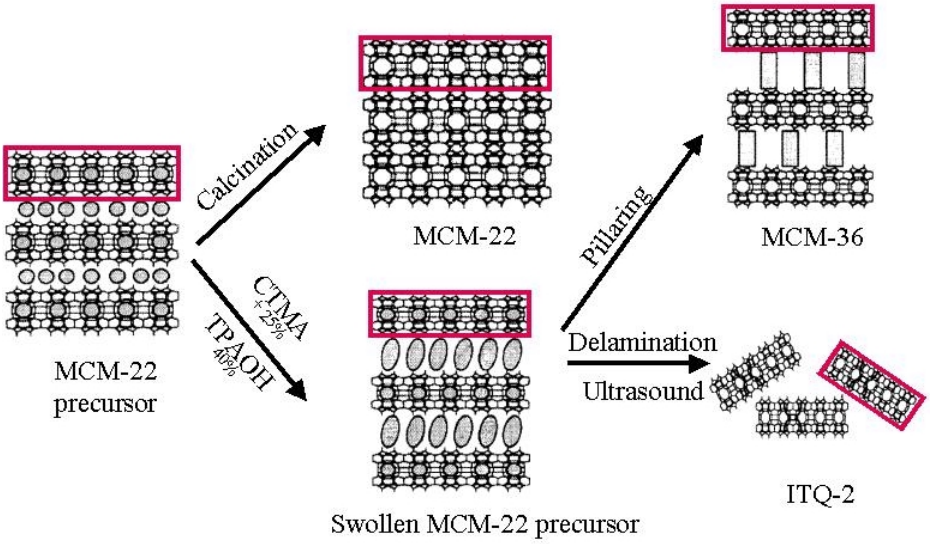

Figure 1.14 Synthesis of MCM-36 and ITQ-2 from the as-synthesized MCM-22 precursor [136].

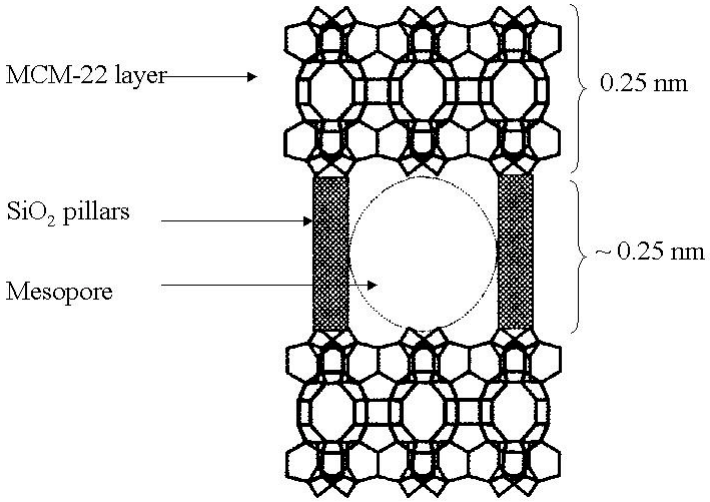

Figure 1.15 Schematic representation of the MCM-36 structure.

1.6 ITQ-2

Another new material with a completely disordered layered structure was able to be achieved by swelling and exfoliating the layers by applying ultrasound treatment also starting from the as-synthesized MCM-22 precursor (Figure 1.14). Delamination of the layered MCM-22 led to monolayers of crystalline aluminosilicates, called ITQ-2 [3,4]. The material consists of 0.25 nm thin sheets with the MCM-22 typical sinusoidal 10-membered ring channel system inside the sheets (Figure 1.16). ITQ-2 exhibits very high specific surface areas and is structurally well defined [137, 120]. Due to exfoliation of the MCM-22 layers, the large cylindrical supercages of MCM-22 were halved and an increasing number of now half open supercages ("cups") are present in a hexagonal array on the new sheet surface (Figure 1.12 and 1.16). These cups show a depth of approximately 0.7 nm and 12-membered ring openings with an aperture of about ~ 0.7 nm [120, 136]. Thus, active sites I, II, and III located previously in the supercages are more easily accessible to larger molecules [138]. This type of transformation depends subtly on the composition of the materials and the chemical methods employed.

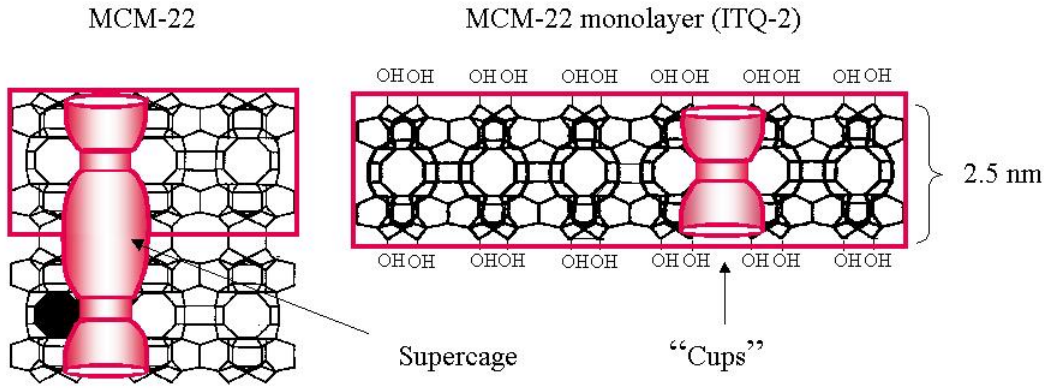

Figure 1.16 Schematic representation of a single-layer hexagonal crystallite of ITQ-2.

1.7 Scope and structure of the thesis

The identification of the active sites in the zeolites is of crucial importance for the design of more efficient catalysts and in order to control processes. Thus, the active sites of zeolites and their interaction with probe molecules, similar or identical to the actual sorbates, have to be characterized in detail. One of the most powerful methods involves spectroscopic investigation of the probe molecules in the adsorbed state, i.e., by IR or INS spectroscopy. The interaction between the adsorption sites of the zeolite and probe molecules perturbs the normal vibrations of the latter and leads to frequency shifts compared to the gas phase. Thus, the sorbate molecule in the adsorbed state yields much useful information concerning the strength and nature of the interactions with the adsorption sites of the zeolite and the sorbate orientation.

This thesis focus on the adsorption of linear C_1-C_4 alcohols and amines on alkali metal cation exchanged zeolites and zeolitic mesoporous materials. The adsorptive properties of zeolites depend both on their structure and on their cations size, charge, and distribution. Adsorption structures of *n*-alcohols are discussed in the view of the charge balancing, Lewis acid cation, i.e., the negative charge on the zeolite oxygen atom in zeolite X (Chapter 3) and their alkyl chain length (Chapter 4). The dependence of the sorbate polarity of short alcohols and amines on adsorption was discussed in Chapter 5. The role of synthesis routes, their modification, and the importance of chemical composition (Al content) of the MCM–22 precursors on the transformation into ITQ-2 are discussed in Chapter 6. The accessibility of the sorption sites on alkali metal cation exchanged MCM-22 and its homologues MCM-36 and ITQ-2 is shown in Chapter 7 and possible sorption sites are discussed. Finally, the relation between the composition of the mixed oxide pillars showing basic properties introduced into MCM-36 and the alcohol sorption behavior is reported in Chapter 8.

1.8 References

[1] Tanabe, K.; Hölderich, W.F. *Appl. Catal. A: General* **1999**, 181, 399.

[2] Albright, L.F.; Kranz, K.E.; Masters, K.R. *Ind. Eng. Chem. Res*. **1993**, 12, 2991.

[3] Anonymous, *Oil & Gas Journal* **1996**, 94, 69 and 1997 12, 45.

[4] Armor, J.N. *Appl. Catal*. **1991**, 78, 141. *The Catalyst Review Newsletter* **1998**, 3, 3.

[5] Hernandez-Robinson, A.; Ram. S.; Smith, C.M. *Proc. Worldwide Solid Acid Proc. Conf*. **1993**, Houston, TX, organized by The Catalyst Consultants.

[6] Hölderich, W.F. *Supramolecular Chem*. **1996**, 7, 671.

[7] Taglieber, V.; Hölderich, W.F.; Kummer, R.; Mross, W.O.; Saladin, E. *EP 0133938* and *EP 0132736*, **1993**, assigned to BASF AG; Hölderich, W.F.; Taglieber, V.; Pohl, R.; Kummer, R.; Baur, K.G. *DE 36342747*, **1987**, assigned to BASF AG.

[8] Mitsui, O.; Yohei, K. *DE 3441072*, **1985**, assigned to Asahi Kasei Corp.

[9] Tanabe, K.; Nishizaki. T *Proc. 6th Int. Congr. Catal.* **1977**, 2, 863.

[10] Bohlmann, G.M. PEP Review 92-2-4, SRI International; Mitsutani, A.; Kumano, S. special Evaluation Report No. 24 of Nippon Chemtec Consulting Inc., September **1996**.

[11] Chemical Marketing Reporter **1997**, 252, 1.

[12] Dartt, C.B.; Davis, M.E. *Catal. Today*, **1994**, 19, 151.

[13] Rustin, G.C.; Rule, M. *J. Catal*. **1994**, 147, 186.

[14] Sumitomo Chem. Ind. Co., Japan Patent Kokai, 61-130240, **1987**.

[15] Puppe, L. *Chemie in unserer Zeit* **1986**, 4, 117.

[16] Ben Taarit, Y. ; Derouane, E.G., Eds.; *Zeolite Microporous Solids: Synthesis, Structure and Reactivity*, NATO ASI Series C352, Kluwer, Dordrecht, **1992,** 291.

[17] Baerlocher, Ch., Meier, W.M; Olson, D.H. *Atlas of Zeolite Structure Types*, Elsevier, London, **2001**.

[18] Ramachandran, S.; Lenz, T.G.; Skiff, W.M.; Rappé, A.K. *J. Phys. Chem*. **1996** 100, 5898.

[19] Uchida, H.; Itoh, S.; Yoneyama. H. *Chem. Lett.* **1995**, 1993; Dagan, G.; Tomkiewicz, M.*J. Phys. Chem*. **1993**, 97, 12651; Augustynski, J. *Electrochim. Acta* **1993**, 38, 43.

[20] Davis, R.J. *J. Catal*. **2003**, 216, 396.

[21] Hsu, Y. S.; Lee, T. Y.; Hu, H. C., *Ind. Eng. Chem. Res.* **1988**, 27, 942. Corma, A. *Chem. Rev.* **1995**, **9**5, 559.

[22] Dyer, A. *An Introduction to Zeolite Molecular Sieves*; J. Wiley & Son, New York, **1988**.

[23] Meier, W. M. *Molecular Sieves*, Soc. Chem. Ind., London, **1968**.

[24] Pelmenschikov, A.G. *J. Phys. Chem. 96*, 7051, **1992**.

[25] Occelli, M.L. O'Connor, P., Eds., *Fluid Cracking Catalysts*, Marcel Dekker, New York, **1997**.

[26] Coster, D.; Blumenfeld, A.L.; Fripiat, J.J. *J. Phys. Chem.* **1994**, *98*, 6201.

[27] Kühl, G.H. *J. Phys. Chem. Solids* **1977**, *38*, 1259.

[28] Boréave, A.; Auroux, A.; Guimon C. *Microp. Mater.* **1997**, *11*, 275.

[29] Aronson, N.T.; Gorte, R.T.J.; Farneth, W.E. *J. Catal.* **1986**, *98*, 434.

[30] Lombardo, E.A.; Sill, G.A.; Hall, W.K. *J. Catal.* **1989**, *119*, 426.

[31] Hunger, B.; Miessner, H.; Szombathely, M.V. Geidel; E*J. Chem. Soc. Faraday Trans.* **1996**, *92*, 499.

[32] Khabtou, S. Chevreau, T. Lavalley; J.C. *Microp. Mater.* **1994**, *3*, 133.

[33] Beyerlien, R.A.; Mc Vicker, B.B.; Yacullo L.N.; Ziekmak, J.J. *J. Phys. Chem.* **1988**, *92*, 1967.

[34] Corma, A.; Fornes, V.; Rey, F. *Appl. Catal.* **1990**, *59*, 267.

[35] Garralon, G.; Corma, A.; Fornes, V. *Zeolites* **1989**, *9*, 84.

[36] Carbajal, R.; Chu, P.J.; Lunsford, H.H. *J. Catal.* **1990**, *125*, 123.

[37] Peters, A.W.; Wu C.C. *Catal. Lett.* **1995**, *30*, 171.

[38] Lohse, U.; Löffler, E.; Hunger, M. Stöckner, J. Patzelove; V. *Zeolites* **1987**, *7*, 11.

[39] Hathaway, P.E.; Davis, M.C. *J. Catal*. **1989**, 116, 263.

[40] Weitkamp, J; Hunger, M.; Rymsa, U. *Micropor. Mesopor. Mater*. **2001**, 48, 255.

[41] Jentys, A.; Lercher, J:A. *Introduction to Zeolite Science and Practice*, van Bekkum, H.; Flanigan, E.M.; Jacobs, P.A.; Jansen, J.C., Eds., Elsevier, Amsterdam, New Yord, **2001**.

[42] Barthomeuf, D. *J. Phys. Chem.* **1984**, *88*, 42.

[43] Yashima, T.; Suzuki, H.; Hara, N. *J. Catal*. **1974**, 33, 486.

[44] Mirodatos, C.; Pichat, P.; Barthomeuf, D. *J. Phys. Chem.* **1976**, 80, 1335; Abou-Kais, A.; Miradatos, C.; Massardler, J.; Barthomeuf, D.; Berdrine, J.C. *J. Phys. Chem.* **1977**, 81, 397. Miradatos, C.; Abou-Kais, A.; Verdrine, J.C.; Pichat, J.; Barthomeuf, D. *J. Phys. Chem.* **1976**, 80, 2366.

[45] Tsuji, H.; Yagi, F.; Hattori, H.; Kits, H. *Stud. Surf. Sci. Catal.* **1992**, 75, 1171; Hathaway, P.E.; Davis, M.E. *J. Catal.* **1989**, 116. 263. Rodrigues, I.; Cambon, H.; Brunel, D.; Laperas, M. *J. Mol. Catal. A. Chem*. **1998**, 130, 195.

[46] Xu, B.; Chen, X.; *J. Phys. Chem*. **1992**, 96, 2642; Beres, A.; Hannus, I.; Kiricsi, I. *J. Therm. Anal.* **1996**, 46, 1301 and 47, 419.

[47] Hannus,I.; Beres, A.; Nagy, J.B.; Halasz, J.; Kiricsi, I. *J. Mol. Struct*. **1997**, 410, 43.

[48] Barthomeuf, D. *Catal. Rev. Sci. Eng*. **1996**, 38, 521.

[49] Vayssilov, G.N.; Rösch, *N. J. Catal*. **1999**, 186, 423.

[50] Mortier, W.J. *J. Catal*. **1978**, 55, 138.

[51] Sanderson, R.T. *J. Am. Chem. Soc*. **1983**, 105, 2259.

[52] van Santen, R.A., van Beest, B.W.H.; de Man, A.J.M. *Guidelines for mastering the properties of molecular sieves*, d. Barthomeuf, Ed., Plenum Press, New York, **1990**.

[53] Keane, M.A. *Microporous Mater.* **1996**, 7, 51; Iu, K.K.; Thomas, J.K. *Langmuir* **1990**, 6, 471.

[54] Ward, J.W. *J. Catal*. **1969**, 14, 365, J. Catal. **1968**, 10, 34.

[55] Yagi, F.; Tsuji, H. Hattori, H. *Micropor. Mater*. **1997**, 9, 237.

[56] Davydov, A.A.; Shepot'ko, M.L.; Budneva, A.A. *Kinet. Katal*. **1994**, 35, 299.

[57] Lavalley, J.C. *Catal. Today* **1996**, 27, 377.

[58] Murphy, D.; Massiani, P.; Franck, R.; Barthomeuf, D. *J. Phys. Chem*. **1996**, 100, 6731.

[59] Gordymova, T.A.; Davydov, A.A. React. *Kinet. Catal. Lett*. **1983**, 23, 233.

[60] Xie, J.; Huang, M.; Kaliaguine, S. React. *Kinet. Catal. Lett.* **1996**, 58, 217.

[61] Choi, S.Y.; Park, Y.S.; Hong, S.B.; Yoon, K.B. *J. Am. Chem. Soc*. **1996**, 118, 9377.

[62] Doskocil, E.J.; Bordawekar, S.V.; Kaye, B.G.; Davis, R.J. *J. Phys. Chem. B* **1999**, 103, 6277.

[63] Knözinger, H.; Huber, S. *J. Chem. Soc. Faraday Trans*. **1998**, 94, 2047.

[64] Eulenberge, G.R.; Shoemaker, D.P.; Keil, J.G. *J. Phys. Chem*. **1967**, 71, 1812.

[65] Buhrke, V.E. *A practical guide for the preparation of specimens for x-ray fluorescence and x-ray diffraction analysis*, Whiley-VCH **1998**, 196.

[66] Jacobs, W.P.J.H; de Haan, J.W.; van de Ven, L.J.M.; van Santen, R.A. *J. Phys. Chem*. **1983**, 97, 10394.

[67] Liu, H.; Grey, C.P. *Micropor. Mesopor. Mater*. **2002**, 53, 109.

[68] Olson D. H., *Zeolites* **1995**, 15, 439.

[69] Shepelev, Yu.F.; Butikova, I.K.; Smolin, Yu.I. *Zeolites* **1991**, 11, 287.

[70] Henson, N.J.; Eckert, J.; Hay; P.J. RedondoA. *Chemical Physics* **2000**, 261, 111.

[71] Fitch, A.M.; Jobic, H.; Tonouprez, A. *J. Phys. Chem*. **1986**, 90, 1311.

[72] Zuh, L.; Seff, K *J. Phys. Chem.* B **1999**, 103, 9512.

[73] Sherry: Zeolites **1993**, 13, 377.

[74] Breck, D. W. *Zeolite Molecular Sieves*, J. Wiley and Sons, **1974**.

[75] Norby, P.; Poshni, F.I.; Gualtieri, A.F.; Hanson, J:C.; Grey, C.P. *J. Phys. Chem. B* **1998**, 102, 839.

[76] Huber, S.; Knözinger, H. *Appl. Catal. A: General* **1999**, 189, 239.

[77] Feuerstein, M.; Accardi, R.J.; Lobo, R.F. *J. Phys. Chem. B* **2000**, 104, 10282.

[78] Plévert, J.; Ménorval, L.C.D.; Renzo, F.C.; Fajula, F. *J. Phys. Chem. B* **1998**, 102, 3412.

[79] Liu, H.; Kao, H.-M.; Grey, C.P. *J. Phys. Chem. B* **1999**, 103, 4786.

[80] Zhu, L.; Seff, K. *J. Phys. Chem. B* **2000**, 104, 8946.

[81] Norby, P.; Poshni, F.I.; Gualtieri, A.F.; Hnason, J.C.; Grey, C.P. *J. Phys. Chem. B* **1998**, 102, 839.

[82] Philippou, A. Anderson, M.W. *J. Am. Chem. Soc.* **1994**, 116, 5774.

[83] Barthomeuf, D.; de Mallmann, A. *Innovation in Zeolite Materials Science*; Grobet, P.J., Mortier, W.J., Vansant, E.F., Schulz-Ekloff, G., Des.; .sevier: Amsterdam, **1988**; 365.

[84] Wieland, W.S.; Davis, R.J.; Garces, J.M. *Catal. Today* **1998**, 173, 490.

[85] Rep, M. *Side Chain Alkylation of Toluene with Methanol over Basic Zeolites*, PhD Thesis, University of Twente, Enschede, The Netherlands, **2002**.

[86] Rabo, J. A. *Catal. Rev. Sci. Eng.* **1985**, 23, 2955.

[87] Engelhardt, G. *Microp. Mater.* **1997**, 12, 369.

[88] Sherry, H. S. *J. Phys. Chem.* **1968**, 72, 4086.

[89] Ramôa Ribeiro, F. *Catal. Lett.* **1993**, 22, 107.

[90] Breck, D. W. *Zeolite Molecular Sieves*, J. Wiley and Sons, **1974**.

[91] Breck, D. W.; Eversole, D. G; Milton, R. M.; Reed, T. B.; Thomas, T. L. *J. Am. Chem. Soc.* **1956**, 78, 5963.

[92] Rabo, J.A.; Gajda, G.C. *Catal. Rev*. **1998/90**, 31, 385.

[93] Eder-Mirth, G.; Lercher, J.A. *Recl. Trav. Chim. Pays-Bas* **1996**, 115, 157.

[94] Ziolek, M.; Czyzniewska, J.; Lamotte, J. ; Lavalley, J.C. *Zeolites* **1996**, 16, 42.

[95] Rep, M.; Palomares, A.E.; Eder-Mirth, G.; van Ommen, J.G.; Rösch, N.; Lercher; J.A. *J. Phys. Chem.* B 2000, 104, 8624.

[96] Kiselev, A.V. *Advan. Chem.. Ser*. **1971**, 102, 37. Kiselev, A.V. Discussion Faraday Soc. **1965**, 40, 228.

[97] Kazansky, V.B.; Yu. V.; Borovkov, A.; Serich, H.G. Karge; *Microp. Mesop. Mater.* **1998**, 22, 251.

[98] Hunger, B.; Klepel, O.; Kirschhock, C.; Heuchel, M.; Toufar, H.; Fuess, H. *Langmuir* **1999**, 15, 5937.

[99] Kirschhock, C.; Fuess, H. *Zeolites* **1996**, 17, 381.

[100] Subramanian, V., Seff, K. *J. Phys. Chem*. **1977**, 81, 2249.

[101] Bae, M.N.; Song, M.K.; Kim, Y.; Seff, K *Micropor. Mesopor. Mater* **2003**, 63, 21.

[102] Jang, S.B.; Jeong, M.S.; Kim, Y.; Seff, K *J. Phys. Chem. B* **1997**, 101, 9041.

[103] Dendooven, E.; Mortier, W.J.; Uytterhoeven, J.B. *J. Phys. Chem*. **1984**, 88, 1916.

[104] Mortier, W.J.; van den Bossche, E.; Uytterhoeven J.B. *Zeolties* **1984**, 4, 41.

[105] Narayana, M.; Kevan L. *J. Am. Chem. Soc*. **1981**, 103, 5729.

[106] William, L.E.; Paul, O.F.; Atholl, A.V.G.; Jack, H.L. *J. Phys. Chem*. **1987**, 91, 2091.

[107] Yanagida, R.Y.; Seff, K. *J. Phys. Chem*. **1972,** 76, 2597.

[108] Kim, M.J.; Jeong, M.S.; Kim, Y.; Seff, K. *Micropor. Mesopor. Mater*. **1999**, 30, 233.

[109] Breck, D.W.; Eversole, W.G.; Milton, R.M.; Reed, T.B.; Thomas, T.L. *J. Am. Chem. Soc*. **1956,** 78, 5963.

[110] Rees, L.V.C.; Berry, T. Molecular Sieves, Society of Chemical Industry, London, **1968**, 149.

[111] Su, B.-L.; Norberg, V *Coll. Surf. A Phys. Eng. Asp*. **2001**, 187-188, 297.

[112] Liu, S.B.; Ma, L.L.; Lin, M.W.; Wu, J.F.; Chen. T.L *J. Phys. Chem*. **1992**, 96, 8120.

[113] Su, B.L *J. Chem. Soc. Faraday Trans*. **1997**, 93, 1449.

[114] Coker, E.N.; Roelofsen, D.P.; Barrer, R.M.; Jansen, J.C.; van Bekkum, H. *Micropor. Mesopor. Mater*. **1998**, 22, 261.

[115] van Koningsveld, H.; Jansen, J.C. *Micropor. Mater*. **1996**, 6, 159.

[116] van Koningsveld, H.; Tuinstra, F.; van Bekkum, H.; Jansen, J.C. *Acta, Crystallogr. Sect. B* **1989**, 45, 423.

[117] Choi, E.Y.; Kim, S.Y.; Kim, Y.; Seff, K. *Micropor. Mesopor. Mater* **2003**, 63, 201.

[118] Bae, M.N.; Song, M.K.; Kim, Y.; Seff, K *Micropor. Mesopor. Mater* **2003**, 63, 21.

[119] Vartuli, J.C.; Kresge, C.T.; Roth, W.J.; Mc Cullen, S.B.; Beck, J.S.; Schmitt, K.D.; Leonowicz, M.E.; Lutner, J.D.; Sheppard, E.W. in *Advanced Catalysts and Nanostructured Materials: Modern Synthesis Methods* (Ed.; Moser, W.R.) Academic Press, New York, **1996**, 119.

[120] Corma, A.; Fornes, V.; Guil, J.M.; Pergher, S.B.; Maesen, Th.L.M.; Buglass, J.G. *Micropor. Mesopor. Mater*. **2000**, 38, 301.

[121] Rubin, M.K.; Chu, P. *US Patent* 4 954 325, **1990**.

[122] Del Rossi, K.J.; Huss, A.Jr. *US Patent* 5 107 047, **1992**.

[123] Huss, A. Jr.; Kirker, G.W.; Keville, K.M.; Thomson, R.T. *US Patent* 4 992 615, **1991**.

[124] Abril, R.P.L.; Bowes, E.; Green, G.J.; Marler, D.O.; Sihabi, D.S.; Sacha, R.F. *US Patent* 5 085 762, **1992**.

[125] Camblor, M.A.; Corma, A.; Diaz-Cabanas, J.M.; Baerlocher, C. *J. Phys. Chem. B* **1998**, 102, 44.

[126] Lawton, S.L.; *Leonowicz, M.E.; Partridge, R D.; Chu P.; Rubin, M.K.* Micropor. Mesopor. Mater. **1998**, 23, 109.

[127] Sastre, G.; Fornes, V.; Corma, A. *Chem. Commun*. **1999**, 21, 2163.

[128] Wasowicz, T.; Prakash, A.M.; Kevan, L *Micropor. Mater*. **1997**, 12, 107.

[129] Kresge, E.T.; Roth, W.J.; Simmons, K.G.; Vartuli, J.C. *US Patent* 5 229 341, **1993**.

[130] Roth, W.J.; Kresge, C.T.; Vartuli, J.C.; Leonowicz, M.E.; Fung, A.S.; McCullen, S.B. *Stud. Surf. Sci. Catal.* **1995**, 94, 301.

[131] He, Y.J.; Nivarthy, G.X.; Eder, F.; Seshan, K.; Lercher, J.A. *Micropor. Mesopor. Mater*. **1998**, 25, 207.

[132] Eder, F.; He, Y.J.; Nivarthy, G.; Lercher, J.A. *Recl. Trav. Chim. Pays-Bas* **1996**, 115, 531.

[133] Meloni, D.; Laforge, S.; Martin, D.; Guisnet, M.; Rombi, E.; Solinas, V. *Appl. Catal. A: General* **2001**, 215, 55.

[134] Chu, C.T.; Altaf, H.; Huss, A.N.J.; Kresge, C.T.; Roth, W.J. *U.S. Patent* 5 258 569, **1993**.

[135] Barth, J.-O.; Jentys, A.; Kornatowski, J.; Lercher, J.A. *Chem. Mater*. **2004**.

[136] Corma, A.; Fornes, V.; Martinez-Triguero, J.; Pergher, S.B. *J. Catal.* **1999**, 186, 57.

[137] Corma, A.; Fornes, V.; Pergher, S.B.; Maesen, Th.L.M. Buglass, J.G. *Nature* **1998**, 396, 353. Micropor. Mesopor. Mater.

[138] Corma, A.; Fornés, V.; Forni, L.; Márquez, F.; Martínez-Triguero J.; Moscotti D. *J. Catal*. **1998**, 179, 451.

[139] Lee, S.H.; Kim, Y.; Kim. D.-S.; Seff, K. *Bull. Korean Chem. Soc*. **1998**, 19, 98.

[140] Mortier, W.J.; Bosmans, H.J.; Uytterhoeven, J.B. *J. Phys. Chem*. **1972**, 76, 650.

Chapter 2

Investigation of the adsorption of methanol on alkali metal cation exchanged zeolite X by Inelastic Neutron Scattering

Abstract

The adsorption of methanol on alkali metal cation exchanged zeolite X was studied by inelastic neutron scattering (INS) and Fourier transform infrared (FTIR) spectroscopy in the range 30-2000 and 1300-3800 cm^{-1}, respectively. Infrared vibrational spectra from solid methanol and methanol adsorbed on the zeolites were compared to INS spectra calculated from ab initio simulations for one, two and three methanol aggregates in order to describe the interactions between the sorbate molecules and the zeolite.

Solid methanol was found to crystallize in the low temperature α-phase by instant cooling to temperatures below 20 K. The primary interaction of methanol and the zeolite occurred between the oxygen atom of the alcohol and the cations located at the ion exchange positions of the zeolite. The increasing shift of the ν(OH) stretching vibration with increasing framework polarity of the zeolite indicates additional interaction between the OH group of methanol and the lattice oxygen atoms as well as intermolecular hydrogen bonding between adjacent adsorbed methanol molecules.

2.1 Introduction

Catalysts with pronounced basic properties are able to catalyze a large number of reactions including olefin isomerization, aldehyde and ketone condensation, side chain alkylaromatic alkylation, dehydrogenation and amination. Crystalline microporous materials such as zeolites are used as catalysts for acid - basic catalyzed reactions [1] as they can be prepared with well defined and isolated acid/base sites [2] in combination with a wide range of pore dimensions [3] matching to the size of the organic reactants. This allows the chemical reactions to take place in a specifically chosen and well-defined environment, i.e., in the cages or channels of the molecular sieves, which act as nano scale reactors. To improve reaction yields and selectivities, knowledge of the chemical and structural properties of the active sites and their relation to the sorbent-sorbate structure is essential for a rational catalyst design.

For the alkylation of toluene with methanol it was found that zeolites with predominately basic properties catalyze side chain alkylation, i.e., the formation of styrene and ethylbenzene, while on zeolites with acid sites a high selectivity to the formation of xylenes (alkylation of the aromatic ring) was observed[4]. A systematic study of the (non-reactive) interaction of methanol with alkali metal cation exchanged molecular sieves using *in situ* IR spectroscopy performed by Rep *et al.* [5] showed, that with increasing framework polarity (i.e., decreasing Si/Al ratio and/or increasing atomic size of the exchanged cations) the interaction between methanol and the lattice oxygen atoms of the zeolite *via* the hydrogen atoms of the hydroxyl group and the methyl groups increased. This was attributed to the increase in the negative charge of the framework oxygen atoms located at the inner surface of the zeolite. However, the direct interaction between the lone-pair electron donor function of methanol *via* the oxygen atom of the hydroxyl group and the electron pair acceptor function of the zeolite (i.e., the alkali metal cations) has been identified as the most important energetic contribution to sorption. The size of the metal cations in the molecular sieve controls the preference for the sorption of methanol versus toluene with the smaller cations having a greater preference for methanol than the larger. While the principle features of these interactions are known, our knowledge of the complex adsorption structures of methanol in these polar materials is still rudimentary.

In this work, we wish to further explore the complex interaction of methanol with alkali metal cation (Na^+, K^+, Rb^+, Cs^+) exchanged zeolite X. Zeolite X belongs to the

faujasite structural group (FAU) consisting of a three dimensional pore system with large supercages and 12 MR-pore openings, which are easily accessible for sorbates. The role of the zeolite basicity on the sorption of methanol was studied by inelastic neutron scattering (INS) and infrared (IR) spectroscopy and potential sorption structures are discussed. The reason for this choice of the spectroscopy is based on the differences between IR and INS spectroscopy. Infrared intensities are determined by the interaction of electromagnetic radiation with the electrons present in the system, while for inelastic neutron scattering the intensity depends on the momentum transfer, the amplitude of vibration and the incoherent scattering cross section. Because the cross section of hydrogen is 10 – 100 times larger than that of all other elements and being the lightest element its amplitude of vibration is large motions involving hydrogen dominate the INS spectrum.

2.2 Experimental Section

2.2.1 Materials

Commercial Na-X zeolite (Si/Al = 1.3; Köstrolith, Südchemie) was exchanged with 0.1 molar alkali metal nitrate solutions (Na^+, K^+, Rb^+ and Cs^+). The suspension was stirred at 535 K for 20 h (solid/liquid ratio = 20 $g \cdot l^{-1}$), cooled to room temperature, washed, dried and subsequently calcined at 723 K under flowing synthetic air for 1h. The complete exchange procedure was repeated three times. Cs^+ ion exchange was performed by IKO minerals. The composition of the materials and the pore volume determined by AAS and N_2-sorption, respectively, are summarized in Table 2.1.

2.2.2 The INS experiments and sample preparation

Inelastic neutron scattering measurements were performed on the spectrometer TOSCA at the spallation neutron source ISIS (Rutherford Appleton Laboratory, UK). TOSCA uses an indirect time-of-flight geometry that allows inelastic neutron scattering spectra to be recorded in the energy transfer range 30 – 4000 cm^{-1} with a resolution of ($\Delta E/E$) ~ 1.5 % [6].

Table 2.1 Characteristics of alkali metal cation exchanged X zeolites determined from AAS analysis and N_2-sorption.

Sample	Si/Al	M^+/Al [mol%]	Na^+/Al [mol%]	Unit cell composition	Mirpore volume [m^3/g]	S_{int} [a]	δ_0 [b]	e/r [c] [Å^{-1}]
Na-X	1.2	100	100	$Na_{88}\,Al_{88}\,Si_{104}\,O_{384}$	0.17	2.314	-0.337	1.05
K-X	1.3	95.3	2.3	$K_{82}\,Na_2\,Al_{84}\,Si_{108}\,O_{384}$	0.15	2.298	-0.341	0.75
Rb-X	1.2	67.5	32.5	$Rb_{60}\,Na_{29}\,Al_{88}\,Si_{104}\,O_{384}$	0.11	2.232	-0.358	0.67
Cs-X	1.3	55.4	44.6	$Cs_{47}\,Na_{38}\,Al_{84}\,Si_{108}\,O_{384}$	0.10	2.239	-0.356	0.59

[a] $S_{int} = (S_P^p \cdot S_Q^q \cdot S_R^r \cdot S_T^t)^{1/(p+q+r+t)}$: for a compound $P_pQ_qR_rT_t$ calculated intermediate Sanderson electronegativity [12, 13].
[b] Calculated average charge $-\delta_o$ on the oxygen of the lattice, using $(S_{int}-S_o)\cdot 2.08\cdot S_o^{1/2}$.
[c] electrostatic potential of sodium cation (e/r).

The zeolite samples were activated under flowing synthetic air at 723 K for 4 h. Sorption of methanol with a loading of 3 molecules per supercage (corresponding to a coverage 0.27 % of the counter cations) was performed at 308 K in helium as carrier gas. Subsequently, 20 g of the zeolite powder was transferred into the sample containers made from aluminum (size 45 x 50 x 20 mm) under inert atmosphere. The cells were sealed and heated to 353 K for 24 h to equilibrate the sorbate. Liquid samples were investigated in flat thin-walled aluminum cells. For recording the spectra the sample containers were placed in a helium cryostat and cooled to ca. 20 K. The spectra were recorded at temperatures below 20 K in the energy range 30-4000 cm^{-1}, measurement times were typically ~10 h. The spectrum of an empty container and of the activated zeolite was subtracted from the spectra of the samples. In general the activated zeolite samples are weak neutron scatterers, therefore, all intensity observed after the sorption results from the H atoms in the methanol molecules.

2.2.3 IR experiments

The sorption experiments were followed by *in situ* IR spectroscopy (Bruker IFS-88, resolution 4 cm^{-1}) at 308 K and methanol partial pressures of 10^{-3} mbar. The samples were pressed into self–supporting wafers (ca. 5 mg) and activated in vacuum ($p < 10^{-6}$ mbar) with a heating rate of 10 K·min^{-1} up to 723 K (holding for 30 min). After adsorption, the physisorbed molecules were removed at 308 K by evacuation

($p < 10^{-6}$ mbar) for 1h and desorbed by heating from 373 K to 723 K with a heating rate of 2 $K \cdot min^{-1}$. The spectra were recorded in the transmission absorption mode and monitored time-resolved during equilibration of the zeolite sample with the sorbate. All spectra were baseline corrected between 3800 and 1100 cm^{-1} and normalized to the integral peak area of the overtones of the framework vibrations in the range 2100 – 1735 cm^{-1}. The spectra presented in this paper are difference spectra, i.e., the spectrum of the activated zeolite is subtracted from the spectrum of the zeolite after adsorption of methanol. In this mode of presentation, IR bands pointing upwards increased in intensity and band pointing downwards decreased in intensity, upon the interaction of the zeolite with methanol.

2.2.4 Computational methods

The structure of single methanol molecules and of clusters consisting of two and three methanol molecules were optimized with respect to the total energy using density functional theory (DFT) as implemented in Gaussian 98 [7]. The 6-31G** basis set and non-local corrections on the B3LYP level were applied. After having achieved the optimized geometry for the different clusters investigated the vibrational modes were calculated. The displacement vectors determined for each vibrational mode were used to simulate the INS (including lattice modes and overtone vibrations) using the program a-CLIMAX [8].

2.3 Results

2.3.1 Dehydrated alkali metal cation exchanged X zeolites

The chemical composition and structural properties of the alkali cation exchanged zeolites are summarized in Table 2.1. Figure 2.1 reports the diffractograms of the parent Na-X material as well as those of the alkali metal cation exchanged X zeolites. All characteristic peaks of the parent Na-X zeolite, reported in the literature [9], are found in the diffraction patterns of the ion exchanged X samples, indicating that the introduction of these cations into the zeolite structure does not influence the structure of the X zeolite. However, the introduction of a larger cation such as Rb^+ or Cs^+ into the zeolite framework causes a considerable modification in the XRD pattern, i.e., a change in intensity and number of the peaks. A stepwise re-exchange of Cs-X back to

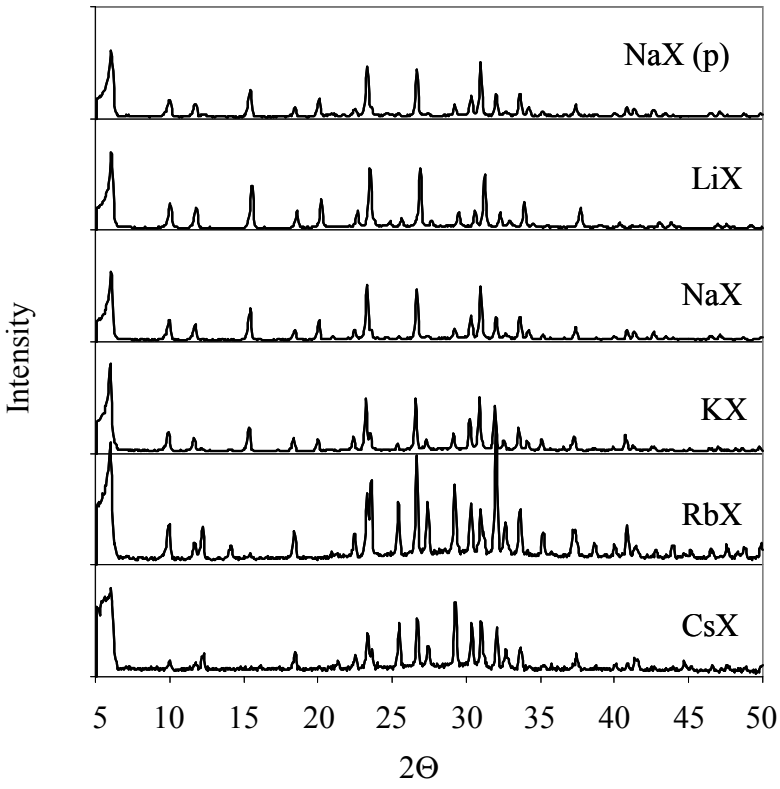

Figure 2.1 Powder X-ray diffraction patterns of parent Na-X and its alkali metal cation exchanged forms.

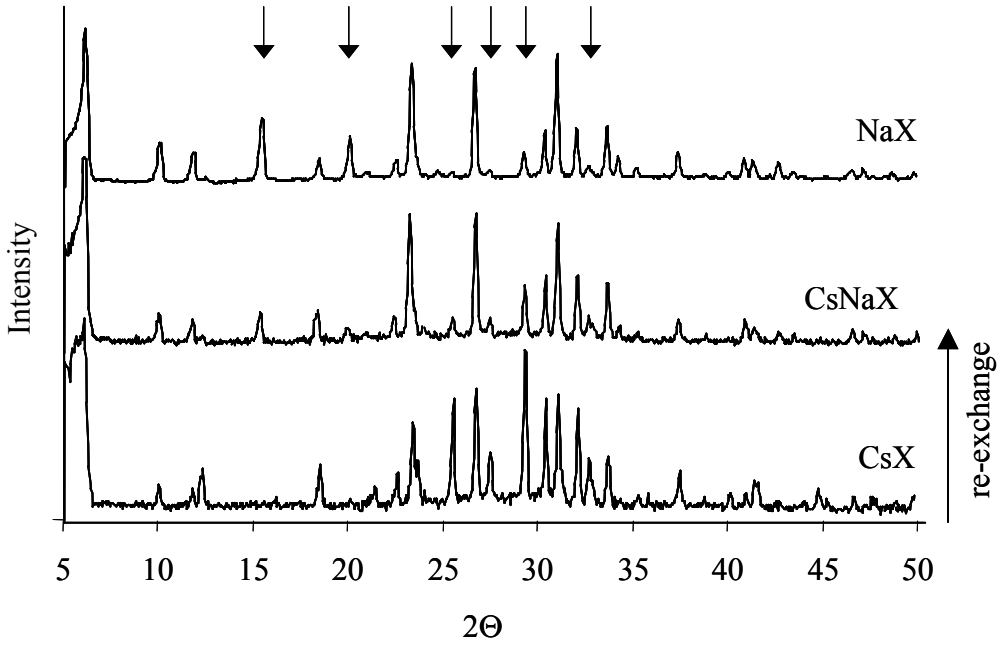

Figure 2.2 Powder X-ray diffraction patterns of parent Na-X, CsNa-X and Cs-X; arrows pointing to changing reflexes.

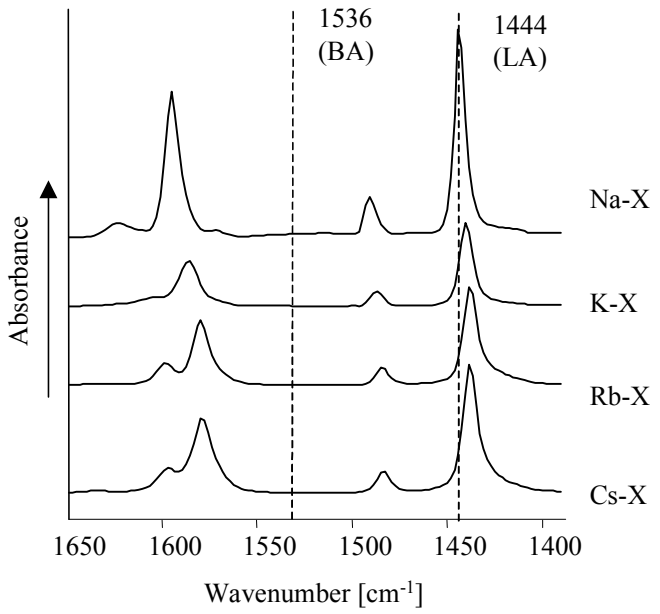

Figure 2.3 Difference infrared spectra of pyridine adsorbed on alkali metal exchanged X zeolites (T = 423 K, $p < 10^{-6}$ mbar).

the pure sodium form results in a decrease of the new reflections and finally in the former pattern of Na-X (Figure 2.2). Thus, it is concluded that, during the modification procedures, the zeolite structures remained unchanged, besides a low amount of amorphous material presumably formed during calcination procedure and identified by a small hump in the pattern of exchanged materials. The diffractograms of the exchanged materials exhibited stronger reflections at 18.4, 22.5 and 30.4°, which are similar to those calculated for hydrated Na-X [9] and indicate the presence of water in the samples. Note that the materials were exposed to atmospheric conditions after calcination.

The ring vibration bands in the range 1700 to 1400 cm^{-1} (Figure 2.3), seen after reaching adsorption-desorption equilibrium on alkali cation exchanged zeolites at $1 \cdot 10^{-2}$ mbar and evacuation for 1 h ($p < 10^{-6}$ mbar), can be assigned to deformation vibrations of pyridinium ions on the Brønsted acid sites (at 1536 cm^{-1}) and pyridine coordinated to the Lewis acid sites (alkali cations; at 1443 cm^{-1} (Na-X)), respectively. As none of the alkali metal exchanged zeolites shows a band at 1536 cm^{-1}, adsorption of pyridine does not indicate any detectable Brønsted acid sites. This leads to the conclusion that the whole negative charge of the framework oxygen atoms may be compensated by cations, while protons are absent. No band is also seen at 1453 cm^{-1}, assigned to pyridine absorbed on extra framework aluminum species, in spite of a

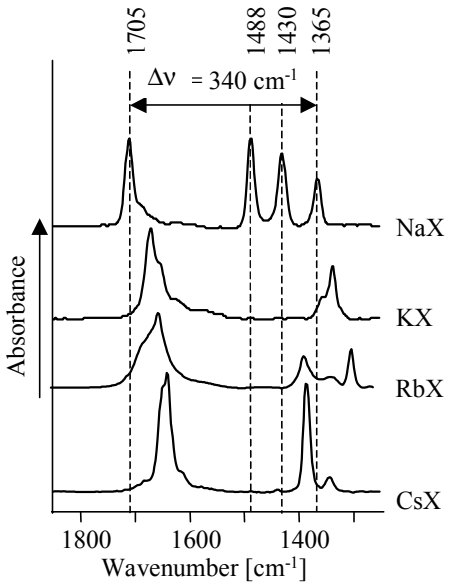

Figure 2.4 Difference infrared spectra of CO_2 adsorbed on alkali metal exchanged X zeolites in the carbonate region (T = 308 K, p = $1 \cdot 10^{-3}$ mbar).

small amount of extra framework Al species are assumed to be present (hydroxyl groups at around 3665 cm^{-1} in the infrared spectra of the activated materials). Thus, the band may be overlapped by the more intense one associated with the alkali metal cations.

For all faujasite materials, ν(OCO) stretching vibration bands, ascribed to carbonate species, are observed in the region between 1725 to 1300 cm^{-1} and indicate that the exchanged faujasite materials have basic properties. Figure 2.4 shows the infrared spectra of CO_2 adsorbed on cation exchanged X zeolites. On Na-X, significantly two types of band pairs are shown at 1711 and 1365 cm^{-1} (*species I*) and at 1488 and 1431 cm^{-1} (*species II*). They are attributed to the asymmetric and symmetric stretching bands, respectively, of two types of carbonate-like species [31]. Except Na-X, significant amounts of the second carbonate species were not found on the other alkali metal cation exchanged materials. On Na-X, species I could be converted to *species II*, while this was not the case for Cs-X [10] as seen from a couple of bands found at 1644 and 1385 cm^{-1}. With increasing alkali cation size and following increase in polarity of the zeolite framework, the splitting of the bond of asymmetric and symmetric ν(OCO) stretching mode for *species I* decreases.

For INS the spectra had to be collected at very low temperatures (< 20 K) in order to reduce the dynamic disorder found for molecules chemisorbed in zeolites [11]. The average partial negative charge of the framework oxygen atoms in the differently ion

exchanged zeolites has been estimated using the Sanderson intermediate electronegativity principle[12, 13]. The results clearly show that the negative oxygen partial charge $-\delta_0$ increases with increasing size of the monovalent cations. Thus, Rb^+- and Cs^+- exchanged zeolite X are the most basic samples in the series of the material studied. The INS spectra of solid methanol, of the dehydrated Na-X sample and of methanol adsorbed on Na-X are shown in Figure 2.5 In the region of the $\nu(CH_3)$ stretching vibrations (around 3000 cm^{-1}) and of the ν(OH) stretching vibrations (around 3500 cm^{-1}) only broad and unresolved bands of low intensity were observed due to the high momentum transfer, therefore, this region was not further analyzed. The INS spectra of the dehydrated Na-X zeolite is very similar to the spectrum of a completely cation exchanged Na-Y reported by Jobic *et al.* [14]. The band at 95 cm^{-1} is located in the region of external unit cell modes, e.g. translational and rotational lattice modes and translation modes of cations to the framework [15]. The broadened band at 200-300 cm^{-1} is attributed to pore opening vibrations [16]. The feature in the

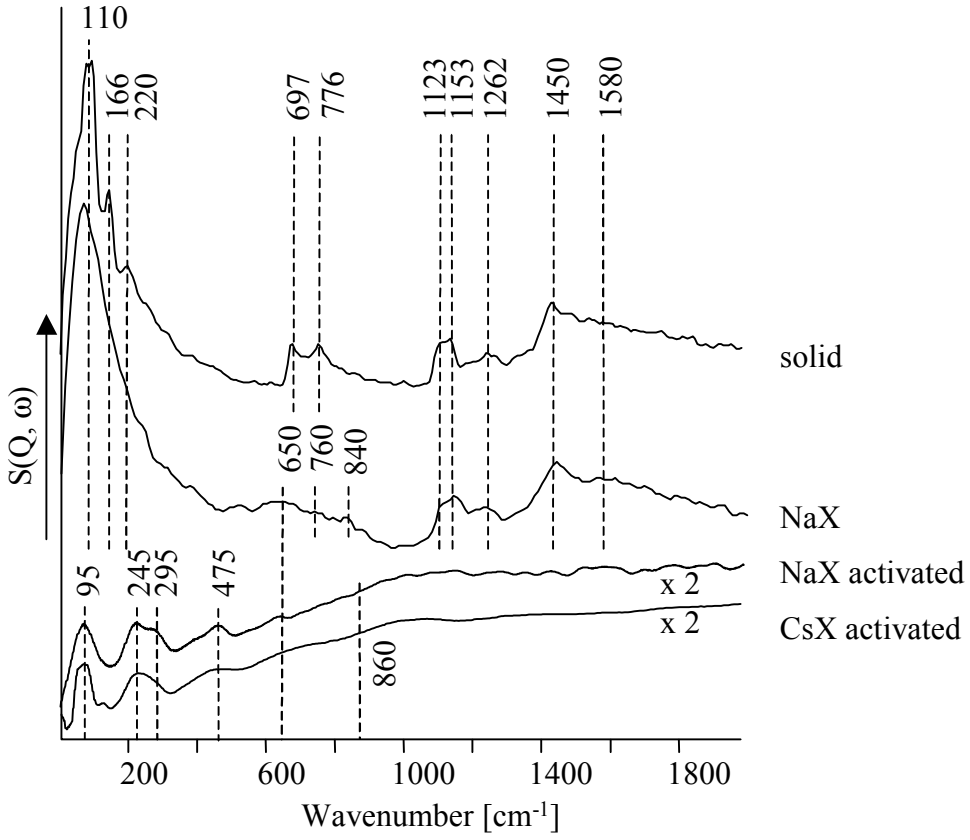

Figure 2.5 Inelastic neutron scattering spectra of dehydrated Na-X and Cs-X, methanol adsorbed on Na-X (loading 3 molecules per supercage, on average), and solid methanol at T < 20 K.

region 300-500 cm^{-1} is assigned to the T-O-T bending vibration (T denotes tetrahedrally coordinated Si or Al atoms), while the weak bands between 600 and 800 cm^{-1} and above 950 cm^{-1} are assigned to symmetric and asymmetric ν(T-O) stretching vibrations of T-O-T units, respectively [15, 17]. The very weak shoulder around 860 cm^{-1} is assigned to the hydroxyl bending vibrations of terminal silanol groups [18]. In general, the intensities of the INS bands observed for the dehydrated samples were small and, moreover, significant differences were not observed for the different alkali metal cation exchanged samples investigated.

The infrared spectrum of Na-X in the activated form showed the typical bands of OH stretching vibrations for terminal and internal Si-OH groups at 3748 and 3720 cm^{-1}, respectively, as well as OH groups of extra framework aluminum species 3669 cm^{-1}, while OH stretching vibrations of Si(OH)Al groups (i.e., Brønsted acidic bridging hydroxyl groups) were not observed. In addition, bands of structural overtone vibrations were present between 2100 and 1735 cm^{-1}, which were used to normalize all IR spectra shown in this paper.

2.3.2 Solid methanol

The vibrational modes calculated for methanol and obtained experimentally for solid methanol are compared to data from the literature in Table 2.2. The INS spectrum of solid methanol (Figure 2.5 and Table 2.2) with bands arising at 1450, 1262, 1153, 1123, 776, 697, 220, 166, 110, and 76 (shoulder) cm^{-1} is in good agreement with the spectrum reported by Jobic *et al.* [19]. The symmetric and asymmetric δ(OH) and δ(CH) deformation modes are located in the region 1380-1520 cm^{-1} with a maximum at 1450 cm^{-1}, which is due to the three unresolved δ(CH_3) bending modes. The very weak signal at 1021 cm^{-1} is assigned to the ν(CO) stretching mode [20] only marginally red shifted from the gas-phase value at 1033 cm^{-1}, while the broad band in the region 1100-1160 cm^{-1} is assigned to ρ(CH_3) rocking modes and their combinations with δ(OH) bending modes. Both signals at 697 and 776 cm^{-1} are methanol clusters, similar to those found by infrared spectroscopy for crystalline methanol [20] in the low temperature α-phase [21]. The shift of the bands observed by INS compared to those obtained by IR spectroscopy (790 and 685 cm^{-1}) [20] is attributed to the higher temperature (93 K) used for the IR measurements, while both frequencies are lower compared to the data reported by Jobic *et al.* [19] obtained at 5 K. In the lower

Table 2.2 Experimental vibrational frequencies, assignments of the INS bands of methanol in the solid and adsorbed (three methanol molecules per faujasite supercage, on average) state (T < 20 K), and theoretical vibrational frequencies of methanol clusters calculated by DFT.

DFT [a]				IR [20]	INS [a]
Monomer	**Linear dimer**	**Cyclic trimer**	**Assignment [b, c]**	**Crystal**	**Solid phase**
	1530 (d)	1530, 1529, 1528, 1505	$\delta_s(CH_3) + \delta(OH)_{ip}$	1458 sh, 1445 sh m, 1426 sh	several bands with maxima at 1476 sh and 1450
1527, 1509	1523, 1513, 1508 (d)	1511, 1510, 1509	$\delta_{as}(CH_3)$		
1499	1500 (d), 1492	1495, 1494, 1490	$\delta_s(CH_3)$		
1386	1445 (d), 1373	1464, 1445	$\delta(OH)_{ip}$	1470 (1492 [d]) m	
1179	1182	1184, 1183	$\rho(CH_3)_{rock}$	1256 w, 1162 vw, 1142 w	1255, 1154, 1130
1095, 1062	1127 (d), 1082	1176, 1142, 1128	$\rho(CH_3)_{rock} + \delta(OH)_{ip}$		
	1089 (d), 1056 w	1091 w, 1074, 1072	$\nu(CO)$	1046 w, 1029 vw	1021 w
---	729 (d)	964, 785, 732	$\delta(OH)_{op}$	790 (824 [d]) s, 685 (698 [d])	776, 697
340	332	---	$\delta(OH)_{op}$	---	---
	217	240, 232, 218	$\nu(OH^{\cdots}O)$		220
	137, 109	173, 124, 121, 116, 109	$\tau(CH_3)$ + translation		168, 110
	87, 72, 44	97, 59, 52, 44	Intermolecular	166, 110 s	
1045, 696, 1400	1458, 776, 663	1301, 1234, 1016, 904, 832, 296, 348	overtones and combination modes	1545 sh vw, 1345m, 520 w, 372 [d] m	1288, 340 w, 284 w

[a] this work.
[b] all frequencies are in cm^{-1}, vs = very strong, s = strong, m = medium, w = weak, vw = very weak, sh = shoulder, br = broad, d = H-donor molecule.
[c] aCLIMAX fit to methanol DFT data.
[d] frequencies extrapolated to 0 K.

energy region a broad and very intense band with a maximum at 110 cm^{-1} and shoulders at 57, 76, 168 and 220 cm^{-1} was observed, which is assigned to strongly overlapping translational and librational modes and to hydrogen-bond bending modes.

2.3.3 Adsorption of methanol on sodium exchanged zeolite X

The INS spectrum of methanol adsorbed on Na-X is shown in Figure 2.5, the assignment of the vibration modes is summarized in Table 2.3. The INS spectrum of methanol absorbed on Na-X exhibited several broad bands in the methyl and hydroxyl in-plane deformation region (1350-1530 cm^{-1}) and in the methyl-rocking region (1080-1180 cm^{-1}). The band at 1447 cm^{-1} was assigned to the (poorly resolved) $\delta(CH_3)$ bending vibrations, the bands at 1160 and 1115 cm^{-1} (shoulder) to $\rho(CH_3)$ rocking modes possibly combined with δ(OH) bending modes. The positions of the bands in both regions are similar to those observed for solid methanol. The significant broadening of those bands, shows that there is no long-range order and may also indicate a perturbation of the methanol-methyl groups. The broad, band centered at

Table 2.3 Experimental vibrational frequencies and their assignments of the INS bands of methanol adsorbed on alkali metal cation exchanged X zeolites (loading 3 molecules per supercage, on average) at T < 20 K.

Assignment [a]	methanol on Na-X	methanol on K-X	methanol on Rb-X	methanol on Cs-X
$\delta(OH)_{ip}$ and $\delta(CH_3)_{ip}$	1900-1400 br m			
	1580 br, 1450	1580 br, 1460	1580 br, 1460	1580 br, 1460
$\rho(CH_3)_{rock}$	1100-1180 br m			
	1160, 1115	1160, 1125	1160, 1130	1160, 1130
ν(CO)	1018 vw	1040 vw	1020 vw	1015 vw
$\delta(OH)_{op}$ H-bound	900-500 br m			
	650, 760	765, 810	765, 820	765, 820
$\tau(CH_3)$ and translation of methanol and methanol-cation cluster	< 450 br vs			
	263 sh, 122 sh, 95 vs	263 sh w, 125 sh w, 98 vs	263 sh w, 125 sh w, 100 vs	263 sh w, 130 sh w, 100 vs
Overtones and combinations	1220-1250 w			
	1010, 845			

[a] all frequencies are in cm-1, vs = very strong, s = strong, m = medium, w = weak, vw = very weak, sh = shoulder, br = broad.

1580 cm^{-1} is attributed to the combination band of the methyl vibration modes and low-frequency external modes of the methanol molecules. The $\delta(OH)_{op}$ deformation vibration modes of hydrogen-bonded hydroxyl groups were observed between 500 and 900 cm^{-1}. One broad band was obtained between 600 and 700 cm^{-1} centered at 650 cm^{-1} and another weak band was located at ~760 cm^{-1}. The lower value was at a similar position to that found for liquid methanol (655 cm^{-1}) [20]. The very intense and unresolved band in the low energy region below 450 cm^{-1} resulted from translational and librational modes of methanol against the zeolite framework as well as from hydrogen-bond bending and stretching modes.

2.3.4 Calculated vibrational frequencies of methanol and methanol cluster

The INS spectra simulated for a single methanol molecule, a cluster of two molecules forming a linear dimer and three molecules oriented as a cyclic trimer cluster are shown in Figure 2.6. The vibrational modes in an isolated methanol molecule are compared to those in hydrogen bonded dimeric and trimeric methanol clusters in Table 2.2. The orientation of the methanol molecules in the clusters has been chosen, because theoretical calculations [22-24] and experimental results [25-27] have shown that the methanol dimers form linear clusters, while trimer to decamer structures form stable monocyclic clusters.

The spectrum of the single methanol molecule presented 8 fundamental vibrations and several overtone vibrations in the range between 30 and 2000 cm^{-1}. The bands at 348, 696, 1045 and 1400 cm^{-1} have been assigned to the $\delta(OH)_{op}$ deformation vibrations of the OH-group and its first, second and third overtone vibrations, respectively. The $\nu(CO)$ stretching vibration, the combination of the $\delta(OH)$ deformation with a $\rho(CH_3)$ rocking mode and the pure $\rho(CH_3)$ rocking mode have been observed at 1081, 1116 and 1206 cm^{-1}, respectively. The in-plane $\delta(OH)_{ip}$ deformation vibration band was located at 1387 cm^{-1} and several bands between 1450 and 1530 cm^{-1} result from $\delta(CH_3)$ bending deformation vibrations and from combination modes of $\delta(OH)_{op} + \delta(CH)$.

The simulated spectra of the hydrogen-bonded linear dimer and the cyclic trimer cluster exhibited 15 and 35 fundamental modes, respectively, and an increased number of overtone and combination vibrations leading to strongly overlapped features. Both spectra have a large number of bands in the low energy region. In this

region, the out-of-plane and in-plane bending modes of the hydrogen-bonded molecules and the translations and librations of the entire methanol molecules are typically found. Those vibrations were mainly combined with translational modes of the molecules. The methanol-methyl torsion vibrations have been assigned to the bands at 108 and 137 cm^{-1} for the linear, hydrogen bonded methanol dimer and to several bands between 109 and 124 cm^{-1} for the hydrogen bonded cyclic trimer. The band at 173 cm^{-1} arose from a simultaneous torsion vibration of all three methanol-methyl groups.

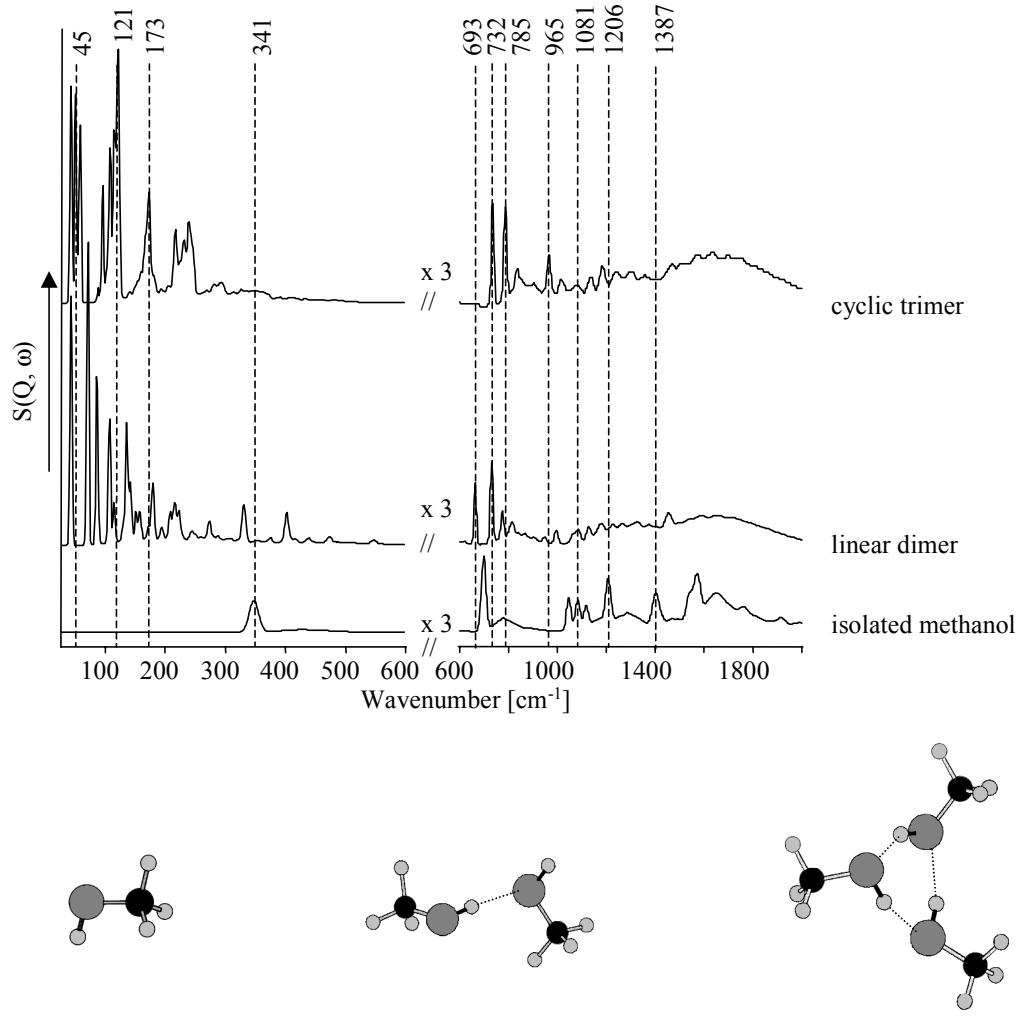

Figure 2.6 Calculated vibrational spectra and their equilibrium structures of (a) isolated methanol molecules, (b) linear dimer and (c) cyclic trimer clusters.

For a cluster of two methanol molecules the deformation vibration bands of the unperturbed as well as the hydrogen-bonded hydroxyl groups $\delta(OH)_{op}$ were observed at 332 and 729 cm^{-1}, respectively. The two corresponding but very weak $\delta(OH)_{ip}$ deformation bands were seen at 1373 and 1445-1450 cm^{-1}. In the calculated spectrum of a cyclic trimer cluster, all hydroxyl groups were hydrogen-bonded and, therefore, no $\delta(OH)_{op}$ deformation band of a freely vibrating methanol hydroxyl group was found. The three bands, observed at 732, 785, and 963 cm^{-1}, have been assigned to hydroxyl deformation vibrations of hydrogen bonded hydroxyl groups. The first has been assigned to the vibration of a single hydroxyl group, while the latter two were due to two and three hydroxyl groups, respectively, vibrating simultaneously. An increasing number of overtone vibration bands and weak band intensities in the region above 1000 cm^{-1} led to strongly overlapped and not well-resolved bands. Besides the most prominent peaks, which have been ascribed mainly to the fundamental vibrations, several medium and small bands corresponding mostly to overtone and combination bands with fundamental vibrations were observed.

2.3.5 Adsorption of methanol on alkali metal cation exchanged zeolite X

The vibrational modes observed after methanol adsorption on the various alkali metal cation exchanged zeolites are shown in Figure 2.7 and summarized in Table 2.3. All materials exhibited a broad band between 1400-1500 cm^{-1} of strongly overlapping $\delta(OH)_{ip}$ and $\delta(CH)$ vibrations with a maximum at about 1460 cm^{-1}. The feature observed in the region 1100-1180 cm^{-1} is associated with methyl rocking modes. All alkali cation exchanged materials have shown two bands at around 1115-1130 and 1160 cm^{-1}. The very weak band around 1018-40 cm^{-1} is assigned to the $\nu(CO)$ stretching mode only marginally red shifted from the gas-phase value at 1033 cm^{-1} [5].

The most significant changes in the INS spectra of the alkali metal exchanged zeolites have been observed in the region of the out-of-plane deformation bending modes of the hydrogen-bonded hydroxyl groups. For Na-X a very broad band between 600 and 900 cm^{-1} was seen and for samples with decreasing Lewis acidity, i.e., for K^+, Rb^+, and Cs^+ exchanged zeolite X, the width of these bands has decreased and shifted to 810 and 765 cm^{-1} for K-X, 820 and 765 cm^{-1} for Rb-X, and 820 and 765 cm^{-1} for Cs-X. For samples with increasing cation size, the tail of the band below 450 cm^{-1} at higher frequencies (assigned to methyl torsion and the hydrogen-bond

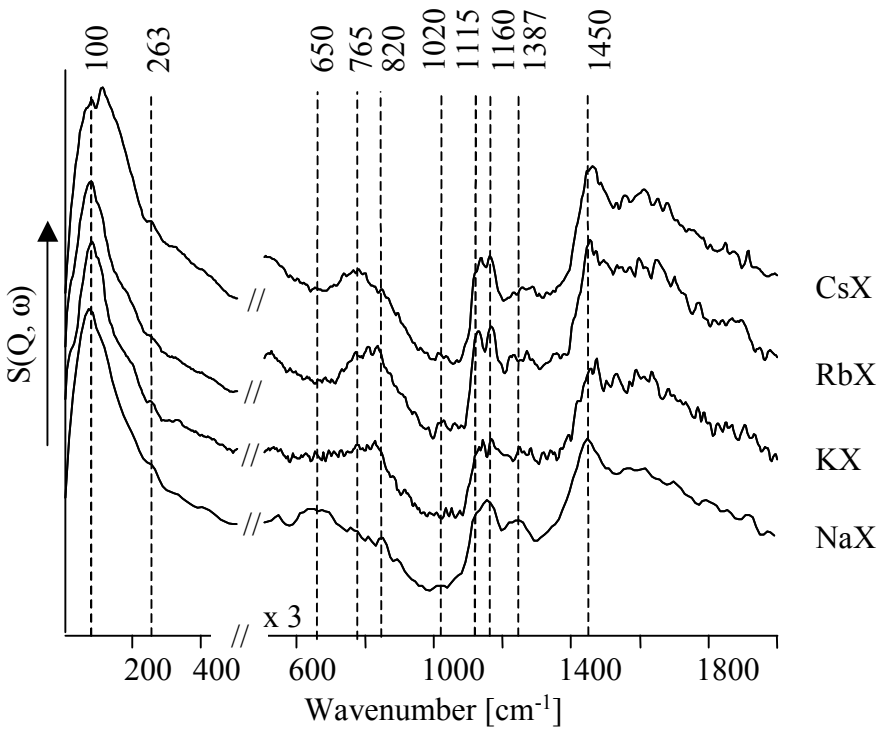

Figure 2.7 Inelastic neutron scattering spectra of methanol adsorbed on alkali metal cation exchanged X zeolites (loading 3 molecules per supercage, on average) at T < 20 K.

bending and stretching modes, as well as to the translational and librational modes of the methanol-cation cluster to the zeolite and methanol to the cation) was more pronounced.

The infrared spectra after adsorption of methanol at a partial pressure of 10^{-3} mbar are shown in Figure 2.8. The frequencies of the OH stretching vibrations (summarized in Table 2.4) are broadened and strongly shifted to lower wavenumbers. The values vary for methanol adsorbed on the different alkali cation exchanged zeolite samples. The broad OH stretching vibration modes showed the highest frequency for methanol sorbed on Na-X (3341 cm^{-1}) and decreased to lower wavenumbers for Rb-X (3219 cm^{-1}). For methanol adsorbed on Cs-X (3238 cm^{-1}), this band is observed at a somewhat higher value than for Rb-X. Similar to the OH stretching vibration, the anti-symmetric and symmetric CH stretching vibration bands were found to be the highest in frequency for methanol sorbed on Na-X (2957 and 2839 cm^{-1}, respectively) and decreased to the frequency of methanol sorbed on Rb-X and Cs-X (2934 and 2820-2823 cm^{-1}), respectively. The infrared data are in perfect agreement to the results reported by Rep *et al.* [5].

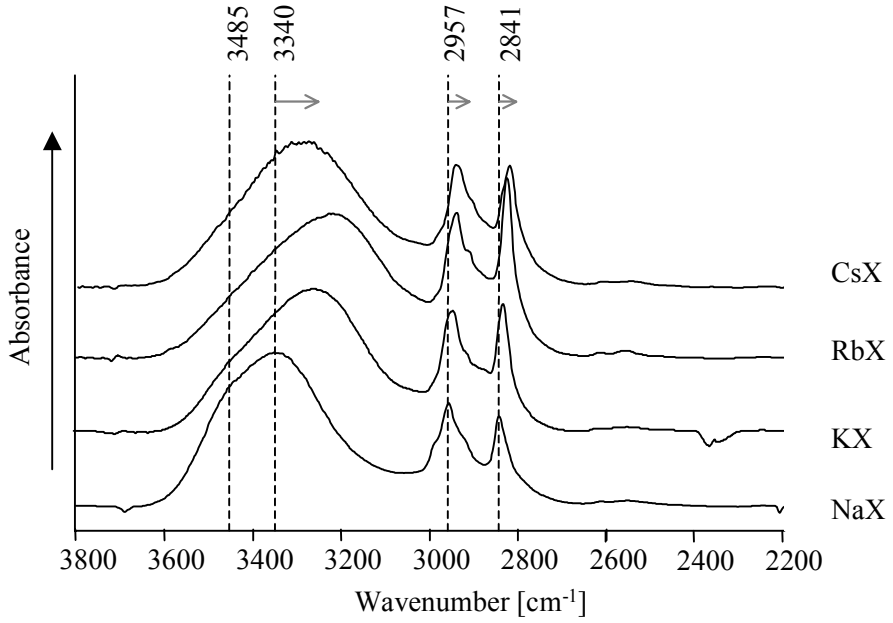

Figure 2.8 Difference IR spectra of methanol adsorbed on Na-X (T = 308 K, $p = 1 \cdot 10^{-3}$ mbar).

Table 2.4 Vibrational IR frequencies of methanol adsorbed on alkali metal cation-exchanged X zeolites (T = 308 K, $p_{(MeOH)} = 1 \cdot 10^{-3}$ mbar).

Assignment	Gas phase [45]	Liquid [20]	Na-X	K-X	Rb-X	Cs-X
ν(OH)	3682 s	3337 s, br	3460 sh, 3341 s, br	3453, 3255 s, br	3356 sh, 3219 s, br	3468 sh, 3238 s, br
$\nu(CH_3)$ as	2999, 2970	2934	2980 sh, 2957 br	2949, 2939	2947, 2934	2946, 2934
$\nu(CH_3)$ s	2844	2822	2839 br	2826	2820	2835 sh, 2823
$\delta_{as}(CH_3)$	1477, 1465, 1454	1475, 1453	1476, 1451	1479, 1450	1480, 1449	1477, 1449
δ(OH), $\delta_s(CH_3)$	1340	1420 br	1423 sh, 1400 br	1419, 1383 sh	1434, 1385 sh	1419 br, 1385 sh
Overtones or combinations	2920		2917	2908	2905	2903 sh

[a] all frequencies are in cm-1, vs = very strong, s = strong, m = medium, w = weak, vw = very weak, sh = shoulder, br = broad.

2.4 Discussion

2.4.1 Dehydrated alkali metal cation exchanged X zeolites

Pyridine adsorption followed by infrared spectroscopy allows to distinguish between Brønsted and Lewis acid sites [28]. The absence of the band at ~1545 cm^{-1}, attributed to protonated pydridne, indicates that no detectable Brønsted acid sites are present. This leads to the assumption that the whole negative charge of the framework oxygen atoms is compensated by cations, while protons are absent. Due to the very low shift of the band at ~1442 cm^{-1} (pyridine coordinated to Lewis acid centers), the alkali metal cations cannot be differentiated, but the trend of a decreasing strength of interaction with increasing Lewis acidity of the cation is clearly visible from the lower wavenumbers (1444 (Na-X) - 1440 cm^{-1} (Cs-X)). It is assumed that the amount of strongly bound pyridine under the fixed conditions used (temperature and partial pressure of the sorbate) is a function of the number and strength of acid sites only [29]. The integrated areas of the band at ~ 1442 cm^{-1}, normalized on the molar mass, have been found to decrease in the sequence Na-X > Cs-X > K-X > Rb-X pointing to a decreasing amount of pyridine adsorbed on materials with increasing basicity. The higher value for Cs-X may be explained by the high concentration of sodium cations possibly present at SII positions in the supercage. From diffraction studies of $Cs_{46}Na_{50}X$ [30], both the sodium and the cesium cations have been detected in the supercages. Well-stabilized sodium cations are found to be located in the S II positions, while the larger cesium cations occupy only the S III' positions.

CO_2 is frequently employed to probe the Lewis acid sites of both the metal oxides and the zeolites. Being amphoteric in nature, it can also monitor the properties of the basic surface centers. Therefore, the acid-base couples (counter cations and framework oxygen atom pairs) of alkali metal exchanged zeolites have been investigated with infrared spectroscopy of adsorbed CO_2 molecules [31]. The formation of surface carbonates is related to the surface basicity of the zeolites where the cation acts as Lewis acid and the neighboring framework oxygen as a base. CO_2 is bi-coordinated to a T atom and an exchangeable cation in a low symmetry in *species I*. S*pecies II* presents a symmetric carbonate structure where the negative charge of the carbonate anion is completely delocalized over two carbon dioxide oxygens and one framework oxygen atom and stabilized by the exchanged cation [32]. The decrease of the band splitting of the asymmetric and symmetric ν(OCO) stretching mode

(*species I*) going from $Na^+ \rightarrow Rb^+$ is related to stronger basic properties of the framework oxygen atoms with increasing cation size (compare $-\delta_O$ in Table 2.1) [10]. The base properties of the cation exchanged zeolites are also determined by the average negative charge $-\delta_O$ on the framework oxygens. This negative charge can be calculated from the theoretical unit cell composition with a simple method [13] based on the averaged electronegativity of the zeolite according to Sanderson *et al.* [12] (see also Chapter 1). It is a measure of the average framework basicity and is found to follow the sequence Na < K < Rb < Cs indicating that higher basic strengths are obtained at lower cation electronegativity, which is in agreement with Barthomeuf *et al.* [33].

The absence of bands in the INS spectra of the exchanged zeolite X materials around 420 and 1060 cm^{-1} as found for HNa-Y [14] (for H-Y predicted at 420 and 1110 cm^{-1} by quantum chemical calculations [34]) and in addition, the low intensities of the band above 480 cm^{-1} [14, 35] clearly demonstrates the absence of Brønsted acid hydroxyl groups in all samples indicating complete cation exchange. The complete ion exchange is also confirmed by the chemical composition, by the adsorption of pyridine as well as by the absence of bands at 3640 and 3540 cm^{-1} assigned to OH stretching vibrations of Brønsted acid hydroxyl groups. The very low intensity of the shoulder around 860 cm^{-1}, which indicates terminal silanol groups [18], demonstrates a low number of defects or extra framework phases.

Due to the similarity of the spectra observed for the different alkali metal cation exchanged samples after activation and the generally broad bands observed, a correlation between the exchange with cations and structural changes of the framework could not be drawn. This may point to a minor influence of the counter cation on the vibrational properties of the faujasite structure. Note that from infrared and Raman spectroscopy shifts in the frequency of cation translational modes and framework bending modes were attributed to different counter cation sizes and to slight structural changes of the framework upon exchange of the counter cations [36, 37]. From the INS spectrum of natrolite, a band at 40 cm^{-1} was assigned to sodium motion, since it was present in both deuterated and hydrogenated spectra [38]. Due to the small scattering cross section of the alkali metal cations, the translational modes of those cations are expected to be very weak in INS spectra and probably contribute to the band at 95 cm^{-1}. Note that the scattering of the sodium cations was found to be negligible for Na-Y materials [39].

2.4.2 Solid methanol

In analogy to the torsion vibration frequencies obtained in the simulation for the methanol clusters at around 109 and 173 cm^{-1}, the distinct maxima at 110 and 168 cm^{-1} in solid methanol are assigned to freely vibrating and hydrogen-bonded methanol-methyl motions, respectively. From far-infrared and Raman studies at 88 K, Durig *et al.* [40] assigned the bands at 196, 160, 109, and 57 cm^{-1} to two in plane and two out-of-plane hydrogen-bond bending modes of solid methanol assuming C_2 symmetry for the methanol chain. The assignment from Durig *et al.* [40] is consistent with that of the methyl motion, as the methyl group, being the center of mass, must also move in the hydrogen-bond bending motion. Aldred *et al.* [41] obtained a band at 160 cm^{-1} in the INS spectrum of methanol and assigned it to the methyl motion on the basis of the disappearance of the band after deuteration of the methyl group. In addition, the band at 270 cm^{-1} was assigned to a translational hydrogen-bond stretching mode [42].

The calculated $\delta(OH)_{op}$ bending mode of isolated OH groups in a single methanol molecule and in dimeric clusters appear at 341 and 330 cm^{-1}, respectively. Both are absent in solid methanol, as all hydroxyl groups are assumed to be hydrogen-bonded. In the liquid and solid state, the molecules preferentially form chains but also ring-like structures and zigzag chains, in which methanol is twofold hydrogen-bonded (Figure 2.9). The $\delta(OH)_{op}$ torsion modes at 697 and 776 cm^{-1} show that methanol was crystallized in the low temperature α–phase [21, 43, 44]. This is supported by the pronounced splitting of the $\delta(OH)_{op}$ bands compared to the single band at 655 cm^{-1}

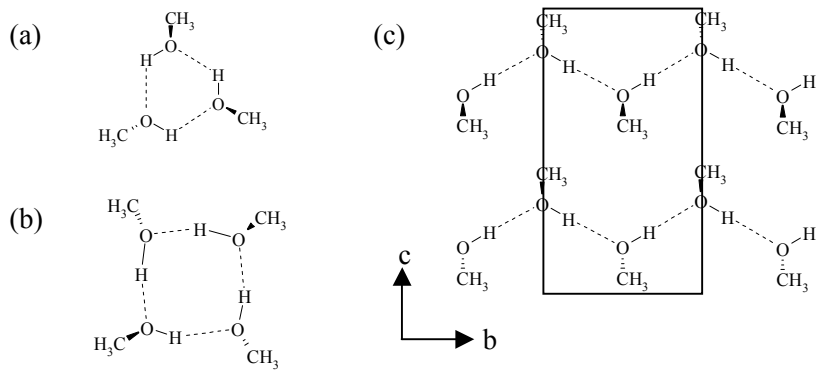

Figure 2.9 (a) hydrogen bonded form of methanol: cyclic trimer and tetramer; (b) crystal structure of the α-phase of methanol; projection on the *bc*-plane. The dashed lines represent hydrogen bonds.

observed for liquid methanol by IR spectroscopy[20]. The doublet is due to torsional modes of hydrogen-bonded methanol-hydroxyl groups of the different symmetric methanol species present in the unit cell. The band at 776 cm^{-1} is located at a lower frequency compared to the position reported by Jobic *et al.* [19], which is explained with a lower temperature (T = 5 K) used by these authors.

2.4.3 Adsorption of methanol on sodium exchanged zeolite X

In analogy to solid methanol, all hydroxyl groups of methanol adsorbed on Na-X appear to be hydrogen-bonded as indicated by the absence of the $\delta(OH)_{op}$ mode of freely vibrating OH-groups at 330 cm^{-1}. In addition, the $\delta(OH)_{ip}$ deformation bending vibration bands of the methanol hydroxyl groups are strongly broadened and overlapped with the $\delta(CH_3)$ bending modes of the methanol methyl groups. The $\delta(OH)_{ip}$ vibrations are found at higher wavenumbers compared to isolated methanol molecules (i.e., gas phase at 1380 cm^{-1}) by infrared spectroscopy [20], which also supports the assumption of hydrogen bonding of the methanol hydroxyl groups. In the region 600-900 cm^{-1} only a broad feature of low intensity was present indicating that self-association of methanol molecules to form the crystalline α-phase did not take place. This suggests that the adsorption structure of methanol in faujasite supercage of Na-X is less ordered compared to the solid phase. It is also possible that more than one methanol adsorption structure is formed at this loading.

The lower frequency of the broad $\delta(OH)_{op}$ bending mode (with maxima at 650 and 760 cm^{-1}) and the strong band broadening, as compared to solid methanol, suggest a less strongly hydrogen-bonded structure. The broadening is attributed to the presence of a large number of perturbed methanol-hydroxyl groups differing in hydrogen bonding strength. This is also indicated by the unresolved group of bands below 450 cm^{-1} with a maximum at 95 cm^{-1} (assigned to methyl torsional and external modes). The formation of the preferred linear structure of the hydrogen bonds in methanol, realized in the methanol crystals, is sterically not possible for methanol adsorbed in the supercages of zeolite X, explaining the decreased hydrogen-bonding strength.

From IR and thermogravimetric studies [5] it has been reported that the interaction energetically controlling the sorption of methanol on alkali metal cation exchanged X zeolites is primarily the coordination of the methanol-oxygen atom to the alkali metal

cation. The observation of two ν(OH) stretching modes at 3460 (shoulder) and 3341 cm^{-1} by infrared spectroscopy (Figure 2.8) together with the low methanol coverage (less than one molecule per cation) points to the presence of two methanol sorption structures of methanol adsorbed on Na-X. These two structures of hydrogen bonded methanol molecules coordinatively bound *via* the methanol oxygen atom to sodium cations without methanol clustering at the exchanged cation [5] proposed are shown in Figure 2.10a and 2.10b. The methanol-hydroxyl bonds of methanol adsorbed on Na-X are weakened as indicated by the strong shift of the hydroxyl stretching vibrations when compared to the sharp band at 3612 cm^{-1} of relatively unperturbed methanol hydroxyl groups observed for methanol adsorbed on Na-ZSM-5 [5] and the band at 3682 cm^{-1} for methanol in the gas phase [45]. The shoulder at 3460 cm^{-1} may result from the coordination and an additional H-bonding interaction formed between the methanol-hydroxyl group and the negatively charged zeolite oxygen atom (Figure 2.10a), while additional methanol–methanol interactions between methanol molecules adsorbed at neighboring cations (Figure 2.10b) are concluded to be most important for the appearance of the adsorption band at 3341 cm^{-1}. Note that ν(OH) stretching bands at 3293 cm^{-1} and 3340 cm^{-1} are found for methanol tetramer clusters [46] and for liquid methanol [47], respectively. Due to the low

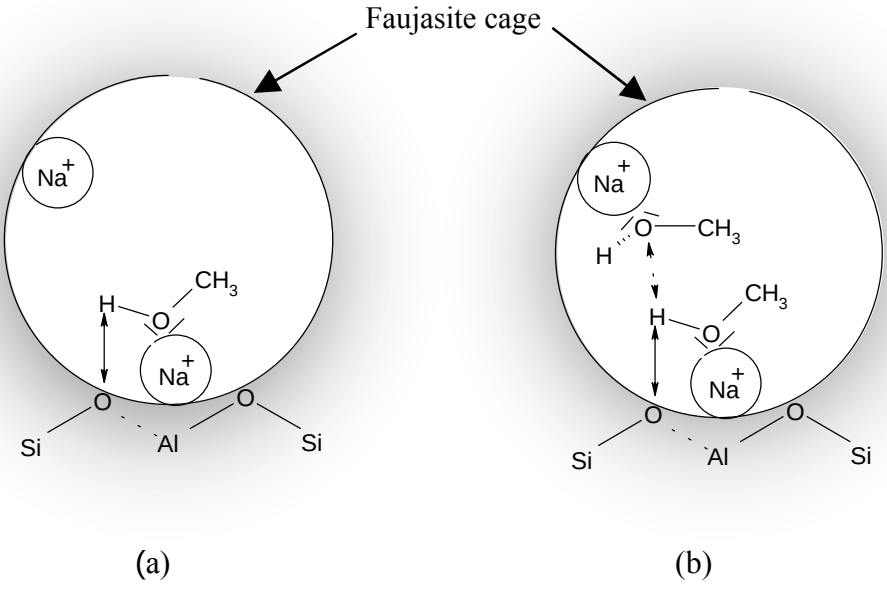

Figure 2.10 Schematic representation of two possible sorption structures of methanol on Na-X.

intensities of the $\delta(OH)_{op}$ bending modes in the INS spectrum, the presence of those two structures cannot be confirmed, but the broadening in the $\delta(OH)_{op}$ band region (600-900 cm^{-1}) supports this proposal.

Diffraction studies by Olson *et al.* [48] reported that 60.8 counter cations are located in the faujasite supercage per unit cell for a $Na_{88}X$ zeolite. (29.8 cations are located in SIII' positions, 31 cations are found on SII, while none are located at SII' and SIII; Figure 2.11). We assume that methanol will preferentially adsorb on the sodium cations located in SIII' positions, where the cation is surrounded by two aluminum sites and a small number of next nearest-neighbor oxygen sites, which are the most basic sites in the framework [49]. These cations are the most easily accessible in the framework, because they are coordinatively less saturated and have the lowest binding energy to the framework oxygen atoms. Note that for cations in SIII' positions (2 Al in four ring) an approximately 40 kJ mol^{-1} lower binding energy was determined compared to cations in SII positions [50, 51]. The weak interaction of cations in SIII' positions and framework oxygen atoms leads to a low charge delocalization between the cations and the oxygen atoms and thus, a higher positive partial charge remains on

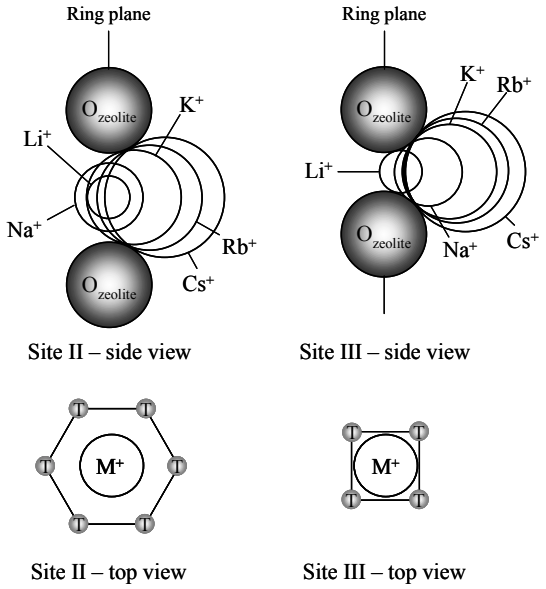

Figure 2.11 Shielding of alkali metal cation through oxygen atoms in the super cage on position SII and SIII [47]; T = Si, Al.

the cations. Note that stronger adsorption was also found for CO adsorption on cations in SIII' compared to adsorption on cations in SII [51]. Due to coverage of 3 molecules per supercage containing 3.7 cations on SIII' positions, on average, we may also assume that there is no clustering at a single alkali cation.

2.4.4 Adsorption of methanol on alkali metal cation exchanged zeolite X

Changing the counter cation from Na^+ to larger alkali metal cations increases the negative charge located on the framework oxygen atom of the zeolite as indicated by the Sanderson intermediate electronegativity principle (Table 2.1). The polarity of the zeolite framework is increased leading to enhanced base strength of the sites (lattice oxygen atoms) of Rb^+ exchanged zeolites compared to Na^+ exchanged zeolites. The increasing framework base strength with increasing counter cation size is demonstrated experimentally by infrared spectroscopy coupled with temperature programmed desorption of adsorbed probe molecules such as carbon dioxide [52, 53] and pyrrole [54, 55]. The interactions between the slightly acidic hydroxyl of methanol and the neighboring lattice oxygen atoms increases remarkably from Na-X to Rb-X, which leads to the formation of stronger hydrogen bonds between the methanol-hydroxyl groups and the framework oxygen atoms. As a result the $\delta(OH)_{op}$ deformation modes are shifted to higher frequencies for a lower Lewis acid cation (for Rb-X at 765 and 820 cm^{-1}) compared to Na-X (650 and 760 cm^{-1}).

In addition to the increased hydrogen-bond strength, with increasing size of the counter cations (K^+, Rb^+, and Cs^+) the displacement into the faujasite cage increases [56, 57] (Figure 2.11) leading to a decrease in the distance between coordinatively adsorbed methanol molecules in the faujasite cages. Compared to Na-X, the $\delta(OH)_{op}$ bandwidths are smaller and the frequencies of the $\delta(OH)_{op}$ vibrations are located at higher values for K-X, Rb-X and Cs-X. Those observations indicate the formation of more uniform and strongly hydrogen-bonded sorption structures of methanol on zeolite samples with increasing counter cation size.

In perfect agreement to the increase of the $\delta(OH)_{op}$ deformation vibration frequencies, IR spectra [5] show a shift to lower frequencies for the $\nu(OH)$ stretching modes from 3341 (Na^+) to 3220 (Rb^+) cm^{-1} accompanied by an increase of the wavenumbers of the $\delta(OH)_{ip}$ deformation vibrations (not shown). This is consistent with the weakening of the methanol hydroxyl bonds with increasing framework base

strength. Note that a frequency shift in the opposite direction is observed for the coordination of the methanol oxygen atom to a counter cation located in an apolar zeolitic environment (e.g., on alkali metal cation exchanged ZSM-5 materials [5]) in which hydrogen bonding to the lattice does not occur. The shoulder at 3460 cm^{-1} is most dominant for Na-X, while it is hardly visible for Rb^+ and Cs^+ exchanged X zeolites. From both spectroscopic methods, the trends clearly indicate a strengthening of the hydrogen bonds with increasing base strength and decreasing cation Lewis acid strength, leading to a more pronounced formation of the sorption structure illustrated in Figure 2.10b and/or a formation of ring-like methanol structures in the supercage.

A further increase in the frequency of the $\delta(OH)_{op}$ deformation vibrations and a decrease in the $\nu(OH)$ stretching frequencies for Cs-X compared to Rb-X was not observed. The large Cs^+ cation may prevent the formation of sterically unhindered sorption complexes between methanol, cation and the pore wall in the supercage resulting in weaker hydrogen bonds, thus in higher methanol hydroxyl stretching values. The peak shapes of $\nu(OH)$ and $\delta(OH)_{op}$ and their low and high frequencies nevertheless indicate the presence of intermolecular hydrogen bonds.

Alternatively, it could be speculated that the presence of sodium cations (for this material a Cs^+-exchange degree of 55.4 % was reached) in the supercage lowers the average framework polarity $-\delta_0$, (calculated in Table 2.1), which may decrease the hydrogen bonding strength. In diffraction studies of a $Cs_{46}Na_{50}X$ sample [30], both, sodium and cesium cations were detected in the supercage. Well-stabilized sodium cations were found to be located in SII, while the larger cesium cations only occupy SIII' positions.

The broad shoulder at high frequencies of the band below 450 cm^{-1} is attributed to enhanced hydrogen bonding of the methyl hydrogen atoms to the negatively charged framework oxygen atoms, resulting in a hindered translational motion. The changes of the band shapes in the rocking vibrational modes of the methanol methyl groups also indicate a change in the steric hindrance of the methyl groups with increasing cation size probably resulting from hydrogen bond formation to the zeolite framework. Hydrogen bonding between the methanol methyl groups and the zeolite oxygen atoms is also supported by the observed red shift and increased bandwidth of the $\nu(CH_3)$ stretching vibration modes from 2957 and 2841 cm^{-1} (Na^+) to 2934 and 2820 cm^{-1} (Rb^+) [5] in the infrared spectra.

2.5 Conclusions

The combination of INS and IR spectroscopy was used to study the sorption structure of methanol on alkali metal cation exchanged faujasite (zeolite X) samples. A significant influence of the different counter cations on the structural vibrations of the faujasite framework was not found. Upon cooling below 20 K, methanol crystallizes in the low temperature α-phase. In the crystalline as well as in the adsorbed phase, all methanol-OH groups appeared to be hydrogen-bonded, while in the later state no self-association of methanol molecules forming the crystalline α-phase was observed. At low sorbate loading, methanol adsorbed on counter cations located in SIII' positions, the energetically preferred sites located in the supercage of zeolite X. Due to the low loading in the zeolite (three methanol molecules per 7.6 cation in the supercage, in average) clustering of more than one molecule per sorption site is not expected. The combination of INS and IR spectroscopy confirmed the presence of at least two sorption structures for methanol in alkali metal cation exchanged faujasite. Hydrogen bonding interactions between the slightly acidic hydroxyl groups of methanol and the neighboring lattice oxygen atom as well as intermolecular interactions between methanol molecules were observed. With increasing cation size, leading to increasing framework basicity, interactions between the hydrogen atoms of the hydroxyl group of methanol and the neighboring lattice oxygen atoms increased remarkably from Na-X to Rb-X. The more uniform and strongly hydrogen-bonded sorption structure points to the formation of ring-like methanol structures on these samples.

2.6 Acknowledgements

The authors would like to thank the Deutsche Forschungsgemeinschaft (DFG) within the Sonderforschungsbereich SFB 338: Adsorption an Festkörperoberflächen: Mikroskopische Analyse von Zuständen und Prozessen Teilprojekt B9.

In particular we thank the ISIS, Rutherford Appleton Laboratory, U.K., for kindly granted measuring time to record the INS spectra.

2.7 References

[1] Lercher, J. A.; Jentys, A. *Handbook of Microporous Solids*; Schüth, F.; Sing, K.; Weitkamp, J. Ed.; Wiley-VCH: Weinheim, **2002,** 1097.

[2] Barthomeuf, D. *Catal. Rev. Sci. Eng.* **1996**, 38, 521.

[3] Csicsery, S.M. *Zeolites* **1984**, 4, 202.

[4] Palomares, A.E.; Eder-Mirth, G.; Lercher, J.A. *J. Catal.* **1997**, 168, 442; Vinek, H.; Derewinski, M.; Mirth, G.; Lercher, J.A. *Appl. Catal*. **1991**, 68, 277.

[5] Rep, M.; Palomares, A.E.; Eder-Mirth, G.; van Ommen, J.G.; Rösch, N.; Lercher, J.A. *J. Phys. Chem. B* **2000**, 104, 8624.

[6] www.isis.rl.ac.uk.

[7] Frisch, M. J.; Trucks, G. W.; Schlegel, H. B.; Scuseria, G. E.; Robb, M. A.; Cheeseman, J. R.; Zakrzewski, V. G.; Montgomery, J. A. Jr.; Stratmann, R. E.; Burant, J. C.; Dapprich, S.; Millam, J. M.; Daniels, A. D.; Kudin, K. N.; Strain, M. C.; Farkas, O.; Tomasi, J.; Barone, V.; Cossi, M.; Cammi, R.; Mennucci, B.; Pomelli, C.; Adamo, C.; Clifford, S.; Ochterski, J.; Petersson, G. A.; Ayala, P. Y.; Cui, Q.; Morokuma, K.; Malick, D. K.; Rabuck, A. D.; Raghavachari, K.; Foresman, J. B.; Cioslowski, J.; Ortiz, J. V.; Baboul, A. G.; Stefanov, B. B.; Liu, G.; Liashenko, A.; Piskorz, P.; Komaromi, I.; Gomperts, R.; Martin, R. L.; Fox, D. J.; Keith, T.; Al-Laham, M. A.; Peng, C. Y.; Nanayakkara, A.; Challacombe, M.; Gill, P. M. W.; Johnson, B.; Chen, W.; Wong, M. W.; Andres, J. L.; Gonzalez, C.; Head-Gordon, M.; Replogle, E. S.; Pople, J. A. *Gaussian*, Inc., Pittsburgh PA, **1998**.

[8] Champion, D. J.; Tomkinson, J.; Kearley, G.J. *Appl. Phys. A-Mater.* **2002**, 74, S1302.

[9] Treacy, M.M.J.; Higgins, J.B. *Collection of Simulated XRD Powder Patterns for Zeolties*, 4th Ed., Elsevier, **2001**.

[10] Jacobs, P.A.; Van Cauwelaert, F.M.; Vansant, E.F. *J. Chem. Soc., Faraday Trans. 1* **1973**, 69, 2130.

[11] Fitch, A.N.; Jobic, H.; Renouprez, A. *J. Phys. Chem.* **1986**, 90, 1311; Jobic, H.; Renouprez, A.; Fitch, A.N.; Lauter, H.J. *J. Chem. Soc., Faraday Trans 1* **1987**, 83, 3199.

[12] Sanderson, R.T. *J. Am. Chem. Soc.* **1983**, 105, 2259.

[13] Mortier, W.J. *J. Catal.* **1978**, 55, 138.

[14] Jobic, H. *J. Catal.* **1991**, 131, 293.

[15] Miecznikowski, A.; Hanuza, J. *Zeolites* **1985**, 5, 188.

[16] No, K.T.; Bae, D.H.; Jhon, M.S. *J. Phys. Chem.* **1987**, 90, 1772.

[17] Jobic, H.; Smirnov, K.S.; Bougeard, D. *Chem. Phys. Lett.* **2001**, 344, 147.

[18] Kustov, L.M.; Borovkov, V.Y.; Kazansky, V.B. *J. Catal.* **1981**, 72, 149.

[19] Jobic, H. *Spectrochimca Acta A* **1992**, 48, 293.

[20] Falk, M.; Whalley, E. *J. Chem. Phys.* **1961**, 34, 1554.

[21] Torrie, H.B.; Weng, S.X. *Molec. Phys.* **1989**, 67, 575.

[22] Buck, U.; Siebers, J.G.; Wheatley, R.J. *J. Chem. Phys.* **1998**, 108, 20.

[23] Mo, O. ; Yanez, N. ; Elguero, J. *J. Chem. Phys*. **1997**, 107, 3592.

[24] Hagemeister, F.C.; Gruenloh, C.J.; Zwier, T.S. *J. Phys. Chem. A* **1998**, 102, 82.

[25] Huisken, F.; Kaloudis, M.; Koch, M.; Werhahn, O. *J. Chem. Phys*. **1996**, 105, 8965.

[26] Buck, U.; Ettischer, I. *J. Chem. Phys.* **1998**, 108, 33.

[27] Provencal, R.A.; Paul, J.B.; Roth, K.; Chapo, C.; Casaes, R.N.; Saykally, R.J.; Tschumper, G.S.; Schaefer, H.F. *J. Chem. Phys*. **1999**, 110, 4258.

[28] Ward, J.W. *J. Catal*. **1969**, 14, 365, *J. Catal*. **1968**, 10, 34.

[29] Rossi, F.P.; Busca, G.; Lorenzelli, V.; Lion, M.; Lavalley, J.C. *J. Catal* **1988**, 109, 378.

[30] Shepelev, Zu.F.; Butikova, I.K.; Smolin Yu.I. *Zeolites* **1991**, 11, 287.

[31] Martra, G.; Coluccia, S.; Davit, P.; Gianotti, E.; Marchese, L.; Tsuji, H.; Hattori, H. *Res. Chem. Intermed*. **1999**, 25, 77.

[32] Doskocil, E.J.; Davis, R.J. *J. Catal*. **1999**, 189, 353.

[33] Barthomeuf, D. *J. Phys. Chem*. **1984**, 88, 42.

[34] Sauer, J. *J. Mol. Catal*. **1989**, 54, 312.

[35] Jacobs, W.P.J.H.; van Wolput, J.H.M.C.; van Santen, R.A.; Jobic, H. *Zeolites* **1992**, 12, 315.

[36] Brémard, C. ; Le Maire, M. *J. Phys. Chem*. **1993**, 97, 9695.

[37] Butler, W.M.; Angell, Ch.L.; Allister, W.Mc.; Risen, W.M. *J. Phys. Chem*. **1977**, 81, 2061.

[38] Line, C.M.B.; Kearley, G. *J. Chem. Phys*. **1998**, 234, 207.

[39] Jacobs, W.P.J.H.; van Wolput, J.H.M.C.; van Santen, R.A.; Jobic, H. *Zeolites* **1994**, 14, 117 and references therein.

[40] Durig, J.R.; Pate, C.B.; Li, Y.S.; Antion; D.J. *J. Chem. Phys*. **1971**, 54, 4863.

[41] Aldred, B.K.; Eden, R.C.; White; J.W. *Discussions, Faraday Soc*. **1967**, 43, 169.

[42] Anderson, A.; Andrews, B.; Meiering, E.M.; Torrie, B.H. *J. Raman Spectrosc*. **1988**, 19, 85 and references therein.

[43] Parkes, G.S. *J. Am. Chem. Soc.* **1925**, 47, 338.

[44] Weng, S.X.; Anderson, A. *Phys. Stat. Sol. (b)* **1992**, 172, 545.

[45] Serallach, A.; Meyer, R. Hs.H. Günthard, *J. Mol. Spectrosc*. **1974**, 52, 94.

[46] Häber, T.; Schmitt, U.; Suhm, M.A. *Phys. Chem. Chem. Phys*. **1999**, 1, 5573.

[47] Buck, U.; Huisken, F. *Chem. Rev*. **2000**, 100, 3863.

[48] Olson, D.H. *Zeolites* **1995**, 15, 439.

[49] Heidler, R.; Janssens, G.O.A.; Mortier, W.J.; Schoonheidt, R.A. *J. Phys. Chem*. **1996**, 100, 19728.

[50] Buttefey, S.; Boutin, A.; Mellot-Drazniekks, C.; Fuchs, A.H. *J. Phys. Chem. B* **2001**, 105, 9569.

[51] Vayssilov, G.N.; Staufer, M.; Belling, T.; Neyman, K.M.; Knözinger, H.; Rösch, N. *J. Phys. Chem. B* **1999**, 103, 7920.

[52] Jacobs, P.A.; van Cauwelaert, F.H.; Vansant, E.F.; Uytterhoeven, J.B. *J. Chem. Soc. Faraday Trans. 1* **1973**, 69, 1056.

[53] Yagi, F.; Tsuji, H.; Hattori, H. *Micropor. Mater*. **1997**, 9, 237.

[54] Lavalley, J.C. *Catal. Today* **1996**, 27, 377.

[55] Murphy, D.; Massiani, P.; Franck, R.; Barthomeuf, D. *J. Phys. Chem*. **1996**, 100, 6731.

[56] Huber, S.; Knözinger, H. *Appl. Catal. A: General* **1999**, 189, 239.

[57] Cooney, R.P.; Tsai, P. *J. Raman Spectr*. **1979**, 8, 195.

Chapter 3

An Infrared and Inelastic Neutron Scattering spectroscopic study of C_1-C_4 alcohols adsorbed on alkali metal exchanged zeolite X

Abstract

The adsorption of short chain C_1-C_4 *n*-alcohols on alkali cation exchanged X zeolites (Si/Al = 1.2) was studied by inelastic neutron scattering and infrared spectroscopy. Vibrational spectra of alcohols adsorbed on the zeolites are compared with those of solid alcohols. The interactions between the sorbate molecule and the zeolite are discussed. The results are compared to INS spectra generated from *ab-initio* calculations for one, two and three alcohol molecule aggregates.

For all alkali metal cation exchanged X zeolites only physically adsorbed alcohol molecules were found on the catalyst surface. The interactions in the channels of alkali cation exchanged X zeolites of the short chain C_1-C_4 alcohols were found to be similar and independent of the chain length. The alcohol oxygen atoms interact *via* their lone electron pairs with the exchanged alkali metal cation and hydrogen bond formation was found between the alcohol-OH protons and the negatively charged oxygen atoms of the framework. With increasing hydrocarbon chain length, the energetic contribution of the hydrogen bonds to the heat of adsorption increased. With increasing framework polarity, i.e., from Na^+ to Cs^+ counter cation, large negative shifts of the frequency of the OH stretching modes indicate the strengthening of the hydrogen bonds.

3.1 Introduction

The use of basic zeolites as a substitute for corrosive liquid bases in chemical processes is favored, as it reduces the environmental impact caused by their disposal[1, 2]. For a rational catalyst design and the optimization of an industrially applied catalyst, knowledge of the sorbate-sorbent interaction is essential. Therefore, one of the basic aims in catalysis is to describe the adsorption structure of reactant and potential product molecules on catalytically active materials.

In alkali metal cation exchanged zeolites, Lewis acid-base pairs are present [3]. The extra-framework cations form Lewis acid sites, while the negatively charged framework oxygen atoms of the zeolite have a (Lewis) basic character [4, 5]. The concentration of extra-framework cations and, thus, the concentration of acid-base sites increases with the concentration of framework aluminum atoms occupying tetravalent cation positions (T sites) in the zeolite lattice. In addition, the base strength of framework oxygen sites adjacent to cations can be modified by changing the type of counter cation. It increases in the order $Li^+<Na^+<K^+<Rb^+<Cs$ [6, 7]. As a consequence, the existence of basic sites in zeolites has been confirmed for numerous catalytic reactions [8, 9, 10, 11] among which the side chain alkylation of toluene with methanol was one of the first clearly demonstrating the possibility of base catalyzed reactions with zeolites [9, 13].

For the adsorption of methanol on aluminum rich alkali cation exchanged X zeolites [14] it was observed that methanol adsorbs in a liquid-like structure. Three types of local adsorption structures were identified: (i) interaction between the alkali metal cation (electron pair acceptor) and the methanol-oxygen atom (electron pair donor), (ii) lateral interactions between the alcohol molecules *via* hydroxyl- as well as methyl-hydrogen atoms and the framework oxygen atoms, and (iii) intermolecular interactions formed between neighboring adsorbed molecules with the formation of ring-like hydrogen bonded structures. The strength of the hydrogen-bonding interaction and the basicity of the framework oxygens can be studied from the broadening and shift in energy of the alcohol OH stretching and bending vibrations relative to their gas-phase counterparts[15]. The spectroscopic investigation of the alcohol molecules adsorbed on basic sites of zeolites can, therefore, yield essential information about the strength and nature of basic sorption sites in zeolite and can

give insight into the influence of the size of the (hydrophobic) hydrocarbon chain of alcohol molecules on their possible orientations within the structure of zeolite X.

Self-association through hydrogen bonding interactions was found for primary alcohol molecules in the liquid state and was reported to be the main reason for the deviation from ideal behavior for mixtures of 1-alcohols and *n*-alkanes [16]. Studies on the electric deflection of molecular beams of the hydrogen bonded clusters $(H_2O)_n$, $(CH_3OH)_n$, and $(C_2H_5OH)_n$, with *n* ranging up to 17, suggests that these species have cyclic and closed ring structures [17]. In addition, methanol dimers were found to form linear structures, while methanol clusters larger than dimers mainly exist in cyclic ring conformations [18]. In the liquid and solid state, methanol molecules preferentially form chains but ring-like structures and zigzag chains were also observed, in which methanol is 2-fold hydrogen bound [19, 20]. The existence of intermolecular structural association *via* hydrogen bonding was also confirmed for liquid and solid ethanol [21, 22, 23] and the presence of trans and gauche conformations (with respect to the CC-OH bond axis of ethanol) was deduced from microwave spectroscopic studies [24, 25, 26]. Theoretical calculations (applying scaled quantum mechanical force field methods; SQM [27]) showed that the trans and gauche conformers are nearly degenerate as their energies differ by only 0.1 kcal/mol [28]. Nevertheless, the gauche conformer dominates over the trans form [28, 29]. Note that two possible gauche forms (g and g') but only one trans (t) conformation exists for ethanol. In the solid state, ethanol molecules were found to form (infinite) U-shaped straight chains of molecules in alternating trans and gauche conformations with two hydrogen bonds per molecule [30]. For 1-propanol, also the existence of trans and gauche conformation with respect to the CC-OH bond axis was observed by microwave spectroscopy and similar to ethanol, the gauche conformation was predicted to be more stable [31]. For 1-butanol monomers, the conformational stability between the trans and gauche form for the C-C bond adjoining the C-OH bond was found to be similar, while the trans form about CC-CCOH axis was reported to be more stable [32]. In general, the stabilization of the gauche conformation was explained by the enhanced van der Waals interactions between the oxygen atoms of the hydroxyl group and the hydrogen atoms in the C_γ position [33]. The assignment of the vibrational spectra for 1-propanol and 1-butanol, with the respect to the conformation about the CC-CO and CC-C-C-O axis, for the gaseous, liquid and solid states and for solutions was reported by Fukushima *et al.* [34]

and Crowder *et al.* [35]. The most stable conformation of 1-butanol in the solid state is the all trans (TTt) and the trans-trans-gauche (TTg; gauche with respect to the CCCC-O axis) conformation, while in the liquid and glassy state various conformers were reported [32].

In the present work, the non-reactive sorption of the short chain aliphatic alcohols (methanol, ethanol, 1-propanol, and 1-butanol) on alkali cation exchanged X zeolites is investigated by inelastic neutron scattering (INS) in combination with infrared (IR) spectroscopy. INS is complementary to transmission or reflection-absorption infrared spectroscopy and allows access to all vibrations of the molecules in the low frequency region without limitations due to selection rules and low transmittance of the samples. Moreover, INS is highly sensitive to the motions of the hydrogen atoms in the molecule, and enables discrimination between vibrational modes of the adsorbate molecules and the (non H containing) host materials [36]. An important difference between INS spectroscopy and IR and Raman spectroscopy is that overtones and combinations are *allowed* transitions within the harmonic approximation. In particular, combinations (phonon wings) between the internal modes and the lattice modes occur. Their importance lies in the fact that the total spectral intensity is distributed between the internal mode and the phonon wing. Their intensity is determined by the momentum transfer (Q, $Å^{-1}$), which for the spectrometer used here (TOSCA) increases with energy transfer (E, cm^{-1}) as: $Q^2 \approx E/16$. Hence at large energy transfer (> 1600 cm^{-1}) most of the intensity occurs in the phonon wing and the fundamental modes are not observed. In contrast, IR spectroscopy can readily access the wavenumber region above 1300 cm^{-1} with good resolution. Thus the methods provide complementary information about the vibrational properties of the molecules adsorbed and the combination of both methods provides a powerful tool for studying hydrogen-bonding interactions [37, 38, 39 40]. Based on the data presented an assignment of the vibrational modes in the range 30-2000 cm^{-1} (INS) and 1300-3800 cm^{-1} (IR) will be given. The influence of the increasing chain length of the alcohol molecules and the framework polarity on the sorption structure will be discussed. The interpretation of the spectra of the alcohol in the solid and the adsorbed state is supported by theoretical calculations of the vibrational modes of single alcohol molecules and aggregates of two and three molecules.

3.2 Experimental

3.2.1 Materials

Commercial Na-X zeolite (Köstrolith) was cation exchanged by liquid phase ion exchange in 0.1 M aqueous alkali metal nitrate solutions (Na^+, K^+, Rb^+ and Cs^+). The chemical composition (Si/Al ratio) of all materials was determined by atomic absorption spectroscopy (AAS, UNICAM 939), the structural integrity was verified by powder X-ray diffraction (recorded with a Philips XPERT PRO diffractometer using the CuK_α line) and nitrogen adsorption isotherms (measured with a PMI sorptometer). The results are compiled in Table 3.1. Methanol, ethanol, 1-propanol, and 1-butanol (purity is p.a. > 99.5 %) were obtained from Merck AG and used without further purification.

Table 3.1 Characteristics of alkali metal cation exchanged X zeolites determined from AAS analysis and N_2-sorption.

Sample	Si/Al	M^+/Al [mol%]	Na^+/Al [mol%]	Unit cell composition	Micropore volume [m^3/g]	S_{int} [a]	δ_0 [b]	e/r [c] [$Å^{-1}$]
Na-X	1.2	100	100	$Na_{88}\,Al_{88}\,Si_{104}\,O_{384}$	0.17	2.314	-0.337	1.05
K-X	1.3	95.3	2.3	$K_{82}\,Na_2\,Al_{84}\,Si_{108}\,O_{384}$	0.15	2.298	-0.341	0.75
Rb-X	1.2	67.5	32.5	$Rb_{60}\,Na_{29}\,Al_{88}\,Si_{104}\,O_{384}$	0.11	2.232	-0.358	0.67
Cs-X	1.3	55.4	44.6	$Cs_{47}\,Na_{38}\,Al_{84}\,Si_{108}\,O_{384}$	0.10	2.239	-0.356	0.59

[a] $S_{int} = (S_P^{p} \cdot S_Q^{q} \cdot S_R^{r} \cdot S_T^{t})^{1/(p+q+r+t)}$: for a compound $P_pQ_qR_rT_t$ calculated intermediate Sanderson electronegativity [10, 11].
[b] Calculated average charge $-\delta_o$ on the oxygen of the lattice, using $(S_{int}-S_o)\cdot 2.08 \cdot S_o^{1/2}$.
[c] electrostatic potential of sodium cation (e/r)

3.2.3 The INS experiments and sample preparation

Inelastic neutron scattering measurements were performed on the spectrometer TOSCA at the spallation neutron source ISIS (Rutherford Appleton Laboratory, UK). TOSCA is an indirect geometry time-of-flight spectrometer that allows INS spectra in the energy transfer range 30-4000 cm^{-1} to be obtained with a resolution of ~ 1.5 % of the energy transfer[41].

The partial pressure of the alcohol molecules during sorption on the alkali metal exchanged zeolite X samples was adjusted to reach a loading of three molecules per

supercage (coverage 0.27 % with respect to the counter cations). The activation, sorption and sample preparation for the INS and IR experiments followed the procedures described in reference 42. The pure alcohols were investigated in flat thin-walled aluminum cells. For recording the spectra the sample containers were placed in a helium cryostat and cooled to *ca* 20 K. The spectra were recorded at temperatures below 20 K, measurement times were typically ~10 hours. The spectrum of an empty container and of the activated zeolite was subtracted from the spectra of the samples in all data presented here. Dehydrated zeolite samples are generally weak neutron scatterers, therefore, all intensity observed after the sorption in INS results from the H atoms in the sorbate molecules.

3.2.4 IR spectroscopy

Sorption of short chain, linear alcohols was followed by *in situ* IR spectroscopy (Bruker IFS–88, resolution 4 cm^{-1}, base pressure below 10^{-6} mbar) at 308 K and partial pressures between 10^{-3}-1 mbar [42]. The spectra were recorded in the transmission absorption mode and monitored time-resolved during the equilibration of the zeolite with the sorbate. All spectra were baseline corrected between 3800 and 1200 cm^{-1} and normalized to the integral peak area of the overtone vibrations of the framework in the range between 2100-1735 cm^{-1}. The spectra presented in this paper are the difference between the spectra of the sample in contact with the alcohol molecules and the spectrum of the activated zeolite. In this mode of presentation, IR bands pointing upwards increased in intensity and bands pointing downwards decreased in intensity, during the interaction of the zeolite with the sorbate molecules.

3.2.5 Computational methods

The structure of single alcohol molecules and of clusters consisting of two and three alcohol molecules were optimized with respect to the total energy using density functional theory methods (DFT) implemented in Gaussian 98 [43]. The 6-31G** basis set and non-local corrections on the B3LYP level were applied. After having achieved the optimized geometry for the different clusters the vibrational modes were calculated. The displacement vectors determined for each vibrational mode were used to simulate the INS (including phonon wings and overtone vibrations) using the program aCLIMAX [44].

3.2.6 Temperature programmed desorption studies (TPD)

Desorption measurements were carried out in a quartz sample holder connected to a UHV chamber with a mass spectrometer (Balzers QMG 420). About 30-50 mg of zeolite powder was activated *in situ* by heating in vacuum ($p < 10^{-3}$ mbar) to 723 K at a rate of 10 K/min and holding this temperature for 1 h. After cooling to 308 K, the sample was exposed to the desired sorbate and equilibrated at a pressure of approximately 10 mbar. After evacuation for 1 h at 10^{-3} mbar and 308 K to remove weakly physisorbed molecules, the TPD profile was recorded during a temperature increment of 10 $K \cdot min^{-1}$ between 35 and 873 K.

3.2.7 NMR spectroscopy

^{1}H MAS NMR spectra were measured at 500 MHz using a Bruker 500 TM Ultrashield NMR spectrometer at room temperature. Prior to the measurements, ZrO_2 rotors of 4 mm size were filled under nitrogen atmosphere with alcohol loaded Na-X zeolite samples (three alcohol molecules per faujasite supercage in average) as prepared for INS studies. The experiments were carried out by single pulse excitation (SPE) in a magnetic field of 11.75 T. The rotation frequency was 14 kHz and the chemical shifts were measured relative to adamantan (2.0 ppm for ^{1}H) as external frequency. ^{1}H NMR spectra of liquid and diluted C_1-C_4 alcohols were measured at 360 MHz using a Bruker AV 360 NMR spectrometer at room temperature. The experiments were carried out in a magnetic field of 8.46 T and the chemical shifts were measured relative to CCl_3D (7.24 ppm).

3.3 Results

3.3.1 Inelastic neutron scattering studies

The observed and calculated frequencies for the C_1-C_4 alcohols (methanol, ethanol, 1-propanol, and 1-butanol) in the range 30-2000 cm^{-1} are listed in Tables 3.2-3.5. The spectrum of the dehydrated zeolite [42] was recorded and used for background subtraction in order to study the vibrational modes of the adsorbed molecules. The experimental and calculated INS spectra of the different alcohols are shown in Figures 3.1-3.4. The assignment of the vibrational frequencies in the spectra of the solid alcohol molecules and the alcohol molecules adsorbed on Na-X is based on

comparisons with vibrational assignments reported for methanol [19, 45, 46], ethanol [25, 47, 48, 49], 1-propanol [31, 34], and 1-butanol [32, 35], as well as on the results of the *ab initio* calculations carried out for monomers, linear dimer and cyclic trimer clusters [50, 51].

Methanol has only one energetically stable geometry, while for ethanol two, 1-propanol five and 1-butanol 14 conformers exist. In the structures used for the calculations, a staggered conformation of the C-C bonds was used for all molecules. The calculation of the INS spectra of the ethanol and 1-propanol monomer (M) was performed for the *all-trans* (t) conformation (M_t and M_{Tt}, respectively), where the CCOH and CCCO dihedral angles are equal to 180^o and the terminal methyl, respectively ethyl groups are in *trans* position with respect to the hydroxyl group. In the linear dimer cluster both ethanol molecules were in the *gauche* (g) conformation ($D_{g'g'}$) (D) with a CCOH dihedral angle of about 300^o (Figure 3.3). Both 1-propanol molecules were in the Tg' conformation ($D_{Tg'\ Tg'}$) in the dimer cluster, while for the trimer (T) cluster the molecules were in the Tg, Gg' and Gt conformation ($T_{Tg\ Gg'\ Gt}$) (Figure 3.5). The 1-butanol monomer was in the TTg' conformation, for the dimer cluster the 1-butanol molecules were oriented in the $D_{GTg'GTt}$ conformation with the donor molecule in the DTg' form (Figure 3.7). Note, that for the C_1-C_4 alcohols *trans* as well as *gauche* isomers were found in the gas phase [24], while the *trans* conformer of ethanol suspended in argon matrices at 20 K was found to be more stable than the *gauche* conformer [52]. In crystalline ethanol, trans and gauche conformers were found to be alternating forming U-shape chains [53]. Similar results were also shown by ab initio calculations [54] and microwave spectroscopy for gaseous and liquid ethanol and 1-propanol [25, 34, 55].

Table 3.2 Experimental vibrational frequencies, assignments of the INS bands of methanol in the solid and adsorbed (three methanol molecules per faujasite supercage, on average) state (T < 20 K), and theoretical vibrational frequencies of methanol clusters calculated by DFT.

DFT				INS	
Monomer	**Linear dimer**	**Cyclic trimer**	**Assignment** [a, b]	**Solid**	**Ads. on Na-X**
1530 sh	1530 sh	1530, 1505	$\delta_{as}(CH_3)$		
1505	1505	1490	$\delta_{s}(CH_3)$	1446 br	1446 br
1386	1445 HB, 1373	1464, 1445	$\delta(OH)_{ip}$		
1179	1182	1184, 1136	$\delta(CH_3)_{rock}$	1149,	1158,
1095, 1062	1127 HB, 1082	1175, 1141, 1128	$\delta(CH_3)_{rock}$ + $\delta(OH)_{ip}$	1123	1114
1083	1089 HB, 1056 w	1090 w, 1073	ν(CO)		
---	730 HB	964, 785, 732	$\delta(OH)_{op}$	773, 697	900-600 br
340	332	---	$\delta(OH)_{op}$	---	---
---	218	240, 232, 218	OH···H stretch	220	90 br + tail
---	137	173, 124, 121, 116	τ (CH_3)	166	
	109, 87, 72, 44	109, 97, 59, 52, 44	Intermolecular	110 s	

[a] all frequencies are in cm^{-1}, vs = very strong, s = strong, m = medium, w = weak, vw = very weak, sh = shoulder, br = broad, d = H-donor molecule.
[b] aCLIMAX fit to methanol DFT data

Table 3.3 Experimental vibrational frequencies, assignments of the INS bands of ethanol in the solid and adsorbed (three ethanol molecules per faujasite supercage, on average) state (T < 20 K), and theoretical vibrational frequencies of ethanol clusters calculated by DFT.

DFT		DFT		DFT		INS [a]	
monomer M_t	**Assignment [b]**	**Linear dimer $D_{g'g'}$**	**Assignment [b]**	**Cyclic trimer T_{ttt} [50]**	**Assignment [b]**	**Solid [47, 48]**	**Ads. on NaX**
1547	$\delta(CH_2)$	1535, 1531, 1513, 1508, 1506, 1504,	$\delta(CH)$	1526, 1528, 1500, 1485	$\delta(CH)$	1480 1457 1426 sh	1340-1700: 1485 1440
1514	$\delta(CH_3)$	1455 (d)	$\delta(COH)_{ip}$	1481, 1466, 1464	$\delta(COH)_{ip}$	1385 br	1390sh
1490	$\delta(CH_2)_{twist}$	1424 (d)	$\delta(CH_2)_{wagg} + \delta(OH)_{ip}$	1405, 1404	$\delta(CH_3)$		1356 sh
1476	$\delta_{as}(CH_3)$	1434, 1412, 1401 (d)	$\delta_s(CH_3) + \delta(CH_2)_{wagg}$	1381, 1322, 1307	$\delta(CH_2)_{wagg} + \delta(OH)_{ip}$		
1470	$\delta(CH_2)_{wagg} + \delta(OH)_{ip}$	1380	$\delta(COH)_{ip}$	1301, 1300	$\delta(CH)_{rock}$	1286	1287, 1230
1413	$\delta_s(CH_3)$	1303 (d), 1295	$\delta(CH_2)_{twist} + \delta(COH)_{ip}$	1178, 1117, 1118	$\delta(CH)_{rock}$	1154 w 1132 w	1080-1200: 1134
1304	$\delta(CH_2)_{twist}$	1154 (d), 1138	$\delta(CH)_{rock}$	1116, 1107	$\delta(CH_3)_{rock}$	1101	1095
1279 sh	$\delta(COH)_{ip}$	1138, 1115 (d)	$\delta(CH_3)_{rock} + \delta(COH)_{ip}$	1076, 1055, 1051	$\nu_{as}(CCO)$	1061 w	1052 w, sh
1190	$\delta(CH)_{rock}$	1081	$\nu_{as}(CCO) + \delta(CH_3)_{rock}$	900, 898, 896	$\nu_s(CCO)$	934 sh	942 w
1123	$\nu_{as}(CCO) + \delta(CH_3)_{rock}$	1076 (d), 1068	$\nu_{as}(CCO) + \delta(COH)_{ip}$	826, 820, 819	$\delta(CH_2)_{rock-twist} + \delta(CH_3)_{rock}$	888 w, br, 809	880, 805
1037	$\nu_{as}(CCO) + \delta(COH)_{ip}$	894	$\nu_s(CCO) + \delta(CH_3)_{rock}$	809, 724, 628	$\delta(OH)_{op}$	715 w, br	640 w, br
909	$\nu_s(CCO) + \delta(CH_3)_{rock}$	813 (d), 810	$\delta(CH_2)_{rock-twist} + \delta(CH_3)_{rock}$	444, 436, 434	$\delta(CCO)$	430	436
826	$\delta(CH_2)_{rock-twist} + \delta(CH_3)_{rock}$	698 (d)	$\delta(OH)_{op}$	262, 261, 257	$\tau(CH_3)$	270 [d]	276
416	$\delta(CCO)$	439, 421 (d)	$\delta(CCO)$		$\nu(OH\cdots O)$	240 sh	240 sh,
293	$\delta(OH)_{op}$	359	$\delta(OH)_{op}$		$\delta(OH\cdots O)$		184 w
249	$\tau(CH_3)$	281, 268 (d)	$\tau(CH_3)$				
		151, 97, 79, 42	Intermolecular	173, 168, 161, 120, 80, 58, 54, 48, 44	Intermolecular	93 br [d]	134, 122 sh, 101 sh, 66 s br

[a] in cm^{-1}; all frequencies are in cm^{-1}, vs = very strong, s = strong, m = medium, w = weak, vw = very weak, sh = shoulder, br = broad, d = H-donor molecule.
[b] aCLIMAX fit to ethanol DFT data.

Table 3.4 Experimental vibrational frequencies, assignments of the INS bands of 1-propanol in the solid and adsorbed (three 1-propanol molecules per faujasite supercage, on average) state (T < 20 K), and theoretical vibrational frequencies of 1-propanol clusters calculated by DFT.

DFT		DFT		DFT		INS [b]		
Monomer M_{Tt}	**Assignment [a]**	**Linear dimer $D_{Tg' Tg'}$**	**Assignment [a]**	**Cyclic trimer $T_{Tg Gg' Gt}$**	**Assignment [a]**	**Solid [34]**	**Ads. on Na-X**	**Ads. on Cs-X**
1532, 1518, 1504	$\delta(CH_2)$	1519	$\delta(CH)$	1525, 1520, 1518, 1509	$\delta(CH)$		1800-1200: 1455, 1380	1800-1200: 1480, 1454 1415 sh, br, 1388
1514	$\delta_{as}(CH_3)$	1534 (d), 1532, 1509 (d), 1505	$\delta(CH_2)$	1501	$\delta(OH)_{ip} + \delta(CH_2)$			
1435	$\delta(OH)_{ip} + \delta(CH_2)_{wagg}$	1516, 1514 (d)	$\delta_{as}(CH_3)$	1536 (C1) 1531, 1505, 1492	$\delta(CH_2)$			
1425	$\delta_s(CH_3) + \delta(CH_2)_{wagg}$	1459	$\delta(OH)_{ip}$	1515, 1511	$\delta_{as}(CH_3)$			
1398, 1254, 1149	$\delta(CH_2)_{wagg} + \delta(C\text{-}OH)_{ip}$	1437, 1429 (d)	$\delta(OH)_{ip} + \delta(CH_2)_{wagg}$	1461	$\delta(OH)_{ip}$	1455		
1340, 1320	$\delta(CH_2)_{wagg}$	1427	$\delta_s(CH_3) + \delta(CH_2)_{wagg}$	1495, 1474	$\delta(OH)_{ip} + \delta(CH_2)_{wagg}$			
1102	$\nu(CC) + \delta(CH_2)_{wagg}$	1424 (d),	$\delta_s(CH_3)_{umbrella}$	1432, 1430	$\delta(OH)_{ip} + \delta_s(CH_3) + \delta(CH_2)_{wagg}$			
1080	$\nu_{as}(CCO)$	1390	$\delta(C\text{-}OH)_{ip} + \delta(CH_2)_{twist} + \delta(CH_2)_{wagg}$	1427, 1424	$\delta_s(CH_3)_{umbrella}$	1425		
1035	$\nu(CC)$	1344 (d), 1341	$\delta(CH_2)_{twist} + \delta(CH_3)_{rock}$	1430, 1412, 1388, 1386	$\delta_s(CH_3) + \delta(CH_2)_{wagg}$	1393		
895	$\delta\ (CH_2)_{\ twist} + \delta(CH)_{rock}$	1324 (d), 1322	$\delta(CH_2)_{twist}$	1367, 1304	$\delta(C\text{-}OH)_{ip} + \delta(CH_2)_{twist} + \delta(CH_2)_{wagg}$	1378		
890	$\delta(CH_3)_{rock} + \nu_s(CCO)$	1264 (d), 1253	$\delta(CH_2)_{twist} + \delta(C\text{-}OH)_{ip}$	1341	$\delta(CH_2)_{wagg} + \delta(CH_3)_{rock}$	1357 sh w	1351 sh	1358
764	$\delta(CH_2)_{rock}$	1158, 1120w	$\delta(CH_2)_{wagg} + \delta(C\text{-}OH)_{ip}$	1310	$\delta(CH_2)_{twist} + \delta(CH_3)_{rock}$			
459	δ (CCO)	1160 (d), 1148, 1100	$\delta(C\text{-}OH)_{ip} + \delta(CH_2)_{twist} + \delta(CH_3)_{rock}$	1329, 1280	$\delta(CH_2)_{twist}$	1295	1297	1286, 1303

Table 3.4 (continued)

328	δ (C-OH)$_{op}$	1072 w	ν(CC) + δ(CH$_2$)$_{wagg}$	1269, 1265	δ(CH$_2$)$_{twist}$ + δ(C-OH)$_{ip}$	1240	1237	1238, 1246
265	δ (CCC)	1095 (d), 1070 w	ν_{as}(CCO)	1176	δ(CH)$_{rock}$	1190	1200 vw	1197 vw
229	τ (CH$_3$)	1038 (d), 1033	ν(CC)	1171	δ(OH)$_{ip}$ + δ(CH$_2$)$_{rock}$			
137	τ (CC)	895, 898 (d)	δ (CH$_2$) $_{twist}$ + δ(CH)$_{rock}$	1149	δ(C-OH)$_{ip}$ + δ(CH)$_{rock}$	1142	1138	1137, 1160 w, br
		891 (d)	δ(CH$_3$)$_{rock}$ + ν(CC)	1133	δ(CH$_2$)$_{wagg}$ + δ(C-OH)$_{ip}$			
		704 (d)	δ(C-OH)$_{op}$	1130	ν(CO) + δ(CH)$_{rock}$			
		472, 461 (d)	δ (CCO)	1128	δ(CH$_2$)$_{twist}$ + δ(CH$_3$)$_{rock}$	1111	1113	1110
		370	δ (C-OH)$_{op}$	1095, 1085, 1080	ν(CC) + ν_{as}(CCO)	1069 vw	1054vw	1054 vw
		280 (d), 268	δ (CCC)	1038	ν(CC)	1021 vw		1012 vw
		237, 230 (d)	τ (CH$_3$)	995, 991	ν(CC) + δ(CH$_3$)$_{rock}$	991 vw		
		166 (d), 142	τ (CC)	960	δ(C-OH)$_{op}$+ δ(CH$_3$)$_{rock}$	969	945 vw, 965 vw	940-90 vw
		125, 82, 60, 46	Intermolecular	928, 915, 896, 894	δ (CH$_2$) $_{twist}$ + δ(CH)$_{rock}$	892	882	886, 922 sh
				869, 865	ν(CC)	860 w, sh	854 sh	851 vw
				779 (C2)	δ(CH$_2$)$_{rock}$	807 vw		793 sh
				782, 767, 761	δ(C-OH)$_{op}$ + δ(CH$_2$)$_{rock}$	760	759	758
				699	δ(C-OH)$_{op}$	690 w	640 vw, br	
				504, 489, 478	δ (CCO)	463 (485)	466 (486)	461 (486)
				335, 321, 290	δ (CCC)	327	327	326
					δ (CCC) + τ (CH$_3$)	274 br	250-300 br	288
				255, 238, 235	τ (CH$_3$)	233	224	232
				210, 205, 186, 153	τ (CC)	158	164 w	
				153, 133, 110, 89, 80, 63, 59, 45, 36	Intermolecular	99 sh, 73 br	130, 100sh, 73 br	127, 83 s, 57 s

[a] aCLIMAX fit to 1-propanol DFT data.
[b] in cm^{-1}; all frequencies are in cm^{-1}, vs = very strong, s = strong, m = medium, w = weak, vw = very weak, sh = shoulder, br = broad, d = H-donor molecule.

Table 3.5 Experimental vibrational frequencies, assignments of the INS bands of 1-butanol in the solid and adsorbed (three 1-butanol molecules per faujasite supercage, on average) state (T < 20 K), and theoretical vibrational frequencies of 1-butanol clusters calculated by DFT.

DFT		DFT		INS [b]	
Monomer $M_{TTg'}$	**Assignment [a]**	**Linear dimer $D_{GTg'\,GTt}$**	**Assignment [a]**	**Solid**	**Na-X**
1562	$\delta_{as}(CH_3)$	1541, 1530 HB	$\delta_{as}(CH_3) + \delta(CH_2(O))$	1458 br	(1800-1200) 1451
1551	$\delta_{as}(CH_3) + \delta(CH_2(O))$	1524, 1522, 1520, 1516 (d), 1511, 1504 (d)	$\delta_{as}(CH_3) + \delta(CH_2(C))$		
1576 (C^1)	$\delta(CH_2(O))$	1499 (d)	$\delta(CH_2(C))$		
1545	$\delta(CH_2(C))$	1466 (d)	$\delta(OH)_{ip}$		
1468 (C^1), 1466	$\delta(CH_2)_{wagg} + \delta_s(CH_3)$	1463	$\delta(CH_2)_{wagg} + \delta(OH)_{ip}$		
1437, 1410	$\delta(CH_2)_{wagg} + \delta(OH)_{ip}$	1431 (d)	$\delta(CH_2)_{wagg} + \delta_s(CH_3)$	1430 sh	
1365	$\delta(CH_2)_{twist}$	1430	$\delta_s(CH_3)$		
1353	$\delta(CH_2)_{twist} + \delta(OH)_{ip}$	1424 (d)	$\delta(CH_2)_{wagg} + \delta(OH)_{ip} + \delta_s(CH_3)$		
1314	$\delta(CH_2)_{wagg}$	1391	$\delta(CH_2)_{wagg} + \nu(CC)$		
1275	$\delta(OH)_{ip} + \delta(CH_2)_{rock}$	1384 (d), 1354 (d)	$\delta(CH_2)_{wagg} + \delta(CH_2)_{twist}$	1368 br	1378
1179	$\nu(CC, CO) + \delta(CH_3)_{rock}$	1375	$\delta(CH_2)_{wagg} + \delta(OH)_{ip}$		
1137	$\delta(CH_2)_{twist} + \delta(OH)_{ip}$	1333	$\delta(CH_2)_{twist}$		
1119	$\nu_{as}(CCO)$	1314	$\delta(OH)_{ip} + \delta(CH_2)_{wagg} + \delta(CH_2)_{twist}$		
1103, 1038	$\nu(CO) + \nu(CC)$	1291 (d)	$\delta(CH_2)_{twist} + \delta(CH_2)_{wagg}$	1296	1298
973	$\delta(CH_2)_{twist} + \delta(C^1H_2)_{wagg}$	1254	$\delta(OH)_{ip} + \delta(CH_2)_{twist}$	1251	1259 sh
940	$\delta(CH_3)_{rock} + \nu(CC) + \delta(CH_2)_{wagg}$	1244	$\delta(CH_2)_{twist} + \delta(OH)_{ip}$		
825, 759	$\delta(CH_2)_{rock}$	1227 (d), 1163 (d), 1112	$\delta(CH_2)_{twist} + \delta(OH)_{ip} + \delta(CH_3)_{rock}$	1218	1214
454	$\nu(CCO)$	1182	$\delta(CH)_{rock}$		
400	$\delta(CCC)$	1124 (d)	$\delta(OH)_{ip} + \delta(CC) + \delta(CH_3)_{rock}$	1115 w, br	1114
324	$\delta(OH)_{op}$	1093 (d)	$\nu_{as}(CCO)$		
186	$\delta(CCC)$	1087, 1073 (d)	$\nu_{as}(CCC)$		
264	$\tau(CH_3)$	1045	$\nu(CO) + \nu(CC)$	1058 vw, br	1052 vw, 1023 vw
128, 110	$\tau(CC)$	981	$\delta(CH_3)_{rock} + (CH_2)_{wagg} + \delta(CH_2)_{twist}$		
		965, 962 (d)	$\nu(CC) + \delta(CH_2)_{twist}$	966 sh	

Table 3.5 (continued)

		976 (d)	$\delta(CH_3)_{rock} + \nu(CC) + \delta(CH_2)_{wagg}$	948	944
		887 (d), 884	$\nu_s(CCC)$	898 w	889 vw
		816,	$\delta(CH_2)_{rock}$	842, 826 w	839 w
		801 (d), 760	$\delta(CH_2)_{rock} + \delta(CH_3)_{rock}$	798 m	797
		755 (d)	$\delta(CH_2)_{rock} + \delta(OH)_{op}$	736	736
		734 (d)	$\delta(OH)_{op}$	690 w, br	640 vw, br
		490 (d, a)	$\delta(CCC) + \delta(OCC)$	516, 453 w	517, 448
		358 (d)	$\delta(CCC) + \delta(OCC)$	394, 351 w	394, 356
		352	$\delta(OH)_{op} + \delta(CCC)$		
		335	$\delta(OH)_{op}$	---	
		296, 225, 212	$\delta(CCC) + \tau(CH_3)$	254 m, 192 vw	285, 190
		290 (d)	$\tau(CH_3)$	254	261
			$\delta(OH\cdots O)$	194 vw, sh	190 w
		135, 120, 112	$\tau(CC)$	139 sh	132 br, 156 sh
		101, 69	$\tau((O)CC)$	82 s	73, 99
		46, 34	intermolecular		42

[a] aCLIMAX fit to 1-butanol DFT data.
[b] in cm^{-1}; all frequencies are in cm^{-1}, vs = very strong, s = strong, m = medium, w = weak, vw = very weak, sh = shoulder, br = broad, d = H-donor molecule.

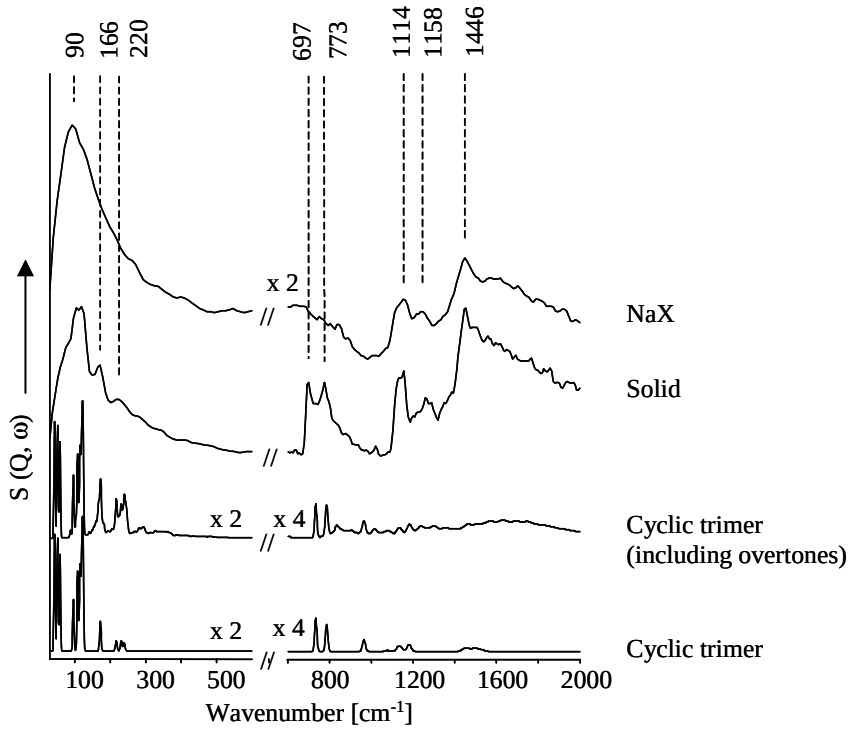

Figure 3.1 Theoretical vibrational spectra of cyclic methanol trimer cluster and inelastic neutron scattering spectra of methanol adsorbed on Na-X (loading three molecules per supercage, on average) and solid methanol at T < 20 K.

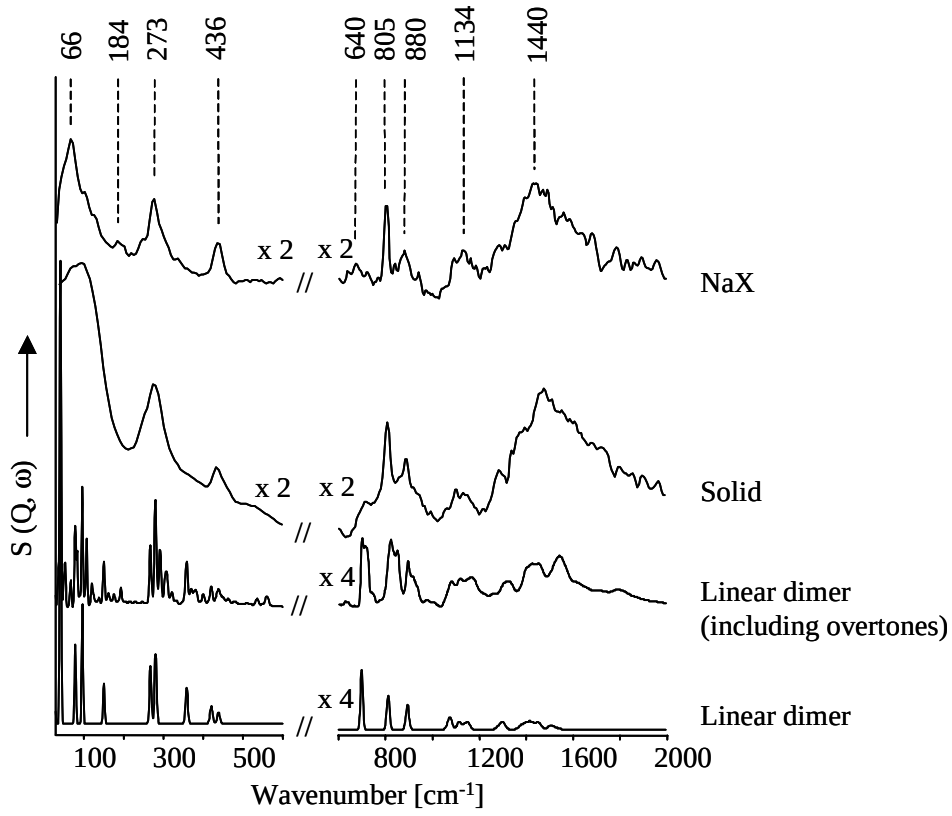

Figure 3.2 Theoretical vibrational spectra of linear ethanol dimer cluster and inelastic neutron scattering spectra of ethanol adsorbed on Na-X (loading three molecules per supercage, on average) and solid ethanol at T < 20 K.

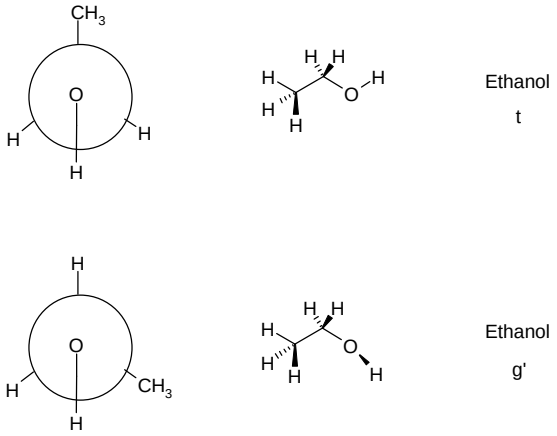

Figure 3.3 The conformers of ethanol used for DFT.

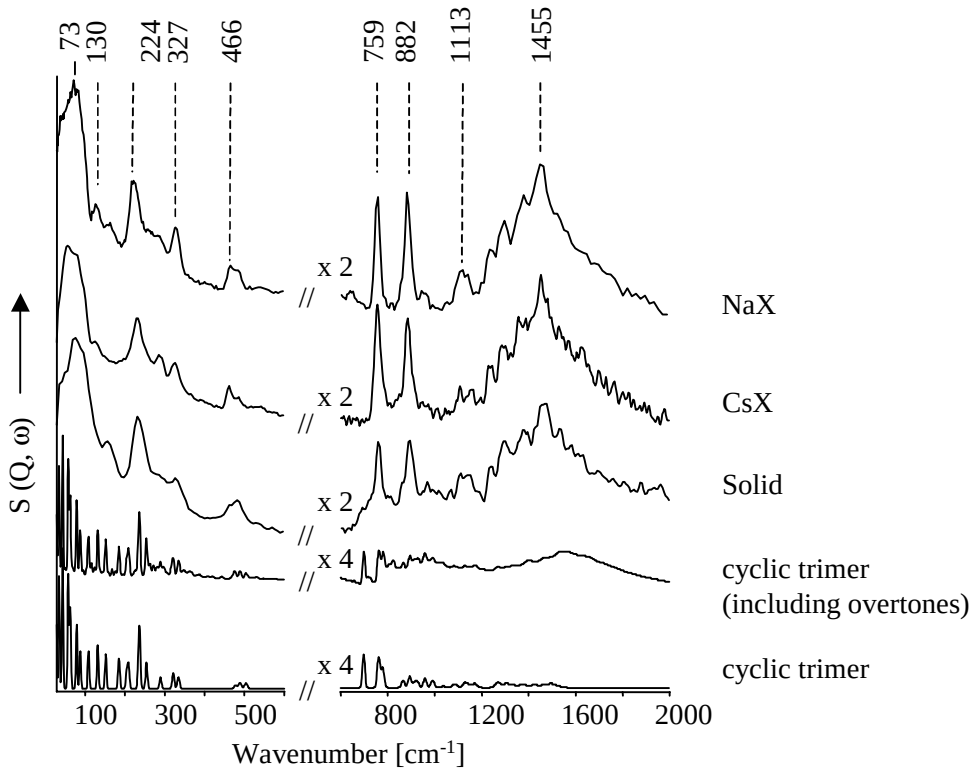

Figure 3.4 Theoretical vibrational spectra of cyclic 1-propanol trimer cluster and inelastic neutron scattering spectra of 1-propanol adsorbed on Na-X (loading three molecules per supercage, on average) and solid 1-propanol at T < 20 K.

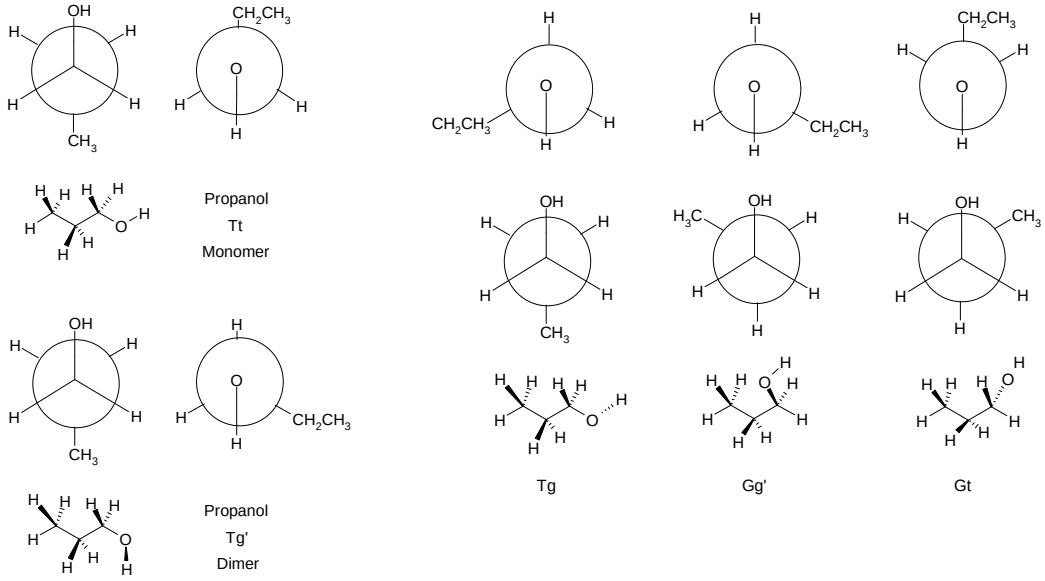

Figure 3.5 The conformers of 1-propanol used for DFT.

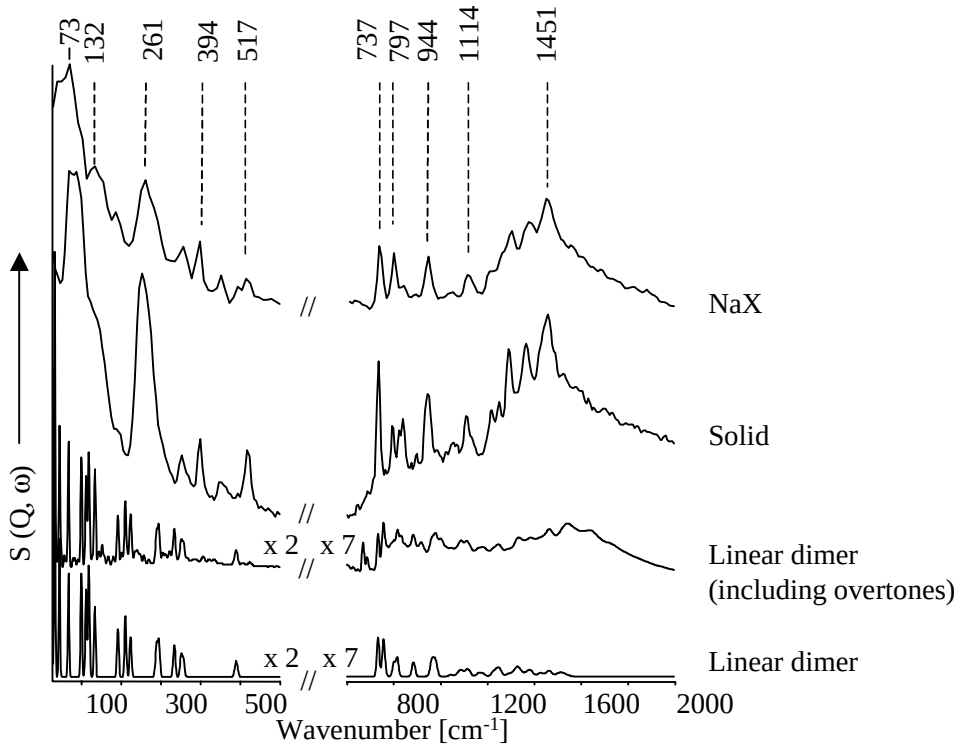

Figure 3.6 Theoretical vibrational spectra of linear 1-butanol dimer cluster and inelastic neutron scattering spectra of 1-butanol adsorbed on Na-X (loading three molecules per supercage, on average) and solid 1-butanol at T < 20 K.

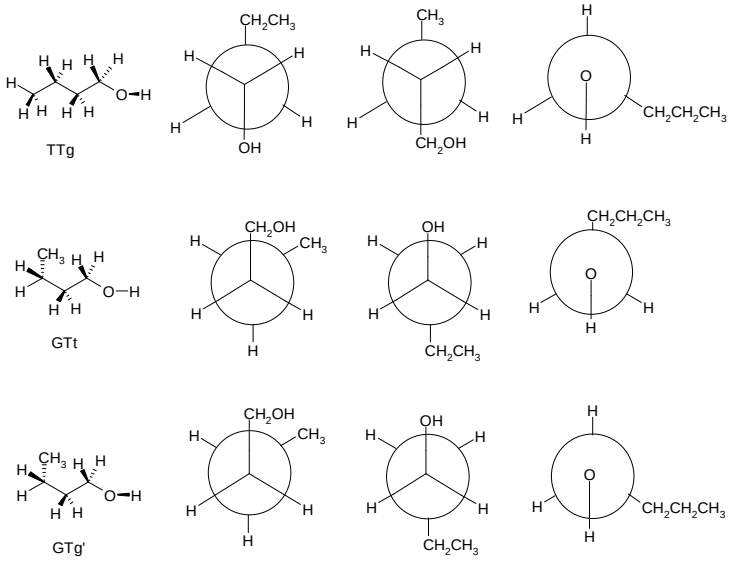

Figure 3.7 The conformers of 1-butanol used for DFT.

3.3.2 Infrared spectroscopy of C_1-C_4 alcohols adsorbed on Na-X

The infrared spectra after adsorption of the series of alcohols with a partial pressure of $1 \cdot 10^{-3}$ mbar at 308 K on Na-X are shown in Figure 3.8. Bands corresponding to adsorbed C_1-C_4 alcohol species were observed and are listed together with their assignment (based on comparisons with literature data) in Table 3.6. All alcohols were found to be adsorbed molecularly. The ν(OH) stretching vibration band of all sorbates was strongly broadened and located a similar frequency value at 3341 cm^{-1} showing a shoulder at 3460 cm^{-1}. With increasing hydrocarbon chain length a slight decrease of the ν(OH) band was observed and the band intensity in the ν(CH) region 3000-2840 cm^{-1} increased due to the increasing number of CH_2-groups.

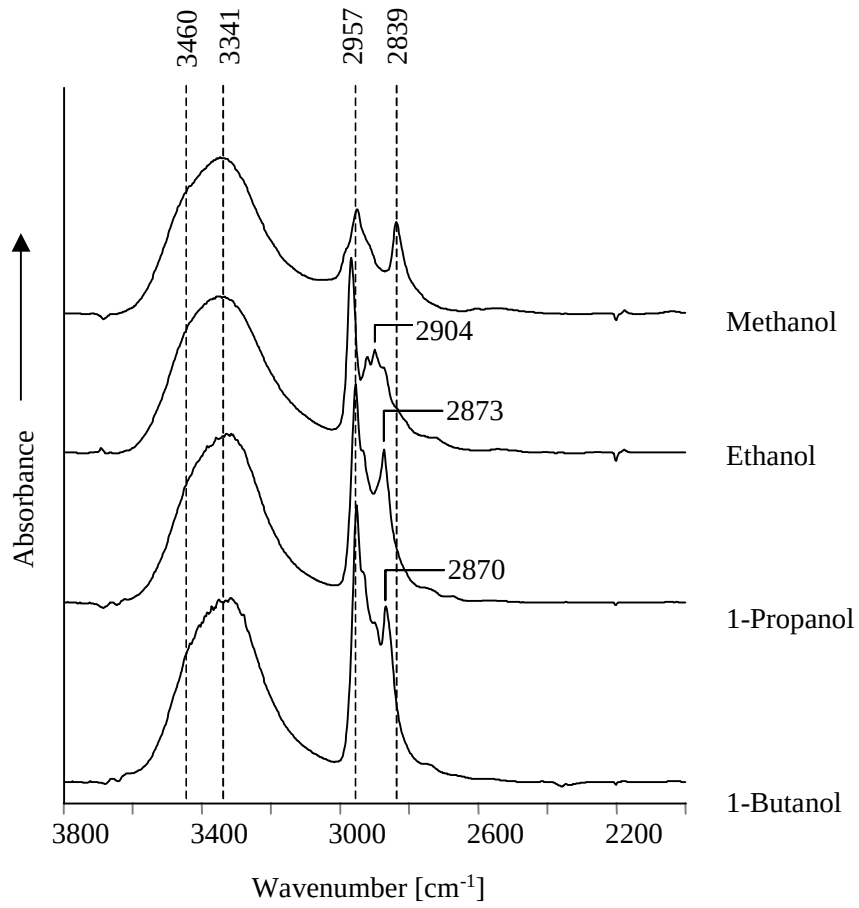

Figure 3.8 Difference infrared spectra of C_1-C_4 alcohols adsorbed on Na-X (T = 308 K, p = $1 \cdot 10^{-3}$ mbar).

Table 3.6 Vibrational IR frequencies of linear C_1-C_4 alcohols adsorbed on NaX (T = 308 K, p = $1 \cdot 10^{-3}$ mbar).

methanol				**ethanol**				
Assignment [a]	**Gas phase** [91]	**Liquid** [45]	**Adsorbed on Na-X**	**Assignment** [a]	**Gas phase** [47, 75]	**Liquid** [48]	**Adsorbed on silica** [88]	**Adsorbed on Na-X**
ν(OH)	3682 s	3337 s, br	3460 sh, 3341 s, br	ν(OH)	3676	3330 [86, 87]	3326	3459 sh, 3335 vs br
$\nu(CH_3)$ as	2999, 2970	2934	2980 sh, 2957 br	$\nu_{as}(CH_3)$	2989	2975	2982	2970 vs
2 x $\delta(CH_3)$	2920		2917	$\nu_{as}(CH_2)$	2948			2955 sh
$\nu(CH_3)$ s	2844	2822	2839 br	$\nu_s(CH_3)$	2943	2927	2932	2923 m
$\delta_{as}(CH_3)$	1477, 1465,	1475, 1453	1476, 1451	$\nu_s(CH_2)$	2900	2886	2908, 2880	2904 m, 2874 m sh
	1454			2x $\delta(COH)_{ip}$	2890			2838 w sh
δ(OH), $\delta_s(CH_3)$		1420 br	1423 sh, 1400 br	$\delta(CH_2)$	1490	1484	1496, 1484	1478 w
δ(OH)	1340			$\delta_{as}(CH_3)$	1452	1455, 1447	1452	1452 m
				$\delta(COH)_{ip}$ + $\omega(CH_2)$		1420		1418 m b
				$\rho(CH_2)$			1400	
				$\delta_s(CH_3)$, $\omega(CH_2)$	1394	1380	1378	1386 sh, 1361
				$\delta(COH)_{ip}$ + $\omega(CH_2)$		1331		1327

Table 3.6 (continued)

1-propanol					**1-butanol**			
Assignment[a]	**Gas phase** [34]	**Liquid** [77]	**Ads. on NaX**	**Ads. on RbX**	**Assignment** [a]	**Matrix** [32] **(15 K)**	**Liquid** [32]	**Ads. on NaX**
ν(OH) monomer	3687				ν(OH) monomer	3670 s, 3663 m br, 3647 w		
ν(OH) polymer		3356	3459 sh, 3329 vs b	3252 vs b	ν(OH) polymer	3517 dimer 3466 vw br,	3336 vs, br	3460 sh, 3327 vs br
$\nu_{as}(CH_3)$	2978	2967	2958, 2953 sh	2956		3434 vw br		
$\nu_{as}(CH_2)$	2946, 2929				$\nu_{as}(CH_3)$	2974 vs, 2970 vs sh	2961 vs	2955 s
$\nu_s(CH_3)$		2933	2937	2932	$\nu_{as}(CH_2)$	2943		
$\nu_s(CH_2)$	2892	2874	2875 s	2867 s	$\nu_s(CH_3)$	2932 s sh	2935 vs	2933 m sh
$\delta(CH_2(O))$			1474 w		$\nu_s(CH_2)$	2910 m, 2903m, 2885 s, 2873 m sh		2899 m sh, 2870 s
$\delta_{as}(CH_3)$, $\delta(CH_2)$	1464	1464	1463 w sh, 1459 m	1459 m b	2x $\delta(COH)_{ip}$ $\delta(CH_2)$			2854 sh
$\delta(CH_2(C))$			1436 sh	1442 w sh	$\delta(CH_2(O))$	1485 vw, 1480 vw,		1478 sh
$\delta(COH)_{ip}$ + $\omega(CH_2)$			1412 b			1470 s		
$\omega(CH_2)$	1393, 1300	1300	1395		$\delta_s(CH_3)$	1470 s, 1466 vs,	1466 s,	1462 m
$\delta_s(CH_3)$	1393		1391	1390		1460 s	1460 s sh	
$t(CH_2)$	1276				$\delta_s(CH_3)$, $\delta(CH_2(C))$	1457 vw, 1454 vw		
$\delta(COH)_{ip}$	1218	1381	1343	1349	$\delta(CH_2(C))$	1440 w, 1437 vw	1434	
					$\delta(COH)_{ip}$ + $\omega(CH_2)$	1434 vw, 1410 vw, 1395 vw br	1425 w sh	1410 br
					$\delta(COH)_{ip}$ + $\delta_s(CH_3)$	1383 m		
					$\delta_s(CH_3)$	1382 m	1379 s	1387
					$\omega(CH_2)$	1348 vw, 1342 vw	1369 w sh	1342 w
					$\delta(COH)_{ip}$		1339 m	
					$\omega(CH_2)$	1309 vw	1328 w sh	

[a] all frequencies are in cm^{-1}, vs = very strong, s = strong, m = medium, w = weak, vw = very weak, sh = shoulder, br = broad, d = H-donor molecule.

3.3.3 Temperature programmed desorption

The strength of interaction between light *n*-alcohol molecules and the zeolites has been evaluated from temperature programmed desorption studies. Signals corresponding to molecularly adsorbed *n*-alcohols were observed by mass spectrometry. In Figure 3.9, the rate of desorption of C_1 to C_4 *n*-alcohols adsorbed on K-X is shown. The desorption temperature increased going from C_1 to C_4. Similar desorption features were observed for the other alkali metal cation exchanged samples.

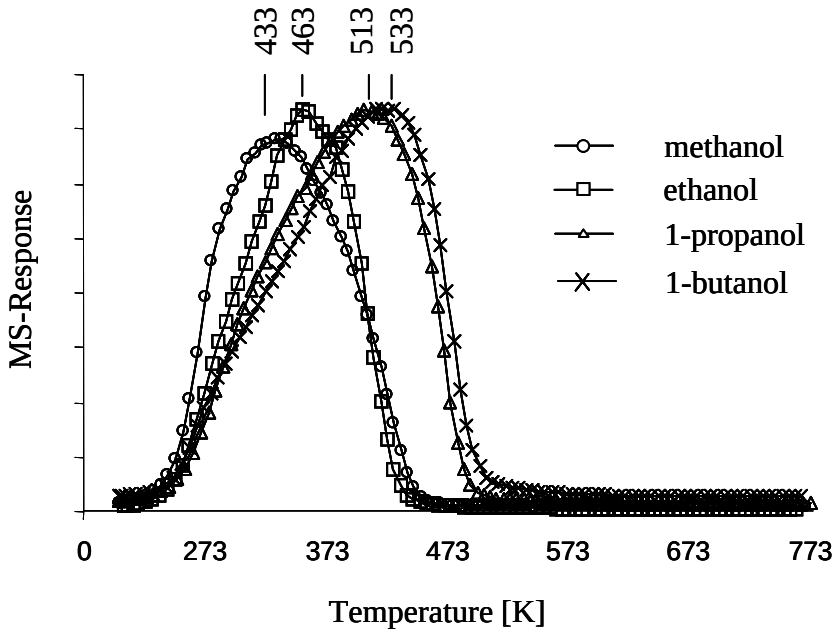

Figure 3.9 Temperature programmed desorption of C_1 to C_4 alcohols adsorbed on K-X.

3.3.4 Solid- and liquid state NMR investigations

Solid-state NMR was used to obtain detailed information on the molecular species within the cavities of microporous catalysts. The ^1H NMR spectra of linear C_1-C_4 alcohols adsorbed on Na-X are shown in Figure 3.10. Their chemical shifts are listed in Table 3.7 together with results obtained for diluted C_1-C_4 alcohols (0.445 M in CCl_3D), pure liquid C_1 and C_4 alcohols and CD_3OH adsorbed on a series of zeolites. In contrast to the neat liquid, showing hydrogen bound OH groups, the hydrogen bridges are broken in the diluted solution.

The spectra of the alcohols adsorbed on Na-X, as well as the neat liquids and diluted solutions show one signal for the OH and each CH_2 and CH_3 group. There was no splitting observed of any of these resonances. The OH, CH_2, and CH_3 resonances of C_1-C_4 alcohols adsorbed on Na-X were shifted to lower field relative to the corresponding alcohols dissolved in CCl_3D [56]. In liquid methanol, which forms hydrogen bonds between the hydroxyl groups, the chemical shift of the hydroxyl resonance was also found at higher frequencies (4.6 ppm [57]). For all alcohols, the strongest shift of the hydrocarbon protons was found for those in α-position, while with rising distance of the CH groups from the oxygen atom, the resonances were located at lower frequencies. The CH resonances from groups at the same chain position were of similar value, while after adsorption, all CH_2/CH_3 resonances were shifted by about 1.3-1.4 ppm to lower field compared to the ones in diluted alcohol solution. A weak increase of the chemical shift of the OH protons of adsorbed alcohols towards higher frequencies was seen with increasing hydrocarbon chain length, while the CH_3 proton resonances for C_2-C_4 alcohols were very similar. In Figure 3.11, the NMR resonances of diluted, pure, and adsorbed 1-butanol are shown. The OH resonance (arrow marked) showed a distinct chemical shift. The signals of adsorbed alcohols show distinct broadening.

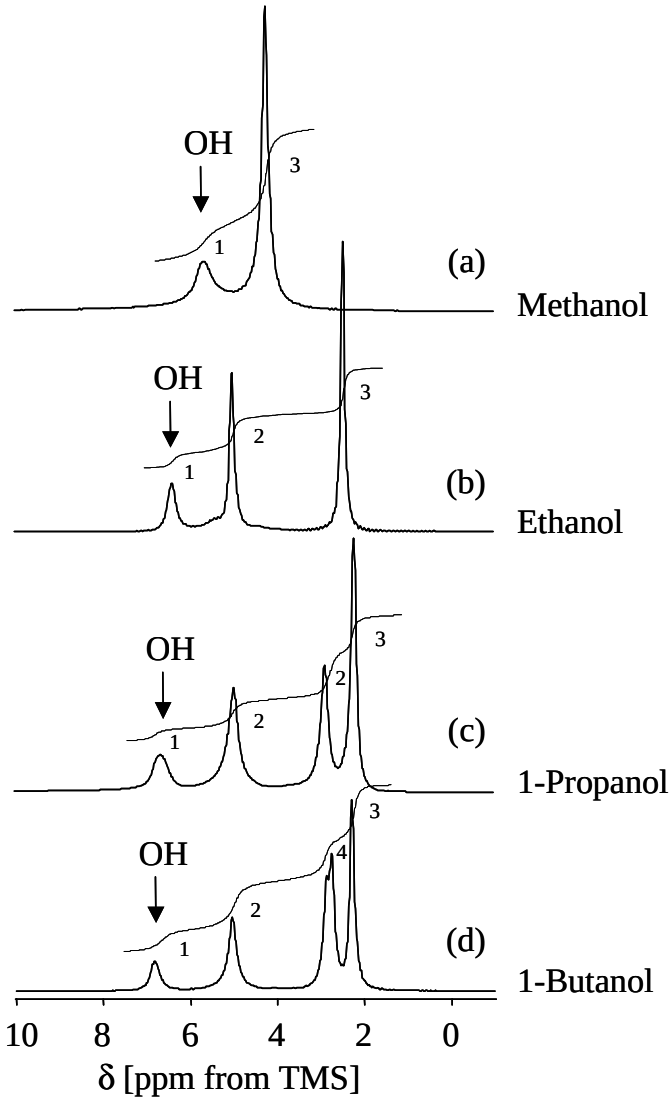

Figure 3.10 ^1H MAS NMR spectra of C_1-C_4 alcohols adsorbed on Na-X.

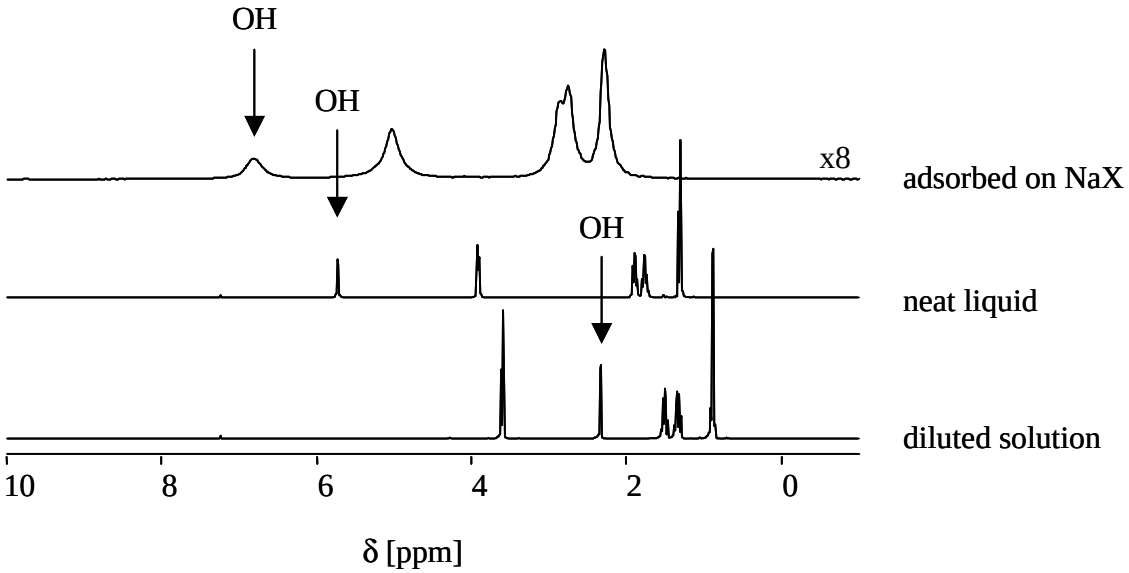

Figure 3.11. ^{1}H MAS NMR spectra of 1-butanol diluted in CCl_3D (0.312 mmol), as neat liquid, and adsorbed on Na-X.

Table 3.7 ^{1}H chemical shifts of alcohols and alcohols adsorbed on zeolites from TMS.

Sorbate/sorbent	**OH**	**-CH_2-**	**-CH_2-**	**-CH_2-**	**-CH_3**
liquid NMR					
methanol (CCl_3D)	2.01				3.44
ethanol (CCl_3D)	2.41	3.67			1.20
1-propanol (CCl_3D)	2.45	3.55	1.54		0.89
1-butanol (CCl_3D)	2.34	3.60	1.51	1.34	0.89
methanol (neat liq.)	5.68				4.09
butanol (neat liq.)	5.73	3.92	1.90	1.77	1.32
solid state NMR					
methanol on Na-X	5.66				4.24
ethanol on Na-X	6.38	5.01			2.46
1-propanol on Na-X	6.65	4.96	2.88		2.21
1-butanol on Na-X	6.82	5.04	2.87	2.76	2.30
CD_3OH on Na-Y [56]	4.7				---
CD_3OH on Na-ZSM-5 [56]	3.6				---
CH_3OH on Na-ZSM-5 [56]	~2.9 sh				4.1
CD_3OH on H-ZSM-5 [56]	9.4				4.1

3.4 Discussion

3.4.1 Solid alcohols

3.4.1.1 Torsional vibration modes

The INS spectra of solid C_1-C_4 alcohols exhibit an increasing number of bands with increasing hydrocarbon chain length. Besides a broad band in the energy region below 200 cm^{-1}, corresponding mainly to the transversal acoustic modes (TAM's), the lower longitudinal acoustic modes (LAM's), and external modes (typically observed for alkanes below 220 cm^{-1}) [58], the methyl torsion modes are also located in the low frequency region. For all alcohols, except methanol (166 cm^{-1}), the methyl torsion modes are observed between 230 and 270 cm^{-1}. Barnes et al. [52] reported a band at 264 cm^{-1} for ethanol in argon matrices at 20 K and assigned it either to the methyl torsion or to the OH out-of-plane mode of an open chain multimer. Assuming the formation of hydrogen bond interactions between the majorities of the ethanol-OH groups, we assign the band at 270 cm^{-1} to the methyl torsion vibrations. Note that for ethane, the CH_3-CH_3 torsional frequency of 275-280 cm^{-1} was reported derived from measurements of the specific heat in ethane [58].

For ethanol, the frequency of the methyl torsion modes (270 cm^{-1}) was higher compared to 1-propanol molecules (233 cm^{-1}), while for 1-butanol the frequency (254 cm^{-1}) was identical to that of the alkane methyl vibrational mode (~ 250 cm^{-1}) [58]. These frequency variations can be explained by the change in the electron withdrawing effect of the alcohol-oxygen atom on the methylene-methyl bond. For methanol, the methyl torsion vibration was found at very low frequencies (at 166 cm^{-1}) [42]. Due to the direct neighborhood of the methyl group to the oxygen atom, the methanol C^{α}-O bond is elongated leading to a simplified torsion around this bond. With increasing carbon number, the -I effect of the hydroxyl group leads to a slightly reduced distance of the C^{α}-C^{β} bond, while the C^{β}-C^{γ} bond length is again similar compared to the C-C distances of alkanes [16, 59]. This further leads to a more, i.e., less hindered methyl torsional vibration for ethanol and 1-propanol, respectively. The inductive effect decreases with the distance and is diminished for 1-butanol, as can be seen from the partial charges calculated for the electron donor molecule of a hydrogen-bonded alcohol dimer (Figure 3.12).

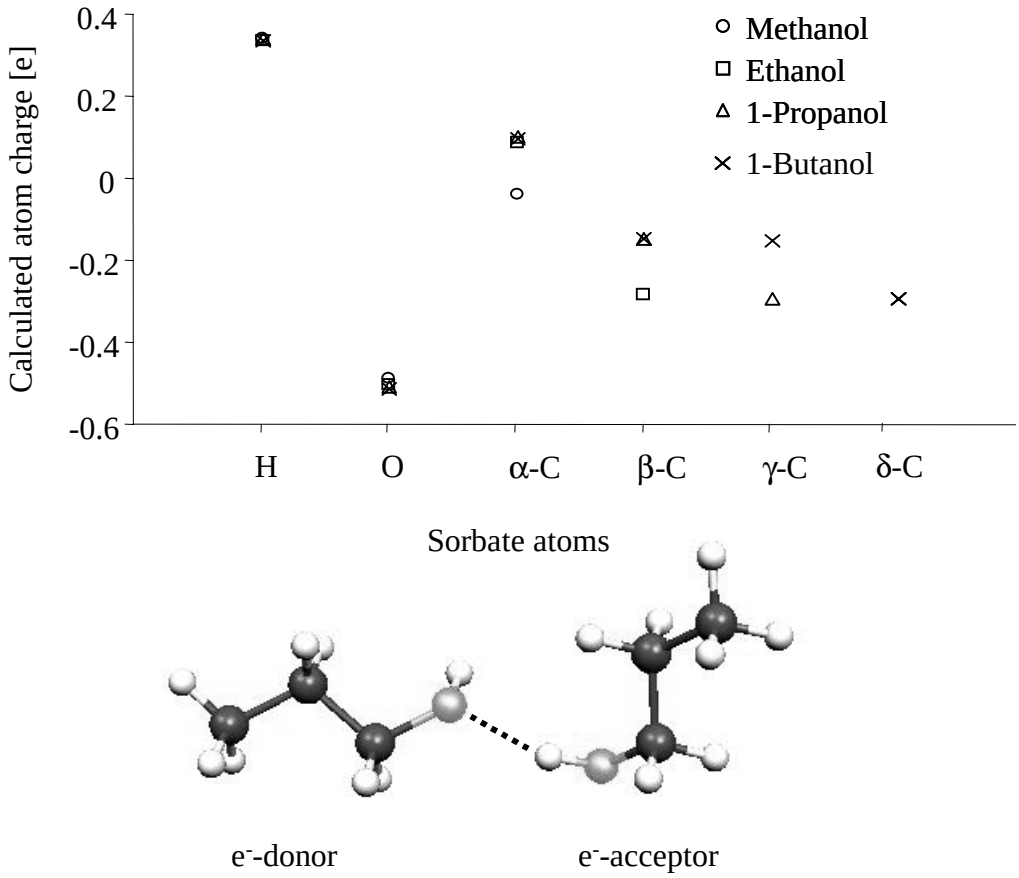

Figure 3.12 Partial charges on *n*-alcohol sorbate atoms calculated by DFT.

In addition, the difference for ethanol and 1-propanol might be also due to an enhanced intramolecular van der Waals interaction between the ethanol-CH_3 protons and the free electron pairs of the oxygen atom, both being on the same site and closer to each other than for 1-propanol. Note that the presence of the OH group in linear alcohols was found to influence mainly the α-CH_2 group being in direct neighborhood to the hydroxyl group but hardly the further carbon groups [60, 61]. For 1-alkanol molecules it was found that the CH_2 or CH_3 groups adjacent to the hydroxyl OH are significantly different with respect to their average O-C^{α} distances from their counterparts (C^{α}-C^{β} distances) in n-alkanes, whereas the properties of the other CH_2 and CH_3 groups in 1-alkanols are almost identical to those in *n*-alkanes [60]. This inductive effect of the oxygen atom on neighboring CH_n groupings was also observed for esters [62]. Therefore, most C-C torsional and other modes without a contribution of the α-CH_2 group are expected at similar positions as the alkane modes [58, 63] and the

alkane chain of the alcohol molecules is assumed to show similar types of interactions.

With increasing hydrocarbon chain length the number of torsional modes of the hydrocarbon chain increases. Generally, an alcohol molecule with a hydrocarbon chain containing *n* carbon atoms has *n-1* torsional modes. There are *n-2* modes of the C-C bonds and one mode of the C-O bond. For alkanes it was found, that the torsional frequency of the methyl groups, which is the mode with the lowest moment of inertia with respect to the torsion axis, is the energetically highest vibrational mode. All torsion modes of C-C bonds further inside the molecules occurred at lower frequencies. The band at 157 cm^{-1} is assigned to the C^{α}-C^{β} torsion mode of 1-propanol, while for propane this mode was found at 167 cm^{-1} [58]. For 1-butanol, the broad band centered at 82 cm^{-1} exhibited several shoulders, the strongest at 139 cm^{-1}, which may indicate torsional modes inside the chain.

3.4.1.2 Hydrogen bonding of functional OH groups

The absence of the $\delta(OH)_{op}$ vibrations of an unperturbed OH group, which should be located in the region 290-370 cm^{-1} for the different alcohols according to the theoretical calculations and experimental IR and Raman data [15, 32, 42, 48], in spectra of all solid alcohols indicates that all hydroxyl groups are hydrogen bonded. For solid methanol, the hydrogen bonded $\delta(OH)_{op}$ vibrations are attributed to the doublet at 650 and 760 cm^{-1} [42], while only a weak and broad band was observed for the other alcohol molecules with a maximum at 715 cm^{-1} for ethanol and 690 cm^{-1} for 1-propanol and 1-butanol.

In contrast to the doublet observed for the $\delta(OH)_{op}$ mode of the ordered structure of solid methanol crystallized in the low-temperature α-phase [19, 20], ethanol as well as the higher alcohols gave strongly broadened peaks for this mode without a defined splitting (Figure 3.1–3.4). For crystalline methanol, band splitting is obtained due to the presence of two crystallographically independent molecules in the unit cell joined by H-bonds [64, 65]. For crystalline ethanol, band splitting is conceptually expected due to the presence of four ethanol molecules consisting of two crystallographically independent molecules joined by H-bonds in the monoclinic unit cell [30]. The absence indicates that ethanol was probably present in an amorphous state or at much lower cluster size than in the crystalline form. Note, that also from a single crystal infrared

study of ethanol [66], splitting was reported with bands at 660 and 580 cm^{-1}, but the second band was broadened and of very low intensity. Splitting of several internal modes of the ordered structure of solid ethanol has been also observed, which may be indicated by the band broadening of our INS signals. Hydrogen bonded OH groups in liquid and amorphous ethanol have been attributed to the broad signals at 660 and 690 cm^{-1} [67], respectively, and in liquid 1-propanol to a band at 670 cm^{-1} [34].

3.4.1.3 Longitudinal acoustic modes (LAM's)

The in-plane deformation vibrations of the C-C-C(O) bond angles and C-C(O) bond stretching vibrations are typically summarized (described) as longitudinal acoustic modes (LAM's) [63]. These are the lowest frequency molecular vibrations involving extension of the (hydrocarbon) chain located in the energy region between 0 and 530 cm^{-1}. The number of bands observed increases as the number of CH_2 units in the hydrocarbon chain increases. For linear alcohol and alkanes with *n* carbon atoms *n-2* LAM modes are expected. When a carboxylate group was substituted for a terminal methyl group in long *n*-alkanes the LAM sequences remained remarkably similar to those of the parent chains [72]. For the short-chain alcohols investigated here, the influence of the functional OH group is still dominant. For linear propane, butane and pentane [58], LAM's were found at 267, at 180 and 425 cm^{-1}, and at 129, 386 and 450 cm^{-1}, respectively, while from band assignment of the theoretical calculations the LAM's of the alcohols with comparable chain length are located at higher frequencies, which can be attributed to the presence of oxygen atoms. For ethanol, the δ(CCO) mode is found at 430 cm^{-1} [48]. For 1-propanol, the bands at 326 and 465 cm^{-1} are assigned to δ(CCO) and δ(CCC) LAM modes, respectively. In the later mode, all CCC bond angles expand or contract in phase. The calculated frequencies of the LAM's of 1-propanol are 335 (Gg + Gt), 321 (Gg + Gt), 290 cm^{-1} (Tg) and 504 (Gg + Gt), 489 (Gg), 478 cm^{-1} (Tg) for the different conformers of the cyclic trimer cluster. The results show clearly that the frequencies depend on the molecule conformation. A normal coordinate treatment of 1-propanol leads also to modes at 336 and 458 cm^{-1} [34]. The first LAM mode was attributed to both, trans and gauche conformers, while the later was only due to the trans conformer.

In the spectrum of solid 1-butanol, 6 INS signals were assigned to LAM's (516, 453, 351, 394, 254, and 192 cm^{-1}) indicating the existence of several conformers

Table 3.8 LAM frequencies of the different 1-butanol conformers.

1-Butanol	Calculated [32]							Raman [32]		INS			
								Liquid-state 295 K	Solid-state 80 K (IR, 295 K)	Solid-state 20 K		NaX 20 K	
Assignment [a]	TTt	TTg	TGt	TGg	TGg'	GTt	GGt			TTt , TTg	TGx	TTt, TTg	TGx
δ(CCO), δ(CCC)			508	518	512		509	516	(515)		516		516
δ(CCC), δ(CCO)						488		488	470 (490)				
δ(CCO), δ(CCC)	436	439						454	445 (452)	453		449	449
δ(CCC)	399	394					392	399	403	394		394	394
δ(CCO), δ(CCC)			343	340	339	344		355			351		356
δ(CCC)			265	269	259	274	266	275	262		254		285
δ(CCC), δ(CCO)	189	186							195	192		195	195

[a] all frequencies are in cm^{-1}, δ = deformation, T, t = trans, G, g = gauche.

(Table 3.8). In comparison to the band assignment obtained by Ohno *et al.* [32], based on a detailed conformational study of 1-butanol, the bands at 192, 398, 452, 798, 898, and 948 cm^{-1} can be attributed to the TTt and/or the TTg conformer, while the bands at 254, 352, 518, 826, 842, and 966 cm^{-1} are due to the TGx conformers, where x indicates t, g or g' conformation about the C-O axis. The first three signals of each series are LAM's, while the later ones are mainly assigned to rocking vibrations. In the solid state of 1-propanol, TTt and/or TTg forms were found to exist, while in the glassy-state and liquid-state also the TGx form was found on the basis of the calculated results [32]. Thus, we may conclude that under the conditions the studied solid 1-butanol is present in an amorphous phase, while for 1-propanol the band at 485 cm^{-1} may indicate an additional LAM frequency and with this also the presence the Gg conformer. In addition, the absence of the splitting of the δ(COH) mode tentatively points to the formation of an amorphous solid state for all C_2-C_4 alcohols [42] formed under the conditions studied. Note that the band at 485 cm^{-1} may also be assigned to the first overtone mode of the methyl torsion vibration at 233 cm^{-1}.

3.4.2 Alcohols adsorbed on Na-X

3.4.2.1 OH stretching and deformation vibrational modes

All hydroxyl groups of the investigated alcohols, adsorbed on Na-X, appear to be hydrogen-bonded as indicated by the absence of the $\delta(OH)_{op}$ mode of freely vibrating OH groups in the INS spectra, which is similar to the INS of the solid alcohols. The weak and broad feature, observed in all INS of the adsorbed alcohols between 570 and 750 cm^{-1}, can be assigned to the hydrogen-bonded $\delta(OH)_{op}$ mode. With increasing chain length, the band maximum is slightly shifted to lower frequencies (675 cm^{-1} for ethanol and 640 cm^{-1} for 1-propanol and 1-butanol), but it appears to be very weak next to the hydrocarbon modes. Note that also in the solid materials, this band was broadened and of low intensity for the C_2-C_4 alcohols, which is attributed to an amorphous state or polycrystalline (very small crystal sizes) state compared to the crystalline phase found for methanol as discussed above. This leads to the conclusion that self-association of the C_2-C_4 alcohols in the faujasite cage forming crystalline clusters does not take place and that the hydrogen-bond strength is lower than in the solid. Due to the broadening, it is also possible that more than one alcohol adsorption structure exists.

In the infrared spectra (Figure 3.8), the stretching mode of the alcohol OH groups is very intense and clearly separable from the stretching vibrations of the CH groups. Compared to the vibration mode in the gas phase the ν(OH) stretching mode was strongly broadened and shifted to lower wavenumbers confirming the hydrogen bond formation already proposed from the INS data. Identical to the adsorption of methanol [42], a shoulder at higher frequencies was observed for the C_2-C_4 alcohols indicating the formation of at least two sorption structures.

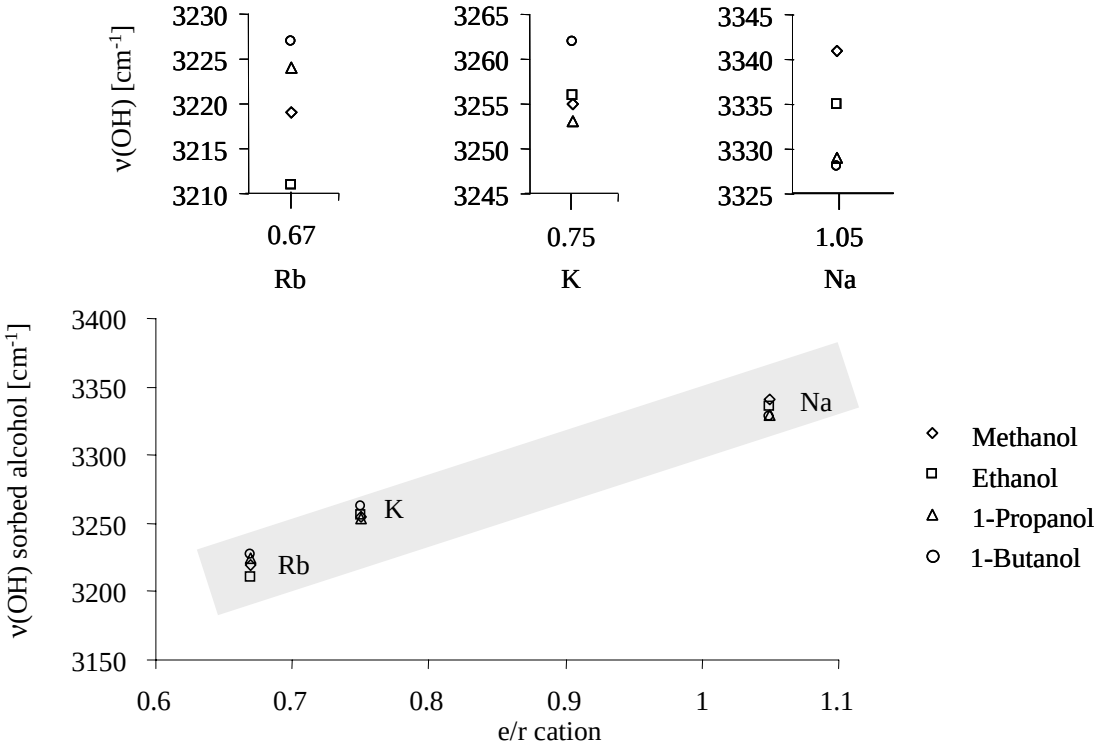

Figure 3.13. Change of the absorption maximum of the ν(OH) of the sorbed alcohol (T_{ads} = 308 K; $p_{ROH} = 1 \cdot 10^{-3}$ mbar) as a function of the electronegativity of the cation [e/r].

In Figure 3.13 the ν(OH) frequency values of the various alcohols, adsorbed on Na^+, K^+ and Rb^+ exchanged X zeolites, are shown in relation to the electronegativity of the counter cation. The frequency shift of the ν(OH) stretching mode showed a strong dependence on the basicity of the zeolite and only a subtle dependence on the chain length of the alcohol molecules. With increasing framework polarity (from Na-X to Rb-X) enhanced hydrogen bonding between the sorbates and the zeolite oxygen atoms is observed, which is reflected by the decreasing ν(OH) frequency. The

OH stretching vibration signal showed the highest frequency value for alcohols adsorbed on the least basic sample Na-X (~ 3350 cm^{-1}) and decreased to lower wavenumbers for the more basic K-X (3270 cm^{-1}) and Rb-X (~ 3250 cm^{-1}) samples.

By exchanging counter cations of lower Lewis acidity into the zeolite structure, e.g., Rb^+, a higher negative charge is located on the zeolite oxygen atom [42], thus stronger basic materials are obtained. For alkali cation exchanged ZSM-5 materials, having a relatively apolar zeolite framework, the extent of the downward shift of the OH group was found to decrease proportionally with increasing radius of the counter cation indicating the dominating interaction between the alkali cation and the oxygen atom of the alcohol [73]. Note that the direct interaction between the lone-pair electron donor function of methanol *via* the oxygen atom of the hydroxyl group and the electron pair acceptor function of the zeolite (the alkali metal cation) was identified by DFT results also for aluminum rich zeolites as the most important energetic contribution to sorption for all samples investigated [74].

For C_1-C_4 alcohols adsorbed on Na-X, the perturbation of the alcohol-OH group increased, though only slightly with increasing hydrocarbon chain length. This increase in the shift may be explained by the larger positive inductive effect (+I) of CH_2R groups ($R \neq H$), in comparison to the electron withdrawing methyl group and thus a slightly enhanced hydrogen bond formation of the alcohol-OH proton. Already for 1-propanol and 1-butanol, similar frequencies were observed, which is typical for the markedly decaying inductive effect [59]. The alcohol oxygen atom receives increasing electron density with increasing *n*-alkyl chain length, but the influence of each added carbon atom diminishes with spatial separation of the carbon atom to the hydroxyl group. Note that for K-X and Rb-X, the ν(OH) shift of adsorbed alcohol first decreases, but then increases again with increasing alcohol chain length. These higher ν(OH) frequency values obtained for 1-butanol, adsorbed on K-X, and 1-propanol and 1-butanol, adsorbed on Rb-X, can be attributed to an increasing steric hindrance with the sorbate molecule size. But, also an increasing hydrogen-bond formation of the CH-groups to the stronger polar framework probably may influence the inductive effect of the hydrocarbon chain and decrease the electron density on the alcohol-O atom, thus strengthen the alcohol-OH bond.

The low resolution of the INS signals makes it difficult to assign frequencies for the $\delta(OH)_{ip}$ deformation bending vibration bands of the alcohol hydroxyl groups,

which are additionally strongly broadened and overlapped by the $\delta(CH)_{ip}$ bending modes of the alcohol methyl and methylene groups. From the calculation, also a combination of the $\delta(OH)$ bending mode with the $\varpi(CH_2)$ band is found, thus the decrease of the modes at 1423 sh, 1418, 1410, and 1410 cm^{-1} cannot related to a decreasing hydrogen bonding strength of the alcohol OH group. However, the $\delta(OH)_{ip}$ vibrations are still found at higher wavenumbers for all adsorbed alcohols as compared to the monomers (e.g. for ethanol in the gas phase 1241 cm^{-1} [75]) supporting hydrogen bonding of the alcohol hydroxyl groups. Evidence of alcohol decomposition into surface methoxy groups or formates, indicated by bands at 1635 and 1610 cm^{-1} was not observed under the adsorption conditions used.

3.4.2.2 CH vibrational modes

The INS spectra of adsorbed alcohol molecules exhibit a typical vibrational CH band structure as found for the solid phase. Most bands are broadened indicating a lack of long-range order and multiple states of alcohols adsorbed on the zeolite possibly arising form a low sorbate density. This might enable high flexibility of the alkane chains in the supercage. But, an interaction of the molecules *via* hydrogen bonding of the hydrocarbon chain to the zeolite oxygen atom or other sorbate molecules is also conceivable.

For ethanol adsorbed on Na-X the methyl torsion mode (276 cm^{-1}) and the LAM (436 cm^{-1}) are shifted to higher wavenumbers, while the torsional mode of adsorbed 1-propanol was found at slightly lower frequencies (224 cm^{-1}) compared to their solid counterparts (233 cm^{-1}). Due to the coordination of the alcohol oxygen atom to the counter cation the electron density decreases and the electron withdrawing effect (-I effect) of the alcohol-OH group on the alkane chain increases leading further to an enhanced contraction and elongation of the C^{α}-C^{β} and C^{β}-C^{γ} bonds, respectively, as already seen for the solid materials and is in line with a more hindered torsional vibration for adsorbed ethanol and a less hindered one for 1-propanol. For 1-propanol adsorbed on Cs-X, the torsion vibration (232 cm^{-1}) was found at a similar value as for the solid alcohol. This can be explained by the coordination of the alcohol oxygen atom to the Cs^{+} counter cation, which is of lower strength than on Na-X due to the lower Lewis acidity of the Cs^{+} cation. The electron density of the alcohol oxygen

atom, and hence the inductive effect of the alcohol-OH group, will not change significantly, leading to an unchanged methyl torsion about the C^{β}-C^{γ} bond.

For the ν(CH) stretching vibration bands, a similar trend, as already described for the ν(OH) stretching vibration, was observed in the infrared spectra. In agreement to the results obtained form Rep *et al.* [14], the bands of adsorbed methanol, assigned to the asymmetric and symmetric ν(CH_3) stretching modes, were found to be broadened and shifted to lower frequency values compared to the gas phase spectrum (2989 cm^{-1} [75]) and explained by a multitude of states due to hydrogen bond formation between the methyl group and the negatively charged zeolite oxygen atom. Similar to methanol adsorption, the symmetric and asymmetric ν(CH_3) stretching vibration bands of adsorbed ethanol exhibit a shift to lower wavenumbers relative to the gaseous alcohol, too. The shift is smaller compared to that with methanol, but also related to hydrogen bond formation. Note that with increasing chain length the signal of the methylene groups increases in intensity and overlaps with the asymmetric ν(CH_3) signal. Thus, assuming that the inductive effect of the alcohol-O atom mainly influences the α-CH_2 group, the methyl stretching vibration is expected at similar frequencies for 1-propanol and 1-butanol as found for ethanol (minor differences may be due to the inductive effect of the hydrocarbon chain as found by INS), while the shift of the band maximum at 2970 cm^{-1} (for ethanol) to 2958 and 2955 cm^{-1} (for 1-propanol and 1-butanol, respectively) is attributed to the increasing contribution of the ν(CH_2) vibration to the band intensity. The increased frequency value of the band assigned to the $\nu_{as}(CH_2)$ vibration of adsorbed ethanol (shoulder at 2955 cm^{-1}) compared to the gas phase value (2948 cm^{-1}) is explained by a decrease in the electron density of the alkyl group due to the coordination of the ethanol-oxygen atom to the cation, which further leads to an increase in the C-H stretching frequency [76]. It may also indicate, that the methylene group is not hydrogen bonded to the framework. From a 1-propanol adsorption complex on non-polar Na-ZSM-5 (Figure 3.14), the interactions between the lattice oxygen and hydrocarbon chain can be assumed to be minimal as compared to the aluminum rich X zeolites. The asymmetric ν(CH_3) vibration band at 2967 cm^{-1} is located at the same value as found for liquid 1-propanol [77], while the symmetric ν(CH_2) is located at higher frequencies (at 2882 cm^{-1} as compared to 2975 cm^{-1}). This shift of the symmetric stretching vibration

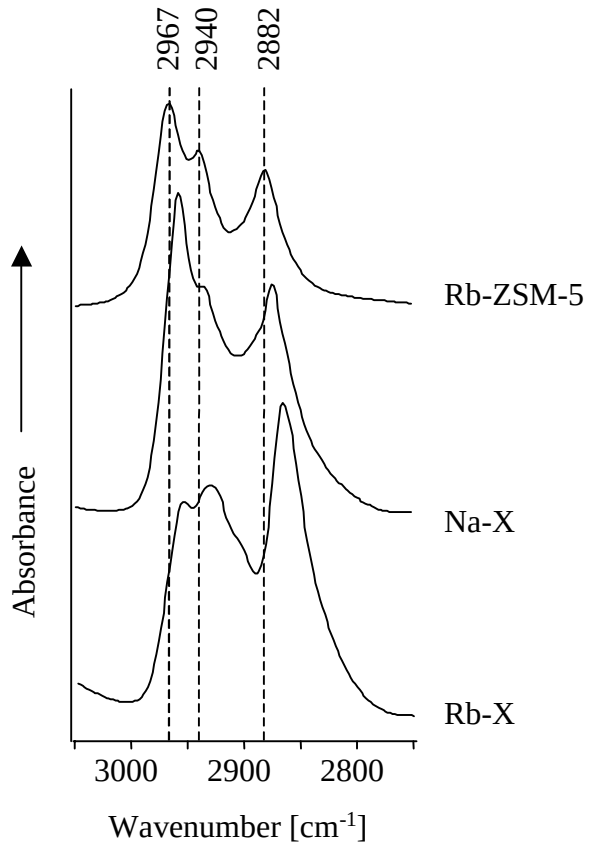

Figure 3.14 Difference infrared spectra of 1-propanol adsorbed on Rb-ZSM-5, Na-X, and Rb-X (T = 308 K, $p = 1 \cdot 10^{-3}$ mbar) in the range 3050-2750 cm^{-1} of ν(CH) stretching vibration bands.

is attributed again to minor strengthening of the C-H bonds in response to the elongation of the C-O bond as a result of the interactions of the sorbate molecule with the metal cation [78]. After adsorption of 1-propanol on Na-X, the symmetric $\nu(CH_2)$ band is shifted in opposite direction to 2875 cm^{-1} indicating lateral interaction of the hydrocarbon chain either to the pore wall or between adsorbed molecules as in the liquid state. With changing the counter cation Na^+ to Cs^+, thus increasing the framework polarity, the ν(CH) bands are further shifted and strengthened hydrogen bonding of the CH groups to the pore wall can be concluded.

The presence of two symmetric $\nu(CH_2)$ stretching bands at 2904 and 2880 cm^{-1} for ethanol and 2899 and 2870 cm^{-1} for 1-butanol may again suggest the presence of different types of adsorption structures. The weak band at 3740 cm^{-1} appears to be caused by weakly adsorbed sorbate molecules, since it is not present after evacuation of the sample at room temperature.

3.4.3 Strength and mode of interaction of the alcohols

The resonance of protons of the $^{\alpha}CH$ group of alcohols adsorbed on Na-X is higher than compared to alcohols highly diluted in CCl_3D, where hydrogen bonding interactions are weakened or not present (Table 3.7). This shift indicates a stronger deshielding of the protons of adsorbed alcohols, thus a lower electron density on the alcohol-O atom. Latter leads to an increased inductive effect (-I) on the neighboring CH_2 group and is related to the coordination of the alcohol molecules via their oxygen atom to the counter cation Na^+. Similarly the CH_3 resonance was also downfield shifted to 4.1 ppm, when methanol was adsorbed on H-ZSM-5 [57] forming strong hydrogen bonds to the Brønsted acidic OH groups, or on zeolite Na-ZSM-5 [56] interacting to the unsaturated sodium cations via the methanol oxygens.

The hydroxyl resonance observed for methanol adsorbed on aluminum rich Na-X (Si/Al = 1.2) was found at much higher values (5.7 ppm) than for diluted methanol (1.5 ppm) (Figure 3.11). The observed downfield shift of the OH resonance in the sequence alcohol/CCl_3D → neat alcohol → alcohol adsorbed on Na-X indicates increasing hydrogen bonding interactions of the protons. Hydrogen bonding is known to cause quite large downfield chemical shifts in alcohols as the protons are deshielded as a result of electrostatic polarization of the OH bond. ^1H NMR spectra for methanol in CCl_3D, where hardly any hydrogen bonding is present between the OH-groups [57], showed signals at 2.01 ppm assigned to the methanol-OH protons. In neat liquid methanol, hydrogen bonding between the OH-groups induced a downfield shift of the OH-proton resonance to 4.6 ppm. The deshielding of the alcohol-OH proton adsorbed on Na-X (5.7 ppm) indicates the formation of relatively strong hydrogen bonds between the alcohol OH-groups and the pore wall. Note, that the deshielding of the OH-proton is more enhanced on Na-X than on Na-ZSM-5 (Si/Al = 30; shoulder at 2.9 ppm [56]) and on Na-Y (4.7 ppm; Si/Al = 2.5). Methanol molecules adsorbed on Na-ZSM-5 do not form hydrogen bonds to the relatively apolar zeolite framework. The downfield shift of the OH resonance relative to methanol in CCl_3D can be related to the coordination of the O-atom to Na^+. The adsorption of methanol on Na-X, however, leads to stronger proton deshielding and is attributed to hydrogen bond formation to the polar faujasite framework. The chemical shift of methanol adsorbed on Na-X is even more enhanced than upon adsorption on Na-Y. The shift is related to a higher site density on Na-X and attributed to additional

sorbate-sorbate interactions. The largest shift has been reported for methanol adsorbed on H-ZSM-5, forming strong hydrogen bonds of the alcohol O to the zeolitic Brønsted acid-OH groups. Note, that besides a compositional effect, structural effects may be also present.

A steady increase of the chemical shift of the OH resonance of adsorbed alcohols towards higher frequencies indicates an increasing deshielding of the alcohol OH protons with increasing chain length. However, the chemical shifts observed for the protons at the C^{α}-atom are nearly the same for ethanol, 1-propanol and 1-butanol (~ 5.0 ppm) indicating very similar electron density on the α-C atom of the alcohols. Thus, the increase of the OH resonances observed can be attributed to a stronger deshielding of the OH proton by hydrogen bonding interaction. It may be assumed that with increasing size of the alkyl chain, the orientation of the sorbate at the active site slightly changes optimizing the interactions between the sorbate, Na^+, the zeolite-O atoms, and the neighboring alcohol, finally leading to stronger hydrogen bonds.

The CH_2/CH_3 resonances of all alcohols were located at higher fields with rising distance from the oxygen atom. This is in line with the decrease of the inductive effect of the electronegative oxygen atom on the CH groups and was also seen for the alcohols in CCl_3D. However, in ROH/Na-X the resonances were still downfield shifted, which cannot be related, except for the $^{\alpha}$CH-protons, to the coordination of the alcohol to Na^+. The CH_2 protons resonate at a similar chemical shift indicating comparable interactions of the hydrocarbon chain independent of the chain length. The higher chemical shift observed as compared to unperturbed alcohols (dissolved in CCl_3D) was constant and about 1.3-1.4 ppm. This indicates a comparable deshielding of all CH_2 protons and suggests hydrogen bond formation of the alkyl protons to the zeolite framework. The thermal desorption of C_1-C_4 alcohols adsorbed on K-X zeolites (Figure 3.9) shows, that the temperature of the desorption-maximum increased linearly with increasing chain length (for C_1 to C_4 *n*-alcohols adsorbed on K-X temperature increase from 433 to 533 K). A comparable increase of the heat of adsorption with the number of carbon atoms in the sorbate molecules was reported for C_1-C_4 *n*-alcohols, as also for ethers and alkanes adsorbed on Na-X [79]. These effects are attributed to an increasing contribution of nonspecific interactions, mainly, lateral interactions between the hydrocarbon chain of sorbed molecules and the zeolite pore wall and/or sorbate-sorbate interactions. This is also supported by our infrared studies

showing that the ν(OH) shift of the alcohol-OH group adsorbed on a given zeolite X is only little influenced by the chain length.

Based on the ν(OH) frequency shift obtained by IR spectroscopy the presence of two adsorption structures was suggested [42]. Therefore it must be assumed that the structures exchange relatively fast on the timescale of the NMR experiment. Note that the signals are broadened and asymmetric. Considering the asymmetric shape of the CH_3 signal at 4.2 ppm of methanol adsorbed on Na-X, a small amount of physisorbed methanol or water, giving rise to peaks at 4.6 ppm [57] and 4.8 ppm (broad) [85], respectively, cannot be completely ruled out.

3.4.4 Adsorption structures

From the results discussed above, similar sorption structures for short chain alcohols are assumed. The proposed structure for 1-propanol is shown in Figure 3.15a. At the low sorbate loading used in this study, a maximum ratio of one sorbate molecule per cation located in the supercage is assumed. Thus sorbate clustering at a single cation is excluded. 1-Propanol and all other alcohols studied are molecularly sorbed and interact with the counter cations *via* electron donation from the oxygen atom in the alcohol to the alkali metal cation. This mode of adsorption corresponds to the alcohol acting as a base and contributes most to the binding energy. Latter depends on the Lewis acidity of the counter cation. The downward shift of the ν(OH) stretching vibration frequency with decreasing Lewis acidity of the counter cation suggests that another type of interaction is simultaneously present that follows the opposite trend to the coordination of the alcohol to the cation. This interaction is attributed to hydrogen bond formation of the alcohol-OH proton and the negatively charged zeolite oxygen atoms and becomes stronger with increasing framework polarity. The asymmetric shape of the ν(OH) stretching bands, as well as the broadened $\delta(OH)_{op}$ bands, suggest a further adsorption structure with a hydrogen bond interaction between sorbate molecules adsorbed at neighboring cations possibly leading to ring-like sorbate clusters in the faujasite cage (Figure 3.15b).

The types of interaction are largely independent of the chain length as the frequency shifts in the infrared spectra and the chemical shifts of the OH-resonances of adsorbed C_1-C_4 alcohols show only marginal differences for a given zeolite. The differences observed may be attributed to an optimization of the sorption structure

with increasing steric hindrance of the larger alcohols leading to slightly enhanced hydrogen bond strength. The increasing inductive effect (+I) of the hydrocarbon chain on the OH-group may also contribute. Hydrogen bond formation between the sorbate hydrocarbon chain and the polar zeolite framework suggests that the hydrocarbon chain of light alcohols is in close contact to the zeolite wall at low loadings. With increasing alcohol concentration in the faujasite cage, enhanced van der Waals interactions between the hydrocarbon chains could be imagined by formation of micelle-like structures.

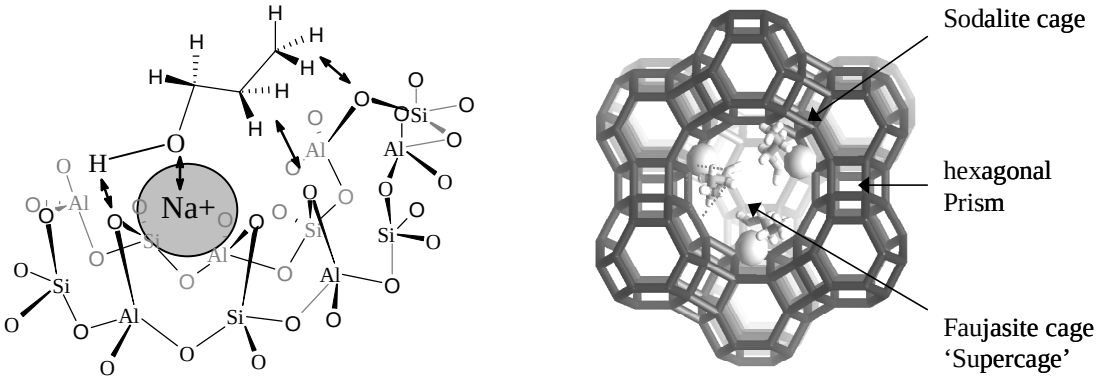

Figure 3.15 Schematic adsorption structure of 1-propanol adsorbed at SIII on Na-X; (a) single molecule, (b) ring-like structure in supercage window.

3.5 Conclusion

The hydroxyl groups of the alcohol molecules are completely hydrogen bonded in the solid materials as well as in the adsorbed state. During rapid cooling to below 20 K, the solid C_1 to C_4 alcohol molecules formed either an amorphous phase or crystals of very small size.

Similar sorption complexes exist for all C_1 to C_4 *n*-alcohols on the alkali metal exchanged zeolites X. Strong specific and less strong non-specific interactions in the monomeric complexes of the alcohol molecules with the cations and the zeolite framework have been detected. For the alkali metal cation exchanged zeolites, the linear alcohols interact primarily *via* the lone electron pair of the alcohol oxygen with the cation of the zeolite. Additionally, interaction *via* the hydrogen atoms of the OH

groups with the lattice oxygens of the zeolite exists. A second adsorption complex is formed that includes strong hydrogen-bond formation to neighbouring adsorbed alcohol molecules. The formation of H-bonds between the zeolite oxygen atom and the sorbate hydroxyl- and methyl-groups depend on the framework polarity and is largest for Rb-X, the material showing the highest negative charge on the zeolite oxygen atom, while the strength of adsorption is dominated by the properties of the counter cation.

3.6 Acknowledgements

The authors would like to thank the Deutsche Forschungsgemeinschaft (DFG) within the Sonderforschungsbereich SFB 338: Adsorption an Festkörperoberflächen: Mikroskopische Analyse von Zuständen und Prozessen Teilprojekt B9.

In particular we thank the ISIS, Rutherford Appleton Laboratory, U.K., for kindly granted measuring time to record the INS spectra.

3.7 References

[1] Tanabe, K. *Appl. Catal.* **1994**, 113, 147.

[2] Tanabe, K.; Hölderich, W.F. *Appl. Catal. A: General* **1999**, 181, 399.

[3] Barthomeuf, D. *J. Phys. Chem.* **1984**, 88, 42.

[4] Rossi, F.P.; Busca, G.; Lorenzelli, V.; Lion, M.; Lavalley, J.C. *J. Catal* **1988**, 109, 378.

[5] Huang, M.; Kaliguine, S.; Muscas, M.; Aurous, A. *J. Catal.* **1995**, 157, 266.

[6] Huang, M.; Adnot, A.; Kaliaguine, S. *J. Catal.* **1992**, 137, 322.

[7] Barthomeuf, D. *Catal. Rev.* **1996**, 38, 521.

[8] Ono, Y. Stud. *Surf. Sci. Catal*. **1980**, 5, 19.

[9] Yashima, T.; Sato, K.; Hara, N. *J. Catal*. **1972**, 26, 303.

[10] Yashima, T.; Suzuki, H.; Hara, N. J. Catal. **1974**, 33, 486.

[11] Sidorenko, Y.N.; Galich, P.N.; Gutyrya, V.S.; Ilin, Neimark, Y.G. I.E. *Dokl. Akad. Nauk. SSSR* **1967**, 173, 132.

[12] Yashima, T.; Sato, K.; Hara, N. *J. Catal*. **1972**, 26, 303.

[13] Sidorenko, Y.N.; Galich, P.N.; Gutyrya, V.S.; Ilin, Y.G.; Neimark, I.E. *Dokl. Akad. Nauk. SSSR* **1967**, 173, 132.

[14] Rep, M.; Palomares, A.E.; Eder-Mirth, G.; van Ommen, J.G.; Rösch, N.; Lercher, J.A. *J. Phys. Chem. B* **2000**, 104, 8624.

[15] Matsumura, Y.; Hashimoto, K.; Yoshida, S. *J. Catal*. **1989**, 117, 135.

[16] Bonzalez, D.; Cerdeirina, C.A.; Rmani, L.; Carballo, E. *J. Phys. Chem. B* **2000**, 102, 11275.

[17] Kay, B.D.; Castleman, A.W. *J. Phys. Chem*. **1985**, 89, 4867.

[18] Provencal, R. A.; Paul, J. B.; Roth, K.; Chapo, C.; Casaes, R. N.; Saykally, R. J.; Tschumper, G. S.; Schaefer, H. F. *J. Chem. Phys*. **1999**, 110, 4258.

[19] Torrie, H.B.; Weng, S.X. *Molec. Phys*. **1989**, 67, 575.

[20] Parkes, G.S. *J. Am. Chem. Soc*. **1925**, 47, 338.

[21] Wertz, D.L.; Kruh, R.K. *J. Chem. Phys*. **1967**, 47, 388.

[22] Narten, A.H.; Habenschuss, A. *J. Chem. Phys*. **1984**, 80, 3387.

[23] Montague, D.G. ; Gibson, I.P.; Dore, J.C. *Mol. Phys*. **1982**, 47, 1405.

[24] Michielsen-Effinger, J. *J. Mol. Spectrosc*. **1969**, 29, 489.

[25] Takano, M.; Sasada, Y.; Satoh, T. *J. Mol. Spectrosc*. **1968**, 26, 157.

[26] Kakar, P. K.; Quade, C.R. *J. Chem. Phys*. **1980**, 72, 4300.

[27] Pulay, P. *Modern Theoretical Chemistry*, H.F. Schaefer III, Ed.; Plenum; New York, **1977**; 153.

[28] Dothe, H.; Lowe, M.A.; Alper, J.S. *J. Phys. Chem*. **1989**, 93, 6632.

[29] Shaw, R.A.; Wieser, H.; Dutler, R.; Rauk, A. *J. Am. Chem. Soc*. **1990**, 112, 5401.

[30] Joensson, P.G. *Acta Crystallogr. Sect. B* **1976**, 32, 232.

[31] Abdurakhmanov, A.A.; Rahimova, R.A.; Imanov, L.M. *Phys. Lett. A* **1970**, 32, 123.

[32] Ohno, K.; Yoshida, H.; Watanabe, H.; Fujita, T.; Matsuura, H. *J. Phys. Chem*. **1994**, 98, 6924.

[33] Houk, K.N.; Eksterowicz, J.E.; Wu, Y.-D.; Fuglesang, C.D.; Mitchell, D.B. *J. Am. Chem. Soc*. **1993**, 115, 4170.

[34] Fukushima, K.; Zwolinski, B.J. *J. Mol. Spectrosc*. **1968**, 26, 368 and references there in.

[35] Crowder, G.A.; Townsend, M. J. *J. Mol. Struct*. **1977**, 42, 27.

[36] Hudson, B. S. *J. Phys. Chem. A* **2001**, 105, 3949.

[37] Fletcher, A.N. *J. Phys. Chem*. **1972**, 76, 2562.

[38] Ibbilson, D.A.; Moore, L.F. *J. Chem. Soc. B* **1967**, 76.

[39] Ibbilson, D.A.; Moore, L.F. *J. Chem. Soc. B* **1967**, 80.

[40] Fletcher, A.N.; Heller, C.A. *J. Phys. Chem*. **1967**, 71, 3742.

[41] www.isis.rl.ac.uk.

[42] Schenkel, R.; Jentys, A.; Lercher, J.A.; Parker, S. F. submitted to *J. Phys. Chem.* **2004**

[43] Frisch, M. J.; Trucks, G. W.; Schlegel, H. B.; Scuseria, G. E.; Robb, M. A.; Cheeseman, J. R.; Zakrzewski, V. G.; Montgomery, J. A. Jr.; Stratmann, R. E.; Burant, J. C.; Dapprich, S.; Millam, J. M.;

Daniels, A. D.; Kudin, K. N.; Strain, M. C.; Farkas, O.; Tomasi, J.; Barone, V.; Cossi, M.; Cammi, R.; Mennucci, B.; Pomelli, C.; Adamo, C.; Clifford, S.; Ochterski, J.; Petersson, G. A.; Ayala, P. Y.; Cui, Q.;
Morokuma, K.; Malick, D. K.; Rabuck, A. D.; Raghavachari, K.; Foresman, J. B.; Cioslowski, J.; Ortiz, J. V.; Baboul, A. G.; Stefanov, B. B.; Liu, G.; Liashenko, A.; Piskorz, P.; Komaromi, I.; Gomperts, R.; Martin, R. L.; Fox, D. J.; Keith, T.; Al-Laham, M. A.; Peng, C. Y.; Nanayakkara, A.; Challacombe, M.; Gill, P. M. W.; Johnson, B.; Chen, W.; Wong, M. W.; Andres, J. L.; Gonzalez, C.; Head-Gordon, M.; Replogle, E. S.; Pople, J. A. *Gaussian*, Inc., Pittsburgh PA, **1998**.

[44] Champion, D. J.; Tomkinson, J.; Kearley, G.J. *Appl. Phys. A-Mater.* **2002**, 74, S1302.

[45] Falk, M.; Whalley, E. *J. Chem. Phys.* **1961**, 34, 1554.

[46] Jobic, H. *Spectrochimca Acta* **1992**, 48A, 293.

[47] Perchard, J.-P.; Josein, M.-L. *J. Chim, Phys. Chim. Biol*. **1969**, 65, 1834.

[48] Perchard, J.-P.; Josein, M.-L. *J. Chim, Phys. Chim. Biol.* **1969**, 65, 1856.

[49] Eng, J.; Raghavachari, K.; Struck, L.M.; Chabal, Y.J.; Bent, B.E.; Flynn, G.W.; Christman, S.B.; Chaban, Ed E.; Williams, G.P.; Radermacher, K.; Mantl, S. *J. Chem. Phys*. **1997**, 106, 9889.

[50] Gonzalez, L.; Mo, O.; Yanez, M. *J. Chem. Phys*. **1999**, 111, 3855.

[51] George, W.O.; Has, T.; Hossain, Md. F.; Jones, B.F.; Lewis, R. *J. Chem. Soc., Faraday Trans*. **1998**, 94, 2701.

[52] Barnes, J.; Hallam, H.E. *J. Am. Chem. Soc., Faraday Trans*. **1970**, 66, 1920.

[53] Sakar, S.; Joarder, R.N. *J. Chem. Phys*. **1994**, 100, 5118.

[54] Radom, L.; Hehre, W.; Pople, J.A. *J. Amer. Chem. Soc*. **1971**, 93, 289.

[55] Yin, P.K.L.; Rao, K.N. *J. Mol. Spectrosc.Notes* **1968**, 489.

[56] Anderson, M.W; Barrie, P.J.; Klinowski, J. *J. Phys. Chem*. **1991**, 95, 235.

[57] Mirth, G.; Lercher, J.A.; Anderson, M.W.; Klinowski, J. *J. Chem. Soc. Faraday Trans*. **1990**, 86, 3039.

[58] Nelligan, W.B.; LePoir, D. J.; Brun, T.O.; Kleb; R. *J. Chem. Phys*. **1987**, 87, 2447.

[59] Levitt, L.S.; Widing, H.F. *Prog. Phys. Org. Chem*. **1976**, 12, 119.

[60] Nitta, T.; Turek, E.A.; Greenkorn, R.A.; Chao, K.C. *AIChE J* **1977**, 23, 144.

[61] Gonzalez, D.; Cerdeirina, A.A.; Romani, L.; Carballo, E. *J. Phys. Chem. B* **2000**, 104, 11275.

[62] Carboll, E.; Mosquera, R.A.; Legido, J.L.; Romani, L. *J. Chem. Soc., Faraday Trans*. **1997**, 93, 3437.

[63] Braden, D.A; Parker, S.F.; Tomkinson, J.; Hudson, B.S. *J. Chem. Phys*. **1999**, 111, 429.

[64] Weng, S.X.; Anderson, A. *Phys. Stat. Sol. (b)* **1992**, 172, 545.

[65] Anderson, A; Andrews, B.; Meiering, E.M.; Torrie, B.H. *J. Raman Spec*. **1988**, 19, 85.

[66] Mikawa, Y.; Brasch, J.W.; Jakobsen, R.J. *Spectrochim. Acta* **1997**, 27, A 529.

[67] Stuart, A.V.; Sutherland, G.B.B.M. *J. Chem. Phys*. **1956**, 24, 559.

[68] Weng, S.X.; Anderson, A. *Phys. Stat. Sol. (b)* **1992**, 172, 545.

[69] Anderson, A; Andrews, B.; Meiering, E.M.; Torrie, B.H. *J. Raman Spec*. **1988**, 19, 85.

[70] Mikawa, Y.; Brasch, J.W.; Jakobsen, R.J. *Spectrochim. Acta* **1997**, 27, A 529.

[71] Stuart, A.V.; Sutherland, G.B.B.M. *J. Chem. Phys*. **1956**, 24, 559.

[72] Vogel-Weill, C.; Corset, J. *Spectrochim. Acta* **1995**, A 51, 2357.

[73] Eder-Mirth, G.; Lercher, J.A. *Recl. Trav. Chim. Pays-Bas* **1996**, 115, 157.

[74] Vayssilov, G.; Lercher, J.A.; Rösch, N. *J. Phys. Chem. B* **2000**, 104, 8614.

[75] Fubini, B.; Bolis, V.; Cavenago, A.; Garrone, E.; Ugliengo, P. *Langmuir* **1993**, 9, 2712.

[76] Chung, J.S.; Bennett, C.O. *J. Catal*. **1985**, 92, 173.

[77] Max, J.-J.; Daneault, S.; Chapados, C. *Can. J. Chem.* **2002**, 80, 113.

[78] Gutmann, V. *The Donor Acceptor Approach to Molecular Interactions*; Plenum Press: New York, **1978**.

[79] Dubinin, M.M; Isirikyan, A.A.; Regent, N.I. *Izv. Akad. Nauk. SSSR, Ser. Khim.* **1976**, 2, 288.

[80] Barrer, R.M.; Davies, J.A. *Proc. R. Soc. London, Ser. A* **1971**, 322, 1.

[81] Derouane, E.G.; Andre, J.A.; Lucas, A.A. *J. Catal.* **1988**, 110, 58.

[82] Avgul, N.N.; Bezus, A.G.; Dzhigit, O.M. *Adv. Chem. Ser.* **1971**, 101, 184.

[83] Dzhigit, O.M.; Karpinsky, K.; Kiselev, A.V.; Melnikova, R.A.; Mikos, K.N.; Muttik, G.G. *Zh. Fiz. Khim*. **1968**, 42, 198.

[84] Majer, V.; Svoboda, V., *Enthalpies of Vaporization of Organic Compounds: A Critical Review and Data Compilation*, Blackwell Scientific Publications, Oxford, **1985**, 300.

[85] Beutel, T; Peltre, M.-J.; Su, B.L. *Coll. Surf. A: Physicochem. Eng. Aspects* **2001**, 187, 319.

[86] Mammone, J.F.; Sharma, S.K. *J. Phys. Chem.* **1980**, 84, 3130.

[87] Graener, H.; Ze, T.Q.; Laubereau, A. *J. Chem. Phys* **1989**, 90, 3413.

[88] Natal-Santiago, M.A.; Dumesic, J.A. *J. Catal*. **1998**, 175, 252.

[89] Mirth, G.; Lercher, J.A.; Anderson, M.W.; Klinowski, J. *J. Chem. Soc. Faraday Trans*. **1990**, 86, 3039.

[90] Beutel, T; Peltre, M.-J.; Su, B.L. *Coll. Surf. A: Physicochem. Eng. Aspects* **2001**, 187, 319.

[91] Serallach, A.; Meyer, R. Hs.H. Günthard, *J. Mol. Spectrosc*. **1974**, 52, 94.

Chapter 4

Interaction of short chain amines and alcohols with alkali metal cation exchanged X zeolites: Infrared Spectroscopic Study

Abstract

Adsorption of water, ammonia, methylamine, and 1-propylamine on alkali cation exchanged X zeolites was studied by Fourier transform infrared (FTIR) spectroscopy and compared to the results obtained for linear *n*-alcohols. At low loadings, similar types of interactions have been found for short polar molecules in the faujasite supercage of alkali cation exchanged X zeolites. The adsorption is described as a general structure: (i) polar sorbate molecules interact with alkali metal cations via the lone electron pair of their electronegative atoms; (ii) the protons of the functional groups of the sorbates and (iii) also those of the alkyl groups form hydrogen bonds with the negatively charged oxygen atoms of the zeolite framework. Amines form only one sorption structure and do not exhibit sorbate-sorbate interactions as found for alcohols. The alcohol molecules of higher polarity are stronger bound to alkali metal cation exchanged X zeolites than amines. In general, the IR band position depends on the cation and decreases with increasing atomic weight of the cation of the zeolites. In the case of water adsorption, not only the band position but also the band intensity depends on the hydration degree due to formation of water clusters at higher water contents.

4.1 Introduction

Substances of small polar molecules like water, ammonia, short chain alcohols as well as amines are important raw materials for chemical synthesis. Zeolites are largely used in the industry as adsorbents, molecular sieves or heterogeneous catalysts [1]. For example, ammonia and methylamine are raw materials for the synthesis of nitrogen-containing organic compounds [2] of industrial importance like resins, fibers, dyes and pharmaceuticals [3], as well as for side chain alkylation of toluene with methanol proceeds over basic zeolite catalysts [4].

The efficiency of a catalyzed reaction is strongly dependent on the interactions between the catalyst and the reaction partners. Therefore, the understanding of adsorption behavior of sorbate molecules within the cavities of zeolites is of the main interest for designing new catalysts. Acidic zeolites exhibit mainly Brønsted acid hydroxyl groups as active sites, while alkali metal exchanged X zeolites reveal acid-base pairs [5]. The exchangeable counter cations are Lewis acidic sites and the negatively charged framework oxygen atoms are Lewis basic sites [6]. The basic strength of the framework oxygen atoms adjacent to the counter cations can be modified by changing the type of cation, and increases from Li^+ to Cs^+ [7].

Both the acidic and the basic adsorption sites present on ion-exchanged zeolites have been found to be simultaneously involved in the adsorption of short polar molecules [8, 9, 10, 11]. The adsorption structure of alcohols on alkali metal exchanged X zeolites [12] depends on the acid-base properties of the zeolite. Typically, the sorbate coordinates strongly via its free electron pair, i.e., that of the oxygen atom in alcohols, to the counter cation located in the zeolite cavities. In addition, hydrogen bonds are formed between the OH protons of the sorbate and the negatively charged oxygen atoms of the zeolite [11]. The amine group may also form hydrogen bonds, which are generally weaker than the corresponding bonds formed by alcohols.

Alkylamines and ammonia are similar to alcohols and water. Besides their amphoteric character, they have high dipole moments and form hydrogen bonds in liquid state. However, amines and alcohols differ in their polarity because the amine nitrogen is much less electronegative than oxygen in the alcohol (Table 4.1). The NH bond is longer, the dipole of amines is weaker, and the acidity of the amines is about 20 times lower than that of comparable alcohols. The boiling points are lower for the

Table 4.1 Dipole moments values of investigated adsorbates.

Sorbates	Dipole moment $[10^{-30}$ C·m] [a]	Sorbates	Dipole moment $[10^{-30}$ C·m] [a]
water	6.16	ammonia	4.9
methanol	5.66	methylamine	4.36
ethanol	5.63	ethylamine	4.06
1-propanol	5.59	1-propylamine	3.90

[a] CRC *Handbook of Chemistry and Physics* 56th Ed. 1975-1976.

amines than for the analogous alcohols, e.g., 321 K for propylamine and 390 K for propanol.

In general, if a hydrogen atom of the ammonia molecule is replaced by an alkyl group which is a stronger electron donor than hydrogen, the electron density on the nitrogen atom of the alkylamine molecule is increased and this results in enhanced basicity [12]. Therefore, alkylamines with the general formula RNH_2 are slightly stronger bases than ammonia. Similarly, addition of electron-donor groups decreases acidic character of alcohols.

The adsorption behavior and the reactivity of ammonia and methanol on alkali metal exchanged zeolites have been studied by Kogelbaur *et al.* [13]. It was found that methanol was significantly stronger adsorbed than ammonia, which causes to the formation of monomethylamine and dimethyl ether in approximately equal concentrations on zeolites with high aluminum content. Theoretical results of co-adsorption processes of methanol and ammonia, using Hartree-Fock (HF) and density functional theory (DFT) approaches, indicated that stronger basic ammonia is preferentially bound to the Brønsted acid sites of H-zeolites, while methanol interacts with the Lewis acid of Na-zeolites [13, 14]. The frequency assignments for infrared spectrum of methylamine have been given for the adsorbed state by Doquir *et al.* [10], while for the gaseous state by Durig *et al.* [15] and by several other researchers [16]. Similarly to the results obtained for the adsorption of methanol on cation-exchanged zeolites [11], it has been observed that, besides the type and the number of counter cations which are factors influencing the interaction of methylamine with zeolites, the location of cations and the zeolite structure can also strongly modify the strength of each kind of interaction and the overall interaction strength [17]. As concluded in the cited papers 10, 15, 16, the frequency shift is enhanced with the increase in the framework polarity.

The ammonia and water molecules are small enough to access the sodalite cavities of the zeolite [18]. However, in the case of a large-pore and aluminum rich zeolite such as zeolite X, the effective pore size may be controlled by the stable interaction between the zeolite cation and the dipole moment of ammonia or water which can form a diffusion block by clustering ammonia or water molecules around the cation in the cavities. It has been shown that, when small amounts of ammonia or water are presorbed on a dehydrated zeolite, the sorption of a second less polar sorbate such as oxygen is drastically reduced [19, 20]. Thus, adsorption of all sorbates, used in the following, is assumed to occur predominantly in the supercages of the faujasite structure.

Non-reactive adsorption of ammonia, methyl- and propylamine, as well as methanol, 1-propanol and water on Na- and Cs-X were investigated using infrared spectroscopy to gain additional information on the interactions of the counter cations and zeolite framework with probe molecules varying in polarity. A full assignment of the vibrational modes is given.

4.2 Experimental

4.2.1 Materials

Commercial Na-X zeolite (Si/Al = 1.3; Köstrolith, Südchemie) was exchanged with 0.1 molar alkali metal nitrate solutions (Na^+ and Cs^+). The suspension was stirred at 535 K for 20 h (solid/liquid ratio = 20 $g \cdot l^{-1}$), cooled to room temperature, washed, dried and subsequently calcined at 723 K under flowing synthetic air for 1h. The complete exchange procedure was repeated three times. The Si/Al ratios were determined by atomic absorption spectroscopy (AAS, UNICAM 939). The structure of all zeolite materials was proved by powder X-ray diffraction (XRD) recorded with a Philips XPERT PRO diffractometer (CuK_α). Nitrogen adsorption isotherms were measured with PMI sorptometer (77.4 K, samples activated *in situ* at 673 K for 20 h). The results have been reported in an earlier work [12] and are summarized in Table 4.2. The sorbates methanol and 1-propanol (p.a. > 99.5 %) were obtained from Merck AG. 1-Propylamine (99 %) was obtained from Fluka. Methylamine (98+ %) and ammonia (3.8) were obtained from Aldrich and Messer Griesheim, respectively. All sorbates were used without further purification. Bidistilled water was used.

Table 4.2 Characteristics of alkali metal cation exchanged X zeolites determined from AAS analysis and N_2-sorption.

Sample	Si/Al	M^+/Al [mol%]	Na^+/Al [mol%]	Unit cell composition	Mirpore volume [m^3/g]	S_{int} [a]	δ_0 [b]	e/r [c] [$Å^{-1}$]
Na-X	1.2	100	100	$Na_{88}\ Al_{88}\ Si_{104}\ O_{384}$	0.17	2.314	-0.337	1.05
Cs-X	1.3	55.4	44.6	$Cs_{47}\ Na_{38}\ Al_{84}\ Si_{108}\ O_{384}$	0.10	2.239	-0.356	0.59

[a] $S_{int} = (S_P^p \cdot S_Q^q \cdot S_R^r \cdot S_T^t)^{1/(p+q+r+t)}$: for a compound $P_pQ_qR_rT_t$ calculated intermediate Sanderson electronegativity [21].
[b] Calculated average charge $-\delta_o$ on the oxygen of the lattice, using $(S_{int}-S_o)\cdot 2.08\cdot S_o^{1/2}$.
[c] electrostatic potential of sodium cation (e/r)

4.2.2 Infrared Spectroscopy Study

The sorption experiments were investigated with *in situ* IR spectroscopy (Bruker IFS–88, resolution 4 cm^{-1}) at 308 K under partial pressures of 10^{-3} to 1 mbar. The measurement unit was a vacuum cell of base pressure below 10^{-6} mbar. The zeolite samples were pressed into self–supporting wafers (ca. 5 mg) and activated at 723 K under vacuum for 30 min (ramp of 10 $K\cdot min^{-1}$). After adsorption, the physisorbed molecules were removed by evacuation ($p < 10^{-6}$ bar) at 308 K for 1h and desorbed by heating from 373 K to 723 K at a rate of 2 $K\cdot min^{-1}$. All spectra were baseline corrected between 3800 and 1100 cm^{-1} and normalized to the integral peak area of the overtones of the framework vibrations in the range 2100–1735 cm^{-1}. The difference spectra hereafter were obtained by subtraction of the spectrum of the activated zeolite from the spectrum of the zeolite with the adsorbed molecules. This way, all IR bands pointing upwards correspond to an increase in intensity, while all pointing downwards mean a decrease in intensity.

4.3 Results

4.3.1 Adsorption of ammonia, methylamine and *n*-propylamine on Na-X

IR spectra for ammonia, methylamine, and propylamine, adsorbed at 308 K on Na-X pretreated under vacuum at 723 K for 1 hour, are shown in Figure 4.1. The assignment of the observed signals is listed in Tables 4.3-4.5 and compared to the frequencies of ammonia [22] and *n*-alkylamines [10] in the gaseous and adsorbed states.

After equilibration of Na-X with $5 \cdot 10^{-3}$ mbar of ammonia, four peaks at 3400, 3363, 3311, and 3239 cm^{-1} in the NH stretching vibration region and two bands at 1652 and 1568 cm^{-1} in the bending vibration region are observed. The bands 3363 and 3311 cm^{-1} can be assigned to the asymmetric and symmetric ν(NH) stretching vibrations, respectively, and the band 1652 cm^{-1} to the asymmetric δ(HNH) bending vibration of ammonia adsorbed on the Lewis acid counter cation [13]. The bands occur

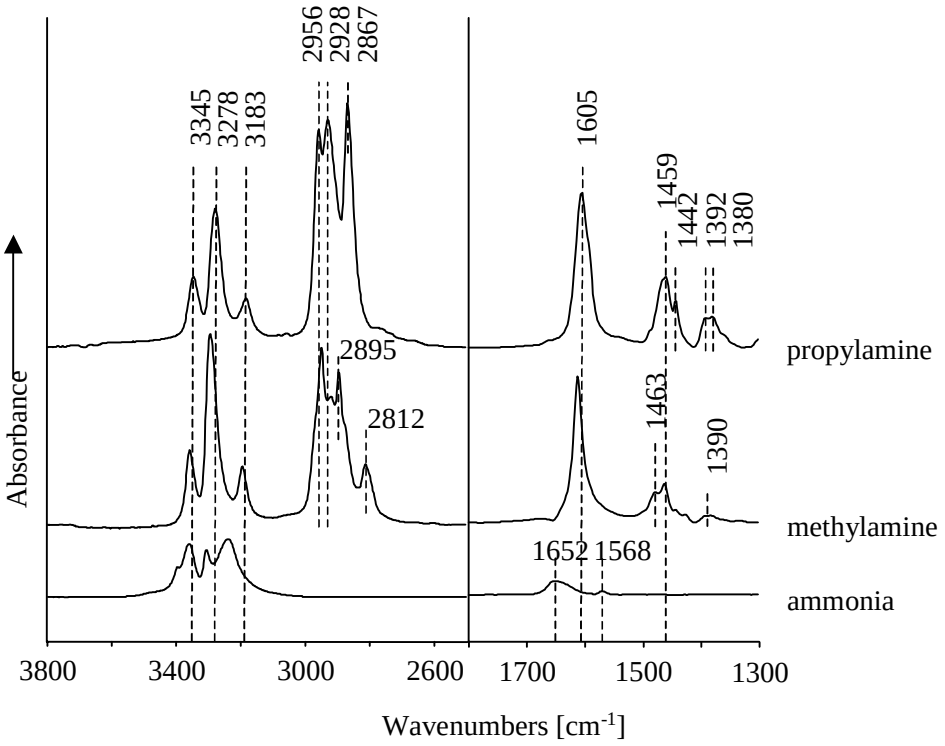

Figure 4.1 Difference infrared spectra of ammonia, methylamine, propylamine adsorbed on Na-X (T = 308 K, p = $5 \cdot 10^{-3}$ mbar).

Table 4.3 Vibrational IR frequencies of ammonia and water in the gaseous and adsorbed states (T = 308 K, p = $5 \cdot 10^{-3}$ mbar). [a]

Ammonia						Water				
Assignment [b]	**Gaseous** [22]	**Liquid** [33]	**Adsorbed on**	**Adsorbed on**		**Assignment** [b]	**Adsorbed on**		**Adsorbed on**	
			Na-MOR 10 (20) [13]	**Na-X**	**Cs-X**		**NaX** [26]	**NaZSM5** [34]	**Na-X** [c]	**Cs-X** [c]
ν(Si-OH)					- 3735 w - 3718 w	ν_{as}(OH)	3695-3688	3683	3688	3650
ν(Al-OH)				- 3665 w		ν_{s}(OH)		3589	3604	3580
ν_{as}(NH)	3444	3375	3383 (3386)	3400, 3363	3403 sh, 3353 b	ν($OH^{\cdots}O_z$)	3400		3550-3000 b, max. at 3360	3630-3000 b, max. at, 3430
ν_{s}(NH)	3336	3285	3314 (3317)	3311	3303	$\nu(OH)_{polymer}$	3250	3249	3230	3250
2* δ_{as}(HNH)		3220	3275 (3275)	3239 b	3251, 3223	δ_{as}(HOH)	1660-1645	1631	1648	1649
δ_{as}(HNH)	1627		1644, 1560 (1640, 1500)	1652, 1568	1656, 1581					

[a] in cm^{-1}

[b] ν_{as} = asymmetric stretching, ν_{s} = symmetric stretching, δ_{as} = asymmetric bending, δ_{as} = symmetric bending, sh = shoulder, b = broad, w = weak

[c] see Chaper 2

Table 4.4 Vibrational IR frequencies of methylamine and methanol in the gaseous and adsorbed states (T = 308 K, p = $1 \cdot 10^{-3}$ mbar). [a]

Methylamine							Methanol		
Assignment [b]	**Gaseous**		**Adsorbed on**		**Adsorbed on**		**Assignment** [b]	**Adsorbed on**	
	Experimental [10]	**Calculated** [10]	**Na-X** [10]	**Cs-X** [10]	**Na-X**	**Cs-X**		**Na-X** [c]	**Cs-X** [c]
$\nu_{as}(NH)$	3427	3440	3363	3358	3358	3352	$\nu(OH)$	3460 sh, 3341	3456 sh, 3298
$\nu_{s}(NH)$	3361	3377	3305	3298	3292	3288	$\nu_{as}(CH_3)$	2980 sh, 2957	2946
$2x\ \delta_{as}(NH)$			3196	3200	3195	3199	$2x\ \delta_{as}(CH_3)$	2917	2907
$\nu_{as}(CH_3)$	2985, 2961	2966, 2965	2975, 2952	2938	2949	2939 sh	$\nu_{s}(CH_3)$	2839	2823
$2x\ \delta_{as}(CH_3)$			2928, 2896	2928, 2884	2922, 2895	2925, 2985	$\delta_{as}(CH_3)$	1476, 1451	1478, 1450
$\nu_{s}(CH_3)$	2820	2810	2812	2803	2813	2804	$\delta(OH)_{ip}$	1423 sh	1419 b
$\delta_{as}(HNH)$	1623	1630	1611	1618	1611	1617	$\delta_{s}(CH_3)$	1400	1391 sh
$\delta_{as}(CH_3)$	1485, 1473	1471, 1466	1478, 1460	1478, 1460	1480, 1463	1477, 1464			
$\delta_{s}(CH_3)$	1430	1426	1426	1422	1428				

[a] in cm^{-1}

[b] ν_{as} = asymmetric stretching, ν_{s} = symmetric stretching, δ_{as} = asymmetric bending, δ_{as} = symmetric bending, sh = shoulder

[c] see Chapter 3

Table 4.5 Vibrational IR frequencies of 1-propylamine and 1-propanol in the gaseous and adsorbed states (T = 308 K, p = $1 \cdot 10^{-3}$ mbar). [a]

Propylamine				Propanol		
Assignment [b]	**Gaseous** [35]	**Adsorbed on**		**Assignment** [b]	**Adsorbed on**	
		Na-X	**Cs-X**		**Na-X** [c]	**Cs-X** [c]
$\nu_{as}(NH)$	3380	3345	3340	$\nu(OH)$ polymer	3459 sh, 3329 b	3266 b
$\nu_{s}(NH)$	3290	3278	3287	$\nu_{as}(CH_3)$, $\nu_{as}(CH_2)$	2958, 2953 sh	2955
2x $\delta_{as}(NH)$		3183	3193	$\nu_{s}(CH_2)$	2937	2930
$\nu_{as}(CH_3)$, $\nu_{as}(CH_2)$	2960	2956	2948 sh	$\nu_{s}(CH_3)$	2875	2869
$\nu_{s}(CH_2)$	2930	2928	2923	$\delta(CH_2(O))$	1474	1473 sh
$\nu_{s}(CH_3)$	2880	2867	2857	$\delta_{as}(CH_3)$, $\delta(CH_2)$	1463 sh, 1459	1459
$\delta_{as}(HNH)$	1610	1605, 1592 sh	1609	$\delta(CH_2(C))$	1436 sh	1435 sh vb
$\delta_{as}(CH_3)$; $\delta(CH_2)$	1460	1466, 1459	1465	$\delta(COH)_{ip}$ + $\omega(CH_2)$	1412 b	
$\delta_{as}(CH_2(C))$		1443		$\omega(CH_2)$, $\delta_{s}(CH_3)$	1395, 1391	1391 b
$\omega(CH_2)$, $\delta_{s}(CH_3)$	1390	1392, 1380	1391, 1349	$\delta(COH)_{ip}$	1343	1346

[a] in cm^{-1}

[b] ν_{as} = asymmetric stretching, ν_{s} = symmetric stretching, δ_{as} = asymmetric bending, δ_{as} = symmetric bending, sh = shoulder, b = broad, vb = very broad

[c] see Chapter 3

at lower wavenumbers and are broadened as compared to gas phase ammonia [22] indicating hydrogen bond formation. The band 3260 cm^{-1} results from the combination of the δ(HN) antisymmetric bending vibrations. The origin of the band 3400 cm^{-1} is not clear. It may be attributed, together with weak negative bands at 3735 cm^{-1} and 3665 cm^{-1}, to ν(NH) vibration of ammonia physically adsorbed on surface hydroxyl groups [23]. The uniform increase in intensity of this band and of the other ν(NH) band with rising equilibrium pressure as well as its occurrence after evacuation at 308 K may also suggest that this band is due to freely vibrating NH groups of ammonia associated to Na^+ cations. The corresponding deformation vibration is attributed to the signal at 1568 cm^{-1}. A feature at 3474 cm^{-1}, reported for ammonia adsorbed on Na-EMT ($\delta_O \sim -0.318$), was assigned to $O_z^{\cdots}HN$ hydrogen bonds formed between protons of ammonia and negatively charged oxygen atoms of the framework [24]. The lower frequency observed for Na-X ($\delta_O \sim -0.337$) is fully in line with higher framework polarity but the low bandwidth of the signal on Na-X is in contrast to the expected broadness of hydrogen vibration bands. Presumably, the broad signal of the $O_z^{\cdots}HN$ hydrogen bond in the spectra of Na-X is covered by the observed ν(NH) bands. The absence of a deformation vibration band at around 1450 cm^{-1} (δ(HNH) of NH_4^+ ions [25]) indicates the absence of ammonium ions.

For methylamine adsorbed on Na-X [10], asymmetric and symmetric ν(N-H) stretching vibration bands were observed at 3358 and 3292 cm^{-1}, respectively, while signals assigned to ν(CH_3) stretching vibration bands appeared at 2949 and 2813 cm^{-1}. The bands at 2922 and 2895 cm^{-1} are assigned to overtone vibrational bands. The signals attributed to δ(CH_3) deformation vibrations were observed at 1480, 1463, 1428, and 1390 cm^{-1}. Both the ν(NH) and the ν(CH) stretching bands are located at lower frequencies and are slightly broadened in comparison to the bands in the gas phase, indicating formation of hydrogen bonds of the NH-groups with the zeolite oxygen atoms. Only one asymmetric ν(NH) stretching band was observed at 3358 cm^{-1}. Assumption that the band at 3400 cm^{-1} is related mainly to rather unperturbed, freely vibrating NH groups of ammonia suggests that the two NH bonds of methylamine are hydrogen bonded with a similar strength.

After adsorption of 1-propylamine, comparable trends of the frequency shift and band broadening as for methylamine were observed. The ν(NH) stretching vibration bands at 3345 and 3278 cm^{-1} were located at slightly lower values and were

broadened as found for not perturbed NH groups. The deformation vibration is attributed to the signal at 1610 cm^{-1}. Intense bands at 2956, 2928, and 2867 cm^{-1} and the bands at 1459, 1442, 1392, and 1380 cm^{-1} were assigned to the asymmetric and symmetric stretching and deformation vibration bands of the propyl groups, respectively. With increasing equilibrium pressure of ammonia and the amines, all bands increased uniformly in intensity.

4.3.2 Adsorption of water and alcohols on Na-X

In Figure 4.2, the infrared spectra of Na-X at 308 K are reported after equilibration with $5 \cdot 10^{-3}$ mbar of water, methanol, and 1-propanol. The adsorption of methanol and 1-propanol on these alkali metal exchanged X zeolites has been reported in detail elsewhere [12] (Chap. 3 and 4). Therefore, the corresponding vibrational frequencies are not further discussed but listed together with those obtained for water adsorption in Table 4.3-4.5. The results are used for the discussion.

Adsorption of water on dehydrated Na-X caused ν(OH) stretching vibration bands at 3688, 3604, two broad bands in the region 3550-3330 cm^{-1} and at approximately 3230 cm^{-1}, and one δ(HOH) water bending vibration at 1648 cm^{-1}. The bands are in good agreement with those reported in literature [26, 27, 28]. The sharp band at 3688 cm^{-1} is close to that of free OH groups of water (3725 cm^{-1}) [29]. This indicates the presence of a rather unperturbed, freely vibrating hydroxyl group, while the broad band at 3360 cm^{-1} corresponds to the perturbed ν(OH) vibration of the second hydrogen bonded OH group. The band at 3604 cm^{-1} is assigned to weakly perturbed ν(OH) stretching vibration of another type of adsorbed water molecules. The strong broadening of the structured band between 3550-3280 cm^{-1} points out that several OH groups interact via hydrogen bonds differing in strength. The band observed at 3230 cm^{-1} is usually attributed to the overtone bending vibration of the water molecules intensified due to Fermi resonance [28]. With increasing equilibrium pressure (up to 1 mbar), the band intensities change (Figure 4.3) [28]. The band 3688 cm^{-1} disappears and a very intense and broad band centered at 3430 cm^{-1} reflects formation of associates with weak hydrogen bonds.

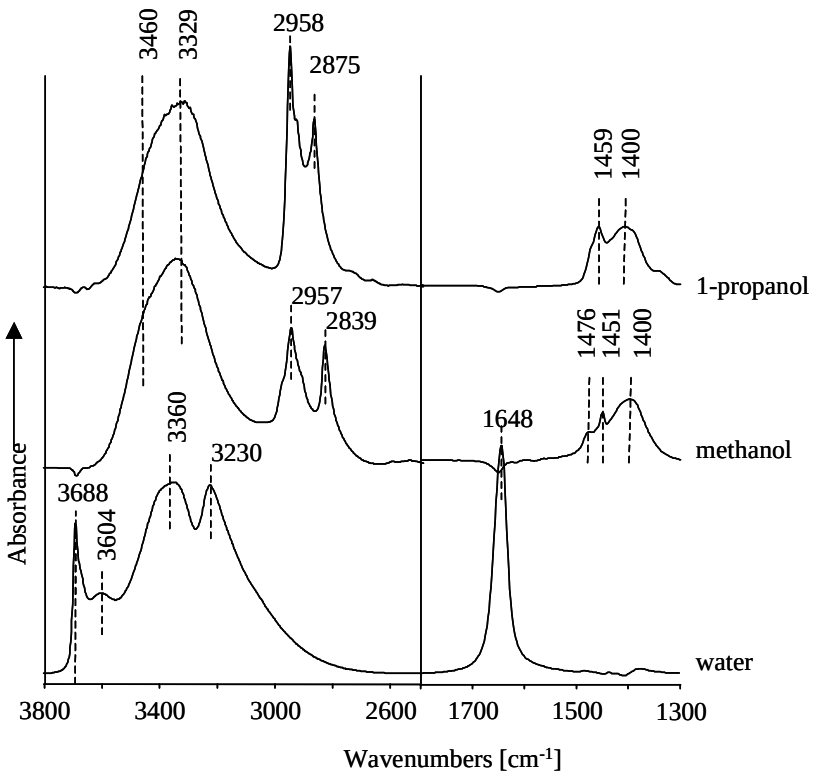

Figure 4.2 Difference infrared spectra of water, methanol, and 1-propanol adsorbed on Na-X (T = 308 K, p = $5 \cdot 10^{-3}$ mbar).

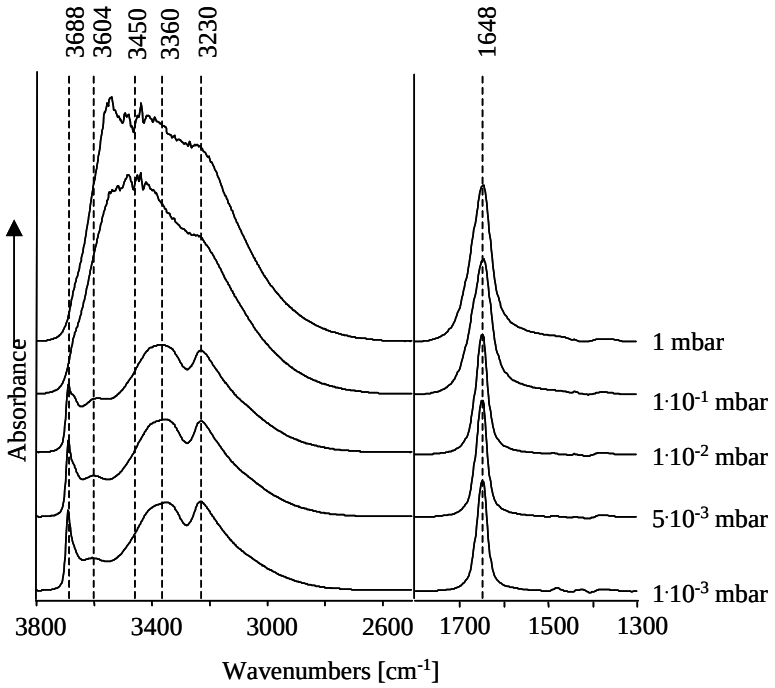

Figure 4.3 Difference infrared spectra of water adsorbed on Na-X at various equilibrium pressure (T = 308 K, p = $1 \cdot 10^{-3}$ to 1 mbar).

4.3.3 Adsorption in a series of cationic X zeolites

After adsorption of alkylamines, methylamine and 1-propylamine, a shift to lower wavenumbers and a slight broadening of the ν(NH) stretching bands have been found in the result of changing the counter cations from Na^+ to Cs^+. This indicates slightly strengthened hydrogen bonds. In line, the signals assigned to the deformation vibrations are located at higher values. However, these frequency shifts as well as the bandwidths of the ν(NH) stretching signals, obtained for nitrogen containing sorbate molecules, are much smaller than those of adsorbed alcohols [12]. Figure 4.4 compiles the changes in infrared absorption spectra induced by adsorption of 1-propylamine on Na- and Cs-X.

The infrared spectra of the ν(OH) bands of water show differences in the band intensities for Na-X and Cs-X (Figure 4.5). The hydroxyl stretching bands and the deformation band for water adsorbed on Cs-X were observed at 3650, 3580, 3630-3000, and 1648 cm^{-1}, respectively (Table 4.3). The absence of the band attributed to freely vibrating OH groups indicates hydrogen bonding of all water protons. The higher frequencies of the most intense and broad band assigned at 3430 cm^{-1} to hydrogen desorption spectra of propylamine from Na- and Cs-X.

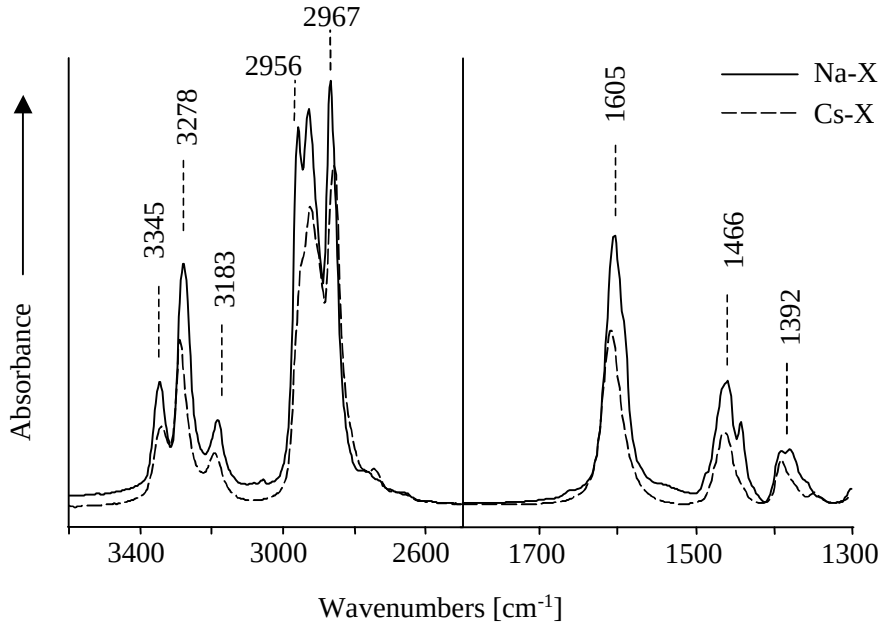

Figure 4.4 Difference infrared spectra of 1-propylamine adsorbed on Na- and Cs-X (T = 308 K, p = $5 \cdot 10^{-3}$ mbar).

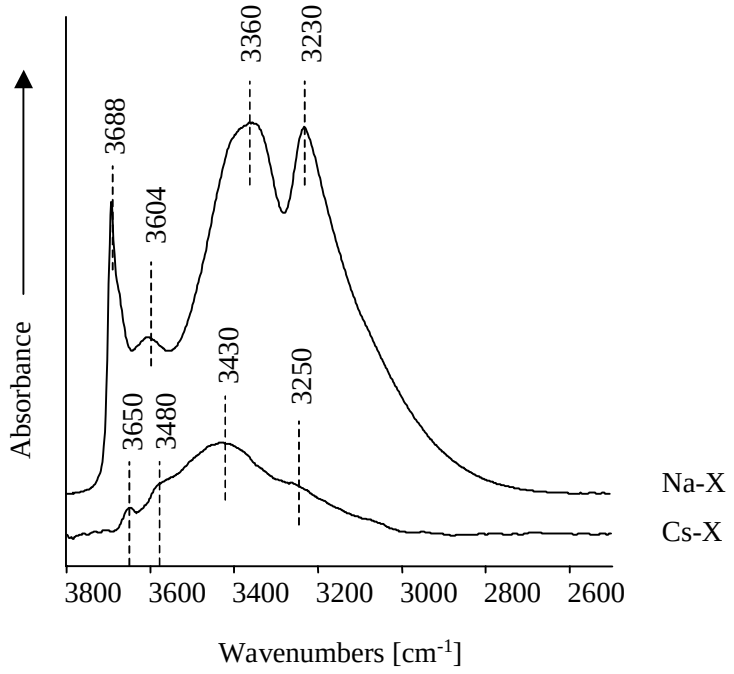

Figure 4.5 Difference infrared spectra of water adsorbed on Na- and Cs-X (T = 308 K, p $5 \cdot 10^{-3}$ mbar).

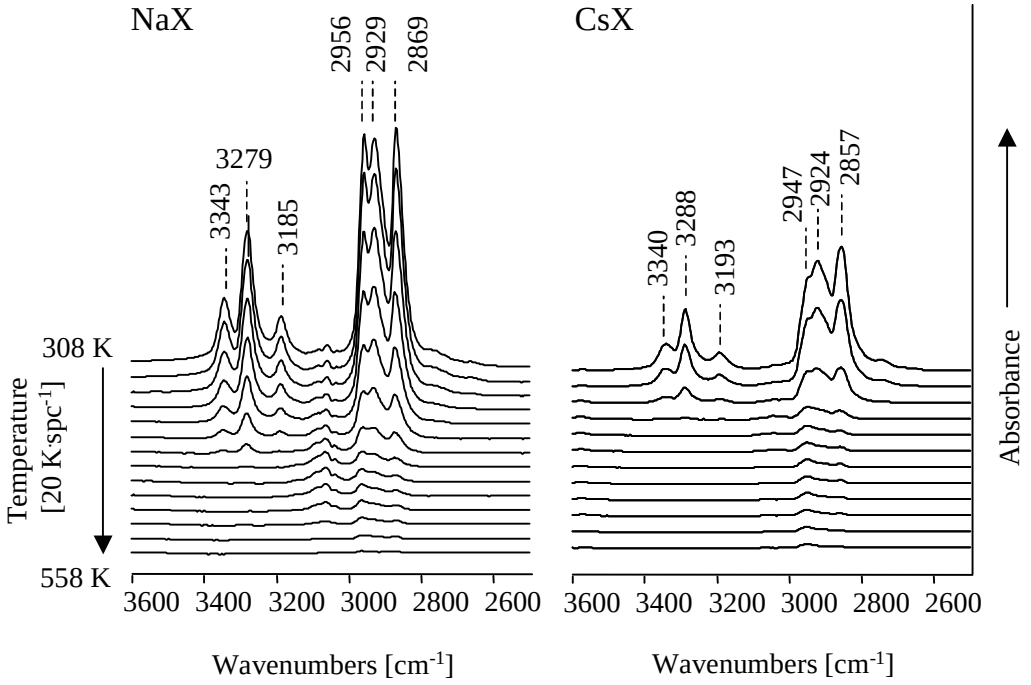

Figure 4.6 IR spectra obtained during temperature programmed desorption of propylamine from Na- and Cs-X (T = 308-558 K, p < 10^{-6} mbar).

Desorption from Na-X has been completed for methylamine and propylamine at 468 K and for ammonia at 538 K. For water and methanol, desorption has been completed at 488 K, and for propanol at 548 K. Except adsorbed water and ammonia, the nitrogen containing compounds are desorption spectra of propylamine from Na- and Cs-X. Desorption from Na-X has been completed for methylamine and propylamine at 468 K and for ammonia at 538 K. For water and methanol, desorption has been completed at 488 K, and for propanol at 548 K. Except adsorbed water and ammonia, the nitrogen containing compounds are removed at lower desorption temperatures than their oxygen analogues and the sorbate molecules are weaker bound to Cs-X than to Na-X. During the desorption process, the infrared bands of all sorbates decrease without indicating the formation of adsorbed reaction products.

4.4 Discussion

4.4.1 Effect of sorbate polarity

Comparison of the infrared vibration bands of gaseous ammonia [22] and *n*-alkylamines [10], shows that the frequencies of the ν_{as}(NH) stretching vibrations of adsorbed molecules are shifted towards lower wavenumbers that indicates a weakening of the NH bonds ($\Delta\nu(NH_3)_{Na\text{-}X}$ = 81 cm^{-1}). This weakening is due to the coordination of the sorbate molecule to Na^+ ions (Lewis acids) via the N-atom and, as seen from the signal broadening, due to the formation of hydrogen bonds between the NH groups and the negatively charged oxygen atoms of zeolite. The adsorption of methanol on the Na-X zeolite, known as polar zeolite [8], leads to a much stronger shift of about $\Delta\nu$(OH) = 340 cm^{-1} and an extreme broadening of the band of ν(OH) stretching vibrations. Note, that the shift and the change in bandwidth upon adsorption in relation to the gas phase, occurring due to formation of hydrogen bonds of different stability, are generally taken as a measure of the strength of the hydrogen bonding interactions. Thus, one can conclude that the OH groups of alcohols form stronger hydrogen bonds with the polar faujasite framework than the NH groups of amines. The weaker polarity of NH bonds results in a lower tendency of amines to deprotonate, and, consequently, in weaker hydrogen bonds between amines and basic zeolite oxygens than those of alcohols and water. The temperatures of desorption of amines are lower than those of alcohols and confirm a weaker strength of interaction

between amines and Na-zeolite. An exception is adsorption of water, which shows a lower desorption temperature than ammonia, related to higher number of hydrogen bonds possible for ammonia.

The infrared spectra of a small amount of water adsorbed on Na-X zeolites is interpreted in terms of isolated water molecules adsorbed due to ion-dipole interaction with exchangeable cations and simultaneously due to hydrogen bonding of one water hydrogen to an oxygen of the zeolite surface [26, 30]. The presence of several ν(OH) stretching and δ(HOH) bending bands for water adsorbed on zeolites indicates differences in their energetic states [31]. Similarly, from the presence of two ν(NH) bands for ammonia coordinated to Na^+ on the exchanged zeolite X, it is assumed that two NH groups are hydrogen bound and one is freely vibrating.

The uniform increase in intensity of the NH-stretching and -bending bands with the growing amount of adsorbed molecules indicates a fairly uniform interaction of the sorbate molecules with the oxygen atoms of the zeolites and with each other. On the other hand, adsorption of alcohol and water show changes in the band intensities with increasing equilibrium pressure, which are attributed to dependences of the molecule-zeolite and molecule-molecule interactions on the amount adsorbed. In the course of cluster formation, the stretching bands of freely vibrating water (at 3680 cm^{-1}) decrease at higher loadings in parallel with an increase of broad band at approximately 3430 cm^{-1} (Figure 4.3). The water molecules form first hydrogen bonds with oxygen atoms in the zeolite framework as well as coordinated with the main adsorption centers, i.e. counter ions in the pores. Then, with increase in the sorbate concentration, additional interactions start to occur with the next neighboring molecules. This means the beginning in formation of clusters. With a further increase in the sorbate concentration, a rearrangement of the sorption structure occurs, which results in final condensation of water into formation of liquid-like water structure in the pores [28]. For alcohol adsorption, a sorption structure with additional sorbate-sorbate interactions to the next neighbor is to accept at higher contents of molecules adsorbed [12].

4.4.2 Effect of compensating cation

Infrared spectroscopy evidences an enhanced formation of hydrogen bond on X zeolites with increasing cation size, as indicated by larger frequency shifts

(Figure 4.7). This phenomenon is found to be less remarkable for amines than for alcohols, as concluded from the lower shift Δν(NH), and is in line with the lower polarity of amines. The frequency decrease is explained by the formation of stronger hydrogen bonds between the sorbate OH/NH group and the zeolite oxygen atoms which are higher negatively charged in Cs-X than those in Na-X (Table 4.2) [10, 12]. Smaller Δν for nitrogen-containing sorbates indicates that the formation of hydrogen bonds between adsorbed amines and the zeolite framework is less influenced by the framework polarity than in the case of adsorbed alcohols. It can be concluded that, in general, an enhanced formation of hydrogen bonds between short polar molecules and the framework at increasing zeolite polarity is lower for the nitrogen than for the oxygen containing compounds. Adsorption takes place mainly as a result of specific molecular interactions between sorbates and zeolite cations. For apolar zeolite frameworks (at a low Al content), like ion-exchanged ZSM-5 [11], a frequency shift to higher wavenumbers has been reported. It indicates increasing interaction strength with the ionic potential of the Lewis acidic cations. This is in agreement with the decreasing heat of adsorption reported for exchanged X zeolites at constant sorbate content [11, 31, 32] and with the increasing temperature of desorption for the materials with increasing cation radius.

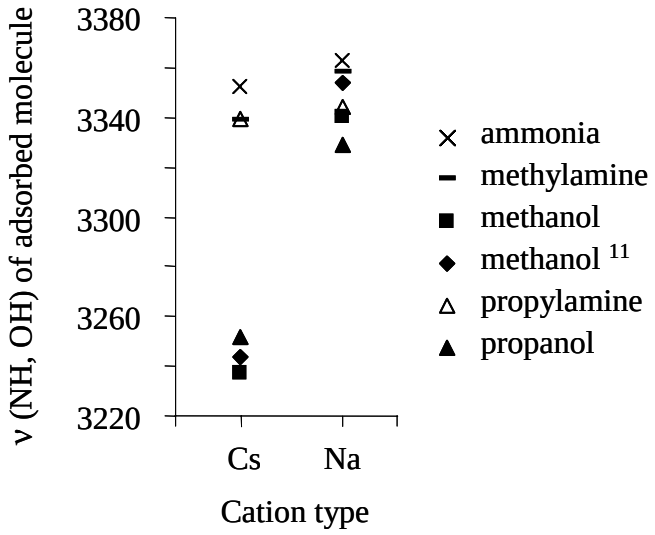

Figure 4.7 Change of the frequency of the ν(OH) for the sorbed alcohols (T_{ads} = 308 K; p = $5 \cdot 10^{-3}$ mbar) as a function of the cation type.

The infrared spectra of the ν(OH) bands of water show stronger differences for Na-X and Cs-X (Figure 4.5) than in the case of adsorption of alcohol or amines. The absence of the sharp band at 3688 cm^{-1} of the freely vibrating OH group of water in the infrared spectra of Cs-X suggests that both hydrogens of the adsorbed water molecules interact with the oxygen atoms of the zeolite [28]. Thus, the hydrogen bond between OH groups and zeolite oxygen is weaker on Cs-X (broad band at 3430 cm^{-1}) than on Na-X (also broad band shifted to 3360 cm^{-1}). This is related to a lower affinity of water to the weaker Lewis acidic cesium cations than to sodium and to a lower orientation of water interacting with both the Cs^+ cation and the framework.

4.4.3 Effect of alkali chain length

Considering the dependence of the hydrogen bond formation on the Lewis acid cation and the framework polarity, the shift of the stretching ν(OH) vibrations upon adsorption is much higher than that of ν(NH) (compare the discussion above). The frequencies of the ν(NH/OH) stretching vibrations, when changing from ammonia or water to the homologues methyl and propyl compounds, slightly downshift by 13 cm^{-1}. The exchange of a hydrogen in NH_3 for an electron-pushing group increases the negative charge on the nitrogen atom, while alkylamines differ very little in basicity with increasing chain length (Table 4.1). The small shift of the ν(NH) and ν(OH) frequency to lower wavenumbers, however, suggests that longer alkyl chains do not strongly influence the interactions between the functional groups and the zeolite structure.

For both the amines and the alcohols, the adsorption on Na^+-exchanged zeolites leads to identical frequency shifts and broadening of the asymmetric and symmetric ν(CH) stretching bands, the effects being even enhanced with increasing cation size (Figure 4.8). The stretching vibrations of the CH groups of amines are stronger influenced by increasing the framework polarity than those of alcohols, which is related to the stronger inductive effect of oxygen atoms. These wavenumber displacements, attributed to hydrogen bonding of the alkyl chain to the zeolite framework [10], indicate an increasing influence of the framework polarity as well as a similar behavior of the alkyl chains of adsorbed alcohols and amines.

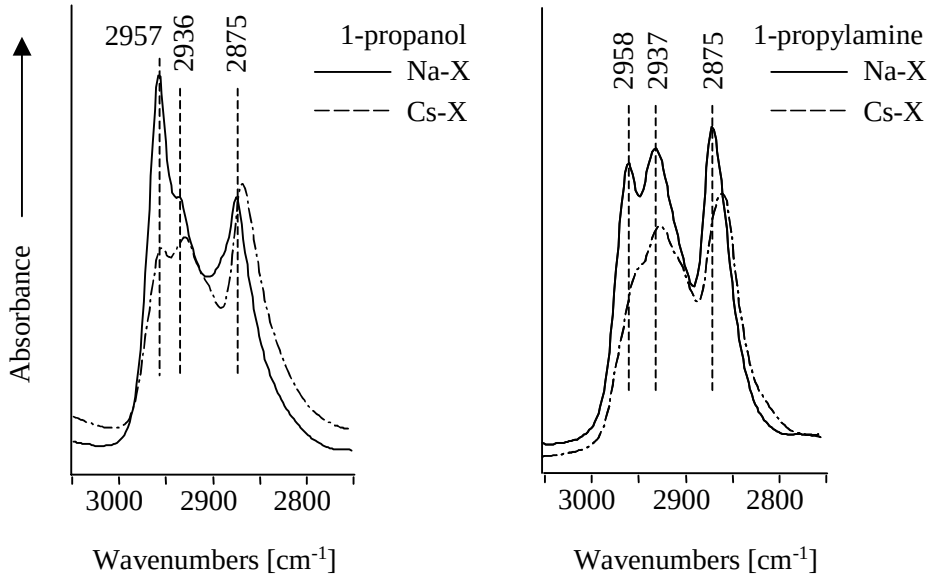

Figure 4.8 Difference infrared spectra in the ν(CH) stretching region of 1propanol and 1-propylamine adsorbed on Na- and Cs-X (T = 308 K, p = $5 \cdot 10^{-3}$ mbar).

4.5 Conclusions

A high similarity of the sorption structure of short polar molecules adsorbed on alkali cation exchanged X zeolites has been found. Three types of interactions, common for *n*-amines and *n*-alcohols adsorbed on exchanged X zeolites, can be concluded from the adsorption results. These interactions, shown in Figure 4.9, are (i) the coordination of the electronegative N/O-atom to a counter cation, (ii) hydrogen bond formation between hydrogen of the NH/OH group and negatively charged zeolite oxygen atom, and (iii) hydrogen bond formation between the alkyl chain and polar zeolite framework.

A similar orientation of the functional groups of amines and alcohols, varying in their alkyl chain length, at the active sites of the zeolite is assumed from the minor frequency shifts of the ν(NH) and ν(OH) bands. The identical shape of the ν(CH) bands points, in addition, to similar types of interactions between the alkyl chains and the framework for amines and their alcohol homologues.

Major differences between adsorbed amines and alcohols are: (i) the Δν(NH) and Δν(OH) frequency shifts in relation to the gas phase and (ii) the presence of the second, broad ν(OH) stretching band at lower frequencies for alcohols. The first effect

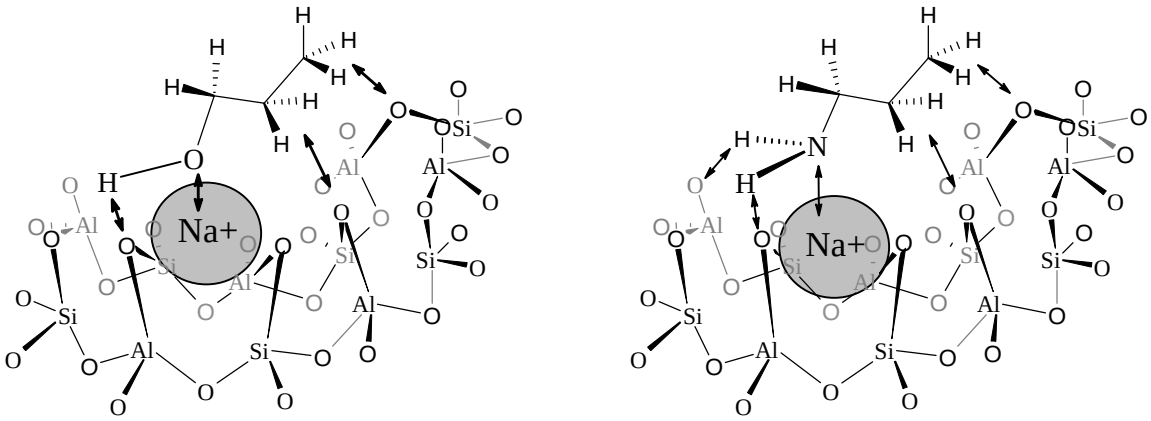

1-propanol on SIII

1-propylamine on SIII

Figure 4.9 Schematic representation of 1-propanol and 1-propylamine adsorbed on SIII position on Na-X.

indicates a stronger elongation of the polar OH bond due to enhanced hydrogen bond formation by alcohols, while the latter reveals the presence of only one adsorption structure for amines instead of the two suggested for linear C_1 to C_4 alcohols [12]. The stronger perturbation of the second structure only available for alcohols is due to additional sorbate-sorbate interactions via hydrogen bonding (Figure 4.10). This formation of hydrogen bonds is enhanced with increasing cation size and equilibrium sorbate pressure [11, 12], while it is hindered for ammonia and amines due to the presence of only one lone pair at the nitrogen atom.

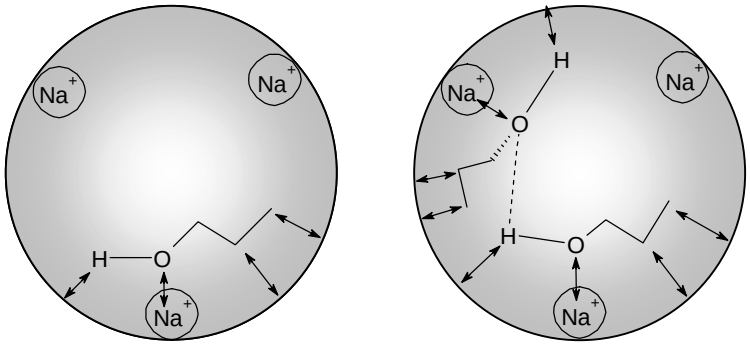

Structure 1 Structure 2

Figure 4.10 Schematic representation of two different sorption structures of 1-propanol on Na-X.

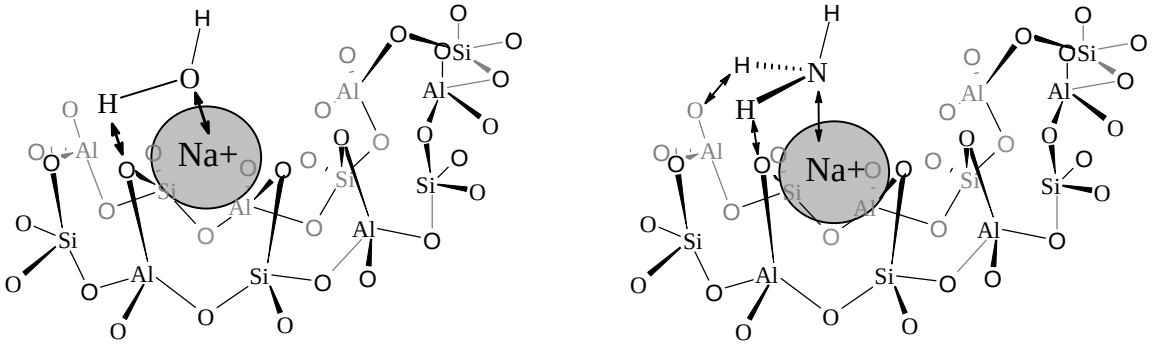

water on SIII ammonia on SIII

Figure 4.11 Schematic representation of water and ammonia adsorbed on SIII position on Na-X.

Water and ammonia can form more than one hydrogen bond with the negatively charged framework oxygen of the zeolites. Simultaneous appearance of the bands corresponding to free and perturbed NH vibrations upon adsorption in Na-X strongly suggests that one NH group of the adsorbed ammonia remains mainly free up to 1 mbar equilibrium pressure of ammonia. The other two NH groups form hydrogen bonds with the zeolite oxygens (Figure 4.11). This mechanism is similar to that known for water adsorbed at low loadings.

4.6 Acknowledgements

The authors thank the Deutsche Forschungsgemeinschaft (DFG) for financial support within the Sonderforschungsbereich SFB 338: *Adsorption an Festkörperoberflächen: Mikroskopische Analyse von Zuständen und Prozessen Teilprojekt B9.*

4.7 References

[1] Bathia, S. *Zeolite Catalysts. Principles and applications*, CRC Press, Boca Raton, **1990**.

[2] Tamioulle, J.; David, A. *Hydrocarbon Process*. **1981**, 60, 113.

[3] Farneth, W.E.; Gorte, R.J. *Chem. Rev*. **1995**, 95, 615.

[4] Yashima, T.; Sato, K.; Hara, N. *J. Catal. 26*, 303, **1972**; Sidorenko, Y.N.; Galich, P.N.; Gutyrya, V.S.; llin, Y.G.; Neimark, I.E. *Dokl. Akad. Nauk. SSSR* **1967**, *173*, 132.

[5] Ono, Y. Stud. *Surf. Sci. Catal. 5* (1980) 19; Yashima, T.; Sato, K.; Hara, N. *J. Catal.* **1972**, 26, 303; Sidorenko, Y.N.; Galich, P.N.; Gutyrya, V.S.; llin, Y.G.; Neimark, I.E. *Dokl. Akad. Nauk. SSSR* **1967**, 173, 132; Yashima, T.; Suzuki, H.; Hara, N. *J. Catal*. **1974**, 33, 486.

[6] Rossi, F.P.; Busca, G.; Lorenzelli, V.; Lion, M.; Lavalley, J.C. *J. Catal* **1988**, 109, 378; Huang, M. J. *Catal.* **1995**, 157, 266.

[7] Huang, M. *J. Catal.* **1992,** 137, 322; Barthomeuf; D. *Catal.Rev. Sci. Eng*. **1996**, 38, 521.

[8] Barthomeuf, D. *J. Phys. Chem*. **1984**, 88, 42.

[9] Doskocil, E.J.; Davis, R.J. *J. Catal.* **1999**, 188, 353.

[10] Docquir, F.; Toufar, H.; Su, B.L. *Langmuir* **2001**, 17, 6282.

[11] Rep, M.; Palomares, A.E.; Eder-Mirth, G.; van Ommen, J.G.; Rösch, N.; Lercher, J.A. *J. Phys. Chem. B* **2000**, 104, 8624.

[12] Schenkel, R.; Jentys, A.; Parker, St.; Lercher, J.A. submitted to *J. Phys. Chem*. **2004**.

[13] Kogelbauer, A.; Grundling, G.; Lercher J.A. *J. Phys. Chem.* **1996**, 100, 1852.

[14] Limtrakul, J.; Onthong, U. J. *Molec. Structure* **1997**, 435, 181.

[15] Durig J.R.; Bush, S.F.; Baglin F.G. *J. Chem. Phys.* **1968**, 49, 2106.

[16] Gray, A.P.; Lord, R.C. *J. Chem. Phys.* **1957**, 26, 690.

[17] Docquir, F.; Norberg, V.; Toufar, H.; Paillaud, J.-L.; Su, B.L. *Langmuir* **2002**, 18, 5963.

[18] Yanagida, R.Y.; Seff, K. *J. Phys. Chem*. **1972**, 76, 2597.

[19] Breck, D.W.; Eversole, W.G.; Milton, R.M., Reed, T.B.; Thomas, T.L. *J. Am. Chem. Soc*. **1956**, 78, 5963.

[20] Rees, L.V.C.; Berry, T. *Molecular Sieves*, Society of Chemical Industry, London, **1968**, p. 149.

[21] Sanderson, R.T. *J. Am. Chem. Soc.* **1983**, 105, 2259; Mortier, W.J. *J. Catal.* **1978**, 55, 138.

[22] Herzberg, G. *Molecular spectra and molecular structure, II infrared and Raman spectra of polyatomic molecules*; Van Nostrand Reinhold Co.: New York, **1945**.

[23] Little, L.H. *Infrared Spectra of Adsorbed Species*, Academic Press, London **1966**.

[24] Su, B.-L.; Doquir, F. *Langmuir* **2001**, 17, 3341.

[25] Kogelbauer, A.; Gründling, C.; Lercher, J.A. *J. Phys. Chem*. **1996**, 100, 1853.

[26] Bertsch, L.; Habgood, H. W. *J . Phys. Chem.* **1963**, 67, 1621.

[27] Ward, J.W. *J. Phys. Chem.* **1968**, 72, 4211.

[28] Kiselev, A.V; Lygin, V.I.; Starodubceva, R.V. *J. Am. Chem. Soc. Faraday Trans. 1* **1972**, 68, 1793.

[29] van Thiel, M: Becker, E.D.; Pimentel, G.C. *J. Chem. Phys*. **1957**, 27, 486.

[30] Angell, C.L.; Schaffer, P.C. *J. Phys. Chem*. **1965**, 69, 3463.

[31] Dzhigit, O.M.; Kiselev, A.V.; Mikos, K.N.; Nuttik, G.G.; Rahmanova, T.A. *J. Am. Chem. Soc. Faraday Trans. 1* **1971**, 67, 458.

[32] Vayssilov, G.N.; Staufer, M.; Belling, T.; Neyman, K.M.; Knözinger, H.; Rösch, N. *J. Phys. Chem. B* **1999**, 103, 7920.

[33] Demidenkova, I.V.; Shcherba, L.D. *Izv. Akad. Nauk SSSR Ser. Fiz.* **1958**, 22, 1122.

[34] Jentys, A.; Warecka, G; Derewinski, M.; Lercher, J.A. *J. Phys. Chem*. **1989**, 93, 4837.

[35] Fripiat, J.J.; Servais, A.; Leonard, A. *Bull. Soc. Chim. Ind*. **1962**, 635.

Chapter 5

Chemical and structural aspects of the transformation of the MCM-22 precursor into ITQ-2

Abstract

MCM-22 materials were prepared from precursors with varying Si/Al ratios. During transformation of swollen MCM-22 into ITQ-2 strong desilication and amorphization were observed, which increased in intensity with decreasing aluminum concentration of the precursor. Delamination became easier in the same order. Exfoliation of the MCM-22 precursor to ITQ-2 was most facile at Si/Al ratios above 20.

5.1 Introduction

Layered materials have a high potential as catalysts and supports, since two-dimensional slit-pores provide easy access to organic molecules exceeding the typical size of zeolitic micropores. These crystalline layered structures can be intercalated [1, 2], yielding materials which show advantages in comparison to amorphous oxides as well as microporous materials (zeolites), i.e., (i) a high internal order and homogeneous distribution of the slit-pores due to the crystallinity of the layers, and (ii) well defined micro-/mesoporosity. MCM-36 [1] is a typical example of such a molecular sieve.

Materials, similar to MCM-36, but with a completely disordered structure of layers, have been reported by Corma *et al.* [3, 4], who observed that the zeolitic layers of the MCM-22 precursor can be fully separated by ultrasonic treatment. This procedure yields crystalline monolayers. The resulting material has been named ITQ-2 [3, 4]. It consists of 2.5 nm thick sheets with a 10-membered ring channel system inside the sheets (Chapter 1, Figure1.16). The specific surface area has been found [3, 4] to be high (600-700 $m^2 \cdot g^{-1}$) and the pore structure well defined. However, delamination depends subtly on the composition of the materials and the methods employed. We report here on the influence of the synthesis routes, their modification, and the importance of chemical composition (Al concentration) of the MCM-22 precursors on the formation and properties of ITQ-2.

5.2. Experimental

MCM-22 precursors were synthesized using the procedure described by He *et al.* [5] (reaction gels with Si/Al = 8, 12, and 50, under static conditions). One part of the precursors was filtered, washed with water, dried at room temperature in air and finally calcined at 823 K under flowing N_2 with 8 % O_2 for 48 h to produce crystalline MCM-22. The other part of the non-dried and non-calcined precursors was swollen [5] with aqueous solutions of hexadecyltrimethylammonium chloride (CTMACl, 25 %) and tetrapropylammonium hydroxide (TPAOH, 40 %) at relative weight ratios MCM-22 (P) / CTMACl / TPAOH equal to 1:4:1.2, and pH adjusted to 13.5 with an NaOH solution. The swollen materials were filtered, washed, dried at room temperature and, in form of *ca*. 5 wt.% water slurries, treated in an ultrasonic bath [3, 4]

(120 W, 35 kHz) at pH = 12.5 [4] for 36 h. Then, several drops of concentrated HCl were added to obtain pH below 2, which allowed an easier recovering of the resulting ITQ-2 solids by centrifugation. After drying at ambient conditions, the organic material was removed by calcination in a procedure analogous to that for calcining MCM-22.

The overall Si/Al ratio was determined from elemental analysis with atomic absorption spectroscopy (AAS, UNICAM 939). Powder XRD patterns were recorded with a Philips XPERT PRO diffractometer using CuK_α radiation. XRD simulations were performed using "Cerius 2" (Version 4.6, MSI). Nitrogen adsorption (PMI automated BET-sorptometer) was measured at 77.4 K for samples activated *in situ* at 673 K for 20 h. Scanning electron microscopy (SEM, JEOL 500) and transmission electron microscopy (TEM, JEOL 2010) were used to characterize crystal habitus and structural aspects. The adsorption of pyridine and 2,6-di-*tert*-butyl-pyridine (2,6-DTBPy) were followed by *in situ* IR spectroscopy (Bruker IFS-88, resolution 4 cm^{-1}) at 373 K under partial pressures of 10^{-3} to 10^{-2} mbar. For this, the zeolite samples were pressed into self-supporting wafers (ca. 5 mg) and activated in vacuum ($p < 10^{-6}$ mbar) with an increment of 10 $K \cdot min^{-1}$ up to 723 K (holding for 30 min). After adsorption, the physisorbed bases were removed by evacuation ($p < 10^{-6}$ mbar) for 1 h and desorbed by heating from 373 K to 723 K with an increment of 2 $K \cdot min^{-1}$. All spectra were baseline corrected between 3800 and 1100 cm^{-1} and normalized to the integral peak area of the overtones of the framework vibrations in the range 2100 - 1735 cm^{-1}.

5.3 Results and Discussion

The Si/Al ratio of the calcined MCM-22 samples was 33.3, 11.4, and 7.6 for the samples A, B and C, respectively (Table 5.1). After swelling, delamination, and calcination of the MCM-22 precursors, the Si/Al ratio of resulting ITQ-2 samples was 20.1, 9.4 and 7.3, respectively. As has been reported for MCM-36, the swelling and pillaring process can result in a partial dealumination of the precursors [6]. A similar effect was expected for the transformation into ITQ-2. However, the opposite was observed, i.e., a significant lowering of the Si/Al ratio implying a strong desilication during the ultrasound treatment under basic conditions. This might result either from

Table 5.1 Elemental analysis of the studied materials.

Sample	Precursor	MCM-22 and ITQ-2 samples in calcined form			
	Si/Al	Si/Al	SiO_2 [mol%]	Al_2O_3 [mol%]	Na_2O [mol%]
MCM-22 A	50	33.3	98.2	1.5	0.4
MCM-22 B	12	11.4	95.5	4.2	0.3
MCM-22 C	8	7.6	89.6	5.9	4.5
ITQ-2 A	50	20.1	97.6	2.4	0
ITQ-2 B	12	9.4	94.9	5.1	0
ITQ-2 C	8	7.3	92.1	6.4	1.6

partial destruction of the zeolite framework, or from removal of various silica species present in the materials. The effect increased with decreasing Al content of the materials.

Samples A and B of MCM-22 had similar BET and micropore surface areas as well as micropore volumes (Table 5.2). For sample C, the BET surface area and the micropore volume were significantly lower. This is attributed to the relatively low Si/Al ratio of this sample. In accordance with Mochida *et al.* [7] and Güray *et al.* [8], the synthesis of MCM-22 is best performed at Si/Al ratios of 12.5-15. The low Si/Al ratio of sample C may have led to a partially collapsed structure.

Transformation of MCM-22 A into ITQ-2 A led to an increase in the specific surface area. This is attributed to the removal of extra framework species during the transformation (mainly increase of the micropore surface area) and the delamination of the layers (mainly increase of the meso-/macropore surface area). The effects of such transformations are in line with the constancy of the micropore volumes (Table 5.2). This is likely the result of two opposite effects. A decrease in the micropore volume should be expected from the lower concentration of supercages in the delaminated materials and the formation of 12-membered ring “cups” on the surface of the zeolite layers [4]. On the other hand, an increase in the micropore volume should be expected as the result of the removal of debris formed during the ultrasound treatment and/or of the extra framework species potentially present between the layers of the precursor materials. Note that the latter effect could also be a consequence of the desilication observed during the transformation from MCM-22 to ITQ-2.

From the observations above, it can be concluded that the exfoliation depends critically on the aluminum concentration of the precursor. The transformation of swollen MCM-22 precursors into ITQ-2, performed for less than 36 h, is ineffective

Table 5.2 Structural properties of the studied materials derived from N_2 sorption techniques.

Sample	Si/Al of calcined samples	BET surface area [m²/g]	Micropore surface area [m²/g]	Meso- and macropore surface area [m²/g]	Micropore volume [cm³/g]
MCM-22 A	33.3	360	191	169	0.08
MCM-22 B	11.4	386	175	211	0.07
MCM-22 C	7.6	157	89	68	0.04
ITQ-2 A	20.1	523	284	239	0.07
ITQ-2 B	9.4	432	188	244	0.08
ITQ-2 C	7.3	354	173	181	0.04

for Si/Al ratios of 20. With decrease in the Al concentration to the Si/Al ratio of 50, the necessary time for ultrasound treatment becomes shorter [3, 4].

The powder X-ray diffraction patterns of the three calcined MCM-22 precursor materials are in good agreement with literature data [9] and exhibit reflection patterns characteristic of the MWW topology. The highest crystallinity was observed for sample B with Si/Al = 11.4 (Figure 5.1a). The broad background observed for sample C indicates the presence of an amorphous phase.

The XRD patterns of the ITQ-2 samples (Figure 5.1b) differ markedly from those of calcined MCM-22. ITQ-2 A hardly shows reflections characteristic of MCM-22 indicating its complete transformation [3, 4, 5]. The peaks are broadened, which is typical for the reduction in structure size to the nm scale. The pattern also does not show the *001* and *002* reflections at $2\theta = 3.1°$ and 6.5°, characteristic of the 2.5 nm periodicity of the MCM-22 precursor. In contrast to ITQ-2 (sample A) with a completely disordered “house of cards” structure (accompanied by a significant amorphization), the XRD patterns of samples B and C display all the characteristic peaks of MCM-22 in spite of the same length of the ultrasonic treatment as for sample A (36 h in contrast to 1 h applied in refs. [3, 4]). The reflections of their pattern, however, are broader and less intense. The XRD pattern of samples B and C resemble more those of MCM-56 type materials [10]. The structure of B and C presents an arrangement of the MCM-22 zeolite layers, which is disordered along the crystallographic *c*-axis (“face to face” - MCM-56 vs. “edge to face” - ITQ-2). The lack of a relevant increase in the BET surface area for ITQ-2 B also suggests a re-aggregation of the layers. The

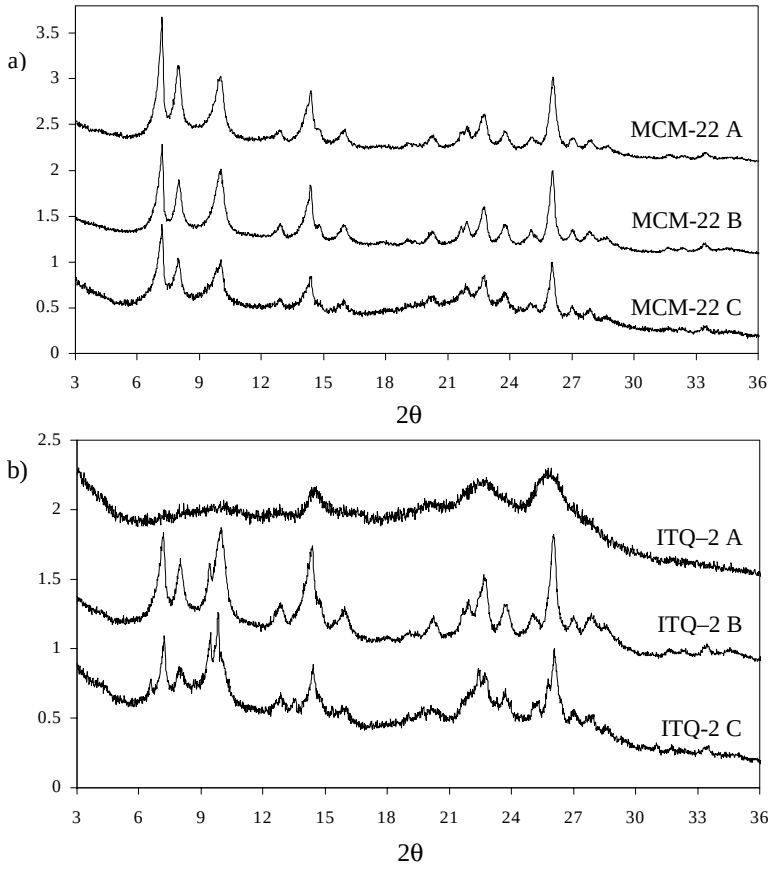

Figure 5.1 Powder X-ray diffraction patterns of (a) MCM-22 (A: Si/Al = 33.3; B: Si/Al= 11.4; C: Si/Al = 7.6) and (b) ITQ-2 (A: Si/Al = 20.1; B: Si/Al = 9.4; C: Si/Al = 7.3) samples.

additional reflections at 2θ = 6.6°, 9.4° and 13.6° in the patterns of samples B and C can be assigned to pure Si-Ferrierite [11]. Synthesis of ITQ-2 occurs at conditions close to zeolite decomposition. Thus, dissolution of the structure as well as formation of new structural units is conceivable. Simulated X-ray diffraction patterns of MCM-22 correspond well to the three MCM-22 samples (Figure 5.2). For ITQ-2, the simulated pattern exhibits sharp and well-resolved signals of the (hk0) planes due to the infinite *a,b*-dimension used for the calculation (peak broadening factor in *c*-axis: 2.6 nm). This is not the case for the synthesized sample; the lines characteristic of MCM-22 layers are hardly visible. They have to be strongly broadened, as a result of a reduction of the particle size to nm scale and a very small thickness of the layers. These observations indicate clearly that (i) exfoliation by ultrasound treatment significantly reduces the long-range order in the ITQ-2 structure, (ii) delamination of

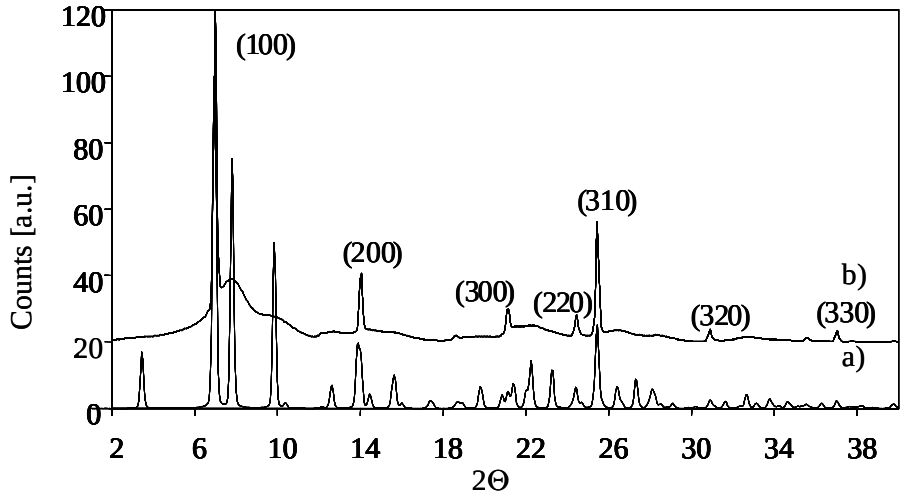

Figure 5.2 Simulated X-ray diffraction patterns of (a) MCM-22 (Si/Al = 12) and (b) ITQ-2 (Si/Al = 12).

the precursors with higher Al concentrations is more difficult, and (iii) a partial amorphization of the zeolite layers cannot be ruled out.

Scanning electron micrographs (Figure 5.3) prove that the MCM-22 samples A, B, and C synthesized under static conditions are mostly platelets, approximately 0.5-3 µm in length and 0.05-0.1 µm in thickness. The platelets are agglomerated into disc-like aggregates with an approximate diameter of 5 µm and height of 3 µm. In contrast, rotation of the autoclaves prevented the crystallites from aggregation [8]. SEM of ITQ-2 A showed particles of irregular shape and size, whereas ITQ-2 B and C are composed to a high extent of original aggregates destroyed only slightly by swelling and delamination.

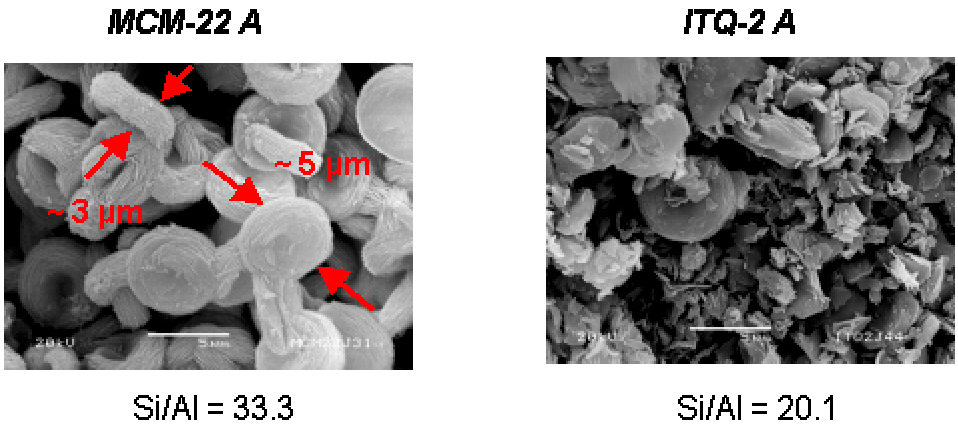

Figure 5.3 SEM of MCM-22 A and ITQ-2 A materials.

Transmission electron micrographs confirmed the well-resolved crystalline structure for all MCM-22 samples. The layer thickness can be estimated to be approximately 2.5 nm, which is consistent with the values reported by Roth *et al.* [1]. TEM of sample ITQ-2 A exhibits 2.5 nm thin single crystalline MCM-22 layers (Figure 5.4a) as well as an amorphous phase. Figure 5.4b is the top view of a layer of this sample, which shows the projection of the array of 12-membered ring half cups of the MCM-22 structure with a unit cell length of 1.3 nm in the *a*,*b*-plane. Note that these micrographs demonstrate that the treatment does not result in complete damage of the crystalline structure of the layers. The layer thickness in sample ITQ-2 B is about 2.5 nm, which is comparable to the parent MCM-22 (Figure 5.4c). The presence of significant amounts of crystalline MCM-22 and possibly MCM-56 phases after ultrasonic treatment proves that the sample has not been completely delaminated. The comparison of all micrographs shows that the sample with the lowest aluminum concentration is the easiest one to exfoliate, while a lower aluminum content of the materials favors a higher amorphization.

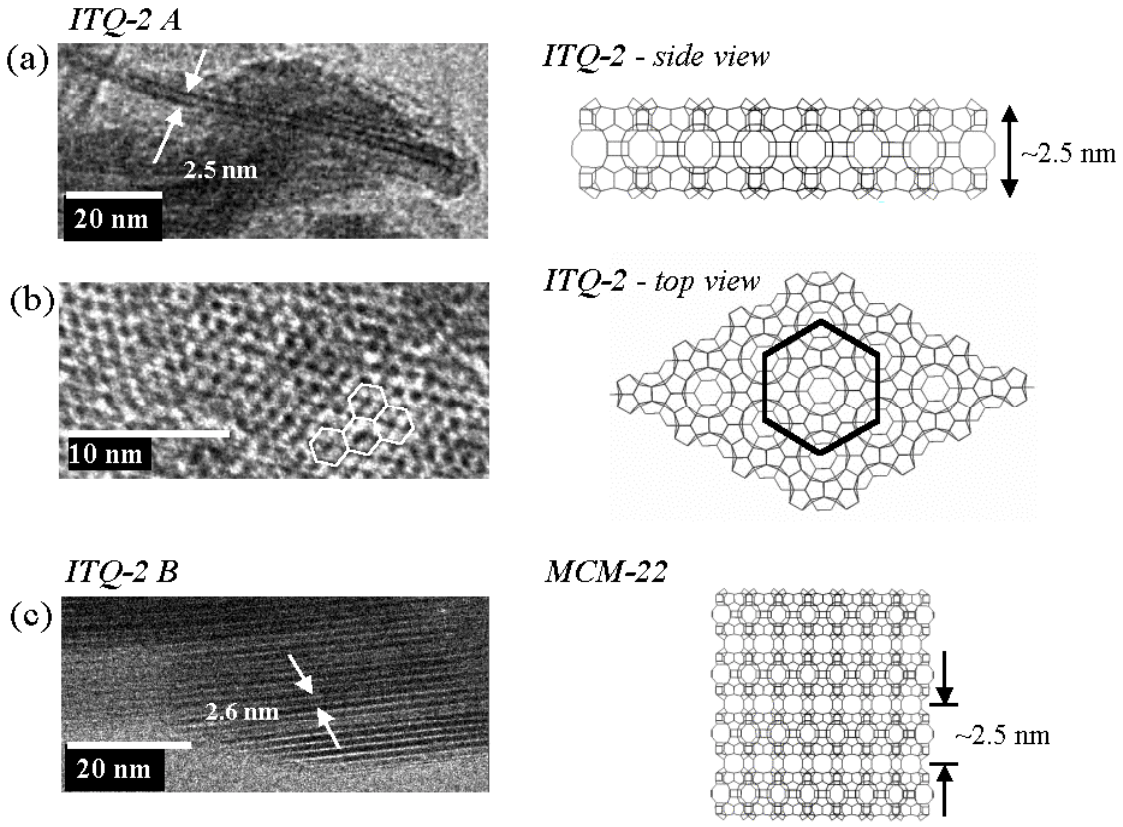

Figure 5.4 TEM of ITQ-2 materials: (a) side and (b) top view of ITQ-2 A (Si/Al = 20.1) and (c) side view of ITQ-2 B (Si/Al = 9.4).

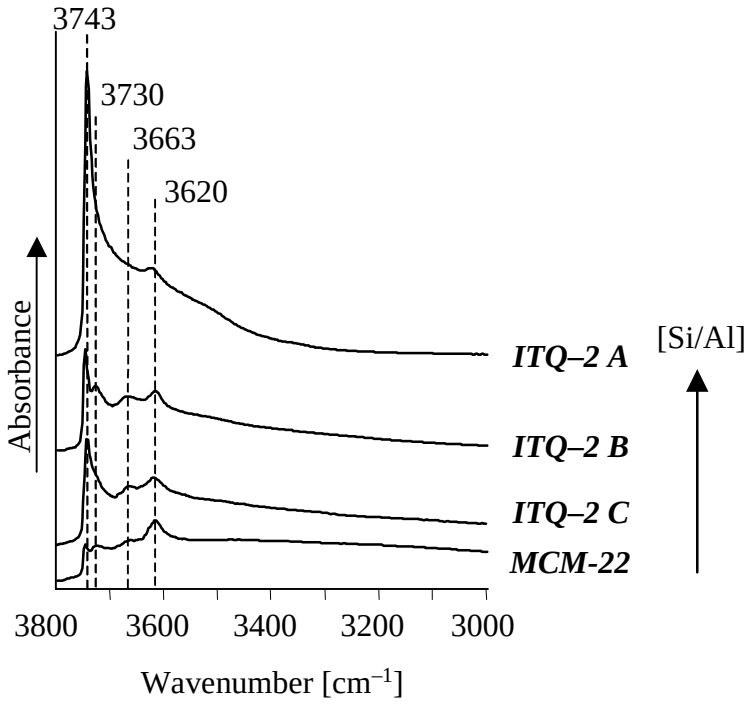

Figure 5.5 IR spectra of activated MCM-22 B and the ITQ-2 samples A, B and C; T = 308K, $p < 10^{-6}$ mbar (activation at 723 K for 30 min).

Infrared spectra of the investigated materials in the activated form (Figure 5.5) show typical bands of OH-stretching vibrations of surface hydroxyl groups. Bands at 3743 and 3730 cm^{-1} are assigned to terminal and internal Si-OH groups, respectively, those at 3663cm^{-1} to OH-groups of extra framework aluminum species, while the bands at 3620 cm^{-1} are attributed to strong Brønsted acidic bridging hydroxyl groups. For MCM-22 B, the band at 3743 cm^{-1} is very weak, while for ITQ-2 A it shows the highest intensity. During the transformation into ITQ-2, the concentration of terminal Si-OH groups increases significantly due to the strong increase of the external surface. The band corresponding to bridging hydroxyl groups at 3620 cm^{-1} appears to be weaker for ITQ-2 sample A than for MCM-22, due to the lower Al concentration of this sample. All spectra show the bands of structural overtone vibrations between 2100 and 1550 cm^{-1}.

^{27}Al MAS NMR spectroscopy was used to determine the nature and the local environment of Al species in the investigated MCM-22 and ITQ-2 materials (Figure 5.6). Two main signals characteristic of aluminum species in a tetrahedral (Al_{Td} ~ 55 ppm) and an octahedral coordination sphere (Al_{Oh} ~ 0 ppm) can be distinguished for both MCM-22 and ITQ-2 materials [12]. The later signal is attributed

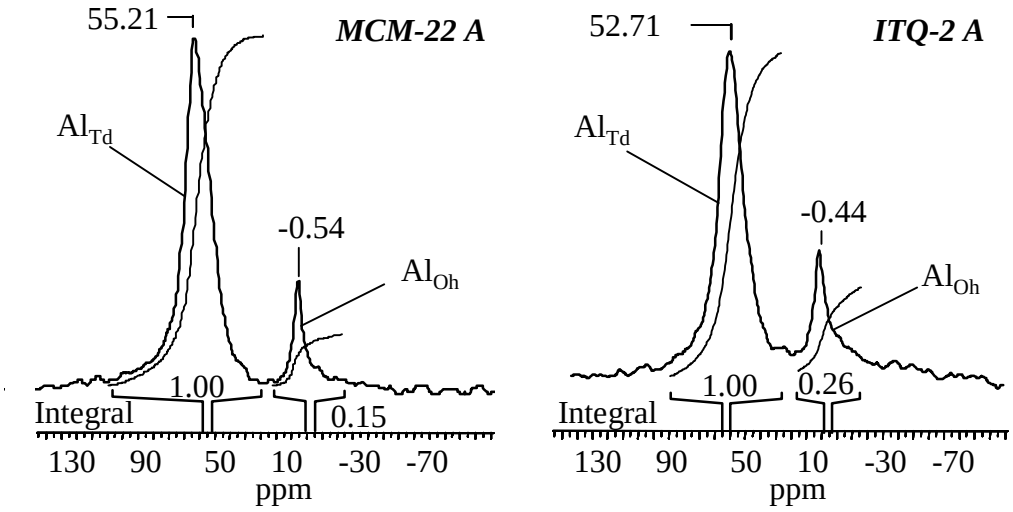

Figure 5.6 ^{27}Al MAS NMR spectra of MCM-22 A and ITQ-2 A.

to extra framework aluminum in an octahedral coordination. The signal at ~ 55 ppm is actually compromised of more than one Al_{Td} signal as shown from NMR spectra observed in a higher field (11.7 T) as shown in Figure 5.7. From high field (17.6 T) NMR spectroscopy, three T_d signals (~ 50, ~ 56, and 61 ppm) have been reported, corresponding to distinct T_d Al species in the framework of MCM-22 [13, 14] (confirmed by multiple field and double rotation NMR experiments; signals are not second order

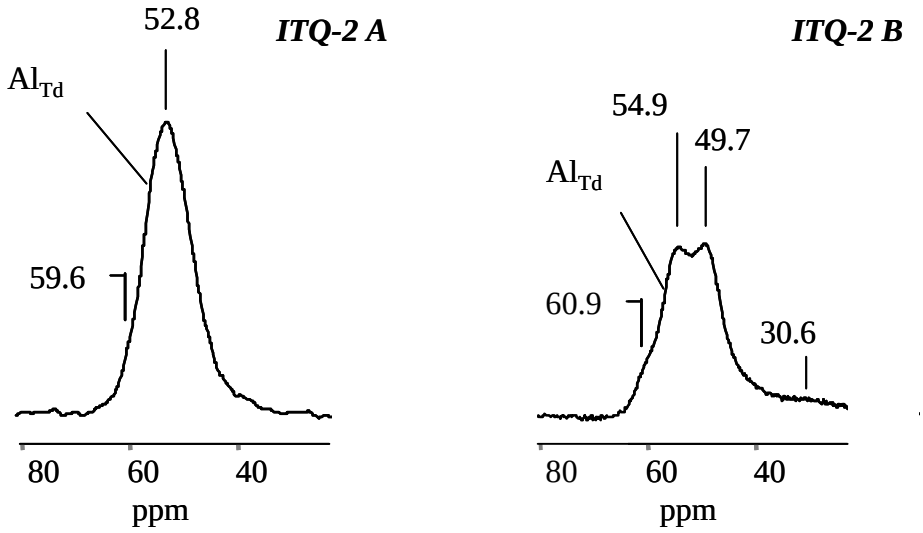

Figure 5.7 Magnification of the 20-80 ppm region in ^{27}Al MAS NMR spectra of MCM-22 A and ITQ-2 A.

quadrupolar interactions). In addition to the two signals of octahedral and tetrahedral aluminum atoms, the ITQ-2 B material showed a third resonance at ~ 30 ppm, which is tentatively attributed to aluminum pentahedrally coordinated. Such species may be attributed to non-framework aluminum oxide species formed during delamination treatments. Chemical shift is another hint to a destruction of the zeolite framework during swelling and delamination processes. The Al_{Td} signal of the ITQ-2 material is located at lower ppm values after delamination. The higher electron density at the aluminum atom, determining the chemical shift, indicates structural changes around the aluminum atom. An increasing distance between the MCM-22 layers up to full exfoliation of the layers presumably leads to an expansion of the T-O-T angle [14]. In the spectrum of ITQ-2 B, two distinct Al_{Td} signals are observed. The signal at lower field (54.9 ppm) can be attributed to aluminum atoms in a structural environment similar to MCM-22 and is in line with the lower degree of delamination for this sample.

The adsorption of pyridine and 2,6-di-*tert*-butylpyridine (2,6-DTBPy) has been used to probe the acidic properties and to distinguish between acid sites located in the zeolite pores and on the external surface/pore mouth of the layered materials (Figure 5.8). During adsorption of pyridine, several bands were observed in the IR spectra with increasing intensity. A group at 3140-2970 cm^{-1} is assigned to C-H stretching vibrations of pyridine, while the bands at 1635, 1620, 1540 and 1450 cm^{-1} are attributed to ring vibrations of pyridinium ions on Brønsted acid sites and of pyridine coordinatively bound to Lewis acid sites [15, 16]. In the spectrum of ITQ-2 C, sodium cations from the synthesis are concluded to cause the shoulder at 1442 cm^{-1} assigned to pyridine coordinated to Na^+.

Adsorbed 2,6-DTBPy exhibits several bands in the regions of 3400-2800 cm^{-1} and 1710-1350 cm^{-1}, assigned to stretching and bending vibrations, respectively, analogous to pyridine. The bands at 3365, 1616 and 1530 cm^{-1} are characteristic of the $DTBPyH^+$ ion. For the quantification of Brønsted acid sites on the external surface [17], the band at approximately 3365cm^{-1} assigned to the $\nu(N\text{-}H^+)$ stretching vibration of the $DTBPyH^+$ ion is used.

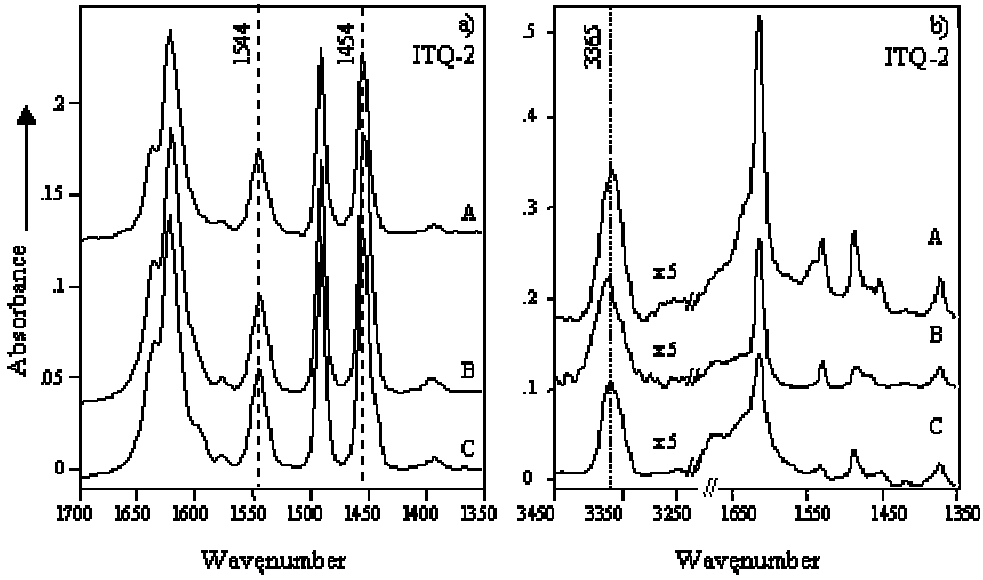

Figure 5.8 Difference IR spectra of adsorbed (a) pyridine and (b) 2,6-DTBPy on ITQ-2 samples A, B and C after reaching adsorption/desorption equilibrium at 10^{-2} mbar partial pressure of the base and evacuation for 60 min.; T = 373 K, p < 10^{-6} mbar.

Due to a larger kinetic diameter (Figure 5.9), 2,6-DTBPy can adsorb only at the pore openings or at the external surface of the zeolitic material and cannot penetrate into the pore system of MCM-22. Pyridine, however, penetrates into the 10- and 12-membered ring channels and interacts with the acid sites in channels and cavities. The area of the 1545 cm^{-1} band of pyridinium ions of the three ITQ-2 samples normalized to the molar concentrations of aluminum in the material (Figure 5.9) show that the concentration of adsorbed pyridine is slightly lower for ITQ-2 A than the concentration adsorbed on ITQ-2 B and C. The large amount of 2,6-DTBPy adsorbed

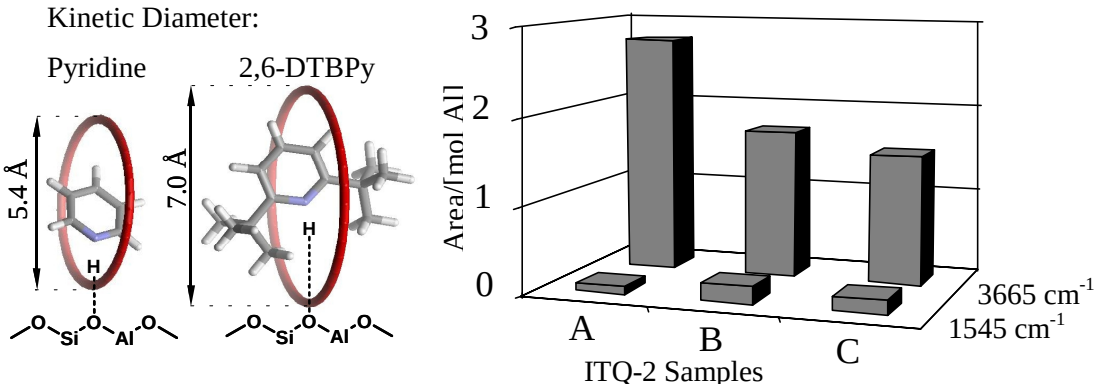

Figure 5.9 Adsorption of pyridine and 2,6-DTBPy on ITQ-2 samples A, B and C.

on sample A relative to samples B and C indicates that a large number of Brønsted acid sites interacts with the bulky base. This is in agreement with the larger external surface area and the better accessibility to the sterically demanding probe molecules. In agreement with the other observations the varying accessibility of the acid sites on the external surface indicates a lower degree of exfoliation of the layered materials B and C.

5.4 Conclusions

Delamination of swollen MCM-22 precursors to ITQ-2 is favored by decreasing aluminum concentration of the parent material. The observations strongly imply that a higher charge density at higher Al contents of the framework results in stronger interactions between the zeolitic layers. This is speculated to cause a more difficult exfoliation. Higher degrees of delamination with lower concentrations of aluminum in the materials are reflected in increasing surface areas and a better accessibility to acid sites located at the external surface of the ITQ-2 layers for 2,6-di-*tert*-butylpyridine. Delamination of the precursor materials is accompanied by significant amorphization and desilication. The extent of this amorphization increases with decreasing aluminum content of the zeolite precursor. For materials with Si/Al ratio below 15, swelling and ultra sound treatment lead to molecular sieves with a structure similar to MCM-56. The transformation process of these materials does not yield a completely disordered layered structure (“edge to face”), but induces a disordering along the crystallographic *z*-axis (“face to face”). Exfoliation of MCM-22 precursor to ITQ-2 can be best performed at a Si/Al ratio higher than 20. First experiments indicated that the use of disperser shortens the delamination treatment time extremely (10 minutes) and reduces the particle size of ITQ-2.

5.5 Acknowledgements

The work was partially supported by the Deutsche Forschungsgemeinschaft (DFG) within the Sonderforschungsbereich 338. Prof. S. Weinkauf and Dr. L. Simon are gratefully acknowledged for the help with TEM and SEM measurements.

5.6 References

[1] Roth, W.J.; Kresge, C.T.; Vartuli, J.C.; Leonowicz, M.E.; Fung, A.S.; McCullen, S.B. *Stud. Surf. Sci. Catal.* **1995**, 94, 301.

[2] Barth, J.-O.; Kornatowski, J.; Lercher, J.A. *J. Mater. Chem*. **2002**, 12, 369.

[3] Corma, A.; Fornes, V.; Pergher, S.B.; Maesen, Th.L.M.; Buglass, J.G. *Nature* **1998**, 396, 353.

[4] Corma, A.; Fornes, V.; Guil, J.M.; Pergher, S.B.; Maesen, Th.L.M.; Buglass, J.G. *Micropor. Mesopor. Mater*. **2000**, 38, 301.

[5] He, Y.J.; Nivarthy, G.S.; Eder, F;. Seshan, K.; Lercher, J.A. *Micropor. Mesopor. Mater*. **1998**, 25, 207.

[6] Barth, J.-O.; Schenkel, R.; Kornatowski, .J.; Lercher, J.A. *Stud. Surf. Sci.Catal*. **2001**, 135, 136.

[7] Mochida, I.; Eguchi, S.; Hironaka, M.; Nagao, S.; Sakanishi, K.; Whitehurst D.D *Zeolites* **1997**,18, 142.

[8] Güray, I.; Warzywoda, J.; Bac, N.; Sacco, A. Jr. *Micropor. Mesopor. Mater* **1999**, 25, 207.

[9] Leonowicz, M.E.; Lawton, J.A.; Lawton, S.L.; Rubin, M.K. *Science* **1994**, 264, 1910.

[10] Fung, A.S.; Lawton, S.L.; Roth, W.J. *US Patent* 5 362 697 **1994**.

[11] Treacy, M.M.J.; Higgins, J.B. *Collection of Simulated XRD Powder Patterns for Zeolties*, 4th Ed., Elsevier, **2001**.

[12] Kennedy, G.J.; Lawton, S.L.; Fung, A.S.; Rubin, M.K.; Steuernagel, S. *Catal. Today* **1999**, 49, 385.

[13] Unverricht, S.; Hunger, M.; Ernst, S.; Karge, H.G.; Weitkamp, *J. Stud. Surf. Sci. Catal*. **1994**, 84, 37.

[14] Lawton, S.L.; Fung, A.S.; Kennedy, G.J.; Alemany, L.B.; Chang, D.C.; Hatzikos, G.H.; Lissy, D.N.; Rubin, M.K.; Timken, H.-K.C.; Steuernagel, S.; Woessner, *J. Phys. Chem*. **1996**, 100, 3788.

[15] Ward, J.W. J. *Catal.* **1967**, 9, 225.

[16] Lercher, J.A.; Gründling, Ch.; Eder-Mirth, G. *Catal. Today* **1996**, 27, 353.

[17] Corma, A.; Fornés, V.; Forni, L.; Marquez, F.; Martinez-Triguero, J.; Moscotti, D. J. *Catal*. **1998**, 179, 451.

Chapter 6

Adsorption of methanol and 1-propanol on alkali metal exchanged MCM-22, MCM-36 and ITQ-2

Abstract

The adsorption of methanol and 1-propanol on three forms of the MWW structure, i.e., protonic and Na^+/Rb^+-exchanged MCM-22, MCM-36 and ITQ-2 was studied by infrared spectroscopy. Isolated alcohol molecules adsorbed on alkali metal cations without hydrogen-bond formation to oxygen atoms of the zeolite pore walls in all three structures. With increasing external surface area of MCM-36 and ITQ-2 the sorbate molecules accessed more Brønsted acid OH-groups of the proton exchanged materials. The dehydration of methanol and 1-propanol adsorbed on MCM-36 forming dimethyl-ether and propene is catalyzed by these Brønsted acid OH-groups. The larger concentration of surface silanol groups on MCM-36 and ITQ-2 additionally enhances sorbate cluster formation. The absence of strong Brønsted acid hydroxyl groups in the fully exchanged MCM-22 and ITQ-2 materials is indispensable for alcohol desorption without reaction. Alkali metal exchanged ITQ-2 is well suited as support or catalyst combining fast establishment of the adsorption-desorption equilibrium and complete absence of Brønsted acidity.

6.1 Introduction

MCM-22 is a zeolite with a layered structure of the MWW type consisting of two non-interconnected pore systems both accessible through 10-membered ring openings which are schematically depicted in Figure 6.1 [1, 2]. The material shows significant promise for catalytic reactions, such as the synthesis of ethylbenzene (EB Max) [3], fluid catalytic cracking [4], toluene disproportionation for the production of *para*-xylene [5] and aromatization of n-butane [6].

The location of the SiOHAl bridging hydroxyl groups (strong Brønsted acid sites) on MCM-22 was explored by Onida *et al.* [7] using the characterization with weakly basic probe molecules such as CO and N_2 and by Meloni *et al.* [8] using pyridine adsorption. The relatively broad ν(OH) stretching vibrational band with a maximum at 3626 cm^{-1} contains three components of Brønsted acid OH-groups. These OH groups are located in the supercages (3628 cm^{-1}), the sinusoidal channel system (3618 cm^{-1}), and the hexagonal prisms between two supercages (3585 cm^{-1}).

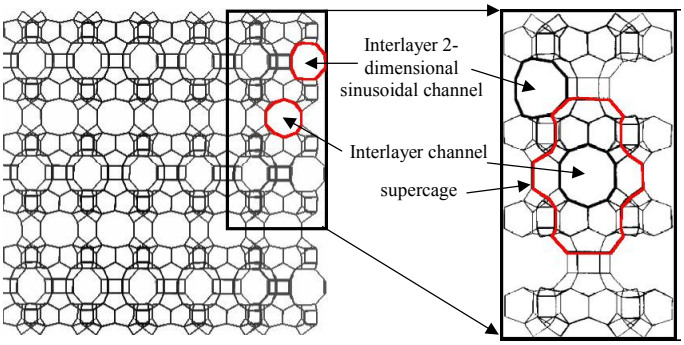

Figure 6.1 Schematic pore structure of MCM-22.

In contrast to many other molecular sieve structures, the corrugated cup-like structure of the (100) plane (note that the cup is half of the structure of the supercage) may stabilize Brønsted acidity in a zeolitic environment, but allowing the access of molecules with larger minimum kinetic diameter than given by the opening of the 10-membered ring of the pore system. Thus strategies to expose a larger fraction of this surface either by swelling and pillaring (MCM-36) or by delamination (ITQ-2) of the sheet structure formed in the precursors to MCM-22 are of great interest[9, 10]. A large probe molecule such as 2,6-ditertbutyl pyridine (2,6-DTBPy) can be used to characterize selectively these Brønsted acid sites located at the exposed corrugated

surface following the ν(NH) stretching band at 3365 cm^{-1} of the protonated amine [11]. It is important to note that the concentration of the Brønsted acid sites in these cups correlates well with the cracking activity for large reactant molecules that would be unable to access the pores of the MWW system.

Materials with controlled surface and pore structure that can act as basic catalysts [12] for reactions such as double bond isomerization of olefins, dehydrogenation of alcohols, Knoevenagel condensation of aldehydes, and side chain alkylation of aromatic molecules [13] face significant interest. The basic properties can be introduced into zeolites by ion exchange with alkali cations[14], deposition of basic oxides in the pores[15], or (in a very mild form) by isomorphous substitution of framework silicon by germanium [16, 17]. However, due to the incorporation of larger alkali metal cations or oxide particles, the void volume of the molecular sieve decreases or pores may become blocked. Additionally, many of the interesting base catalysed reactions involve large and complex molecules for which the pore diameter of conventional zeolites would be to small. Therefore, materials with sites accessible for large molecules but well controlled environments of the active sites are very attractive. With that in mind we chose to explore the sorptive properties of delaminated and pillared variants of the MWW structure (MCM-36, and ITQ-2) and compare it to the microporous MCM-22 material for small polar molecules such as methanol and 1-propanol. The purpose is to characterize the local interaction of the polar molecules with the alkali cations in the different environments, as the orientations and surface chemistry will guide complex reactions such as Knoevenagel condensations of larger molecules.

6.2 Experimental

6.2.1 Materials

The synthesized MCM-22 [2], MCM-36 [10] and ITQ-2 [18] materials were ion exchanged with 0.1 molar alkali metal nitrate solutions (Na^+ and Rb^+). The suspension was stirred at 535 K for 20 h (solid/liquid ratio = 20 $g \cdot l^{-1}$), cooled to room temperature, washed, dried and subsequently calcined at 723 K under flowing synthetic air for 1 h. The complete exchange procedure was repeated three times. The chemical composition (Si/Al ratio) of all materials was determined by atomic

absorption spectroscopy (AAS, UNICAM 939), the structural integrity was verified by powder X-ray diffraction (recorded with a Philips XPERT PRO diffractometer using the CuK_α line) and nitrogen adsorption isotherms (measured with a PMI sorptometer). The acid-base properties and accessibility to the active sites were probed by adsorption of CO_2, pyridine, and 2,6-DTBPy followed by *in situ* IR spectroscopy (Bruker IFS-88). The sorbates CO_2, pyridine, methanol and 1-propanol (> 99.5 %) were obtained from Merck AG and used without further purification.

6.2.2 Infrared Spectroscopy Studies

The sorption experiments were followed by *in situ* IR spectroscopy (Bruker IFS-88, resolution 4 cm^{-1}) at 308 K under partial pressures of 10^{-3} to 1 mbar. The spectrometer was equipped with a vacuum cell (base pressure below 10^{-6} mbar). The spectra were recorded in the transmission absorption mode and monitored time-resolved. The zeolite samples were pressed into self–supporting wafers (ca. 5 mg) and activated in vacuum with an increment of 10 $K \cdot min^{-1}$ up to 723 K (holding for 30 min). After adsorption, the physisorbed molecules were removed at 308 K by evacuation ($p < 10^{-6}$ bar) for 1 h and desorbed by heating to 723 K with an increment of 2 $K \cdot min^{-1}$. All spectra were baseline corrected between 3800 and 1100 cm^{-1} and normalized to the integral peak area of the overtones of the framework vibrations in the range 2100 - 1735 cm^{-1}. The spectra presented in this chapter are difference spectra, i.e., the spectrum of the activated zeolite is subtracted from the spectrum of the zeolite after adsorption of the molecules. In this mode of presentation, all IR bands pointing upwards increased in intensity and all pointing downwards decreased in intensity, upon sorbate adsorption.

6.2.3 Temperature programmed desorption (TPD)

Desorption measurements were carried out in a quartz sample holder connected to a UHV chamber with a mass spectrometer (Balzers QMG 420). About 30-50 mg of zeolite powder was activated *in situ* by heating up in vacuum ($p < 10^{-3}$ mbar) to 723 K at a rate of 10 $K \cdot min^{-1}$ and holding this temperature for 1 h. After cooling down to 308 K, the sample was exposed to the desired sorbate and equilibrated at a pressure of approximately 10 mbar. After evacuation for 1 h at 10^{-3} mbar and 308 K to remove

weakly physisorbed molecules, the TPD profile was recorded during a temperature increment of 10 $K \cdot min^{-1}$ between 308 and 873 K and normalized to the sample weight.

6.3 Results

The elemental composition of the studied materials is given in Table 6.1. The results show that the Si/Al ratio of MCM-22 is comparable to that of ITQ-2, while the absolute Al concentration in the MCM-22 layer of the MCM-36 materials is higher than the overall Si/Al ratio, due to the incorporation of silica pillars. The Na^+/Al and Rb^+/Al ratio of approximately 1 for MCM-22 and ITQ-2 indicates that the samples were completely in the cation form, while for MCM-36 with M^+/Al ratios of 0.52 and 0.42 for the Na^+- and Rb^+-samples a fraction of protons remained unexchanged. The Si/Al ratio of MCM-22 was more affected by the ion exchange than the ratio of MCM-36 and ITQ-2 attributed to extra framework species present in the pore system of the MCM-22 precursor material. Those species are removed either during ion exchange of MCM-22 or by the further modification treatments of the precursor to MCM-36 and ITQ-2. The XRD patterns of the parent materials and their exchanged forms [12] correspond well to those reported in the literature [19]. A slight broadening of the peaks in the patterns of Rb-MCM-22 might result from a structural disordering of the framework caused by these large cations. Also the broadening of the XRD lines of cation exchanged MCM-36 [12] is attributed to structural disordering caused by alkali cations or/and the exchange treatment. The low-angle XRD of MCM-36 and its alkali derivatives exhibited intense peaks centered at $2\theta = 1.62°$ indicating *d*-spacing of ca. 5.4 nm and interlayer distances of 3 nm. For ITQ-2, the XRD lines characteristic of MCM-22 layers are hardly visible. They have to be strongly broadened, as a result of a reduction of the particle size to nm scale and a very small thickness of the layers during ultrasound treatment [23]. The specific BET surface area and micropore volume of the materials are also summarized in Table 6.1. The MCM-36 materials and the Na^+-exchanged materials exhibited the largest specific surface areas and micropore volumes. Enhanced increase of the specific BET surface area after modification and ion exchange for all MCM-36 and ITQ-2 indicates successful pillaring and exfoliation. The lowering of the micropore volume for ITQ-2 is in line to the loss of the supercages on MCM-22 monolayers due to delamination of the MCM-22 precursor.

Table 6.1 Elemental composition and structural properties of the studied MCM-22, MCM-36, and ITQ-2 materials.

Sample	MCM-22, MCM-36, and ITQ-2 samples in calcined form					
	Si/Al	SiO_2 [mol%]	Al_2O_3 [mol%]	Na_2O or Rb_2O [mol%]	BET surface area [$m^2 \cdot g^{-1}$]	Micropore volume [$m^3 \cdot g^{-1}$]
MCM–22	35.0	97.9	1.4	0.8	360	0.08
Na-MCM–22	34.8	97.5	1.4	1.7	285	0.06
Rb-MCM–22	35.5	95.1	1.3	1.4	242	0.03
MCM–36	28.4	98.3	1.7	0.1	710	0.14
Na-MCM–36	29.9	97.2	1.6	1.2	664	0.11
Rb-MCM–36	29.4	97.1	1.7	1.2	600	0.03
ITQ–2	33.3	98.5	1.5	0	523	0.06
Na-ITQ–2	35.7	97.3	1.4	1.4	489	0.05
Rb-ITQ–2	36.0	97.2	1.3	1.4	422	0.04

6.3.1 Infrared spectra of the activated materials

The IR spectra of the Rb^+-exchanged materials after activation are compiled in Figure 6.2. The spectra show typical bands in the ν(OH) stretching region of surface-OH groups. The sharp band at 3745 cm^{-1} is assigned to isolated Si-OH groups mainly located on the external surfaces of the zeolite crystals, while the weak and somewhat broader band at 3720 cm^{-1} is assigned to weakly hydrogen bonded Si-OH groups at defect sites. The band at 3670-3660 cm^{-1} is ascribed to Al-OH groups partially anchored to the zeolite framework (a product of incipient dealumination [7]) and to hydroxylated, extra framework aluminum species. The broad band between 3300 and 3600 cm^{-1} is attributed to hydrogen bonded external and internal Si-OH goups[20]. With increasing specific surface area of the activated materials the intensity of the IR bands of the terminal and internal Si-OH and extra framework Al-OH groups increased. Bands indicating bridging SiOHAl hydroxyl groups (3620 cm^{-1}), were only detected in the IR spectrum of MCM-36, assuming the presence of a low concentration of Brønsted acid hydroxyl groups on these materials.

6.3.1.1 Adsorption of carbon dioxide

In Figure 6.3, the infrared spectra of CO_2 adsorbed on several Rb^+-exchanged zeolites and zeolitic materials are shown after equilibration with $5 \cdot 10^{-3}$ mbar CO_2 at 308 K. The ν(CO) stretching band of CO_2, coordinated with one of the oxygen atoms

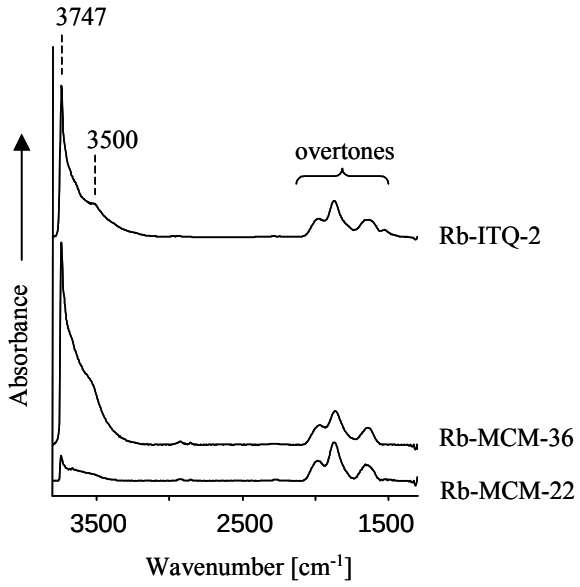

Figure 6.2 IR spectra of the Rb^+-exchanged MCM-22, MCM-36, and ITQ-2 after activation for 1 h at 723 K; T = 308 K, $p < 10^{-6}$ mbar.

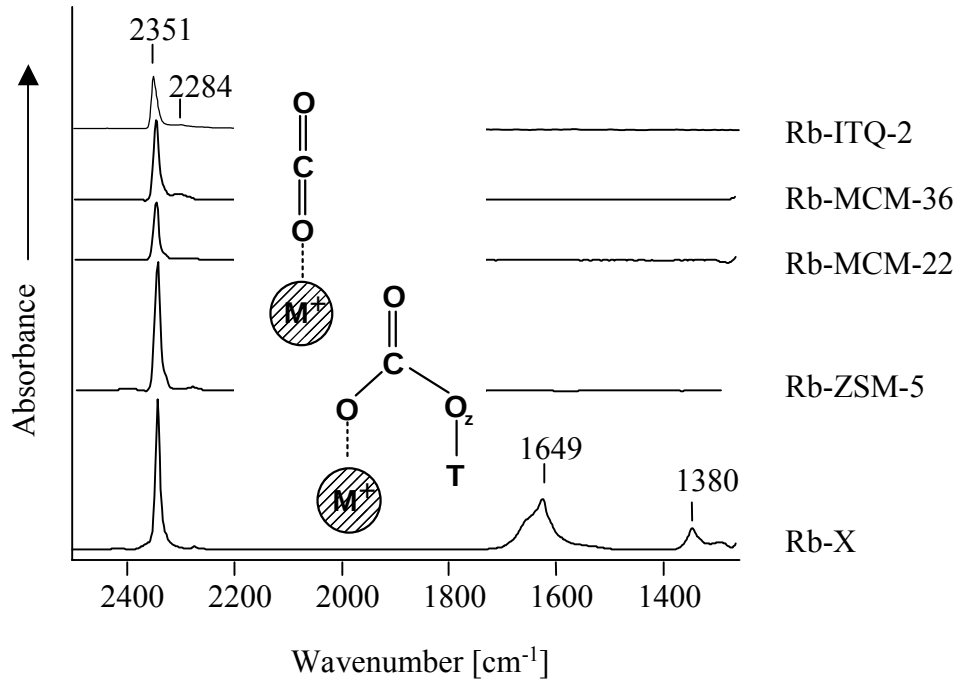

Figure 6.3 Difference IR spectra of adsorbed CO_2 on Rb^+-exchanged MCM-22, MCM-36, and ITQ-2 after reaching adsorption-desorption equilibrium at 1 mbar partial pressure; T = 308 K, $p = 5 \cdot 10^{-3}$ mbar.

to the rubidium cation was seen at 2351 cm^{-1}. The weak band at 2284 cm^{-1} is due to the $\nu(^{13}CO)$ stretching vibration of the natural abundant $^{13}CO_2$ isotope [21]. None of the MCM-type materials showed bands in the carbonate region 1700-1300 cm^{-1}. Only for the aluminum rich Rb-X, bands were seen at 1649 and 1380 cm^{-1}. These bands are assigned to the antisymmetric and symmetric ν(OCO) stretching vibration, respectively [22].

6.3.1.2 Adsorption of pyridine and 2,6-DTBPy

IR spectroscopy of adsorbed pyridine [8] and 2,6-ditertbutyl pyridine (2,6-DTBPy) [11] (Figure 6.4) on Brønsted acidic materials was used to probe the ion exchange sites and to distinguish between sites located in the zeolite pores and on the external surface/pore mouth of the layered materials [11, 23]. The band at 1542 cm^{-1} indicates pyridinium ions formed on strong Brønsted acid sites, pyridine adsorbed on strong Lewis acid (accessible Al^{3+}) species sites leads to a band at 1453 cm^{-1} [24, 25]. The band at 3365 cm^{-1} after adsorption of 2,6–DTBPy [11] on the Brønsted acidic materials, is assigned to the ν(NH) stretching vibration of $DTBPyH^+$ ions. For the quantification of the total concentration of Brønsted acid sites and the concentration (of Brønsted acid sites) on the external surface, the intensities of the characteristic bands of adsorbed pyridine and 2,6-DTBPy (1453 cm^{-1} and 3365 cm^{-1}) were used. The areas of the 1545 cm^{-1} band of pyridinium ions (Table 6.2) of H^+-exchanged MCM-22, MCM-36, and ITQ-2 show that the relative concentrations of adsorbed pyridine differ slightly for the three samples. Note that the presence of sodium in MCM-22 reduces the amount of pyridine adsorbed. The lower value for fully H^+-exchanged MCM-36 in combination with the high overall concentration of aluminum in the sample points to a lower concentration of aluminum in tetrahedral positions. Some of those sites might also not be accessible due to the introduction of the silica pillars. The relative concentration of adsorbed 2,6-DTBPy is increasing from MCM-22 to MCM-36 and to ITQ-2. This indicates an enhanced number of sites accessible to 2,6-DTBPy present after pillaring and exfoliation.

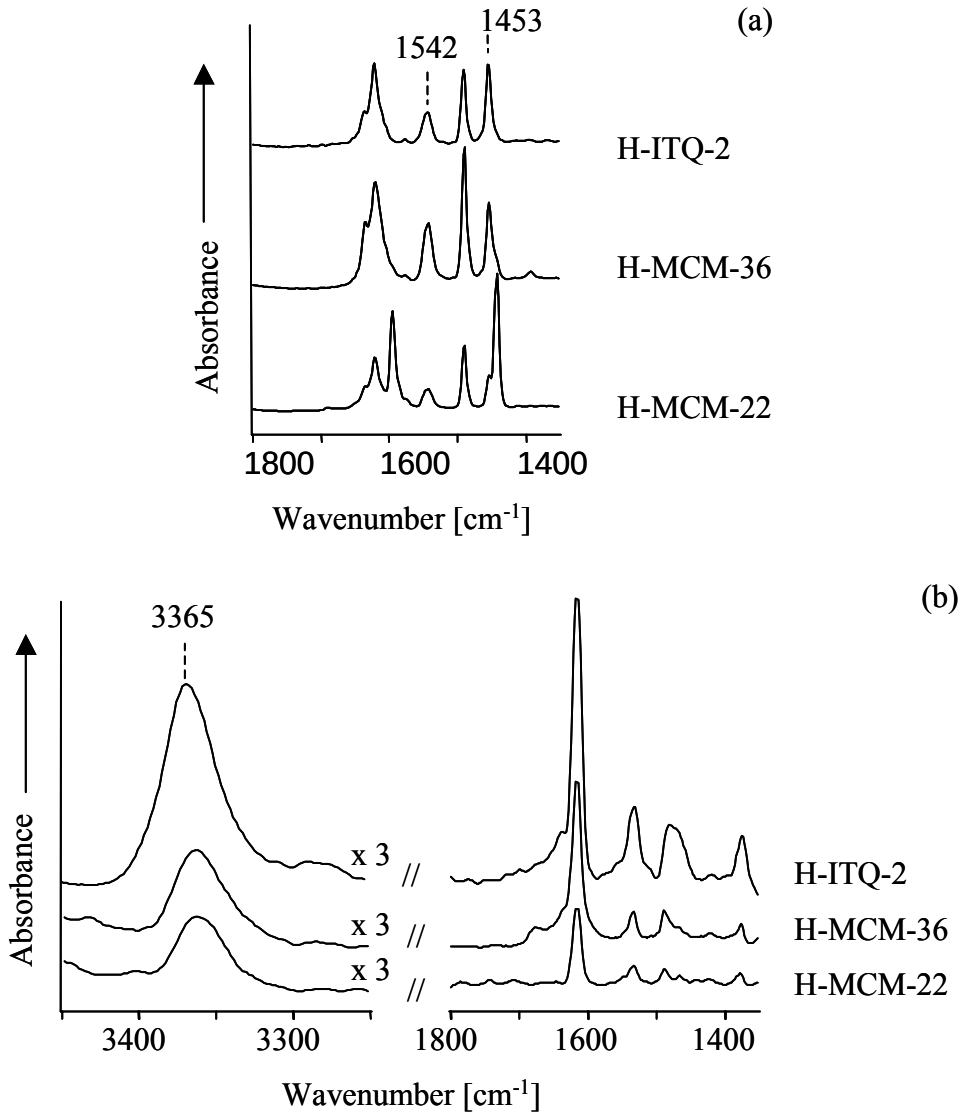

Figure 6.4 IR spectra of adsorbed (a) pyridine and (b) 2,6–DTBPy on H-MCM-22, H-MCM-36, and H-ITQ-2 after reaching adsorption/desorption equilibrium at 10^{-2} mbar partial pressure of the base and evacuation for 60 min.; T = 373 K, $p < 10^{-6}$ mbar.

Table 6.2 Relative adsorption capacity of H-MCM-22, H-MCM-36, and H-ITQ-2 for pyridine and 2,6-DTBPy adsorbed on Brønsted acid hydroxyl groups; the areas of the bands at 1534 and 3365 cm^{-1} are normalized to the molar concentrations of aluminum in the material.

Sample	Pyridine [IR area 1534 cm^{-1}/mol Al]	DTBPy [IR area 3365 cm^{-1}/mol Al]
H-MCM-22	1.0	1.0
H-MCM-36	0.9	1.6
H-ITQ-2	1.2	3.4

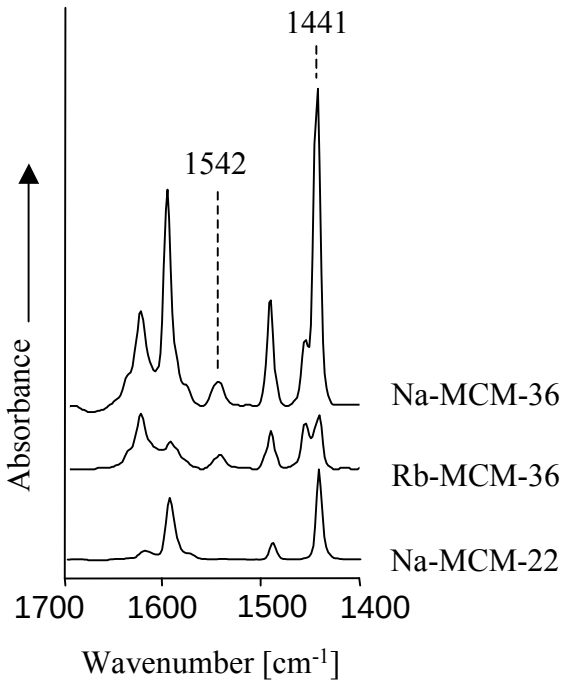

Figure 6.5 IR spectra of adsorbed pyridine on Na^+- and Rb^+-exchanged MCM-36 after reaching adsorption/desorption equilibrium at $1 \cdot 10^{-2}$ mbar partial pressure of the base and evacuation for 60 min.; T = 373 K, $p < 10^{-6}$ mbar.

After adsorption of pyridine, only alkali metal cation-exchanged MCM-36 showed a band at 1543 cm^{-1} indicating the presence of Brønsted acid sites (Figure 6.5). In order to preserve the zeolitic structure, the ion exchange had to be performed at pH 4, which did not provide complete alkali metal cation exchange [12]. Note, that a great selectivity of zeolite A and X for H_3O^+ has been reported at near neutral pHs [26, 27]. As the pH decreases, the extent of H_3O^+ exchange increases [28, 29]. The band at 1442 and 1440 cm^{-1} are assigned to pyridine coordinated to Na^+ and Rb^+, respectively [12].

6.3.1.3 Adsorption of methanol and 1-propanol

The bands of adsorbed alcohols were assigned using IR spectra of methanol (Table 6.3) and 1-propanol (Table 6.4) in the gaseous, liquid and adsorbed state. In Figure 6.6, the IR spectra of methanol adsorbed on Na^+-exchanged materials at 308 K are shown after equilibration at $5 \cdot 10^{-3}$ mbar. The difference of the IR spectra of Na-MCM-22 in contact with $5 \cdot 10^{-3}$ mbar methanol and the infrared spectrum of the activated material showed that the ν(OH) stretching vibration band of terminal silanol groups at 3747 cm^{-1} decreased in intensity, while the ν(OH) bands of methanol-OH

groups at 3604 cm^{-1} and 3478 cm^{-1} appeared. In addition, $\nu(CH_3)$ stretching vibration bands appeared at 2994, 2957, and 2851 cm^{-1}. After adsorption of methanol on MCM-36 a strong negative Si-OH band at 3743 cm^{-1} and a negative band at 3674 cm^{-1} assigned to hydroxylated, extra framework aluminum species appeared, while in the region 3610-3100 cm^{-1} a very broad band with structures at 3606, 3511 and 3420 cm^{-1} was seen indicating adsorbed methanol monomers and polymers, as well as silanol OH-groups perturbed by hydrogen bond formation. The adsorption of methanol on Na-ITQ-2 exhibited similar to MCM-36 strong and broad negative bands in the ν(OH) stretching vibration region 3750-3600 cm^{-1} and a broad ν(OH) feature between 3600 and 3100 cm^{-1}. Both materials (MCM-36 and ITQ-2) exhibited $\nu(CH_3)$ bands similar to MCM-22.

Methanol adsorption on the Rb^+-exchanged materials led to infrared spectra also shown in Figure 6.6. The OH-stretching bands of methanol adsorbed on Rb-MCM-22 appeared at 3609 cm^{-1}. This is markedly lower than the band in gaseous methanol, but slightly higher than for methanol adsorbed on Na-MCM-22. The negative OH-bands

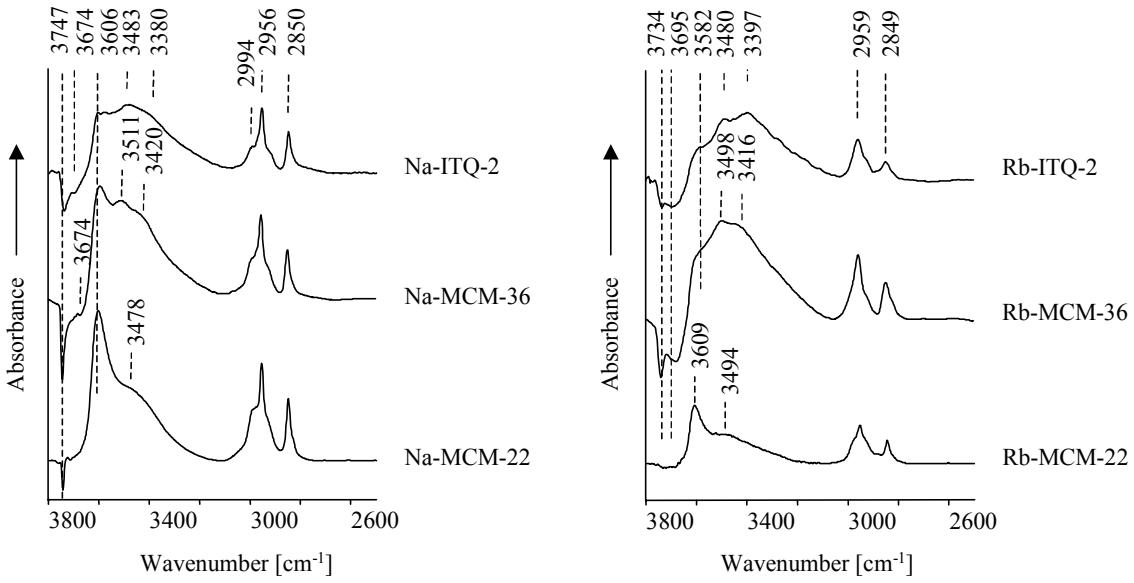

Figure 6.6 Difference IR spectra of adsorbed methanol on Na^+- and Rb^+-exchanged MCM-22, MCM-36, and ITQ-2 after reaching adsorption/desorption equilibrium at $5 \cdot 10^{-3}$ mbar partial pressure; T = 308 K.

Table 6.3 Infrared vibrations of methanol in the gaseous and adsorbed states. [a]

gaseous [36]	liquid [41]	Adsorbed on		Assignment [b]	Adsorbed on					
		Na-X [13]	Na-ZSM-5 [13]		Na-MCM-22	Na-MCM-36	Na-ITQ-2	Rb-MCM-22	Rb-MCM-36	Rb-ITQ-2
				ν(OH) terminal Si-OH	3747	3743	3739		3738	3734
				ν(OH) internal Si-OH	3716	3716 sh				
				ν(OH) extra framework Al-OH		3674	3698		3679	3695
3682 s			3612	ν(OH) MeOH monomer	3604 s	3606	3606	3609	3605	3582
	3337 s, br	3460 sh, 3341 s, br		ν(OH) MeOH polymer	3478 sh,	3511	3483	3494	3498	3480
				ν(OH) surface Si-OH	3390 sh	3420 sh	3394		3416 sh	3397
2999, 2970	2934	2980 sh, 2957 br	2991, 2957	$\nu_{as}(CH_3)$	2994, 2957	2992, 2957	2991, 2955	2976, 2954	2958 br	2959 br
2920		2917		2 x $\delta(CH_3)$	2919	2919	2919	2919	2919	2919
2844	2822	2839 br	2853	$\nu_s(CH_3)$	2851	2851	2850	2946	2849 br	2849 br
1477, 1465, 1454	1475, 1453	1476, 1451	1473, 1463, 1454	$\delta_{as}(CH_3)$	1476, 1454	1474, 1453	1469 br	1478, 1451	1472 br	1464 br
1340	1420 br	1423 sh	1357, 1344	δ (OH)	1359	1359	1360			

[a] in cm^{-1}

[b] ν_{as} = asymmetric stretching, ν_s = symmetric stretching, δ_{as} = asymmetric bending; sh = shoulder; br = broad

Table 6.4 Infrared vibrations of 1-propanol in the gaseous and adsorbed states [a].

gaseous [42]	liquid [42,43]	Adsorbed on NaX [b]	Assignment [c]	Adsorbed on					
				Na-MCM-22	Na-MCM-36	Na-ITQ-2	Rb-MCM-22	Rb-MCM-36	Rb-ITQ-2
				3742	3743	3744	3738	3742	3742
						3690 sh	3685 w sh	3684	3675 br
3687			ν(OH) monomer	3595	3588	3588	3601	3592	3597
	3356	3459 sh, 3327 br	ν(OH) polymer	3484 sh, br	3434 br	3481 sh, br 3385 sh, br	3496 sh, br	3460 br	3465 sh, 3370 br
2978	2967	2958, 2953 sh	$\nu_{as}(CH_3)$	2969	2968	2969	2965	2967	2967
2946	2933	2937	$\nu_{as}(CH_2)$, $\nu_s(CH_3)$	2940	2942	2942	2939	2941	2940
2892	2874	2875 s	$\nu_s(CH_2)$	2883	2885	2885	2882	2884	2883
		1474 w	$\delta(CH_2(O))$	1476 sh	1488 sh 1477 sh	1477 sh	1477 sh	1488 sh 1476 sh	
1464	1464	1463 sh, 1459	$\delta_{as}(CH_3)$ $\delta(CH_2)$	1461	1462 b	1461	1461	1463	1463
		1436 sh	$\delta(CH_2(C))$	1440 sh	1443		1442	1442 sh	1441 w
1393	1381	1395	$\omega(CH_2)$	1392 br	1398	1398	1400	1399	1397
1393		1391	$\delta_s(CH_3)$		1380 sh	1380 sh,	1381 sh	1381 sh	1378 sh
1218	1340	1343	$\delta(COH)_{ip}$		1347		1345	1346	1346

[a] in cm^{-1}

[b] see Chapter 3

[c] ν_{as} asymmetric stretching, ν_s = symmetric stretching, δ_{as} = asymmetric bending; sh = shoulder; br = broad

at 3679 and 3695 cm^{-1} (OH groups on extra-framework species) of Rb-MCM-36 and Rb-ITQ-2, respectively, were more intense than with Rb-MCM-22 suggesting that an increased fraction of OH defect sites interacted with methanol. It is important to note that the shape of the broad band 3600-3100 cm^{-1} changed compared to the Na^+ exchanged materials, i.e., the intensities of the contributions at 3416 and 3397 cm^{-1} are more pronounced for the samples containing cations with lower Lewis acid strength.

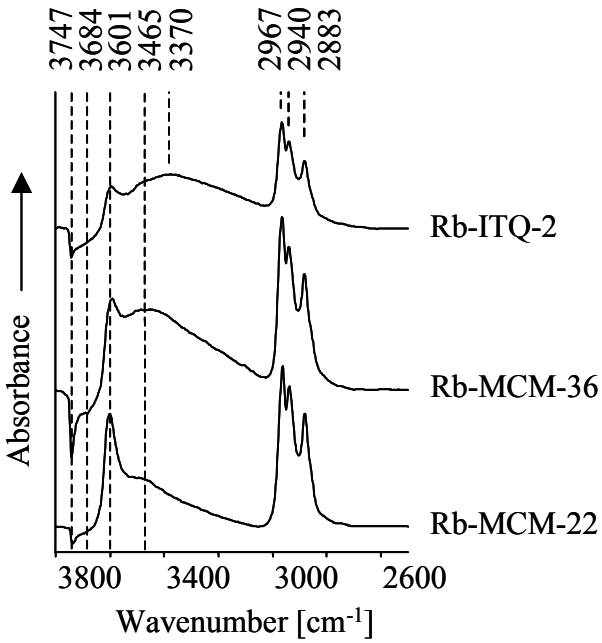

Figure 6.7 Difference IR spectra of adsorbed 1-propanol on Rb^+-exchanged MCM-22, MCM-36, and ITQ-2 after reaching adsorption/desorption equilibrium at $5 \cdot 10^{-3}$ mbar partial pressure; T = 308 K.

When $5 \cdot 10^{-3}$ mbar of 1-propanol was adsorbed on alkali metal cation exchanged MCM-22, MCM-36 and ITQ-2 (Figure 6.7) similar band profiles were seen. The materials differ in the intensity of the negative OH-bands of silanol groups and hydroxyl groups located on extra framework aluminum species. The ν(OH) band at around 3600 cm^{-1} attributed to weakly perturbed methanol-OH groups was better visible for adsorbed 1-propanol than for methanol, while the broad band at 3600-3100 cm^{-1} was less structured indicating a higher number of different sorption states of hydrogen-bonded silanol groups. The ν(CH) bands (3000-2880 cm^{-1}) were similar to those of liquid 1-propanol [30].

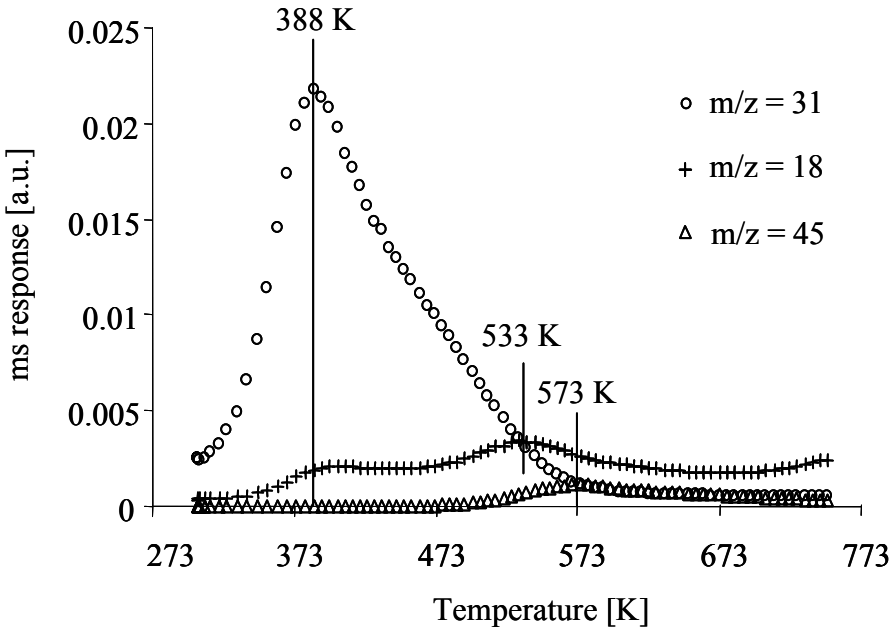

Figure 6.8 Temperature programmed desorption of methanol (m/z = 31), water (m/z = 18), and dimethyl ether (m/z = 45) from Na^+-MCM-36; T = 308-723 K; $p < 10^{-3}$ mbar.

6.3.2 Temperature programmed desorption of methanol adsorbed on MCM-36

In Figure 6.8, the TPD of methanol adsorbed on Na-MCM-36 is shown. Methanol desorption occurred over a broad temperature range (300-573 K) and showed a maximum at 388 K and a very broad shoulder at higher temperatures between 373 and 573 K. The maximum is attributed to methanol molecules hydrogen bonded to surface silanol groups and weakly coordinated to the counter cations. The broad shoulder is tentatively attributed to methanol coordinated to strong Brønsted acid sites, and strong Lewis acid sites (generated by dealumination). The masses 18 and 45 corresponding to water (m/z 18) and dimethylether (m/z 45) desorbed with maxima at 533 and 573 K from MCM-36, respectively. The acid catalyzed formation of dimethylether from methanol agrees with that experimentally found over H-ZSM-5 [31] and was also calculated using density functional theory [32].

Ion exchange of MCM-36 did not shift the first maximum of desorption of methanol (Figure 6.9) significantly to lower temperatures supporting its attribution to the desorption of methanol from silanol groups presumably located in the interlayer galleries. The decreased shoulder of methanol desorption for Rb-MCM-36 [12] indicates that methanol coordinatively bound to alkali metal cations desorbed at relatively low temperatures. Note that the lower amount of methanol adsorbed on the sample

containing the less Lewis acid counter cation is also correlated with the lower number of cations present per sample weight and the lower micropore volume (Table 6.1). If 1-propanol was used as sorbate on Rb-MCM-36 (Figure 6.10), besides molecular desorption occurring up to 500 K, dehydration of 1-propanol to water and propene (masses 18 and 41) was seen at 530 K.

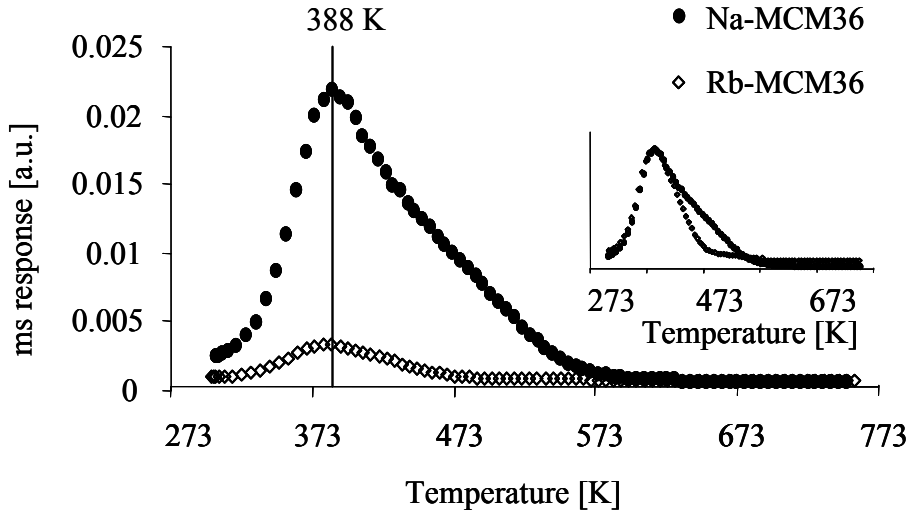

Figure 6.9 Temperature programmed desorption of methanol (m/z = 31) adsorbed on Na^+- and Rb-MCM-36; T = 308-723 K; p < 10^{-3} mbar.

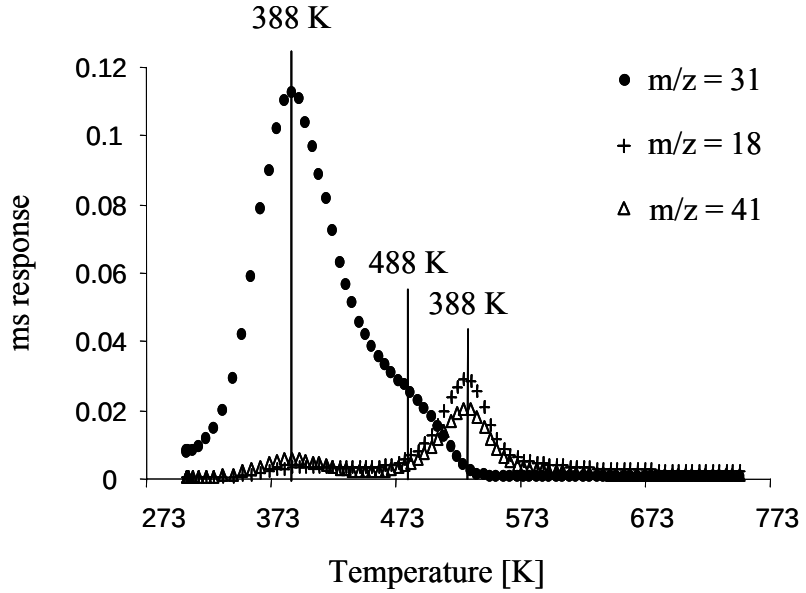

Figure 6.10 Temperature programmed desorption of 1-propanol (m/z = 31), water (m/z = 18), and propene (m/z = 41) from Rb-MCM-36; T = 308-723 K; p < 10^{-3} mbar.

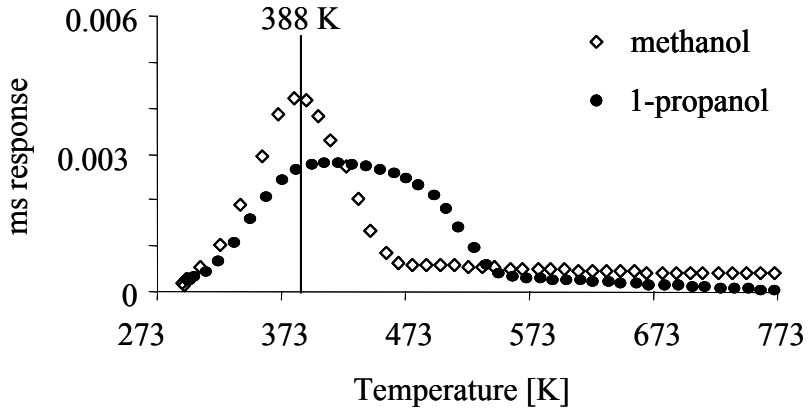

Figure 6.11 Temperature programmed desorption of methanol (m/z = 31) and 1-propanol (m/z = 31) adsorbed on Rb-MCM-22; T = 308-723 K; $p < 10^{-3}$ mbar.

TPD of methanol and 1-propanol from Rb-MCM-22 are shown in Figure 6.11. Similar to the results obtained for MCM-36, the main desorption peak occurred at 388 K, attributed mainly to methanol coordinated to the alkali metal cations (The Si-OH concentration in MCM-22 is low). Desorption of 1-propanol is distributed over a wider temperature range (323-553 K).

6.4 Discussion

6.4.1 Structural and acid-base properties

6.4.1.1 Structural properties

The transformation of the MCM-22 precursor to MCM-36 and ITQ-2 materials leads to an increased specific surface area (Table 6.1) and an improved accessibility of larger molecules to the active sites on the external surface/pore mouth (Table 6.2). The rising concentration of terminal silanol groups (Figure 6.2) indicates the expansion of the specific surface area due to incorporation of silica pillars and delamination. Additionally, the concentration of defect sites increased. These sites are mainly formed during calcination. Note, that before calcination, the MCM-22 precursor exhibits a low number of defect sites [12]. Both alkali metal cation exchanged (Na^+ and Rb^+) materials exhibit defect sites. The broad band around 3670 cm^{-1} of the Rb^+-exchanged materials is more intense, compared to the one of Na^+-exchanged samples, indicating a higher degree of structural defects, which is attributed to the

stronger alkaline condition of the liquid ion-exchange using aqueous $RbNO_3$ solution. Note in this context that after treatment of the zeolitic materials in an acid or alkaline solution, morphological changes on the surface have been directly detected [33].

6.4.1.2 Acid-base properties

The absence of a band at 3622 cm^{-1}, assigned to Brønsted acid OH-groups, in the IR spectra of activated alkali metal cation exchanged MCM-22 and ITQ-2 (Figure 6.2) and the absence of the band at 1542 cm^{-1} after pyridine adsorption (Figure 6.5) indicate complete cation exchange in both materials. In contrast, on MCM-36 a small concentration of Brønsted acid sites is present; also suggested from the results of the elemental analysis (Table 6.1).

On all samples, CO_2 (Figure 6.3) was concluded to interact weakly with the metal cations *via* an $M^{+\cdots}O=C=O$ (end on) complex. This was inferred from the band at 2351 cm^{-1} being close to the antisymmetric stretching vibration of gas phase CO_2 (2349 cm^{-1}) [34]. The higher intensity of the band for materials with higher aluminum content (ZSM-5, MCM-36 and X) indicates that a larger concentration of CO_2 molecules was adsorbed, associated with a higher concentration of cations present per unit cell. In the IR spectrum of the alkali metal exchanged zeolite X, ν(OCO) stretching bands between 1725 to 1300 cm^{-1} (ascribed to carbonates) indicate that only the faujasite material show stronger basic properties. Under such circumstances the alkali metal cation acts as Lewis acid site and the adjacent framework oxygen as a basic site [22]. Thus, the absence of carbonates for all other materials is attributed to a lower average negative charge of the lattice oxygen due to the higher Si/Al ratio, impeding the formation of stable carbonates.

While the nature of the metal cation in materials with a relatively high Si/Al ratio is insufficient to influence the base properties so strongly that formation of carbonates is possible, the cations influence the strength of the Lewis acid sites sufficiently to induce weaker bonding of base molecules such as pyridine.

6.4.1.3 Increasing of the site accessibility

In MCM-36, the insertion of SiO_2 pillars between the MCM-22 layers increases the interlayer distance to about 3 nm [35], while exfoliation of the MCM-22 precursor

leads to single MCM-22 layers (ITQ-2) [18]. In both materials, the pore system consisting of sinusoidal 10-membered-ring channels remains intact [35]. The adsorption of pyridine and its larger derivative 2,6-DTBPy [23] is used to distinguish between acid sites located in the zeolite pores and on the external surface/pore mouth of the layered

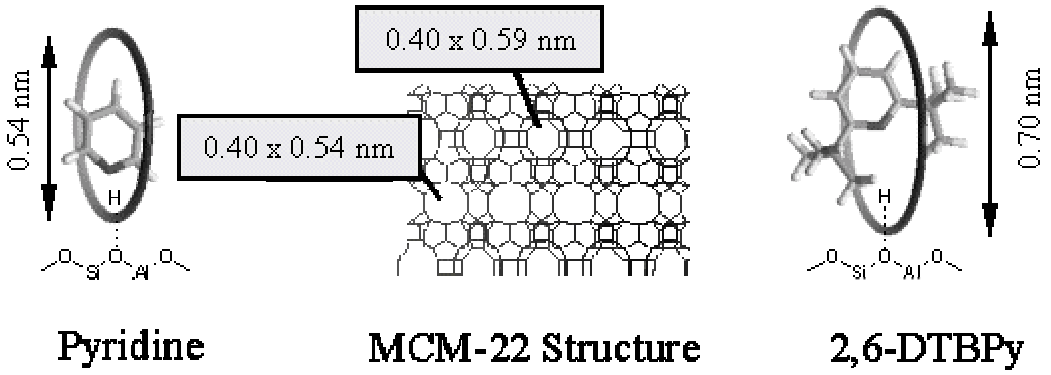

(a)

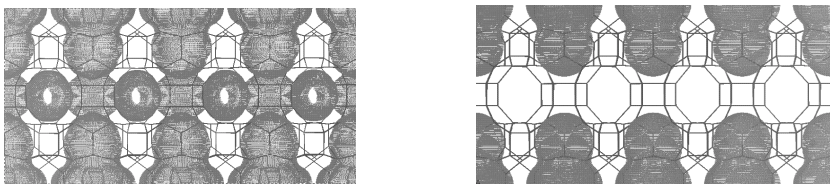

(b)

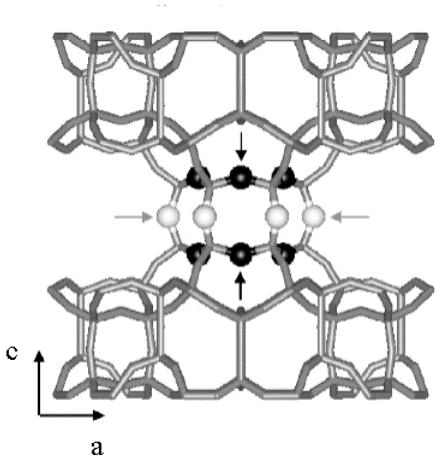

Figure 6.12. (a) Probing of accessibility to acid sites of MCM-22 monolayers by pyridine and 2,6-DTBPy adsorption; schematic representation of the zeolitic structure; (b) Possible locations of the bridged hydroxyl groups linked to hexagonal prisms between two supercages[7]; hydrogen atom pointing in the bottom of supercages (black) or in the sinusoidal pore channels (gray).

materials (Figure 6.12). Due to a larger kinetic diameter [23], 2,6-DTBPy cannot penetrate into the pores of MCM-22, while pyridine accesses the 10- and 12-membered ring channels and interacts with all acid sites. The similar amount of pyridine adsorbed per mol aluminum for all three materials indicates that a similar fraction of sites is accessible per aluminum atom. The rising concentration of adsorbed 2,6-DTBPy observed with MCM-36 and ITQ-2, indicates that an increased fraction of Brønsted acid sites interacts with the bulky base due to the better accessibility of the acid sites. Note that the larger fraction adsorbed on ITQ-2 fits especially well to the increased specific surface area and is in line with the distribution of Brønsted acid sites in the MCM-22 structure [7]. Meloni *et al*. [8] reported that about 50-70 % of all Brønsted-OH groups are located in the supercages, which should be accessible to 2,6-DTBPy after delamination. Further 20-30 % are in the sinusoidal channel and up to 25 % are linked to hexagonal prisms between two supercages for MCM-22 materials having a Si/Al ration of 30. The increased 2,6-DTBPy adsorption after pillaring and layer exfoliation is attributed mainly to the enhanced number of half-cups on the external surface of the MCM-22 layer, thus to the better accessibility of bridged hydroxyl groups trapped in the supercages of the MCM-22 crystal. Hydroxyl groups linked to the hexagonal prisms and pointing into the bottom of the supercage are not assumed to be reached by the steric challenging 2,6-DTBPy, while they might be considered for the slight enhanced pyridine adsorption on ITQ-2.

6.4.2 Adsorption of methanol on Na-MCM-22

The shift value of stretching and bending vibration bands of methanol adsorbed on Na-MCM-22 is expected to be related to the interaction of counter cations with the lone electron pair of the oxygen atom of the methanol molecule. This interaction weakens the O-H bond and results in a shift of the stretching and bending vibration bands of methanol. The ν(OH) stretching vibration band (3604 cm^{-1}), of methanol OH was found at significantly lower wavenumbers than in the gas phase (3682 cm^{-1} [36]). The narrow OH- and also the ν(CH_3) stretching vibration bands point to the absence of hydrogen bonds to the pore wall. The band of the symmetrical ν(CH_3) vibration (2851 cm^{-1}) is located at higher wavenumber than in the gas or liquid phase (band at

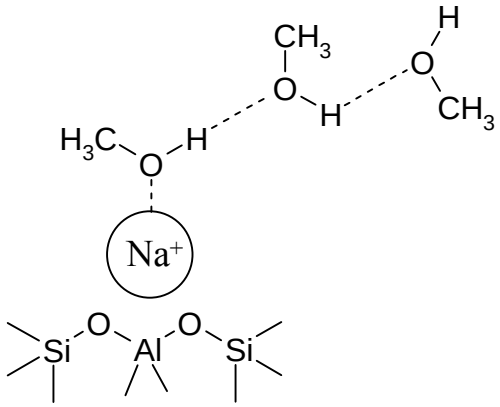

Figure 6.13 Schematic sorption structure of methanol coordinated to the sodium counter cation on Na-MCM-22.

2844 and 2822 cm^{-1}, respectively). This suggests that isolated methanol is coordinated *via* the oxygen atom to the counter cation without interaction to the zeolite framework as illustrated in Figure 6.13. Due to the low aluminum content, the zeolite framework oxygen is not strongly negatively charged, as already shown by the absence of carbonate formation after adsorption of carbon dioxide (Figure 6.3). Note that such an adsorption structure agrees well with structures, reported by Rep *et al.* [13], for Na-ZSM-5 with a similar Si/Al ratio.

With increasing equilibrium pressure, the broad band (maximum at 3478 cm^{-1}) increased in intensity with increasing equilibrium pressure and shifted to lower wavenumbers (3450 cm^{-1} at 1 bar). It is attributed to methanol OH groups of molecules adsorbed on the free hydroxyl group of an already adsorbed methanol [37]. Cluster formation has been confirmed also from gravimetric measurements, which show an average sorption of about three methanol molecules per cation site (at 13 mbar), similar to values found for ZSM-5 [13]. In addition, the band at 3747 cm^{-1} (associated with isolated Si-OH surface groups) decreased and the band at 3420 cm^{-1} increased suggesting weak hydrogen bonding of methanol on SiOH groups[38, 39].

6.4.3 Adsorption of methanol on Na-MCM-36 and Na-ITQ-2

6.4.3.1 Methanol adsorbed on MCM-36

On Na-MCM-36 (Figure 6.6), the adsorption of methanol caused several negative and broad ν(OH) bands (3750-3100 cm^{-1}) indicating that methanol is adsorbed at various surface OH groups. Beside (i) the interaction of isolated methanol molecules

to the exchanged alkali metal cations located in the MCM-22 zeolite layers (ν(OH) of the perturbed methanol-OH group at 3604 cm^{-1}), methanol interacts to (ii) a high number of Si-OH groups (negative band at 3747 cm^{-1} accompanied with a broad and intense band with signals approximately at 3511 and 3420 cm^{-1}) present due to the incorporation of silica pillars, and to (iii) a low number of Brønsted acid sites (negative band at 3622 cm^{-1}). The increased bandwidth between 3610-3100 cm^{-1} suggests a more pronounced distribution of the silanol and methanol-OH bonds. It is tentatively concluded that the mesoporous MCM-36 structure and the higher number of Si-OH groups enhances methanol clustering in the interlayer galleries.

6.4.3.2 Methanol adsorbed on ITQ-2

Besides the coordination of the sorbate molecules to the Lewis acid cations as described for MCM-22 (shoulder at about 3604 cm^{-1}), a high number of surface-OH sorption sites on ITQ-2, like on MCM-36, interacts to methanol seen by broad negative bands in the region 3750-3600 cm^{-1} accompanied with a very broad band between 3600-3100 cm^{-1}. The high number of terminal silanol groups (at 3747 cm^{-1}) is related to the high specific surface area upon delamination, while structural defects evidenced by internal silanol groups (3720 cm^{-1}) and OH groups on aluminum species (3670 cm^{-1}) are related to the hard conditions during delamination [18]. We speculate that the high site density together with the aggregation of small particles increase the number of silanol nests and enhance methanol clustering between the particles.

6.4.4 Comparison between sorption on Na^+ and Rb^+ cation exchanged materials

The ν(OH) stretching vibration of methanol, adsorbed on Rb-MCM-22 appeared at 3609 cm^{-1} compared to 3604 cm^{-1} after adsorption on Na-MCM-22 (Table 6.3). This shows that cations of low Lewis acid strength weaken the OH bond of the alcohol adsorbed less than Na^+. From the narrow half width of the methanol OH band, we conclude that hydrogen bonding between the methanol OH group and oxygen of the zeolite pore wall does not take place. For methanol coordinated to the counter cations on MCM-36 and ITQ-2, a similar trend is observed. The band at 3606 cm^{-1} decreased relatively in intensity when going from Na^+ to Rb^+ and the intensity of

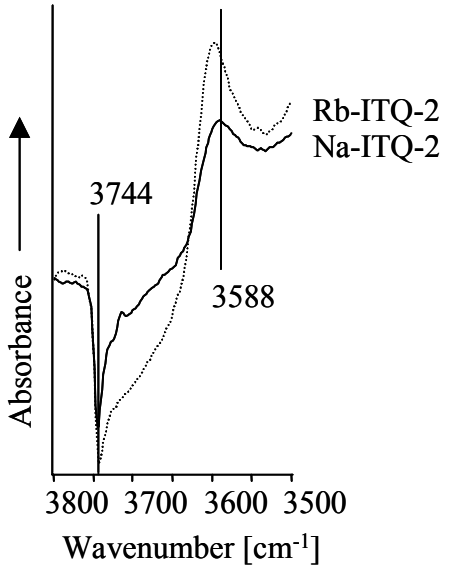

Figure 6.14 Difference IR spectra of adsorbed methanol on Na- and Rb-ITQ-2; T = 308 K; p = $5 \cdot 10^{-3}$ mbar.

fraction of stronger perturbed OH bands increased. It should be emphasized that the stronger perturbation is not a sign of a markedly stronger interaction between the zeolite and the sorbate, but rather indicative of molecule-molecule interactions. In this context it is noteworthy that the desorption of methanol from Rb-MCM-36 occurred at lower temperatures than with Na^+ cations indicating stronger sorption on the latter material. The adsorption of methanol on MCM-22 is completely reversible and all infrared absorption bands due to adsorbed species disappear upon evacuation and heating to 573 K. The stronger interaction of methanol with internal Si-OH and OH groups of extra framework Al species of Rb-MCM-36 and Rb-ITQ-2 (Figure 6.14) is attributed to a higher number of defects in these materials.

6.4.5 Influence of the hydrocarbon chain length on the sorption behavior

The ν(OH) stretching bands of adsorbed propanol and methanol are very similar. (Table 6.4). Thus, we conclude that the main interaction occurs with both molecules between the oxygen atom of the OH group and the alkali metal cation. The narrow half-width of the band between 3588 and 3601 cm^{-1} indicates only minor interactions between the OH group and other molecules and/or the zeolite surface. Thus, it is concluded that the increased chain length of 1-propanol does not affect the sorption structure. Again, cluster formation seems to be enhanced with increasing external

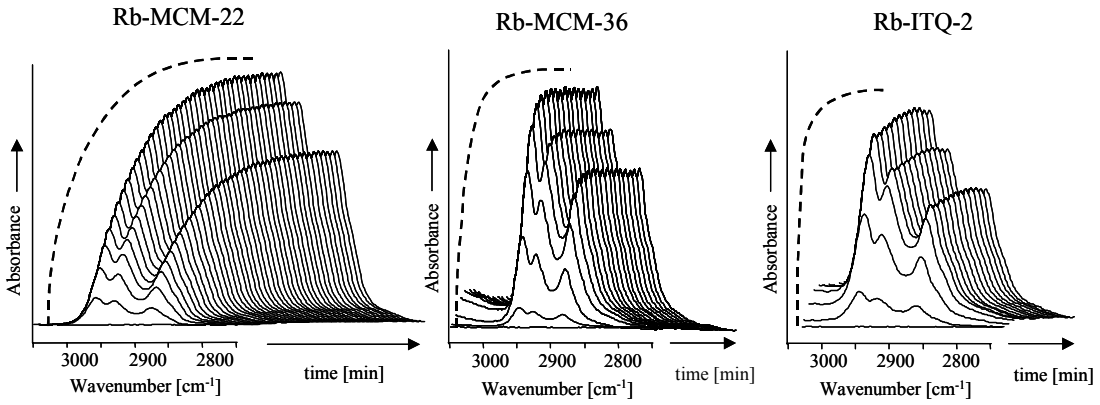

Figure 6.15. Time resolved difference IR spectra of adsorbed 1-propanol on Rb-MCM-22, Rb-MCM-36, and Rb-ITQ-2 during adsorption; one spectrum taken per min.; T = 308 K; p = 0 - $1 \cdot 10^{-3}$ mbar.

surface area thus increasing amount of Si-OH groups as seen from the broad band in the region 3600-3100 cm^{-1} in the spectra of MCM-36 and ITQ-2. With MCM-36 and even slightly earlier with ITQ-2, the adsorption-desorption equilibrium of 1-propanol at $1 \cdot 10^{-3}$ mbar is reached much faster than with MCM-22 (see Figure 6.15). Note that the difference between these materials is larger for 1-proapnol than for the smaller methanol. The faster equilibration, suggests a simplified accessibility of the active sites and a higher fraction of easily available sorption sites as concluded by 2,6-DTBPy adsorption.

6.4.6 Formation of dimethyl ether over acid sites

During TPD of adsorbed methanol from Na-MCM-36 desorption of water (m/z = 18) and dimethyl ether (DME; m/z = 46) occurred with maxima at 533 and 573 K. Note that molecularly sorbed methanol (m/z = 31) is mainly removed around 388 K (Figure 6.8) and the broad shoulder of this desorption peak indicates a high number of sites varying in strength. While in principal such reaction can be catalyzed by Brønsted and Lewis acid sites [40]. However, the Lewis catalyzed pathway is energetically by far more demanding. Thus, we attribute the formation of DME over the alkali metal cation exchanged MCM-36 materials to the presence of minor concentrations of Brønsted acid sites. Subsequent reactions of the ethers formed were not observed. Note that TPD of methanol from Rb-MCM-36 did not produce a significant amount of DME and water. The equilibrium in the ether formation is

minor shifted to DME on Rb-MCM-36 due to the lower amounts of protons and methanol present. After 1-propanol adsorption the simultaneous desorption of the masses m/z = 18 and 41 indicates the dehydration of 1-propanol to propene and water over Na- and Rb-MCM-36, which is also related to the presence of Brønsted acid hydroxyl groups.

6.5 Conclusions

The adsorption of short alcohols on structural related, alkali metal cation exchanged materials MCM-22, MCM-36, and ITQ-2 was investigated by IR spectroscopy. Methanol adsorption on alkali metal cation exchanged MCM-22 materials is similar to the adsorption on alkali metal cation exchanged ZSM-5. The adsorption of CO_2 on such materials does not lead to the formation of carbonate species. Thus, materials of the MWW structure type with Si/Al ratios about 30 do not exhibit pronounced basic properties. The low aluminum content, and the resulting low negative charge on the oxygens of the zeolite lattice impedes hydrogen-bond formation between the sorbate molecules and the zeolite framework leading to quasi-isolated alcohol molecules ordinated to the alkali metal counter cations. Next to the interactions with the alkali metal cations the high concentration of Si-OH groups on MCM-36 and ITQ-2 (due to delamination and/or incorporation of silica pillars into the MCM-22 structure) leads to sorbate clustering in the interlayer galleries of MCM-36 and in sheet aggregates of ITQ-2.

Adsorption of the sterically demanding base 2,6-DTBPy on the Brønsted acidic materials shows the accessibility to active Brønsted acid OH-groups to be enhanced with increasing interlayer space (MCM-36) or degree of delamination (ITQ-2). The larger concentration of 2,6-DTBPy adsorbed on ITQ-2 fits well to the higher number of Brønsted acid hydroxyl groups located in the supercages of MCM-22. The adsorption-desorption equilibrium is reached faster on ITQ-2 and MCM-36 than on MCM-22. The difference is even more dominant for 1-propanol than for methanol.

The presence of some Brønsted acid sites on MCM-36 leads to the dehydration of methanol and 1-propanol producing dimethyl ether and propene. These Brønsted acid sites have not been exchanged by cations during ion exchange due to the low pH value necessary to preserve the pillared MCM-36 structure and the high selectivity of zeolites to H_3O^+ ions. For catalytic reactions requiring the absence of Brønsted acid

sites, it is important to avoid leaching of the alkali cations. For catalysis by strong bases the concentration of aluminum in the lattice of such materials needs to be increased, which in turn leads to difficulties in the delamination procedure [23].

6.6 Acknowledgements

The authors thank the Deutsche Forschungsgemeinschaft (DFG) for financial support within the Sonderforschungsbereich SFB 338: *Adsorption an Festkörperoberflächen: Mikroskopische Analyse von Zuständen und Prozessen Teilprojekt B9*.

6.7 References

[1] Leonowicz, M.E.; Lawton, J.A.; Lawton, S.L.; Rubin, M.K. *Science* **1994**, 264, 1910.

[2] Rubbins, M.K.; Chu, P. *US Patent 4 954 325*, **1990** assigned to Mobil Oil Corporation.

[3] Cheng, J.C.; Degnan, T.F.; Beck, J.S.; Huang, Y.Y.; Kalyanaraman, M.; Kowalski, J.A.; Loehr C.A.; Mazzone, D.N.A. *Stud. Surf. Sci. Catal.* **1998**, 121, 53.

[4] Corma, A.; Marinez-Triguero, J. *J. Catal*. **1997**, 165, 102.

[5] Wu, P.; Komatsu, T.; Yashima, T. *Mircropor. Mesopor. Mater*. **1998**, 22, 343.

[6] Kumar, N.; Lindfors, L.-E. *Appl. Catal. A* **1996**, 147, 175.

[7] Onida, B.; Geobaldo, F.; Testa, F.; Crea, F.; Garrone, E. *Mircorpor. Mesopor. Mater.* **1999**, 30, 119.

[8] Meloni, D.; Laforge, S.; Martin, D.; Guisnet, M.; Rombi, E.; Solinas V. *Appl. Catal. A, General* **2000**, 215, 55.

[9] Roth, W.J.; Kresge, C.T.; Vartuli, J.C.; Leonowicz, M.E.; Fung, A.S.; McCullen, S.B. *Stud. Surf. Sci. Catal.* **1995**, 94, 301.

[10] He, Y.J.; Nivarthy, G.S.; Eder, F.; Seshan, K.; Lercher, J.A. *Micropor. Mesopor. Mater.* **1998**, 25, 207.

[11] Corma, A.; Fornés, V.; Forni, L.; Marquez, F.; Martinez-Triguero, J.; Moscotti, D. *J. Catal*. **1998**, 179, 451.

[12] Barth, J.-O.; Schenkel, R.; Kornatowski, J.; Lercher, J.A. *Stud. Surf. Sci. Catal*. **2001**, 135, 136.

[13] Rep, M.; Palomares, A.E.; Eder-Mirth, G.; van Ommen, J.G.; Rösch, N.; Lercher, J.A. *J. Phys. Chem. B* **2000**, 104, 8624.

[14] Huang, M.; Adnot, A.; Kaliaguine, S. *J. Catal.* **1992**, 137, 322.

[15] Mirodatos, C.; Pichat, P.; Barthomeuf, D. *J. Phys. Chem*. **1976**, 80, 1335.

[16] Barthomeuf, D. *Catal. Ref.-Sci, Eng*. **1996**, 38, 521.

[17] van Santen, R.A.; van Beest, B.W.H.; de Man, A.J.M, *Guidelines for Mastering the Properties of Molecular Sieves*, Plenum Press, New York, Ser. B: Physics **1990**, 221, 201.

[18] Corma, A.; Fornés, V.; Pergher, S.B.; Maesen, R.H.L.M.; Buglass, J.G. *Nature* **1998**, 396, 353.

[19] Lawton, S.L.; Leonowicz, M.E.; Partridge, R.D.; Chu, P.; Rubin, M.K. *Micropor. Mater*. **1998**, 25, 207.

[20] Bolis, V.; Busco, C.; Bordiga, D.; Uglieng, P.; Lamberti, C.; Zecchina, A. *Appl. Surf. Sci.* **2002**, 196, 56.

[21] McManus, J.B.; Zahniser, M.S.; Nelson, D.D.; Williams, L.R.; Kolb, C.E. *Spectrochim. Acta A* **2002**, 58, 2465.

[22] Doskocil, E.J.; Davis, R.J. *J. Catal*. **1999**, 183, 353.

[23] Schenkel, R.; Barth, J.-O.; Kornatowski, J.; Lercher, J.A. *Stud. Surf. Sci. Catal*. **2002**, 142, 69.

[24] Ward, J.W. *J. Cat*al. **1967**, 9, 225.

[25] Lercher, J.A.; Gründling, Ch.; Eder–Mirth, G. *Catal. Today*, **1996**, 27, 353.

[26] Zhu, L.; Seff, K.; Olson, D.H.; Cohen, B.J.; Von Dreele, R.B. *J. Chem. Phys. B* **1999**, 103, 10365.

[27] Cook, T.E.; Cilley, W.A.; Savitsky, A.C.; Wiers, B.H. *Environ. Sci. Technol*. **1982**, 16, 344.

[28] O'Connor, J.F.; Townsend, R.P. *Zeolites* **1985**, 5, 158.

[29] Drummond, D.; De Jonge, A.; Rees, L.V.C. *J. Phys. Chem*. **1983**, 87, 1967.

[30] Max, J.-J.; Daneault, S.; Chapados, C. *Can. J. Chem*. **2002**, 80, 113.

[31] Lercher, J.A.; Mirth, G.; Stockenhuber, M.; Narbeshuber, T.; Kogelbauer, A. Acid-Base Catalysis II, *Communication* **1994**, 2.6, 147.

[32] Blaszkowski, S.R.; van Santen, R.A. *J. Phys. Chem. B* **1997**, 101, 2292.

[33] Yamamoto, S.; Sugiyama, S.; Matsuoka, O.; Kohmura, K.; Honda, T.; Banno, Y.; Nozoye, H. *J. Phys. Chem*. **1996**, 100, 18474.

[34] Concepción-Heydorn P.; Jia, C.; Herein, D.; Pfaender, N.; Karge, H.G.; Jentoft, F.C. *J. Mol. Catal. A: Chemical* **2000**, 162, 227.

[35] Roth, W.J.; Kresge, C.T.; Vartuli, J.C.; Leonowicz, M.E.; Fung, A.S.; McCullen, S.B. *Stud. Surf. Sci. Catal.* **1995**, 94, 301.

[36] Serallach, A.; Meyer, R.; Günthard, Hs.H. *J. Mol. Spectrosc*. **1974**, 52, 94.

[37] Mirth, G.; Lercher, J:A.; Anderson, M.W.; Klinowski, J. *J. chem.. Soc., Faraday Trans*. **1990** 86, 3039.

[38] Hair, M. L. *Infrared Spectroscopy in Surface Chemistr*y; Marcel Dekker: New York, **1967**.

[39] Morrow, B.A.; Thomson, L.W.; Wetmore, R.W. *J. Catal*. **1973**, 28, 332.

[40] Ballantine, J.A.; Davis, M.; Purnell, H.; Payanakorn, M.; Thomas, J.M.; Williams, K.J.; *J. Chem. Soc. Chem. Commun.*, **1981**, 427.

[41] Falk, M.; Whalley, E. *J. Chem. Phys.* **1961**, 34, 1554.

[42] Fukushima, K.; Zwolinski, B.J. *J. Mol. Spectr*. **1986**, 26, 368.

[43] Max, J.-J.; Daneault, S.; Chapados, C. *Can. J. Chem*. **2002**, 80, 113.

Chapter 7

Adsorption of methanol on MCM-36 derivatives with strong acid and base sites

Abstract

The sorption of methanol on MCM-22 and MCM-36 materials was studied using mainly IR spectroscopy. MCM-36 materials pillared with (mixed) oxides such as SiO_2, Al_2O_3, MgO-Al_2O_3, and MgO-Al_2O_3-SiO_2, exhibit widely varying acid-base properties. Methanol is associatively adsorbed on Brønsted acid sites in the zeolitic micropores and associatively and dissociatively on acid and base sites in the mesopores. Lewis acid/base sites are responsible for dissociative adsorption. Stable formates were only formed upon heating MgO-Al_2O_3-MCM-36 saturated with methanol.

7.1 Introduction

Expansion of distances between zeolitic layers by oxide incorporation leads to materials, which combine the microporosity of the zeolitic layers with regular mesopores. MCM-36 [1] is a typical example of such a material. It is synthesized from an uncalcined MCM-22 [2] precursor. The two-dimensional pore system of the MCM-22 layers with 10-membered ring openings is maintained in the pillared MCM-36 materials, while the pillars incorporated between the layers create mesopores with widths of 2 to 3.5 nm and high BET surface areas of 600-800 m^2/g [3]. Depending upon the nature of the intercalating material the pillaring process yields MCM-36 derivatives with specific acid-base properties [4, 5]. Materials with basic properties result from intercalation of appropriate alkaline earth metal oxide aluminates [4, 5]. Their occurrence together with strong BA-sites present in the material skeleton opens new perspectives for applications in heterogeneous catalysis.

The distinctively different sorption zones of the zeolitic and the (mixed) oxide pillars increase the complexity of the surface structures and chemical reactivity. However for both zones, excellent reference studies exist, covering adsorption in zeolitic materials (see e.g., refs. [3, 6, 7, 8, 9, 10]) and on (mixed) oxides (see e.g., refs [5, 11, 12, 13, 14] for materials with acidic and refs. [15, 16] for materials with basic properties). On acid zeolites, and, hence, also in the crystalline part of MCM-36, methanol interacts mainly with Brønsted acid OH groups leading to molecularly sorbed species stabilized by hydrogen bonds as well as to methoxy groups. Methanol adsorption at elevated temperatures on Si-O-Si sites [17] of silica leads also to $SiOCH_3$ and Si-OH surface species. With respect to the sorption on the pillars it should be noted that on silica, methanol is weakly hydrogen bonded to Si-OH groups [18]. Adsorption of methanol on alumina leads to a variety of species, including methanol hydrogen bonded to surface OH groups and basic oxygen, strongly chemisorbed methanol molecules, and bridging methoxy species coordinated to Lewis acid sites [19]. Surface methoxy and dimethyl ether species are formed from dissociative adsorption of methanol taking place on the surface Lewis acid-base pairs. For methanol adsorbed on MgO [20], molecularly adsorbed methanol, methoxy species, and basic hydroxyl groups on magnesium were identified. Density Functional Theory (DFT) studies showed that coordination of oxygen and magnesium atoms determine the surface reactivity [21].

In this work, methanol has been used to probe the chemical reactivity of mixed oxide pillared MCM-36 materials. Materials based on single and mixed oxides of SiO_2, Al_2O_3, MgO pillars are discussed.

7.2 Experimental

The MCM-22 precursor (Si/Al = 11.4) was synthesized under static conditions following the procedure of Rubin *et al.* [2, 22] and modified by He *et al.* [23]. Crystalline MCM-22 was prepared from the precursor washed with water, dried at room temperature in air, and finally calcined at 823 K under flowing N_2 with 8% O_2 for 48 h. For the MCM-36 synthesis [23], the non-dried and non-calcined precursor was swollen with aqueous solutions of hexadecyltrimethylammonium chloride (CTMACl, 25%) and tetrapropylammonium hydroxide (TPAOH, 40%) at relative weight ratios MCM-22 (P) / CTMACl / TPAOH equal to 1:4:1.2, and pH adjusted to 13.5 with an NaOH solution, then treated with tetraethoxysilane (TEOS) hydrolyzed in water, dried, and finally calcined analogous to MCM-22, yielding SiO_2-MCM-36. The other pillared materials were prepared using the Al_2O_3 or MgO-Al_2O_3-pillaring solutions with or without TEOS, as described in detail by Barth *et al.* [4, 5].

The Si/Al ratios were determined by atomic absorption spectroscopy (AAS, UNICAM 939). The structure of all zeolite materials was proved by powder X-ray diffraction (XRD) recorded with a Philips XPERT PRO diffractometer (CuK_α). Nitrogen adsorption isotherms were measured with PMI sorptometer (77.4 K, samples activated *in situ* at 673 K for 20 h). Scanning electron micrographs (SEM) and transmission electron micrographs (TEM) were recorded with JEOL 500 and JEOL 2010, respectively. The acid/base properties were probed by (i) adsorption of pyridine, CO_2, and MeOH followed by *in situ* IR spectroscopy (Bruker IFS-88) at 373 K under partial pressures of 10^{-3} to 1 mbar and (ii) temperature programmed desorption of ammonia (QMG 420 mass spectrometer) after adsorption from the gas phase. The zeolite samples for the IR studies were pressed into self-supporting wafers (ca. 5 mg) and activated at $p < 10^{-6}$ mbar and 723 K for 30 min (10 $K \cdot min^{-1}$). The physisorbed bases were removed by evacuation at $p < 10^{-6}$ mbar for 1 h and desorbed by heating from 373 to 723 K (2 $K \cdot min^{-1}$). All spectra were baseline corrected between 3800 and 1300 cm^{-1} and normalized to the integral peak area of the overtones of the framework vibrations in the range of 2100-1735 cm^{-1}.

7.3 Results and Discussion

The chemical analysis (Table 7.1) and structural properties of the materials studied have been described elsewhere [4]. The BET surface areas, mesoporosity (BJH) and the micropore volumes (*t*-plot) have been evaluated from nitrogen adsorption isotherms. The sample compositions have been determined with AAS and EDX analysis; while crystal structures were proved by XRD. Intercalation of (mixed) oxide pillars between MCM-22 layers has yielded MCM-36 type materials in the case of all oxides used. The XRD patterns (Figure 7.1) correspond well to those reported in the literature for MCM-22 and MCM-36 [1, 23, 24]. At the transfer of MCM-22 precursor into MCM-36, the *hk0* reflections remain unchanged (unaffected are *100*, *220*, and *310* at $2\theta = 7.2°$, 25.1°, and 26.1°; CuKα), while the expansion of the MCM-22 along the crystallographic c-axis causes a shift and broadening of hkl reflections. Upon swelling, the *001* (3.2°) and *002* (6.5°) reflections of the MCM-22 precursor disappeare. The new *c*-parameter of MCM-36 is reflected in an intense low angle peak at about 1.6° corresponding to a *d*-spacing of about 5 nm and an interlayer distance of about 2.5 nm.

Table 7.1 Elemental composition of the MCM-22 and MCM-36 materials studied (AAS analysis for all materials except MgO-Al_2O_3-MCM-36 investigated with EDX surface analysis).

Sample	Si/Al	Si [wt.%]	Al [wt.%]	Na [wt.%]	Mg [wt.%]
MCM-22	11.4	45.4	3.9	0.3	---
SiO_2-MCM-36	25.9	43.1	1.6	< 0.1	---
Al_2O_3-MCM-36	6.2	36.5	5.7	< 0.1	---
MgO-Al_2O_3-MCM-36	1.3	27.9	21.3	< 0.1	0.6
Al_2O_3-SiO_2-MCM-36	10.3	41. 7	3.9	< 0.1	---
MgO-Al_2O_3-SiO_2-MCM-36	8.9	39.9	4.3	< 0.1	0.2

7.3.1 Infrared spectra of activated materials

All materials have exhibited Brønsted acid OH groups (~3624 cm^{-1}), terminal and internal silanol groups (3746 and 3729 cm^{-1}, respectively), and varying concentration of OH groups on Lewis acid extra framework aluminum species (3673 cm^{-1}) in their activated form (Figure 7.2) [3, 23]. The expansion of the distances between the MCM-22 layers and the incorporation of (mixed) oxide pillars is concluded to be the reason for

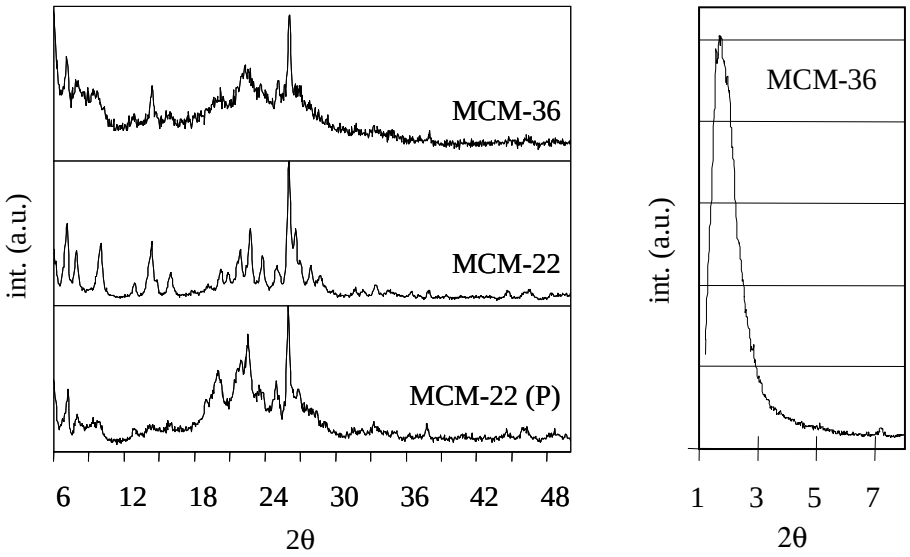

Figure 7.1 Powder X-ray diffraction patterns of MCM-22 (P) precursor, MCM-22 and MCM-36 (full range and low angle).

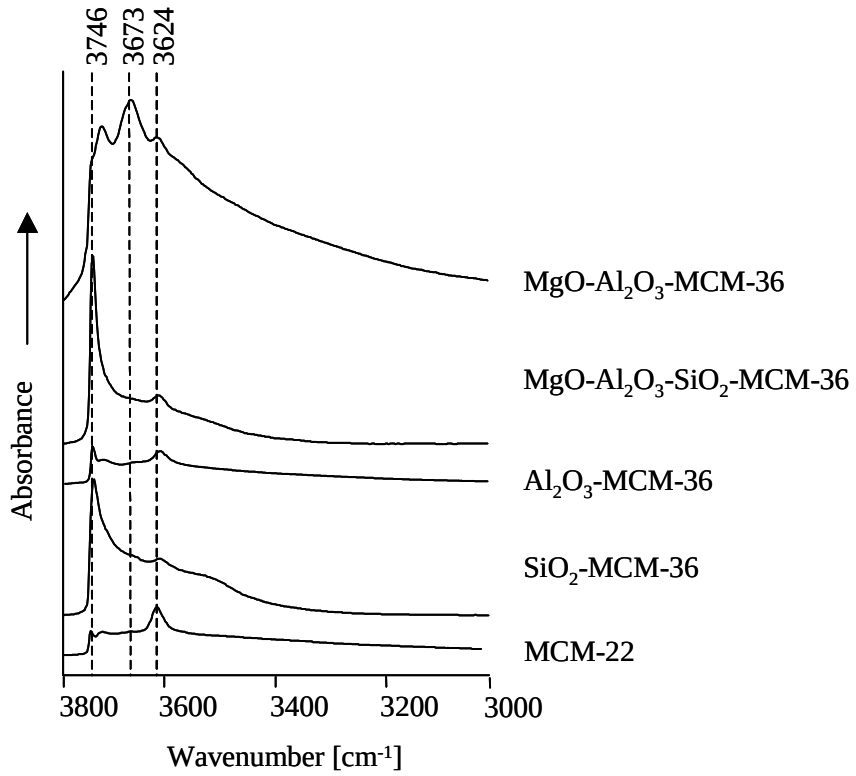

Figure 7.2 IR spectra of the hydroxyl region for MCM-22 and four MCM-36 derivatives; T = 308 K, $p < 10^{-6}$ mbar.

the increased concentration of surface OH groups, i.e., silanol groups on SiO_2-MCM-36. In analogy to γ-alumina [25], the bands between 3700 and 3640 cm^{-1} are attributed to hydrogen bonded hydroxyl groups for Al_2O_3-MCM-36. A broadening of the bands, seen for all materials except MgO-Al_2O_3-SiO_2-MCM-36, points to a wide distribution of different hydroxyl groups on these pillars. For MgO-Al_2O_3-SiO_2-MCM-36, a sharp and intense band of terminal silanols was observed, while the band of hydroxyl stretching vibrations of internal silanol groups was weak. This indicates that the concentration of isolated, terminal silanol groups increased after intercalation of MgO-Al_2O_3-SiO_2 into MCM-36 and that well structured pillars are formed compared to SiO_2-MCM-36 having a low number of defect sites. The presence of MgO caused a band at 3740 cm^{-1} attributed to MgOH groups [26]. The lower concentration of MgOH groups in silica containing MgO-Al_2O_3-SiO_2-MCM-36 is attributed to the low concentration of alkaline earth metal cations in those materials.

7.3.2 Interaction of methanol with the zeolitic Brønsted acid sites on MCM-22

After methanol adsorption, the difference spectra of all materials (Figure 7.3) showed negative OH bands (3745 - 3600 cm^{-1}) indicating a marked decrease in the intensity of these bands after contact with methanol. For MCM-22, the strongest decrease was found for the band at 3622 cm^{-1} indicating that the interaction of methanol with the Brønsted acid sites dominated at low equilibrium pressures. A similar observation was previously made for HZSM-5 [27]. Four broad bands appeared at 3530, 2900, 2500, and 1700 cm^{-1}. The first one is assigned to the weakly perturbed OH group of methanol and the other to the triplet (ABC) band of strongly perturbed zeolitic OH groups [28]. The complex structure is attributed to combinations of the (perturbed) hydroxyl stretching band and Si-OH (or Al-OH) bending modes due to Fermi resonance. All of them are broadened by combining with low-frequency modes, such as the stretching of hydrogen bridge bonded OH of methanol [29]. Similar infrared spectra have been observed previously also for other zeolites [30].

A comparable concentration of Brønsted acid sites accessible to pyridine [5] was found with MCM-22 and the MCM-36 materials, which indicates that Brønsted acid OH groups located in the zeolitic layer of MCM-36 are accessible and the pore structure of the crystalline layer was not severely modified by the preparation

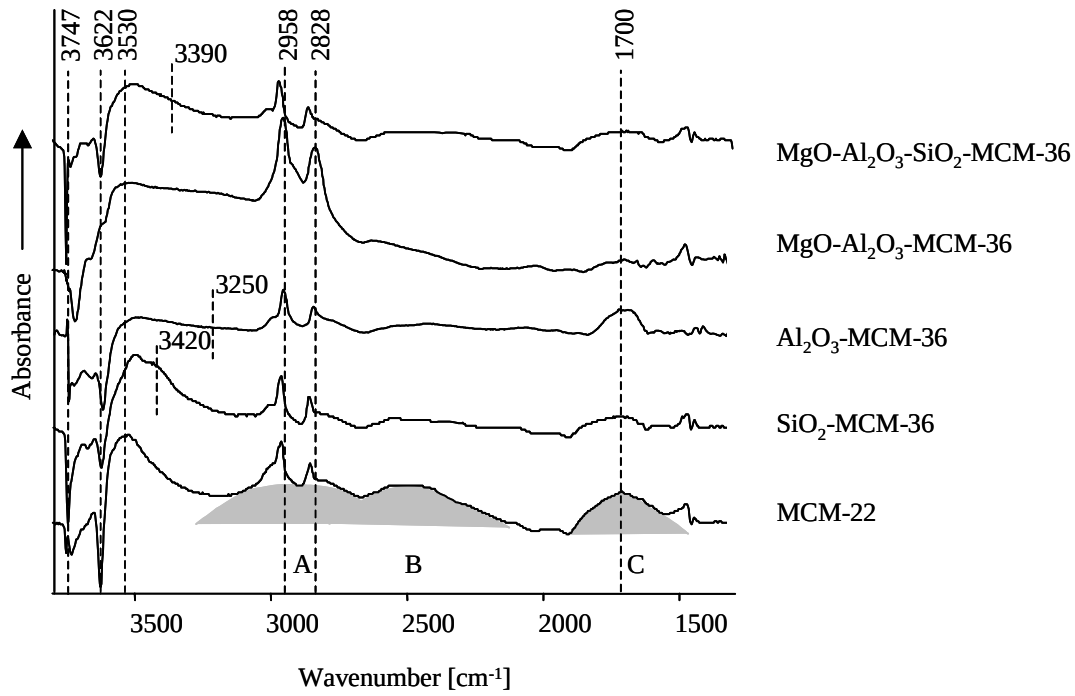

Figure 7.3 Difference IR spectra of MCM-22 and MCM-36 derivatives after adsorption of methanol, 10^{-3} mbar, 308 K.

procedure. Thus, the appearance of the negative band at 3622 cm^{-1} together with the ABC pattern (though of lower intensity) after methanol adsorption is attributed to the interaction of methanol with Brønsted OH groups inside the zeolite layer. For MgO-Al_2O_3-MCM-36 the Brønsted acid OH band seems to be overlapped.

The bands at 3008 (shoulder), 2991, 2969 (shoulder), 2959 are attributed to asymmetric $\nu(CH_3)$ stretching vibrations of methanol on MCM-22 (3008 and 2991 cm^{-1} are also related to center rotational bands). The 2920 cm^{-1} band is an overtone or a combination of methyl deformation modes, while the 2853 cm^{-1} band is due to symmetric CH stretching vibration [29, 31]. All bands are assigned to methanol adsorbed on the Brønsted acid sites, while the shoulder at 2969 cm^{-1} is tentatively attributed to the interaction between methanol and silanol groups. The higher wavenumber of the symmetric stretching vibration (2853 cm^{-1}), as compared to that of methanol vapor (2844 cm^{-1}) [32], is attributed to a minor strengthening of the CH bonds in response to the weakening of the CO bonds when methanol interacts with a metal cation [33].

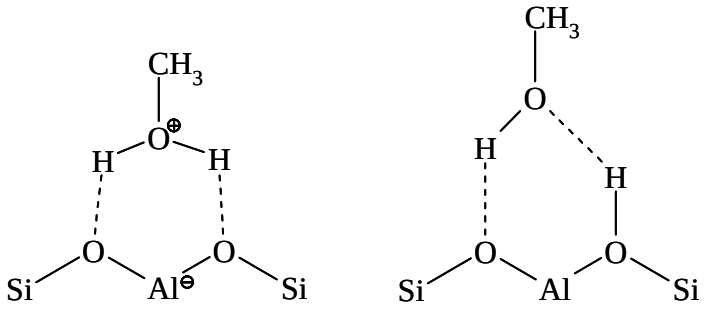

ion-pair complex neutral complex

Figure 7.4 Adsorption structures of methanol coordinated to Brønsted acid sites.

The assumed adsorption structure of methanol bound with two hydrogen bonds to the Brønsted acid site is shown schematically in Figure 7.4. Note, that such hydrogen bonded structures are well known for water and methanol in liquid phase [8]. *Ab initio* molecular dynamics simulations [34] show that the formation of an ion-pair adsorption complex resulting in oxonium ion is less stable than the neutral complex and may exist only in special geometric environments.

7.3.3 Adsorption of methanol on (mixed) oxide pillared MCM-36 materials

The Si-OH and Al-OH bands at 3745 and between 3700-3640 cm^{-1} of the silica and alumina pillars from the interlayer galleries decrease also strongly upon methanol adsorption. The mesoporosity together with the high surface area are concluded to enhance the interaction of methanol with the surface hydroxyl groups. Already at $1 \cdot 10^{-3}$ mbar equilibrium pressure a broad band between 3600 and 3000 cm^{-1} was found with maxima at 3494 and 3420 cm^{-1} for SiO_2-MCM-36 and at 3250 cm^{-1} for Al_2O_3-MCM-36. For both materials, a further increase of this band with increasing sorbate pressure was seen. These bands have also been observed for methanol adsorbed on pure oxides [25, 35, 36]. Moreover, methanol is known to interact strongly with the Lewis acid-base pairs on aluminum oxide surfaces [19]. In total, three different types of species have been detected resulting from methanol adsorption on alumina activated at 773 K and are assigned to a bridging methoxy species, coordinated to two Al^{3+} Lewis acid sites, methanol molecules strongly chemisorbed to a single Lewis acid site, and methanol molecules hydrogen bonded to surface hydroxyl groups or surface oxygen ions.

The ν(OH) stretching region of MgO-Al_2O_3-MCM-36 shows high intensities and larger widths after exposure to methanol than in the case of the more acidic materials SiO_2- and Al_2O_3-MCM-36. Besides the typical surface ν(OH) stretching bands (3743, 3663, and 3620 cm^{-1}) of methanol interacting with silanol groups and acid sites, the strong negative band at 3730 cm^{-1} indicates marked adsorption on Mg-OH groups. A broad band in the hydroxyl-stretching region between 3700 and 2200 cm^{-1} accompanied the decrease of the surface hydroxyl stretching bands. Methanol molecules, dissociatively and associatively adsorbed on the pillars, have been assumed to contribute with a broad band at 3700-3400 cm^{-1} (surface hydroxyl groups) and with a small, flat band at even lower frequencies (hydrogen bonded methanol, maximum at around 3150 cm^{-1}), respectively.

The high intensity of the negative band at 3740 cm^{-1} already at low equilibrium sorbate pressures ($1 \cdot 10^{-3}$ mbar) for MgO-Al_2O_3-SiO_2-MCM-36 indicates interaction to a larger number of terminal Si-OH groups. This increased concentration of Si-OH groups is in line with the larger surface area after pillaring. Note that strong Brønsted acid sites are formed during synthesis on the oxide pillars of MgO-Al_2O_3-SiO_2-MCM-36, while strong basic properties were not observed by CO_2 adsorption on this material [5]. Thus, we attribute the broad band at 3390 cm^{-1} to the adsorption of methanol on strong Brønsted acid sites present in the interlayer gallery.

The $\nu(CH_3)$ stretching modes associated to methanol coordinated to Brønsted acid sites (2991, 2969 (shoulder), 2959, and 2858 cm^{-1}) were clearly seen for the silica containing materials at low equilibrium methanol pressures. At increased concentration of acid sites, e.g., for alumina pillared materials, as also at higher loading, those methyl vibration bands are mostly overlapped due to the presence of several bands associated to methanol interacting with different sites. Infrared spectra of methanol adsorbed on Al_2O_3-MCM-36 exhibited bands at 3004, 2967, 2920, and 2856 cm^{-1} indicating that molecularly adsorbed methanol predominated also on the alumina pillars at low methanol pressures. For the (basic) MgO-Al_2O_3-MCM-36, the ν(CH) methyl vibration modes were broadened and shifted to lower wavenumbers (2951 and 2833 cm^{-1}) indicating interaction between the methyl group and the basic oxygen of the pillar.

7.3.4 Reaction of methanol on Al_2O_3-MCM-36

Only for Al_2O_3-MCM-36, drastic changes were seen in the $\nu(CH_3)$ stretching region with increasing pressure (Figure 7.5). New frequencies at 2942 and 2882 (shoulder) cm^{-1} appeared at pressures of $5 \cdot 10^{-3}$ mbar, indicating dissociation of methanol. In analogy to the assignment for the vibrational spectra of gaseous and liquid dimethyl ether by Kanazawa and Nukada [37], as well as of dimethyl ether adsorbed on alumina [38], those bands may be assigned to dimethyl ether formed from methanol at 308 K on the alumina surface. An assignment of the frequency at 2942 cm^{-1} to methoxy groups is also conceivable. The bands of asymmetric and symmetric $\nu(CH_3)$ vibrations of methoxy species on alumina [5, 19] were reported at 2950-2940 and 2850-2840 cm^{-1}, respectively. Note that the symmetric one would then to be superimposed in our spectrum by the broad band 2856 cm^{-1}.

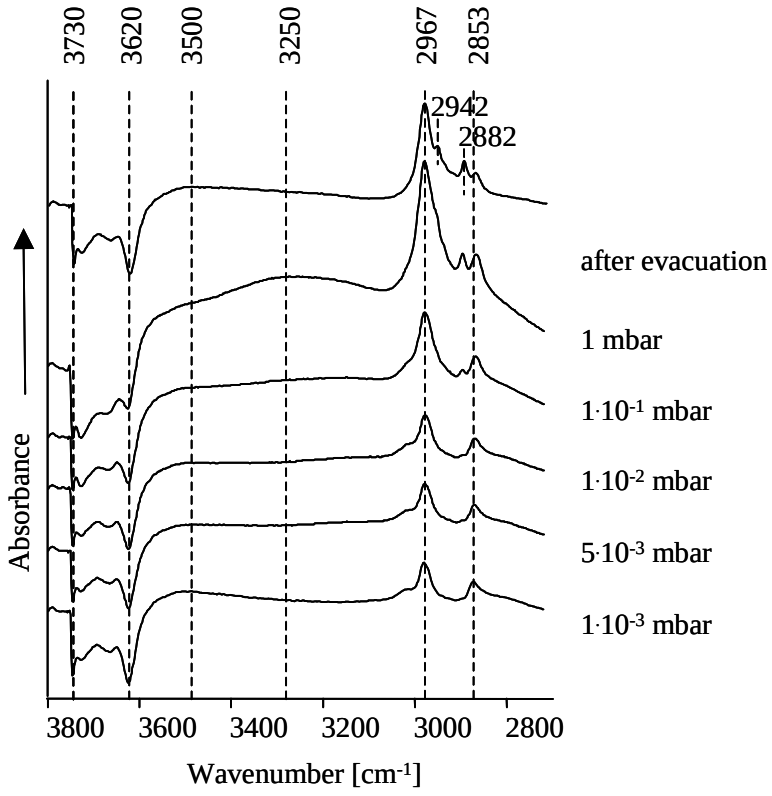

Figure 7.5 Infrared spectra of methanol adsorbed on Al_2O_3-MCM-36 at increasing equilibrium sorbate pressure and 308 K.

After desorption of physisorbed methanol, relatively more silanol groups were restored than aluminum hydroxyl groups and the new bands of hydrocarbon stretching vibrations did not decrease in intensity. From the intensity change of the silanol ν(OH) mode, it is concluded that reversible methanol adsorption occurs on the silanol groups, while dissociation on alumina, forming stable surface species, is related to strong acid-base sites.

7.3.5 Thermal decomposition of adsorbed methanol species

During heating, the broad bands at 3530, 2900, 2440 and 1700 cm^{-1}, assigned to methanol adsorbed on Brønsted acid sites, decreased in intensity and vanished at 498 K. Only MgO-Al_2O_3-MCM-36 exhibited bands in the region of the *ν*(CO) vibration indicating that methanol was oxidized (Figure 7.6). Upon heating to 588 K, stable surface species were formed on MgO-Al_2O_3-MCM-36 as concluded from bands appearing at 1630, 1600, 1580, 1400 and 1390 cm^{-1} and point to a decomposition of methanol. Relatively strong bands remained up to 723 K. The bands are assigned to asymmetric (1630, 1600, and 1580 cm^{-1}) and symmetric (1400 and 1376 cm^{-1}) ν(OCO) stretching vibrations. The δ(CH) deformation mode is assigned to the band at 1390 cm^{-1} [39]. The absence of the ν(C=O) absorption mode (at about 1715 cm^{-1})

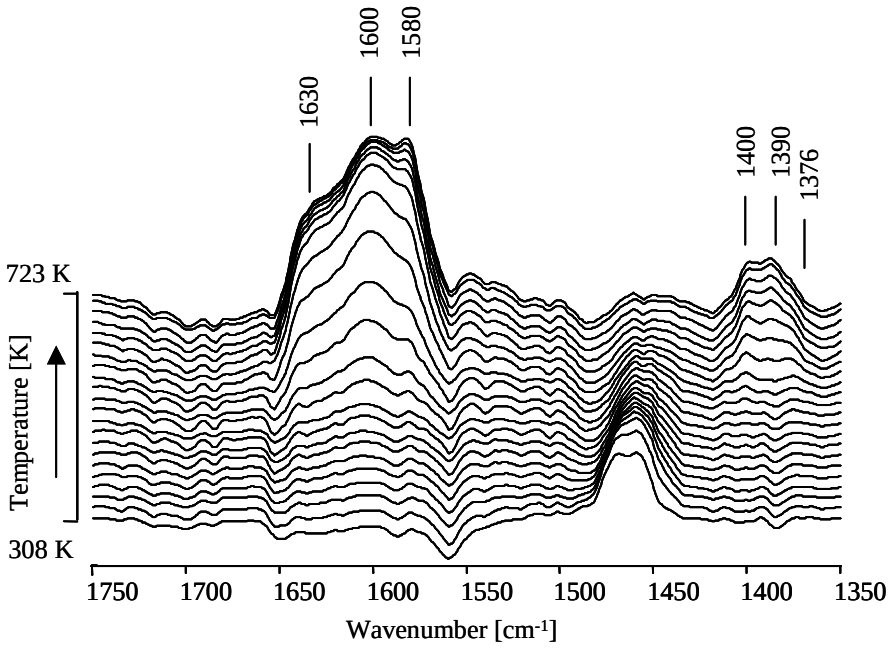

Figure 7.6 Temperature programmed desorption of methanol adsorbed on MgO-Al_2O_3-MCM-36 at 20 $K \cdot spc^{-1}$ and $p < 10^{-6}$ mbar.

indicates that the adsorbed species are due to formates. The observance of three ν_{as}(OCO) is indicative for at least three types of formate species. Results from literature indicate that the bands at 1630 and 1600 cm^{-1} are due to two types of formate species adsorbed on magnesium oxide species (Figure 7.7), while the band at 1585 cm^{-1} may be also attributed to formate species adsorbed on alumina [39]. Note that the pure alumina pillared MCM-36 materials does not show the formation of formate species.

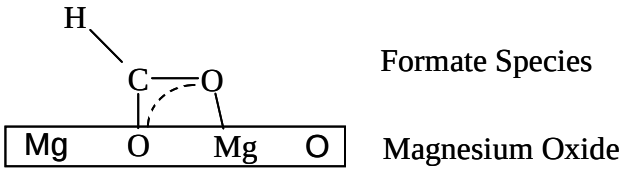

Figure 7.7 Schematical representation of surface formate species on magnesium oxide.

7.4 Conclusions

Pillaring with various (mixed) oxides allows to prepare mesoporous materials, which have accessible zeolitic layers and pillars with differing acid-base properties. The variety of the sites and their number increased by incorporation of the oxide pillars. On all materials, methanol is strongly hydrogen bonded on the Brønsted acid sites at low equilibrium methanol pressure.

With silica-pillared materials a large number of methanol molecules adsorbed on silanol groups already at low equilibrium methanol pressures. With increasing equilibrium pressure, methanol, weakly physisorbed in the interlayer space has been found. Methanol is dissociatively adsorbed on strong Lewis acid-base sites of Al_2O_3-MCM-36. This adsorption structure is enhanced with increasing pressure. The introduction of basic properties in MgO-Al_2O_3-MCM-36 leads to surface methanol structures indicating also strong polarization of CH bonds. During temperature programmed desorption methanol reacts with coordinatively unsaturated oxygen and forms stable formate species in the interlayer galleries.

7.5 Acknowledgements

The work was partially supported by the Deutsche Forschungsgemeinschaft (DFG) within the Sonderforschungsbereich 338.

7.6 References

[1] Roth, W.J.; Kresge, C.T.; Vartuli, J.C.; Leonowicz, M.E.; Fung, A.S.; McCullen, S.B.; *Stud. Surf. Sci. Catal.* **1995**, 94**,** 301.

[2] Rubins, M.K.; Chu, P.; *US Patent 4,954,325* **1990**.

[3] Eder, F.; He, Y.J.; Nivarthy, G.S.; Lercher, J.A. *Recl. Trav. Chim. Pays-Bas* **1996**, 115, 531.

[4] Barth, J.-O.; Kornatowski, J.; Lercher, J.A. *J. Mater. Chem*. **2002**, 12, 369.

[5] Barth, J.-O.; Jentys, A.; Kornatowski, J.; Lercher, J.A. *Chem. Mater*. **2004**.

[6] Zecchina, A.; Spoto, G.; Ricchiardi, G.; Bordiga, S.; Bonino, F.; Prestipino, C.; Lamberti, C.; *Stud. Surf. Sci. Catal*. **2002**, 142, 3.

[7] Corma, A.; Corell, C.; PerezPariente, J. *Zeolites* **1996**, 16, 7.

[8] Meloni, D.; Laforge, S.; Martin, D. *Appl. Catal. A - Gen*. **2001**, 215, 55.

[9] Ryczkowski, J.; *Catal. Today* **2001**, 68, 263.

[10] Lercher, J.A.; Gründling, Ch.; Eder-Mirth, G. *Catal. Today* **1996**, 27, 353 and refs therein.

[11] Kagel, R.O. *J. Phys. Chem*. **1967**, 71, 844.

[12] Meisel, S.L.; McCullogh, J.P.; Lechthaler, C.H.; Weisz, P.B. *Chem. Tech*. **1976**, 6, 86.

[13] Kaeding, W.W.; Chu, C.; Young, L.B.; Weinstein, B.; Butter, S.A. *J. Catal*. **1981**, 67, 159.

[14] Stoecker, M. *Micropor. Mesopor. Mater*. **1999**, 29, 3.

[15] Lee, S.C.; Lee, S.W.; Kim, K.S.; Lee, T.H.; Kim, D.H.; Kim, J.C. *Catal. Today* **1998**, 44, 253.

[16] Rep, M.; Palomares, A.E.; Eder-Mirth, G.; van Ommen, J.G.; Rösch, N.; Lercher, J.A. *J. Phys. Chem. B* **2000**, 104, 8624.

[17] Wovchko, E.A.; Camp, J.C.; Glass, J.A.; Yates, J.T. *Langmuir* **1995**, 11, 2592.

[18] Pelmenschikov, A.G.; Morosi, G.; Gamba, A. *J. Phys. Chem. A* **1997**, 101, 1178 and refs. therein.

[19] Busca, G.; Rossi, P.; Lorenzelli, V.; M. Benaissa, M.; Travert, J.; Lavalley, J.-C. *J. Phys. Chem.* **1985**, 89, 5433.

[20] Tench, A.J.; Giles, D.; Kibblewhite, J.F.J. *Trans. Faraday Soc*. **1971**, 67, 854.

[21] Branda, M.M.; Ferullo, R.M.; Belelli, P.G.; Castellani, N.J. *Surf. Sci*. **2003**, 527, 89.

[22] Leonowicz, M.E.; Lawton, J.A.; Lawton, S.L.; Rubbin, M.K. *Science* **1994**, 264, 1910.

[23] He, Y.J.; Nivarthy, G.S.; Eder, F.; Seshan, K.; Lercher, J.A. *Micropor. Mesopor. Mater*. **1998**, 25, 207.

[24] Roth, W.J.; Vartuli, J.C.; Kresge, C.T. *Stud. Surf. Sci. Catal*. **2000**, 129**,** 501.

[25] Peri, J.B. *J. Phys. Chem*. **1965**, 69, 211.

[26] Lercher, J.A. *Z. Phys. Chem*. **1982**, 129, 209.

[27] Mirth, G.; Lercher, J.A.; Anderson, M.W.; Klinowski, J. *J. Chem. Soc. Faraday Trans*. **1990**, 86, 3039.

[28] Haase, F.; Sauer, J. *Mircopor. Mesopor. Mater*. **2000**, 35-36, 379.

[29] Pelmenschikov, A.G.; Morosi, G.; Gamba, A.; Yecchina, A.; Bordiga, S.; Paukshtis, E.A. *J. Phys. Chem*. **1993**, 97, 11979.

[30] Fujino, R.; Kashitani, M.; Kondo, J.N.; Domen, K.; Hirose, C.; Ishida, M.; Goto, F.; Wakabayashi, F. *J. Phys. Chem*. **1996**, 100, 11649 and refs. therein.

[31] Natal-Santiago, M.A.; Dumesic, J.A. *J. Catal*. **1998**, 175, 252.

[32] Serallach, A.; Meyer, R.; Günthard, Hs.H *J. Mol. Spectr*. **1974**, 52, 94.

[33] Vayssilov, G.N.; Lercher, J.A.; Rösch, N. *J. Phys. Chem. B* **2000**, 104, 8614.

[34] Haase, F.; Sauer, J.; Hutter, J. *Chem. Phys. Lett*. **1997**, 266, 397.

[35] Boiadjiev, V.; Tysoe, W.T. *Chem. Mater*. **1998**, 10, 334.

[36] Hannan, R.B. *J. Phys. Chem*. **1960**, 64, 1526.

[37] Kanazawa, Y.; Nukada, K. *Bull. Chem. Soc. Jpn*. **1962**, 35, 612.

[38] Chen, J.G.; Basu, P.; Ballinger, T.H.; Yates J.T., Jr. *Langmuir* **1989**, 5, 352.

[39] Busca, G.; Lamotte, J.; Lavalley, J-C.; Lorenzelli, V. *J. Am. Chem. Soc*. **1987**, 109, 5197.

Chapter 8

General conclusions

Successful combination of economic efficiency and environmental protection in catalyzed industrial processes efforts a directed design of catalysts, which can maximize selectivity and yield and simultaneously minimize costs and waste. Zeolitic materials are very promising materials for heterogeneous catalysis. The particular advantages of molecular sieves (zeolites) as catalysts in comparison with non-functionalized macro- and mesoporous oxides are connected with several factors: (i) The high surface density of active sites (in comparison with oxides) results in very active catalysts. (ii) The defined pore structure allows the reactants to be not converted and/or the products to be formed or transported out of the pores. (iii) The active site and the environment of that site can be designed on the atomic level for example by ion exchange or chemical functionalization of the framework. (iv) The crystalline nature of the material allows of tailoring the chemical properties of molecular sieves in a more subtle way than in macro- and mesoporous oxides.

In contrast to the acidic form in which the role of the active sites in catalyzed reactions is well characterized, zeolites of basic properties are less determined. This is related to the fact that the number and strength of the basic sites, i.e., the negatively charged oxygen atom of the zeolite framework on zeolites with basic properties, depends on the structure as well as on the chemical composition of the material. In addition, the basic zeolites typically contain alkali cations, which also act as (weak) Lewis acid sites.

The aim of this thesis was to gain more knowledge on sorption and self-organization of small polar molecules on micro- and mesoporous zeolitic materials in the absence of Brønsted acid sites. The combination of inelastic neutron scattering (INS) and infrared (IR) spectroscopy was used to study the sorption structure of linear alcohols (C_1 to C_4) on faujasite (zeolite X) samples exchanged with alkali metal cation (Na, K, Rb, Cs). The influence of the charge balancing cations in the exchanged zeolite X and of the alkyl chain length on the sorption structure is discussed in Chapter 2 and 3, respectively. Very broad bands of the ν(OH) stretching vibrations were observed in the IR spectra after adsorption of the linear alcohols, which reflect from the coordination of the oxygen atom of the alcohol to the exchanged cation and hydrogen bonding of the OH groups of the adsorbed alcohol with the negatively charged framework O atoms. The shape of the ν(OH) band in the IR spectra and the broad $\delta(OH)_{op}$ band in INS confirm the presence of at least one

other sorption structure for alcohol molecules in alkali metal cation exchanged faujasite. Due to the high density of the sites and the closeness of the exchanged cations in zeolite X, alcohol molecules adsorbed at neighboring counter cations may interact and form presumably ring-like structures. At low sorbate loading, alcohol molecules were mainly adsorbed on the counter cations located in SIII' positions (the energetically preferred sites), while the formation of clusters can be excluded. Self-association of methanol forming the crystalline α-phase inside the faujasite cages has not been observed. It has been observed that, with decreasing electrostatic potential of the charge balancing cation, the interaction of the hydrogen atoms of the hydroxyl and alkyl groups with the framework increases, although this does not result in an increased binding energy. The more uniform and strongly hydrogen-bonded sorption structure points to the formation of ring-like methanol structures on these samples.

For a given zeolite X sample, the interactions of C_1-C_4 alcohols in the faujasite cage with the framework O atoms and between the molecules have been found to be similar. The both sorption structures have been observed independent by the alcohol chain length. All sorbates showed hydrogen bonding of the alkyl groups inducing frequency shifts of the ν(CH) stretching bands. Interaction of the CH-protons with the polar framework of zeolite X has been concluded. Comparable changes in the ν(CH) stretching frequencies and widths of the ν(CH) bands have not been observed for alcohols adsorbed on apolar Na-ZSM-5.

Chapter 4 focuses on the dependence of the polarity of short alcohols and amines on their adsorption structures in alkali metal cation exchanged X zeolites. Similar sorption structure have been found for the short polar *n*-amines (C_1, C_3) and their homologues alcohols. Besides the coordination of the N atom to the exchanged cation, both protons of the NH_2 groups form hydrogen bonding interactions to the zeolite framework. Also for short amines, hydrogen bond formation of the alkyl groups has been observed. The main difference in adsorption of amines and alcohols is a lower perturbation of the functional groups. Weaker hydrogen bonds between the NH group and the framework result from the lower polarity of the amine groups. The absence of the second sorption structure including additional sorbate-sorbate interactions with neighboring sorbate molecules has not been observed for the amine molecules due to the presence of only one lone pair electron pair at the nitrogen atom.

The dimensions of the channels and cavities of zeolites limit their application in the adsorption of larger molecules. One possibility to overcome these limitations is to generate mesopores by incorporation of oxide pillars between the layers of a laminar zeolite precursor. Another way is the delamination of the laminar precursor. By these methods MCM-36 und ITQ-2 can be synthesized, respectively. The two materials belong to the crystallographic family of zeolite MCM-22 but show a more open structure.

The role of the synthesis routes, their modification (synthesis under static and rotating conditions) and of the chemical composition (Al content) of the MCM-22 precursors for transformation into ITQ-2 (MCM-22 monolayers) are discussed in Chapter 5. The delamination has been favored by decreasing aluminum content of the parent material and yields best results at Si/Al ratios higher than 20. A higher delamination is related to a lower charge density of the framework at lower Al content, which results in weaker interactions between the zeolitic layers. The delamination degree is reflected in increasing surface areas and a better accessibility to acid sites located at the external surface of the ITQ-2 layers for sterically demanding probe molecules (2,6-DTBPy). For materials with Si/Al ratio below 15, molecular sieves with structures similar to MCM-56 and pure Si-Ferrierite have been observed. The transformation process has been performed under conditions close to those of zeolite dissolution. Thus, partial structural decomposition as well as reorganization are conceivable. In addition, delamination of the precursor materials is accompanied by significant amorphization and desilication increased for materials having high Si content.

Chapter 6 deals with the adsorption of alcohols on alkali metal cation exchanged MCM-22 and its structurally related materials MCM-36 and ITQ-2. Adsorption of the sterically demanding base 2,6-DTBPy on the Brønsted acidic materials has shown the accessibility to active Brønsted acid OH-groups to be enhanced with increasing interlayer space (MCM-36) or degree of delamination (ITQ-2). The larger concentration of 2,6-DTBPy adsorbed on ITQ-2 fits well to the higher number of Brønsted acid hydroxyl groups located in the supercages of MCM-22. The low aluminum content of MCM-22 and the resulting low negative charge on the oxygens of the zeolite framework in the alkali metal cation exchanged materials have impeded hydrogen-bond formation between the alcohol molecules adsorbed and the zeolite framework, leading to quasi-isolated alcohol molecules coordinates to the exchanged

cations. On cation exchanged MCM-36 and ITQ-2, methanol coordinates in a identical way as on MCM-22 with the alkali metal cations, but sorbate clustering occurs in the interlayer galleries of MCM-36 and in sheet aggregates of ITQ-2. Due to the exposure of a high number of active sites on the external surface, adsorption equilibrium is reached faster on ITQ-2 than MCM-22. Low pH value, at which the cation exchange of H-MCM-36 has to be preformed, causes incomplete exchange. The presence of the Brønsted acid sites leads to the dehydration of methanol and 1-propanol producing dimethylether and propene. It is important for catalytic reactions requiring the absence of Brønsted acid sites and complete cation exchange has to be ensured. For ITQ-2 materials, a complete exchange of Brønsted acid protons by alkali metal cations is given. For catalysis by strong bases the concentration of aluminum in the framework should to be increased, although this leads in turn to difficulties in the delamination procedure.

The relation between the composition of mixed oxide pillars of basic properties introduced into H-MCM-36 and the alcohol sorption behavior are discussed in Chapter 7. The introduction of (mixed) oxides allows the preparation of mesoporous materials, which have accessible zeolitic layers and pillars with differing acid-base properties. However, the increased accessibility as well as the enhanced number and types of active sites lead to various sorption structures. Methanol is associatively adsorbed on Brønsted acid sites in the zeolitic layers and associatively and dissociatively adsorbed on acid and basic sites in the mesopores. Strong basic sites present on MgO-Al_2O_3-MCM-36 have led to stable formates upon heating the material saturated with methanol.

All together, the short polar alcohols and amines adsorbed on alkali metal exchanged faujasites of high framework polarity (zeolite X), have one adsorption structure in common: the sorbate coordinate on the exchanged cation via the O or N atom and form simultaneously hydrogen bonds between its functional groups as well as alkyl protons and the oxygens of the polar zeolite framework. Only in the case of alcohol molecules, a second sorption structure including sorbate-sorbate interactions is possible.

For the layered mesoporous materials (ITQ-2) the lateral hydrogen bonds are minimal. It can be overcome by an increase of the aluminum content in the zeolite layers, thus, zeolite polarity. However, a higher polarity is unfavorable for to the

degree of exfoliation of the MCM-22 layers. This increases in the reverse order of Al content, thus zeolite polarity. Alkali metal cation exchanged ITQ-2 seems to be well suited as support of catalyst combining fast establishment of the adsorption-desorption equilibrium and complete absence of Brønsted acidity. The absence of strong Brønsted acid OH groups as well as strong basic sites is indispensable for alcohol desorption without reaction.